SHAFT TRANSDUCERLESS VECTOR CONTROL OF THE INTERIOR
PERMANENT MAGNET MOTOR WITH SPEED AND POSITION ESTIMATION
USING HIGH FREQUENCY SIGNAL INJECTION AND FLUX OBSERVER
METHODS

A THESIS SUBMITTED TO
THE GRADUATE SCHOOL OF NATURAL AND APPLIED SCIENCES
OF
MIDDLE EAST TECHNICAL UNIVERSITY

BY

ÖMER GÖKSU

IN PARTIAL FULFILLMENT OF THE REQUIREMENTS
FOR
THE DEGREE OF MASTER OF SCIENCE
IN
ELECTRICAL AND ELECTRONICS ENGINEERING

MAY 2008

Approval of the thesis:

SHAFT TRANSDUCERLESS VECTOR CONTROL OF THE INTERIOR PERMANENT MAGNET MOTOR WITH SPEED AND POSITION ESTIMATION USING HIGH FREQUENCY SIGNAL INJECTION AND FLUX OBSERVER METHODS

submitted by **ÖMER GÖKSU** in partial fulfillment of the requirements for the degree of **Master of Science in Electrical and Electronics Engineering Department, Middle East Technical University** by,

Prof. Dr. Canan Özgen   _____
Dean, Graduate School of **Natural and Applied Sciences**

Prof. Dr. İsmet Erkmen   _____
Head of Department, **Electrical and Electronics Engineering**

Assist. Prof. Dr. Ahmet M. Hava   _____
Supervisor, **Electrical and Electronics Engineering Dept., METU**

Examining Committee Members:

Prof. Dr. Kemal Leblebicioğlu   _____
Electrical and Electronics Engineering Dept., METU

Assist. Prof. Dr. Ahmet M. Hava   _____
Electrical and Electronics Engineering Dept., METU

Prof. Dr. Murat Eyüboğlu   _____
Electrical and Electronics Engineering Dept., METU

Prof. Dr. Aydın Ersak   _____
Electrical and Electronics Engineering Dept., METU

Assist. Prof. Dr. Metin Aydın   _____
Mechatronics Engineering Dept., Kocaeli University

Date: 08/05/2008

I hereby declare that all information in this document has been obtained and presented in accordance with academic rules and ethical conduct. I also declare that, as required by these rules and conduct, I have fully cited and referenced all material and results that are not original to this work.

Name, Last name : Ömer Göksu

Signature   :

ABSTRACT

SHAFT TRANSDUCERLESS VECTOR CONTROL OF THE INTERIOR
PERMANENT MAGNET MOTOR WITH SPEED AND POSITION ESTIMATION
USING HIGH FREQUENCY SIGNAL INJECTION AND FLUX OBSERVER
METHODS

Göksu, Ömer

M.S., Department of Electrical and Electronics Engineering

Supervisor: Assist. Prof. Dr. Ahmet M. Hava

May 2008, 223 pages

In this thesis, shaft transducerless vector control of Interior Permanent Magnet (IPM) motor with speed and position estimation using saliency based high frequency signal injection and fundamental model based flux observer methods will be investigated. The magnetic saliency characteristic of a 2.2-kW IPM motor will be experimentally extracted by means of high frequency signal injection. High frequency signal injection method will be used to estimate the speed and position at zero and low speed based on the magnetic saliency of the IPM motor. At high speed, fundamental model based flux observer method will be utilized for speed and position estimation. Seamless transition between the two estimation methods will be provided. Using the estimated speed and position information, the motor will be closed loop vector controlled and the drive motion performance over wide speed and load range will be investigated. The IPM motor drive and the estimation/control algorithms will be modeled and their performance will be demonstrated by detailed computer simulations. A three-phase voltage source inverter and a motor test bench will be built, and the estimation/control algorithms will be implemented on a DSP based

motor control platform. The IPM motor drive system will be tested in the laboratory and the theory and simulation results will be verified by the experiments.

ÖZ

DAHİLİ SÜREKLİ MIKNATISLI MOTORUN YÜKSEK FREKANSLI İŞARET UYGULAMA VE AKI GÖZLEMLEME YÖNTEMLERİ KULLANILARAK HIZ VE KONUM KESTİRİMLİ MİL DUYARGASIZ VEKTÖR DENETİMİ

Göksu, Ömer

Yüksek Lisans, Elektrik ve Elektronik Mühendisliği Bölümü

Tez Yöneticisi: Yrd. Doç. Dr. Ahmet M. Hava

Mayıs 2008, 223 sayfa

Bu tezde, dahili sürekli mıknatıslı motorun, manyetik çıkıntıya dayalı yüksek frekanslı işaret uygulama ve temel modele dayalı akı gözlemleme yöntemleri kullanılarak konum ve hız kestirimli mil duyargasız vektör denetimi araştırılacaktır. 2.2-kW gücünde dahili sürekli mıknatıslı bir motorun manyetik çıkıntı karakteristiği yüksek frekanslı işaret uygulama yolu ile deneysel olarak çıkarılacaktır. Dahili sürekli mıknatıslı motorun manyetik çıkıntı özelliğini kullanan yüksek frekanslı işaret uygulama yöntemi sıfır ve düşük hızlarda hız ve konum kestirimi için kullanılacaktır. Yüksek hızlarda hız ve konum kestirimi için temel modele dayalı akı gözlemleyicisi yönteminden yararlanılacaktır. İki kestirim yöntemi arasında yumuşak geçiş sağlanacaktır. Kestirilen hız ve konum bilgileri kullanılarak, motor kapalı döngü vektör denetim yöntemiyle denetlenecek ve geniş hız ve yük bölgelerinde hareket başarımı incelenecektir. Dahili sürekli mıknatıslı motor sürücüsü ve kestirim/denetim algoritmaları modellenecek ve başarımları ayrıntılı bilgisayar benzetimleri ile gösterilecektir. Üç fazlı gerilim kaynaklı bir evirici ve motor test düzeneği imal edilecek, ve kestirim/denetim algoritmaları DSP tabanlı bir motor denetim ortamında gerçekleştirilecektir. Dahili sürekli mıknatıslı motor sürücü

sistemi laboratuarda test edilecek ve teori ve benzetim sonuçları deneyler ile doğrulanacaktır.

Anahtar Kelimeler: Dahili sürekli mıknatıslı motor, duyargasız, vektör denetim, hız ve konum denetimi, yüksek frekans işaret uygulama, akı gözlemleyici, evirici, manyetik çıkıntı, izleme, uyarlamalı denetim, yönbağımlılık

To my family,

Safettin Göksu
Hatice Göksu
Figen Güren
Halil Hakan Göksu
Betül Yorulmazbaş

ACKNOWLEDGMENTS

TABLE OF CONTENTS

CHAPTER

LIST OF TABLES

LIST OF FIGURES

FIGURES

xviii

CHAPTER 1

INTRODUCTION

1.1 AC Motor Drives

Almost entire devices and applications in the world employ an electric motor for the purpose of obtaining motion or an outcome based on motion. For instance; air conditioners, elevators, electric vehicles, printers, hoists, cranes, refrigerators, washing machines, etc. all includes electric motors. Most of the industrial applications, manufacturing systems, daily life equipments (computers, printers, etc.), medical instruments, military systems (radars, gimbals, etc.), buildings, facilities, and vehicles make use of different types of electric motors. Therefore, nearly 65% of the electrical energy utilized by the industry is consumed by the electric motors in the world. More than 25% of the energy consumption in residential areas is also through the electric motors. Every house has a lot more than 10 motors in the modern world.

Although some motor types can be fed directly from the mains supply, usually electric motors are driven by special devices which are called as motor drives, in order to obtain proper operation, high efficiency, and high performance. The motor drive, which is a unit composed of a power electronic converter (the body) and a controller (the mind), supplies the power to the motor such that the motor is operated with high motion quality and energy efficiency. The motor drive gets its power from the available power supply (the AC utility or DC power supply such as a battery), takes the commands from the human user or from the other devices in the application, reads the feedback sensors for the purpose of feedback control and

protection, and drives the motor with the necessary control signals to properly energize and steer the motor with high performance. The architecture of a motor drive is given in Figure 1.1 in block diagrams to be discussed in the following.
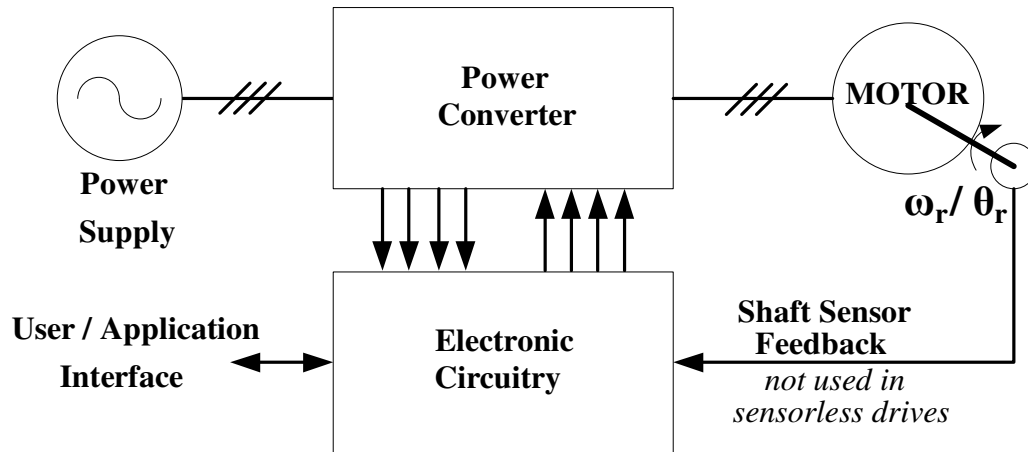
Figure 1.1 Motor drive basic architecture.

The motor drive hardware consists of a power converter and an electronic circuitry. The power converter typically involves a rectifier, DC bus capacitors, an inverter consisting of power transistors, freewheeling diodes, gate drivers for the power transistors, the DC bus pre-charge circuit, voltage and current transducers etc. The electronic circuitry involves overvoltage, overcurrent, etc. protection circuits, measurement signal conditioners, peripheral interface circuits for capturing the shaft sensor (e.g. encoder) signals and for user/application communication interface, and the controller. The controller unit can be based on a microcontroller and/or a digital signal processor (DSP) and/or a Field Programmable Gate Array (FPGA). Depending on the application requirements, interface needs, and the motor type, the motor drive structure can become simpler or more complex.

Performance criteria such as power rating, energy efficiency, motion accuracy, and reliability requirements determine the motor type to be used in an application. In the past, Direct Current (DC) motors have been widely used in most of the applications. DC motors have been preferred since the torque and speed of a DC motor can be easily controlled by means of controlling its armature voltage (and therefore

controlling its armature current). This method was invented by Ward Leonard and depending on the technological progress it has been implemented by manual voltage control methods in the early stages and via power electronics in motor drives in modern times. A modern DC motor drive simply outputs a variable DC voltage necessary for the motor speed control. For high bandwidth speed control, a current controlled DC/DC step-down converter is utilized and operated in current control mode such that the current reference (torque reference) requested by the motion controller is met by the current controller with high bandwidth. Hence, high bandwidth speed control is obtained and also automatic current limit is inherent which avoids overloading the drive. However, DC motors have maintenance problems due to the presence of commutators/brushes. As a result, the utilization of DC motors has experienced a limited growth in the recent decades and this growth has been mainly for very low power applications (sub kilowatt levels), while Alternating Current (AC) motors have experienced substantial growth overall.

Presently, industrial applications use AC motors much more often than DC motors. Especially three-phase induction motors are widely used. The wound rotor induction motor was invented by Nicola Tesla more than one century ago, followed by the invention of the squirrel cage induction motor by Dolivo Dobrowolsky. The squirrel cage induction motor is commutator-less and it has low maintenance requirements. It also has higher overload capability than the DC motor. Therefore it is more robust than the DC motor. Additionally, the induction motor is more economical. An induction motor can be fed directly from the mains AC supply. However, if an induction motor is fed from a fixed frequency, fixed voltage magnitude utility grid (such as 50 Hz, 400 Vrms line-to-line), the motor provides a specific fixed torque-speed characteristic and it is impossible to effectively control the induction motor torque /speed/position without external means. The start-up is also problematic as large inrush currents are a problem for the motor itself and the AC power line. Therefore, induction machines are mostly driven by AC motor drives, which supply the induction motor with variable voltage magnitude and variable frequency to obtain controllable torque, speed, and high efficiency from the induction motor.

3

Generally, the power converter structure of an AC motor drive is composed of two stages; the rectifier, which is the power input stage and the inverter, which is the power output stage. The simple representation of the AC motor drive power structure is given in Figure 1.2.
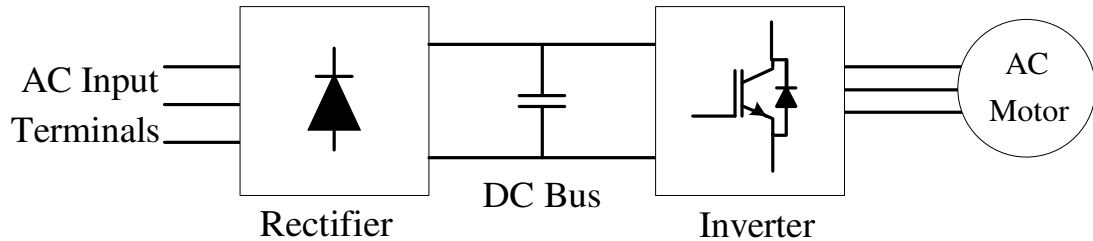
Figure 1.2 Basic power structure of an AC motor drive.

The power input stage is a rectifier which is the AC to DC conversion stage that obtains DC voltage from the AC utility grid. The rectifier is usually formed by diodes connected in bridge form (hence, called as full-bridge diode rectifier). A large capacitor or capacitor banks are connected to output of the rectifier to obtain ripple free DC voltage. The second stage involves DC to AC conversion and such a device is called an inverter. AC motor drives make use of the voltage source inverter (VSI), to produce three-phase AC output voltages with variable magnitude and variable frequency.

Of the well known VSI topologies, shown in Figure 1.3, the three-phase two-level VSI is the most widely employed inverter topology for three-phase AC motor drives as DC/AC converter with variable voltage variable frequency output. This topology is also employed in regenerative motor drive applications (instead of a diode rectifier) as AC/DC converter (opposite of inverter mode implying regeneration) with variable (controlled) voltage and fixed frequency. In Uninterruptible Power Supply (UPS) applications this topology is utilized in both the AC/DC and DC/AC conversion stages. The phase output voltage waveform of the inverter takes the values of $-V_{dc}/2$ or $+V_{dc}/2$ with respect to the virtual/real midpoint potential of the DC bus (0), that is "the inverter has two levels of output voltage."
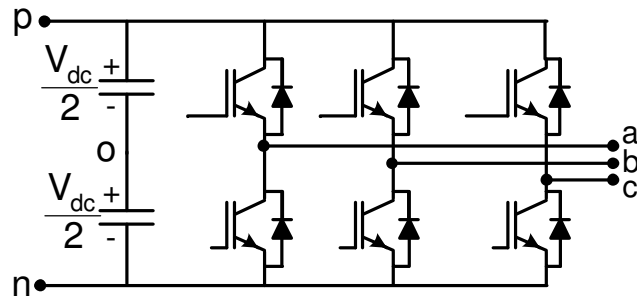
Figure 1.3 The three-phase, two-level voltage source inverter (VSI) circuit topology.

The three-phase two-level VSI is composed of six controllable semiconductor switching devices and their freewheeling diodes. Pulse Width Modulation (PWM) method is utilized to produce the variable voltage variable frequency at the VSI outputs. Operation of the VSI is provided within the controller of the AC motor drive, which is also responsible for the control of the motor. Generally, three-phase currents drawn by the motor from the VSI are measured within the drive unit via Hall-effect based current transducers and used for current control and overcurrent protection purposes.

Early AC induction motor drives employed the constant volts-per-hertz (constant V/f or constant flux) operation principle as it was a simple means of speed regulation method (the best achievable at that time). The performance of the open-loop V/f method was sufficient for fan and pump type applications requiring only crude speed regulation. The new generation induction motor drives utilize a wide range of modern control techniques, including the vector coordinate based Field Orientation Control (FOC) principle [1], [2] to obtain high bandwidth torque/speed/position control and to provide high motion quality. Field oriented control is a special case of vector control for the induction motor where the field flux and armature mmf are separately created and controlled based on the vector coordinate transformations. Modern motor drive systems employ modern DSPs and/or microprocessors to meet the closed loop torque and speed regulation requirements over a wide operating range with high accuracy. The vector control method is used in most of the AC motor drives to obtain high torque bandwidth and control performance. However, the

5

vector control method needs the motor flux position (angle) information and relies on the current regulation. Current regulation is realized within the motor drive employing advanced feedback control methods based on the current measurements taken at the output of the inverter. The motor flux position information can be obtained by using a shaft transducer (e.g. encoder) on the motor and then processing this information to reach the flux estimate. However, sensorless control algorithms, such as the methods implemented in this thesis work, eliminate the need for an encoder on the shaft.

Although induction machine drives with modern control techniques have brought high performance and robustness to the motion control area, research has continued for developments in the AC motors and drives technology. The motivation is to improve the technology for high efficiency and for high performance. Efficiency is important due to the energy scarcity of the world and higher performance is needed for modern motion control applications. Permanent magnet synchronous motors which meet these criteria have been developed. Permanent magnet synchronous motors are different from the well-known wound field synchronous motors. The stator structure of a permanent magnet synchronous motor is similar to the wound field synchronous motors. However, the difference is only between the rotor structures. In the wound field synchronous motors, field is created on the rotor by separate excitation through the brushes (slip rings), where the field of the permanent magnet synchronous motors is created by the permanent magnets placed on the rotor. Therefore, permanent magnet synchronous motors are brushless motors. Since they are brushless, they are more robust than the DC motors; and since the field is created by permanent magnets and there are not any rotor currents, they are more efficient than the induction motors, where the rotor field currents cause rotor copper losses.

Permanent magnet synchronous motors are classified mainly into two groups with respect to their rotor structures as; Surface Mount Permanent Magnet (SMPM) Synchronous Motors and Interior Permanent Magnet (IPM) Synchronous Motors [3], [4]. SMPM motors have the permanent magnets mounted on the outer surface the rotor, and IPM motors have the permanent magnets buried in the rotor core. SMPM

motors are also classified into two types with respect to the stator winding as; concentrated winding and distributed winding. Concentrated winding SMPM motor's back-emf waveform is trapezoidal; distributed winding SMPM motor's back-emf waveform is sinusoidal. Concentrated winding SMPM motors are called as Brushless DC (BLDC) motors and driven with trapezoidal signals. The distributed winding SMPM motors are called as Permanent Magnet AC (PMAC) motors and driven with sinusoidal signals. PMAC motors are also designated as servo motors or brushless AC motors. PMAC motors are generally built with strong magnetic material (samarium cobalt, neodymium boron iron) and have high dynamic performance, high efficiency, robustness, high torque density and significantly better short-time overload capability than induction motors (400% to 150%). PMAC motors are mostly employed in high performance servo (robotics, machining, etc.) applications. Some PMAC motors are built with low cost permanent magnet materials (ferrites) to be used in low cost (fan) applications. BLDC motors do not have so high performance as the PMAC motors and are mostly employed in low cost low performance adjustable speed applications.

IPM motors are newly developed motors with high torque density, high efficiency characteristics as the SMPM motors and additionally provide field weakening operation [5]-[7], which is impossible with the SMPM motors. IPM motors are preferred in the industrial applications such as adjustable speed drives as a replacement for the squirrel cage induction motors, to improve the efficiency and the performance. IPM motors are also used in high power servo applications where the SMPM motors can not meet the power requirements. In contrast to the induction motors, IPM motors also have the advantage of providing position control loop with accuracy, without a shaft encoder.

Permanent magnet synchronous motors (especially PMAC and IPM motors) have gained wide acceptance in the modern applications. In order to meet the efficiency requirements of the modern energy-hungry world, the IPM motor which is a better alternative to the induction motor in terms of efficiency and motion performance is used in large number of applications. PMAC motors are mostly used in high

performance servo applications. However, PM synchronous motors can not be fed directly from the mains supply and need to be driven by the AC motor drives. Similar to the induction machine, vector control method is employed for the PM synchronous motors to obtain high bandwidth torque control performance. For vector control, the rotor flux angle needs to be known by the AC motor drive. Therefore, sensors (e.g. an incremental encoder) on the motor shaft are utilized to sense the rotor flux angle and AC motor drives use this angle information for vector coordinate transformations. With vector coordinate transformations, the AC motor in the control coordinates is converted to a DC motor where torque control is a simple issue of current control to be achieved by the current regulator. Thus, the vector control method enables high bandwidth torque control of an AC machine, which brings high bandwidth of speed and position control.

Control of motors is not limited to the torque control. Most of the applications require accurate speed control and servo applications involve position control of the motor. Again, a sensor on the motor shaft (e.g. an incremental encoder with/without pole sensor) is needed for speed and position feedback. For high performance speed and position control, high performance torque control is obtained by the modern vector control method, which is based on rotor flux position feedback. The need for the shaft transducer in vector control and speed/position control can be eliminated by the sensorless AC drives which will be discussed in the following section.

1.2 Sensorless AC Drives

Both asynchronous (induction) and synchronous (SMPM, IPM…) AC motors require rotor position/speed information for vector control, speed control, and position control. Rotor position and speed information can be provided by a transducer on the motor shaft. This shaft transducer can be a position sensor such as an encoder, a resolver, or a Hall effect sensor; and from these position sensors, speed information can be derived. In some applications, flux sensors such as search coils on the motor have been used to sense the flux. Use of special search coils makes the method

inapplicable to general purpose motors and has limited motion performance. Use of the shaft transducers provide the necessary feedback for the control of the motor, however they bring many problems. First of all, additional transducers for the control of the motor bring additional cost for the AC drive. A shaft transducer can be more expensive than the motor itself. The second major problem is about the mechanical installation of the transducer on the motor. Precise and rugged installation of the transducer on the shaft needs machining and so much labor. Although the installation is well-made, there can be mechanical damage due to the harsh environmental conditions and electrical faults may occur due to the damage. Moreover, integration of the sensor to the AC drive requires additional hardware (wiring, interface circuits, etc.) and software interface, which makes the AC drives more complex and more prone to failure (considering large number of field failures in a factory floor are due to bad connectors and loose cables). Similar to the brushes of the DC motor, shaft transducers bring maintenance problems and increase the cost of the AC motor drive systems.

With strong motivation to avoid the use of shaft transducers due to the cost and reliability problems, they have been eliminated from motor drive systems in the modern sensorless AC motor drives. Modern sensorless AC motor drives make use of intelligent observer algorithms to estimate the rotor flux angle and the motor speed directly from the electrical measurements and parameters within the drive without using any mechanical transducer on the motor shaft. The voltages applied to the motor terminals can be measured or after measurement of the DC bus voltage, they can be calculated within the AC motor drive since the variable voltage is produced by the inverter itself, and the drawn motor currents can be measured by the current transducers within the AC motor drive. The measured currents and commanded output voltage values are used by sensorless estimation algorithms (observers) in the motor drive to obtain the rotor flux angle, motor speed, and in some cases the rotor position information. The observers typically make use of the motor model, motor parameters and physical properties of the motor. Hence the torque/speed/position of an AC motor can be controlled via only the power connection of the motor without any mechanical transducer on the motor shaft.

9

Sensorless torque, speed, and position control of AC machines has been intensively researched over the last four decades [8], [9]. Research has been conducted to eliminate the use of a mechanical sensor on the motor shaft. Different sensorless methods are developed for different motor types. The early developed methods for the induction motor rely on the motor's steady-state model and mathematical equations of the motor equivalent circuit [10], [11]. These simple algorithms involve analysis and mathematical equation solving with the known motor parameters and variables. Sensorless methods for induction motors are improved with state observers, which are based on the fundamental model of the induction motor [12], [13]. State observers rely on the fundamental model and parameters of the induction motor, and mainly involve integration to estimate the rotor flux, flux angle, and motor speed. Fundamental model (the model using the induction machine basic equations based on lumped parameters) based observers are enhanced with adaptive mechanisms to improve the estimation accuracy [14], [15]. Advanced methods, such as Kalman filters, fuzzy controls, neural networks, etc. are also developed [16], [17]. However, for zero and low speed, the back-emf voltage of the induction motor, which is the variable that is directly or indirectly observed, is too small and negligible with respect to voltage drop on the stator resistor. Furthermore, at very low speed and thus voltage levels, the VSI has voltage gain characteristic which is nonlinear and difficult to model. Hence, employing the fundamental model of the induction motor, the rotor flux as a state of variable is not observable for zero and low speed. The fundamental model based methods could be enhanced to provide low and zero speed region operation [18], [19]; however stable sensorless control of the induction motor can not be provided with fundamental model based methods for low and zero speed region. Nevertheless, there are successful sensorless induction motor drives in the industrial applications, which work stably for the moderate and high speed regions. Typically 50-100 rpm is the lowest speed that a vector controlled sensorless drive with 1500 rpm rating can achieve. At lower speed, full torque capability or speed regulation with accuracy is not provided without a shaft encoder. Thus, applications involving operation at zero speed, such as elevators involve an encoder and its cost and complications. To overcome this difficulty, for the low and zero speed sensorless control of the induction motor, estimation algorithms based on

10

the magnetic saliency (spatial anisotropy) of the induction motor are developed [20]-[22]. Of the saliency based methods, the high frequency signal injection method has been successfully applied to the induction motor. The standard induction motor, which is known to be non-salient and spatially symmetric (magnetically), becomes slightly salient pole as a result of saturation of the flux in one axis, and due to eddy currents caused by the high frequency signal injection. As a result, the motor impedance becomes space angle dependent. Saliency based high frequency signal injection methods provide low and zero speed sensorless control of the induction motor. However, the artificial saliency (forced by saturating the machine in one axis) of the naturally non-salient induction motor is very low, and the saliency is highly affected by loading. Therefore, it is hard to achieve high performance sensorless control of the induction motor using the saliency based high frequency signal injection method. However, successful results of this technique have been reported in [22]. It is claimed that this method works well with closed slot rotor induction motors, but has limited performance in open slot rotor type induction motors. Modifying the motor structure by creating intentional and significant magnetic saliencies in the rotor is only possible for custom design motors and this technique has been applied in some fields [21]. The sensorless control performance of the induction motor for low and zero speed region can be improved by hybrid methods, which utilize the estimations from both of the fundamental model based observer method and saliency based high frequency signal injection method [23]-[28].

Sensorless control methods for the permanent magnet synchronous motors are similar to the methods for the induction motor. For the BLDC motors, there exist simple methods detecting the back-emf of the permanent magnet motor [29]. Sensorless control of the PMAC motors (SMPM and IPM) at the high speed region is successfully provided by the fundamental model based state observer methods [30]-[32] similar to the observers for the induction motors. Similar to the induction motor, back-emf of the PMAC motor is zero for zero speed and the flux becomes unobservable for low and zero speed region. For low and zero speed sensorless control, the saliency based high frequency signal injection method is also utilized for the SMPM and IPM motors [33]-[37]. For the SMPM motors, which are non-salient

11

as the induction motors, saliency based high frequency signal injection method provides low performance. However, for the IPM motor, which is naturally significantly salient due to its rotor structure, the saliency based high frequency signal injection method provides high performance sensorless control for the zero and low speed region. Therefore, in addition to its energy efficiency and smaller size advantages, the IPM motor brings another advantage of shaft sensorless operation with high performance. The combination of attributes is believed to favor the IPM motor as the most widely utilized motor in industry provided that the Neodymium magnet prices are retained within reasonable range. With the potential of IPM for wide utilization being enormous, the sensorless control of the IPM motor is the main subject of this thesis.

In the IPM application, the fundamental model based observers are successfully used for sensorless control at moderate and high speeds. Saliency based high frequency signal injection algorithms provide reliable speed and position estimations for low and zero speed regions where the fundamental model based observers can not perform well. However, injection algorithms have high speed limitations since they require additional voltage from the VSI, which has a limited DC link. Therefore, saliency based injection algorithms are not used for high speed regions in order to effectively use the VSI. Hence, both fundamental model based observers and saliency based injection algorithms are implemented together in the modern AC drives. The combined methods work in cooperation to provide the whole speed range sensorless operation such that the saliency based method works at the zero and low speeds and the fundamental model based algorithm works at the moderate and high speeds [38]. The combined algorithm, where the transition between the two methods depends on the speed of the motor, is called as the hybrid method.

1.3 Scope of The Thesis

Research and development on the all aspects of the AC motor drive technology has been continuing in the drive industry and in the academic world. Academic research

is mainly focused on the design of the motors and the control algorithms of the motor drives, where the drive industry utilizes these academic researches for their drives. Motivation is to design and produce more efficient and cost effective drives. As given in the previous section, development of intelligent control algorithms, which results in efficient, robust and cost-effective drives for the sensorless motor drives is challenging. Among the motors, the IPM motor is becoming more and more important for many applications due to its favorable characteristics.

In this thesis, shaft transducerless vector control of the IPM motor with speed and position estimation using high frequency signal injection and flux observer methods is implemented and investigated with simulations and experiments. The literature of the AC drives and the motor technology, and the IPM motor characteristics are reviewed first. Then, vector control theory for the AC motors and the torque/speed/position control of the IPM motor in the motion control applications are discussed.

The high frequency signal injection based estimation and control theory is investigated. The high frequency model of the salient pole IPM motor is investigated by its mathematical equations, simulations, and experiments. The saliency of the IPM motor is extracted by the high frequency signal injection method. Based on the saliency, the high frequency signal injection method is utilized for the low and zero speed region rotor flux angle and rotor speed/position estimations. Transducerless vector control and speed/position control of the IPM motor are realized by simulation and experiments including the loaded cases.

An established fundamental model based flux observer method is investigated and implemented for moderate and high speed region operation. Its performance is verified by means of simulations and experiments including the loaded operating condition of the IPM motor. The fundamental model mathematical equations of the IPM motor are investigated and the rotor flux angle is estimated by the flux observer. The estimated rotor flux angle is used for vector control and motor speed is derived from the estimated rotor flux angle. Speed and position loop of the IPM motor are

closed via the estimations from the flux observer which performs well at moderate and high speed regions.

The two independent solutions; the high frequency signal injection method for low and zero speed and the flux observer method for moderate and high speed, are combined in a hybrid method for a solution covering the whole speed range. Smooth transition from the high frequency signal injection algorithm to the flux observer algorithm and vice versa are performed based on the estimated speed feedback. Transducerless vector and speed control of the IPM motor for wide speed and load range is realized by simulations and experiments.

In addition to the IPM motor, sensorless vector control of the induction motor is realized by two different algorithms, the saliency based high frequency signal injection algorithm and the speed adaptive flux observer algorithm. The artificial saliency of the induction motor is investigated experimentally and based on this saliency rotor flux angle is estimated. The speed adaptive flux observer algorithm, which is based on the fundamental model of the induction motor, is implemented and speed of the induction motor is closed loop sensorless controlled, also for loaded operation.

The outline of the thesis is as follows. In the second chapter, basic information about the IPM motor and its applications are given. In the third chapter, the basic vector control and speed and position control theory are briefly reviewed to set the background for the motion control loops, where the estimated variables are used. The fourth chapter includes all the theory of the two sensorless control methods and the hybrid method, which combines the two methods. The fifth chapter involves the simulation results of the theory discussed in the previous chapter. The experimental results are reported in the sixth chapter. The seventh chapter investigates the high frequency injection method and adaptive flux observer methods applied to the induction motor and mainly theory and experimental results are provided. The eighth and last chapter provides the conclusion of the thesis with remarks and points towards future work.

CHAPTER 2

INTERIOR PERMANENT MAGNET (IPM) MOTOR STRUCTURE, OPERATING PRINCIPLE, AND STEADY-STATE OPERATING CHARACTERISTICS

2.1 Electric Motors

Electric motors and motor drives are important elements of the modern industrialized world, and technology of the motors and drives has been under consistent improvement. Since the Michael Faraday's early experiments, the electric motor technology has come a long way. The aim has been to make the electric motors more powerful, dynamic, efficient, robust, and small sized.

There are various types of motors such as separately excited direct current (DC) motors, permanent magnet DC motors, asynchronous induction motors, separately excited wound field synchronous motors, permanent magnet (PM) synchronous motors, synchronous reluctance motors, switched reluctance motors, stepper motors, linear motors, etc. In recent decades, mainly three types of electric motors have taken place in the industry; DC motors, induction motors, and PM synchronous motors.

DC motors make use of the carbon brushes for commutation of the armature current and the brushes provide spatial orthogonality between the field flux and armature mmf, which results in high torque density and high dynamic performance. DC motors can provide high torque performance with simple driving methods; however it can be said that DC motors are no more favorable due to their problematic brushes and heavy structures. Induction motors are still mostly used motors today and have a great usage in adjustable speed drives due to their low cost, robustness, simple structure for driving and line starting properties. However, driving the induction motors directly from the mains result in low performance torque/speed control, poor

energy efficiency, and cause problematic starting (inrush) current. In order to provide current control and prevent overcurrent faults, to satisfy the torque/speed control performance requirements of the applications, and to improve the efficiency and dynamic performance of the induction motors, AC motor drives are used instead of supplying the induction motors directly from the AC power line. Induction motor drives are mostly used for adjustable speed drive applications such as elevators, air conditioners, etc. However, induction motors provide limited dynamic performance and are not suitable for high performance servo applications. Their magnetization current also results in additional losses, yielding relatively low energy efficiency. PM synchronous motors have been used in high performance servo applications and are in a contest with the induction motors for adjustable speed drive applications. PM synchronous motors are preferred due to their high dynamic performance, high efficiency, high torque density, and robust and small structure characteristics. However, synchronous motors can not be driven from the power line directly and they require the utilization of an inverter drive and an encoder. Due to the expensive rare earth element based permanent magnet materials utilized (mostly NdFeB, which exist mostly in China (80%) and its market is monopolized) the cost of the PM synchronous motor is much higher than the induction motor. Regardless, PM synchronous motors are required in high performance servo applications and are favored over the induction machine in energy efficiency critical adjustable speed drive applications. Table 2.1 provides a basic comparison of the three major motor types.

Table 2.1 Performance comparison of most widely utilized industrial and servo motors

DC Motor	Induction Motor	PM Synchronous Motor
Good dynamic performance of torque production	Poor dynamic performance of torque production	Good dynamic performance of torque production
High efficiency	Low efficiency	Very high efficiency
Not robust	Robust	Robust
Large in size	Large in size	Small in size
Easy to control	Easy to control	Difficult to control
Low-cost	Very low-cost	High-cost

2.1.1 Permanent Magnet Synchronous Motors

PM synchronous motors have a wide range of types. However, they can be classified into two main groups according to the installation of the permanent magnet materials on the rotor; Surface Mounted Permanent Magnet (SMPM) motors and Interior Permanent Magnet (IPM) motors. In surface mounted permanent magnet (SMPM) motors, the permanent magnets are located on the outer surface of the rotor, as shown in Figure 2.1. [39].
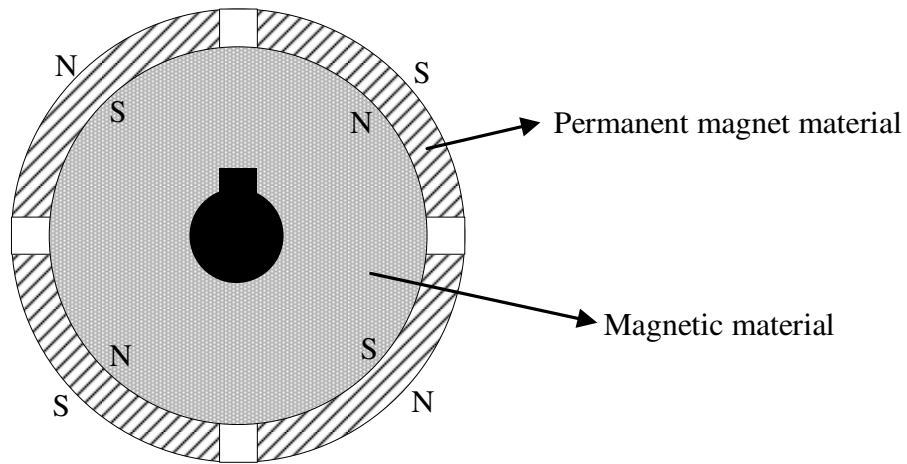
Figure 2.1 PM rotor construction using surface mounted magnets (SMPM motor).

Permanent magnets are embedded inside the rotor core in the interior permanent magnet (IPM) motors; the structure of the IPM rotor is shown in Figure 2.2 and a picture of an IPM rotor is given in Figure 2.3. Interior permanent magnet motors are also designated as "internal," "embedded," "buried," "built-in" rotor type permanent magnet motors.
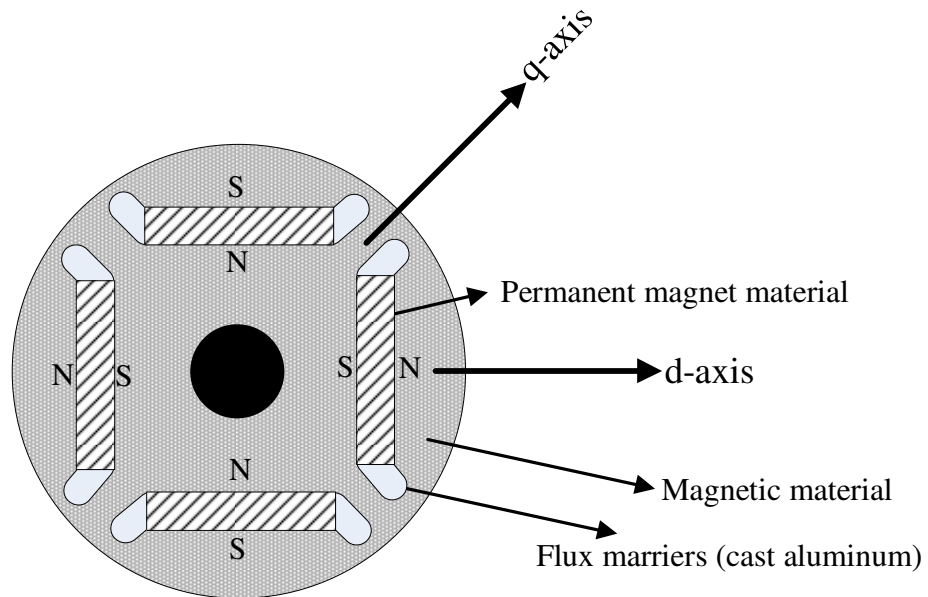
Figure 2.2 Rotor construction using buried, radially polarized magnets (IPM motor).
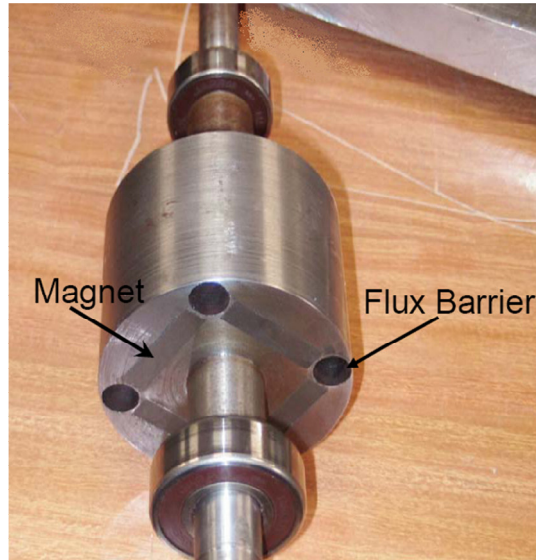
Figure 2.3 The IPM rotor with embedded magnets.

The axis of the rotor on which the field flux (permanent magnet flux) exists is called as the direct axis (d-axis) or flux axis; and the axis orthogonal to the direct axis is called as the quadrature axis (q-axis) or torque axis of the rotor. For instance, for the four pole motor in Figure 2.2, the torque axis and the flux axis are mechanically 45° apart from each other, resulting in electrical orthogonality (90°). In salient pole wound rotor synchronous motors the rotor is not round and has large air-gap on the q-axis. Therefore, q-axis has higher reluctance than the d-axis. The d-axis reactance is in the 1 p.u. range while the q-axis reactance is significantly smaller. In contrast, in many IPM motors the d-axis has a higher reluctance than the q-axis; because of the presence of the permanent magnet material (with low permeability) on the d-axis flux path, where there is only magnetic material (with high permeability) on the q-axis flux path. This results in the inductance of the q-axis (L_q), being larger than the inductance of the d-axis (L_d).

$$L_q > L_d \qquad (2.1)$$

Since the airgap in the IPM motors is relatively small (comparable to the induction motor airgap), the reactances of both axes are significant compared to the stator winding leakage inductance of the motor. This significant saliency and large

19

reactance values (as large as 0.9 p.u.) imply that IPM motor is a salient pole motor and this saliency characteristic creates the reluctance torque component in addition to the main permanent magnet torque component. Also, saliency characteristic of the IPM motor provides convenience for the sensorless control of the IPM motor at low and zero speed, as implemented in this thesis.

The SMPM motors have the permanent magnet material for the whole surface of the rotor; hence they have symmetrical reluctance in both axes and they are non-salient pole synchronous motors. Since the permanent magnet material has low permeability, the d and q axes reactances of the SMPM motors are typically small (significantly smaller than those of the IPM motors) and equal ($L_q = L_d$). The IPM motor has higher reactance values than the SMPM motor; hence the IPM motor has the feasibility for field weakening operation, which is an important issue for the applications and will be discussed in the following parts.

Table 2.2 shows the range of the saliency ratios of two different motor types, utilized in this thesis; the IPM motor and the induction motor. The saliencies are derived experimentally via applying high frequency voltages on the stator terminals and observing the current response. The source of the saliency of the induction machine is discussed in the related chapter. The per-unit saliency ratio is calculated with the equation (2.2) below, where saliency ratio of zero means the machine is non-salient and saliency ratio of one means infinitely salient pole machine. For the IPM motor Z_{max} is on the torque axis and for the induction machine Z_{max} is on the flux axis.

$$\text{saliency ratio} = \frac{Z_{max} - Z_{min}}{Z_{max}} \tag{2.2}$$

Table 2.2 Comparison of per-unit saliency ratios for the IPM motor and the induction motor, when high frequency signals are applied

	The IPM Motor (YASKAWA-686SS)	The Induction Motor (SIEMENS-1LA7113-4AA)
saliency ratio (per-unit)	0.456	0.222

The saliency ratio of the IPM motor utilized in this thesis is found to be 0.456 and the reactance values are in the range of 0.11 to 0.15 pu. In [7], IPM motors, which are utilized for the hybrid electric vehicles, are shown to have higher reactance values, such as 0.9 to 2.2 pu, and higher saliency ratios, such as 0.66.

2.1.2 IPM Motor Characteristics

The IPM motor is developed in order to meet the efficiency and performance requirements of the modern industrial and servo motion control applications. Major attributes of the IPM motor are high torque and power density in small size, high efficiency, robust structure, and field weakening capability.

For adjustable speed drive applications (industrial drive applications) such as air conditioners, fans, pumps, spindles, etc. the induction motors have been mostly used, since they are low cost, robust and can be simply driven from the mains lines. However, almost in all induction motor drive systems, AC motor drives are used to control the induction motor with high torque/speed performance and high efficiency. Since the AC motor drives are already used for the induction motors, the quest for the replacement of the induction motor with the IPM motor arises to increase the efficiency and performance of the motor drive system. In spite of the higher cost of the IPM motors with respect to the low cost induction motors, IPM motors are preferred in adjustable speed drive applications when the efficiency, performance and maintenance are considered. Additionally, for high power servo applications,

where the SMPM motors could not meet the power requirements, IPM motors are employed and provide high power density and high performance.

The favorable characteristics of the IPM motors are listed below;

o Embedded permanent magnet structure creates superior flux density and flux distribution, and provides the improvement in torque density and power density; and also causes the saliency which creates the reluctance torque component. As a result high efficiency is achieved.

o With the embedded magnet design, effective air gap length can be very short due to the core material at the surface. Short air gap length results in high synchronous reactance values and the armature reaction mmf can create enough flux for field weakening. Field weakening is almost impossible with the SMPM motor which has very small synchronous reactance due to very long air gap length between the magnets and the stator core. Field weakening method with the IPM motor provides constant power over a wide speed range of operation and helps to extend the operating speed range, similar to the induction motors (very critical for many industrial drive applications).

o Embedded magnets of IPM motor are not affected from the centrifugal forces at high speeds, in contrast to the stick magnets on the rotor surface of SMPM motors. Hence, a mechanically robust, well-balanced rotor provides higher speed operation and robustness.

o The large saliency characteristic of the IPM motor simplifies the sensorless operation, as realized in this thesis work, where it is appropriate for the application.

o Via optimum flux distribution, cogging torque has been reduced and low cogging torque improves accuracy for the precision required applications.

o The interior magnet configuration results in compact sized rotor with lower inertia and this makes the IPM motor particularly suitable for highly dynamic applications and reduces the overall size of the motor.

o For some IPM motors electrically conducting bars or cage segments (copper or aluminum) are placed as rotor windings inside the rotor core in addition to

the permanent magnets. These conducting cage segments act as the cage of the induction motor and provide asynchronous operation for starting directly from the power line. Hence, the motor becomes an induction-start synchronous-run permanent magnet motor.

On the other hand, in the IPM motor, the rotor design is more complex and embedding the magnets inside the rotor rather than gluing the magnets on the rotor surface of SMPM is a more complex procedure. This design complication adds to the cost of the IPM motor slightly. However, flat-shaped, simple magnets can be used for the IPM motor where, curve-shaped complex magnets are used for the SMPM motors. Also, small inertia of the rotor and reluctance torque component of the motor requires critically tuned and quicker servo loop for stable operation. The major drawback of the IPM motors (and all the PM synchronous motors in general) appears to be the dependency on the permanent magnet material, as previously discussed. However, this drawback does not inhibit its wide utilization due to its favorable properties.

In summary, IPM motors are preferred for adjustable speed drive (industrial drive) applications as a replacement for induction motors and as the only available technology for very high power servo drive applications. IPM motors are widely used in air conditioners, fans, pumps, cranes, lifts, escalators, ship propellers, locomotive traction drives, electric and hybrid electric vehicles. The power rating of the IPM motors goes from few watts to hundreds of kilowatts [7].

2.2 Steady-State Analysis of SMPM Motor

Before pursuing the steady-state analysis of the salient pole IPM motor, steady-state analysis of the SMPM motor, which is non-salient pole and can be represented by the per-phase steady-state equivalent circuit in Figure 2.4 (a), is given in this section. Steady state phasor diagram (neglecting the stator resistor) for the SMPM motor is given in Figure 2.4 (b).
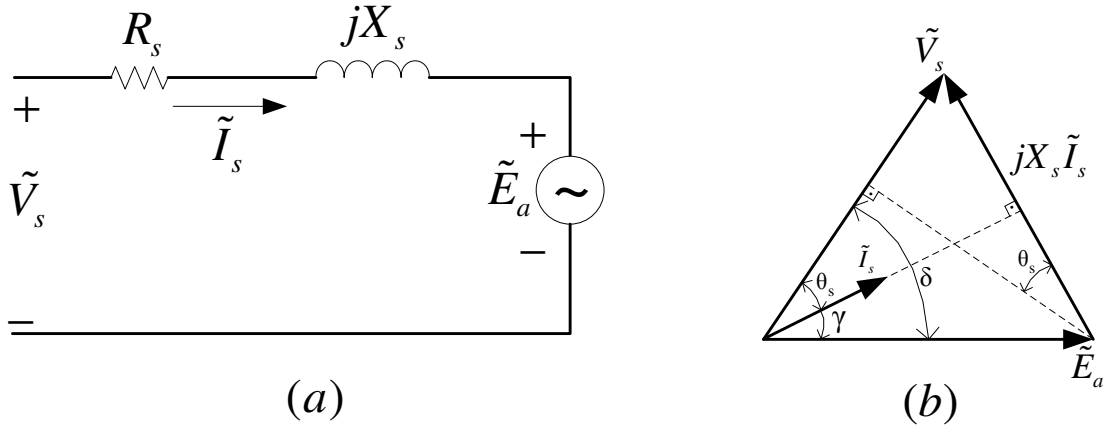
Figure 2.4 Equivalent circuit (a) and phasor diagram (b) of the non-salient SMPM motor.

In Figure 2.4, V_s is the motor terminal voltage and E_a is the internal (back emf) voltage produced by the field excitation (the permanent magnet flux). Amplitude of E_a is proportional to the flux produced by the permanent magnets and to the rotor speed, similar to the back-emf of the DC motor.

The well-known wound field synchronous motors have usually been utilized as synchronous generators. Therefore, in the literature and textbooks, steady state analysis and power/torque equations of the synchronous machines are expressed as voltage equations since for those cases the synchronous machine is operated with constant voltage or it generates constant voltage. The power/torque output equation is deduced from the power input to the machine, given with the equation below, neglecting the R_s resistance;

$$P_s = 3V_s I_s \cos\theta_s \qquad (2.3)$$

From the phasor diagram in Figure 2.4 (b);

$$I_s X_s \cos\theta_s = E_a \sin\delta \qquad (2.4)$$

$$I_s \cos\theta_s = \frac{E_a \sin\delta}{X_s} \qquad (2.5)$$

Then the output power can be expressed as below;

$$P_s = 3V_s I_s \cos\theta_s = 3\frac{V_s E_a \sin\delta}{X_s} \qquad (2.6)$$

The δ is called as load angle (or torque angle) and the maximum power is obtained for $\delta=90°$. The electromechanical torque of the machine can be found by the mechanical power equation;

$$P_{mechanical} = T_{em} \times \omega_{mechanical} \qquad (2.7)$$

Neglecting the stator resistance and rotational losses, mechanical power output is equal to the input power. Then;

$$T_{em} = \frac{P_s}{\omega_r} \qquad (2.8)$$

where ω_r is the mechanical rotor speed in rad/sec.

For the synchronous machines, the mechanical rotor speed is related with the electrical speed (excitation frequency) via the pole pair relation;

$$\omega_r = \frac{\omega_e}{p/2} \qquad (2.9)$$

where p is the pole count.

Electromechanical torque output of the synchronous machine can be calculated as;

$$T_{em} = \frac{P_s}{\omega_r} = \frac{P_s}{\frac{\omega_e}{p/2}} = 3\frac{p}{2}\frac{V_s E_a \sin\delta}{\omega_e X_s} \qquad (2.10)$$

The above power/torque equations are expressed with the terminal voltage, the internal back-emf voltage, and the load angle between them. This expression is suitable for the cases where constant voltage is applied to synchronous motor or generator. Generally, wound field synchronous machines are utilized for high power generator applications. However, for modern motion control applications, permanent magnet synchronous machines are utilized and they are driven by AC motor drives, as in this thesis. As discussed previously, modern AC motor drives control the current of the motor utilizing the VSI, which supplies variable frequency and variable magnitude voltage to the AC motor. Therefore, it is more suitable to analyze the steady-state of the SMPM motor with the power/torque equations based on the current phasor as below. Power delivered to the shaft of the machine can be calculated from the internal power;

$$P_s = 3E_a I_s \cos\gamma \qquad (2.11)$$

Similarly, the developed electromechanical torque can be found in the following.

$$T_{em} = 3\frac{p}{2}\frac{E_a I_s \cos\gamma}{\omega_e} \qquad (2.12)$$

The angle between the back-emf voltage phasor E_a and the current phasor γ is called as the internal power factor angle. The maximum power/torque output can be obtained by $\gamma = 0°$. The internal voltage E_a is proportional to the speed of the rotor and the field flux (permanent magnet flux), and can be expressed with the formula;

26

$$E_a = \omega_e \lambda_f = \frac{p}{2} \omega_r \lambda_f \qquad\qquad (2.13)$$

where λ_f is the flux linkage due to the permanent magnets.

Substituting E_a from the equation above into the torque equation, torque equation of the SMPM motor becomes;

$$T_{em} = 3 \frac{p}{2} \lambda_f I_s \cos\gamma \qquad\qquad (2.14)$$

It is seen from the torque equation above that the torque of the SMPM motor can be directly controlled by controlling the I_s current magnitude and the angle γ between the phasors of E_a and I_s. The voltage phasor E_a, which is produced by the rotor permanent magnet flux, leads the flux λ_f by 90° as known from the Faraday's Law as shown in the Figure 2.5.
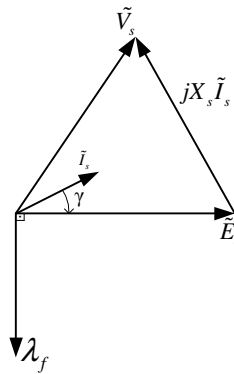
Figure 2.5 Phasor diagram of a non-salient SMPM motor and the rotor flux.

Since the back-emf voltage leads the rotor flux by 90° as in the Figure 2.5, the γ angle can be controlled using the rotor position feedback for commutation of the current. Rotor position feedback, which is required for controlling the angle γ between the E_a and I_s phasors, can be obtained by using a position sensor (e.g.

encoder) on the motor shaft or without using any mechanical shaft transducer in the sensorless drives as realized in this thesis. Obtaining maximum torque per ampere from the SMPM motor can be achieved by selecting the angle $\gamma=0°$. Controlling the current such that $\gamma=0°$, results in maximum torque for the SMPM motor and torque becomes proportional to the armature (stator) current, as in the case of the DC motor. Operating the SMPM motor as a DC motor via current control based on the vector coordinate transformations, which is called as vector control is discussed in the next chapter.

2.3 Steady-State Analysis of IPM Motor

Since the IPM motor is a salient pole motor (not spatially symmetric), a simple steady-state equivalent circuit does not exist for the IPM motor. The IPM motor is best described directly in terms of the phasor diagrams.

The direction of the magnet flux is called as field flux axis (direct-axis or d-axis) and the direction normal to and leading the flux axis is called as quadrature axis or q-axis; and the voltage phasor E_a, which is leading the flux λ_f by 90°, lies on the q-axis. The current phasor I_s can be decomposed into two components on the d and q axes (the d-q axis theorem). For the IPM motor, the synchronous reactances encountered by the d and q axis current components are different and the q-axis inductance is larger than the d-axis inductance ($L_{qs}>L_{ds}$). The phasor diagram of the salient pole IPM motor is given in Figure 2.6.
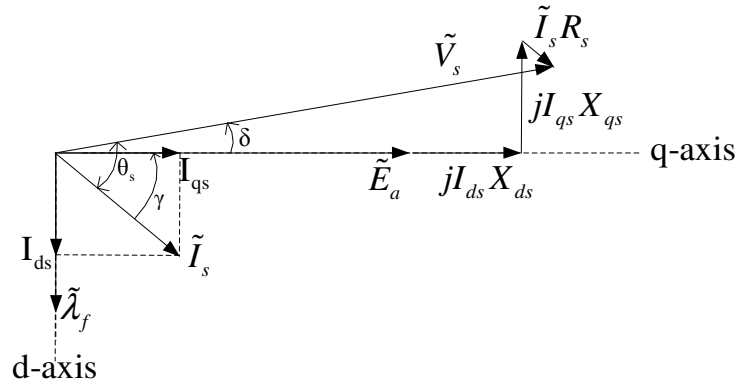
Figure 2.6 Phasor diagram of the salient pole IPM motor.

The d-axis is chosen to be on the rotor flux and this is achieved by the rotor position information which can be obtained from a sensor (e.g. encoder) on the shaft or from the intelligent sensorless algorithms as realized in this thesis.

Steady-state torque of the IPM motor can be extracted as for the SMPM motor case by dividing the input power to the mechanical speed neglecting the stator (R_s) losses.

$$P_s = 3V_s I_s \cos\theta_s \tag{2.15}$$

$$P_s = 3V_s (I_{qs}\cos\delta - I_{ds}\sin\delta) \tag{2.16}$$

$$V_s\cos\delta = E_a + X_{ds}I_{ds}$$
$$V_s\sin\delta = X_{qs}I_{qs} \tag{2.17}$$

For the case E_a lags V_s the load angle becomes greater than zero ($\delta > 0°$). Calculating I_{ds} and I_{qs} from the above equations, substituting them in (2.16), the power equation becomes as in (2.18). From here the shaft torque can be found as in (2.19) and in expanded form as in (2.20).

29

$$P_s = 3 \frac{V_s E_a}{X_{ds}} \sin\delta + \frac{3}{2} V_s^2 \frac{(X_{ds} - X_{qs})}{X_{ds} X_{qs}} \sin 2\delta \tag{2.18}$$

$$T_{em} = \frac{P_s}{\omega_e / (p/2)} \tag{2.19}$$

$$T_{em} = \underbrace{\frac{3p}{2\omega_e} \frac{V_s E_a}{X_{ds}} \sin\delta}_{\text{magnet reaction torque}} - \underbrace{\frac{3p}{2\omega_e} \frac{1}{2} V_s^2 \frac{(X_{ds} - X_{qs})}{X_{ds} X_{qs}} \sin 2\delta}_{\text{reluctance torque}} \tag{2.20}$$

For the IPM motor which is a salient pole motor ($L_{qs} > L_{ds}$), a reluctance torque is developed in addition to the reaction torque. Therefore, the load angle δ which results in maximum power/torque output is different from 90°, which is the maximum power/torque angle for the SMPM motor.

It is convenient to express the power/torque of the synchronous motor with the current magnitude and angle, since the modern AC drives perform current control, as in this thesis. The torque of the IPM motor, originating from the magnets, can be expressed with (2.21), which is derived from the power delivered to the E_a back emf voltage, same as (2.12), the torque equation of the SMPM motor,

$$T_{reaction} = 3 \frac{p}{2} \frac{E_a I_s \cos\gamma}{\omega_e} \tag{2.21}$$

where γ is the angle between the back emf voltage and the current and becomes positive for I_s lagging E_a. For the IPM motor, the additional reluctance torque and the total torque are expressed in (2.22) and (2.23), respectively.

$$T_{reluctance} = 3 \frac{p}{2} (L_{ds} - L_{qs}) I_s^2 \cos\gamma \, \sin\gamma \tag{2.22}$$

$$T_{em} = T_{magnet} + T_{reluctance} \tag{2.23}$$

30

For the IPM motor, which has $L_{qs}>L_{ds}$, reluctance torque becomes positive for $\gamma<0°$ in contrast to the wound field synchronous motor, which has $L_{ds}>L_{qs}$. Therefore, for the IPM motor, maximum torque per ampere (MTPA) is achieved for $\gamma<0°$, where MTPA is obtained for $\gamma=0°$ for the non-salient SMPM motor.

Control of the internal power factor angle γ can be realized by the vector control method, which is mainly based on the mathematical transformation of the AC motor to the synchronously rotating vector coordinates, which is discussed in the next chapter. Via vector control method, current vector of the AC motor is controlled to provide the requested operation. For instance, γ angle can be controlled to achieve $\gamma=0°$ or (different from the zero) to provide maximum torque per ampere (MTPA) or to provide field weakening operation.

Field weakening, which is an important characteristic of the industrial AC drives, is utilized to effectively use the VSI for high speed operation. At high speed back-emf of the motor increases, hence the voltage commands from the current regulator to the VSI, which is limited with the DC link value, increases. In order to increase the speed of the motor or to perform the current control without saturating the VSI, the back-emf voltage, which is proportional to the field flux and motor speed, is reduced by field weakening. Field weakening is mainly to attenuate the field flux, by creating an armature mmf component opposite to the field flux; and this is performed by controlling the current such that $\gamma<0°$ [5], [6]. For the non-salient AC motors, such as induction motor and SMPM motor (for which field weakening is unfeasible or even impossible), field weakening causes decrease in the torque/ampere parameter due to the deviation from the maximum torque condition, which is $\gamma=0°$. For the wound field synchronous machines, the field weakening condition ($\gamma<0°$), causes decrease in the reaction torque parameter and moreover negative reluctance torque is created. For the IPM motor, the field weakening condition ($\gamma<0°$) can have a positive effect on the motor torque output in addition to its main effect on the back-emf voltage for high speed operation, since MTPA is achieved for particular negative

γ angles. Therefore IPM motor is operated with γ<0° for the whole speed range (including zero and low speed) in order to obtain maximum efficiency, in addition to the field weakening operation utilized at high speed. The operation of the IPM motor with MTPA and the field weakening requires external controllers to derive the necessary optimum γ angle. In this thesis, main scope is the sensorless vector and speed/position control of the IPM motor. The maximum efficiency and field weakening operation are beyond the scope of this thesis. Therefore, current vector is controlled such that $\gamma = 0°$.

The steady state analysis of the SMPM motor and IPM motor is discussed based on the time domain AC phasors in this section. For transient analysis and DC (zero speed) cases, complex vector interpretations are used in the next chapter. Vector control, based on the vector coordinate transformations is discussed in the next chapter, where the AC quantities in the stationary frame are transformed to DC quantities for a reference frame rotating with the electrical speed (excitation frequency) of the motor.

CHAPTER 3

VECTOR CONTROL OF AC MACHINES

3.1 Introduction

Vector control is a well-known and common method which has been implemented in AC motor drives for the last several decades in order to improve the torque control performance and hence the speed/position control performance of AC motors [1], [2], [8], [9]. Vector control enables AC motors to behave the same as the separately excited DC motor where the torque control capability is high and the motion control quality is excellent. With the use of the vector control method, the torque output of the AC motor becomes instantaneously proportional to the drawn current as in the DC motor. The theory of vector control is reviewed in this chapter. Additionally, speed and position control loops, which are closed with the estimated speed/position feedback, are discussed in conjunction with the vector control theory.

3.2 Motion Control

Control of the speed and/or position of an electromechanical system is called as the motion control. If the motion is provided by the electric motors, then motor drives are employed in the application. In a motion control application, the motor drive may be requested to perform;

> ➢ only the torque control of the electric motor, where the speed and/or position control of the mechanical system can be realized by an external controller.

> ➤ the speed control of the electric motor such as in adjustable speed drive applications (elevators, fans, etc.) and electric vehicles. For high performance speed control, high performance torque control is required as an inner loop. Here, also the outer position loop of the mechanical system can be realized by an external controller.

> ➤ the position control of the motor, such as in robotics, conveyors, etc.. Position control of the motor can be realized by a cascaded control structure as outer motor position loop, then inner motor speed loop, and the inner most torque loop.

Briefly, motion control is to control the motion output of an electromechanical system. Within the motion control applications, AC drives performing torque/speed/position control of the electric motors are utilized. As listed above, it can be said that in all motion control applications essentially the torque of the electric motor is controlled.

In the old industrial applications, separately excited DC motor was employed for its easy to control structure. High dynamic torque performance of the DC motor stems from its structure such that the armature mmf is always spatially orthogonal to the field flux axis with the use of brushes. Therefore, torque of the DC motor is always proportional to the armature current. In order to obtain the same high dynamic torque performance of the DC motor from AC motors (induction motor, SMPM motor, IPM motor, etc.), the vector control (field oriented control) principle is employed in the AC motor drives.

3.3 Vector Control (Field Oriented Control)

Basically, vector control is to operate the AC motor such that the AC motor behaves as a DC motor and the torque production performance of the AC motor is improved. This is provided by mathematical transformation of the AC motor variables to the vector coordinates where the AC motor can be modeled the same as the DC motor.

AC motor drives employing the vector control method are called as vector controllers because they control both the amplitude and phase of the current (flux), i.e. they control the current (flux) vector. The control of the current (flux) vector results in the control of spatial orientation of the electromagnetic fields in the motor and has lead to the term "field orientation" or "field oriented control". There is a basic set of three requirements for vector control of the AC motor, which are originating from the DC motor [40];

1) an independently controlled armature (stator) current to overcome the effects of armature (stator) winding resistance, leakage inductance and induced voltage;
2) an independently controlled or constant value of the field (rotor) flux;
3) an independently controlled orthogonal spatial angle between the field (rotor) flux axis and the armature (stator) mmf axis to avoid the interaction of the mmf and the flux;

If all of these requirements are met at every instant, the torque instantaneously follows the drawn current, and high performance torque control becomes possible by high performance current control.

3.3.1 Vector Control of The IPM Motor

In the previous chapter, steady-state analysis of the IPM motor was discussed based on the phasor diagrams. Phasor diagrams are utilized for the steady-state operation of the IPM motor and AC steady-state variables are time domain variables represented in the stationary frame. In order to analyze the dynamic behavior of the IPM motor both for steady-state and transient operation, and also for zero excitation frequency (DC) case (i.e. zero speed case), complex vector variables are utilized. Complex vector variables are represented in the synchronous frame, which is rotating with the excitation frequency of the AC variables (excitation frequency of the stator phase windings). AC variables in the stationary frame are transformed to complex vectors

in the synchronously rotating frame, where they become DC quantities in the steady-state. The vector controller operates on these DC quantities (in two orthogonal axes with one of them being real and the other imaginary) such that the control action is performed and the IPM motor exhibits dynamic performance comparable to that of the separately excited DC motor. Application of the vector control theory to the IPM motor can easily be visualized when the steady-state vector equations of the IPM motor are represented in the de,qe axes in Figure 3.1. The superscript "e" is used for synchronous frame variables and the superscript "s" is used for stationary frame variables. The subscript "s" designates stator variables and the subscript "r" designates rotor variables.
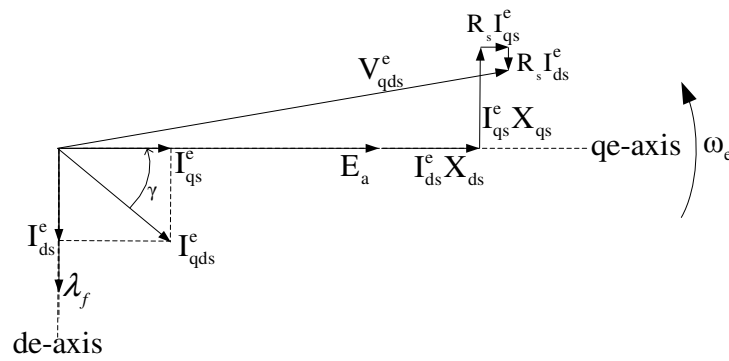
Figure 3.1 de-qe vector diagram of the IPM motor.

The de-qe coordinates are rotating with the electrical excitation frequency of the stator windings (ω_e), hence the variables are DC quantities (for steady-state) in the synchronous frame. The internal power factor angle γ of the conventional steady-state theory (based on phasors); here is the spatial angle between the current vector and the qe-axis (where E_a is located). If the spatial orientation of the current vector and the γ angle is controlled by the motor drive, then the IPM motor is controlled as a DC motor. For instance; if the current vector is created spatially on the qe-axis, which is in quadrature (normal) to the permanent magnet flux axis, then $\gamma=0°$ is satisfied as shown in Figure 3.2.
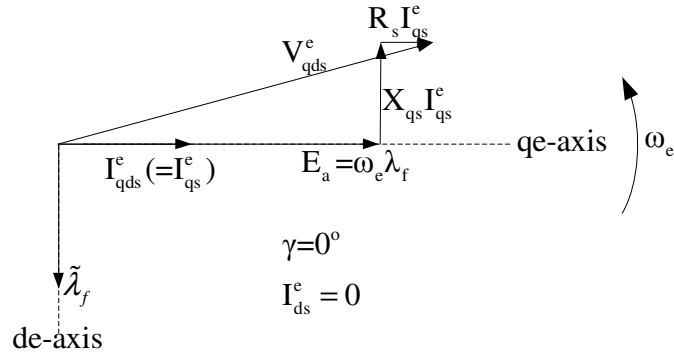
Figure 3.2 de-qe vector diagram of the IPM motor for $\gamma=0°$.

If the current vector is created such that $\gamma=0°$ is satisfied, then the armature mmf is created on the quadrature axis and the third requirement of the vector control (orthogonal spatial angle between the field flux axis and the armature mmf axis) is satisfied. When the third requirement is accomplished, the armature mmf and the field flux are orthogonal to each other and there is no interaction between the field flux and armature mmf; thus, the second requirement of the vector control (constant value of the field flux) is satisfied. If the current vector magnitude is also controlled by the stator phase current controller of the motor drive, then the first requirement (controlled armature current) is also satisfied. Thus, high performance control of the IPM motor similar to the DC motor control is obtained.

From equations (2.21) – (2.23), the torque of the IPM motor is found to be instantaneously proportional to the drawn current and no reluctance torque is created for the $\gamma=0°$ case. For $\gamma=0°$, the current vector is located on the qe-axis ($I_s = I_{qs}^e$) and I_{ds}^e is equal to zero. Therefore, the qe-axis (quadrature axis) is also called as the torque axis, where the de-axis (direct axis) is also called as the flux axis.

Due to the additional reluctance torque component of the IPM motor (for machines with $L_{ds}^e < L_{qs}^e$) maximum torque per ampere (MTPA) is achieved for $I_{ds}^e < 0$ ($\gamma < 0°$) cases. Also, for field weakening purposes armature reaction is created opposite to the field flux (permanent magnet flux) by negative I_{ds}^e current. For $I_{ds}^e \neq 0$ ($\gamma \neq 0°$)

37

cases, the current vector (I_{qds}^e) has two components on the two axes; torque component (I_{qs}^e) is on the torque axis (qe-axis) and flux component (I_{ds}^e) is on the flux axis (de-axis). Even when the current vector is created such that $I_{ds}^e \neq 0$, three requirements of vector control can still be satisfied if the current vector is controlled in two spatial axes separately. If the flux component of the stator current is created on the flux axis (de-axis) and the torque component on the torque axis (qe-axis), the torque and flux are still decoupled and dynamic performance of the motor drive is still retained.

Briefly, vector control of the IPM motor is the control of spatial orientation of the current vector and its components on the synchronously rotating coordinate frame based on the angle of the rotor permanent magnet flux. The vector control based on the transformations with respect to the rotor flux angle is called as rotor flux oriented vector control. In this thesis, rotor flux oriented vector control theory is realized. There are also stator flux and air-gap flux oriented vector control methods which are utilized for different purposes e.g. for unity power factor operation. Also, vector control of the other AC motor types, such as induction motor, is almost the same of the IPM motor. Application of the vector control theory is realized by the transformation of the stationary frame variables to the synchronous frame and vice versa. The visualization of the magnetic axes of three-phase windings of the IPM motor with the stationary ds-qs axes and the rotating synchronous frame de-qe axes is given in the Figure 3.3.
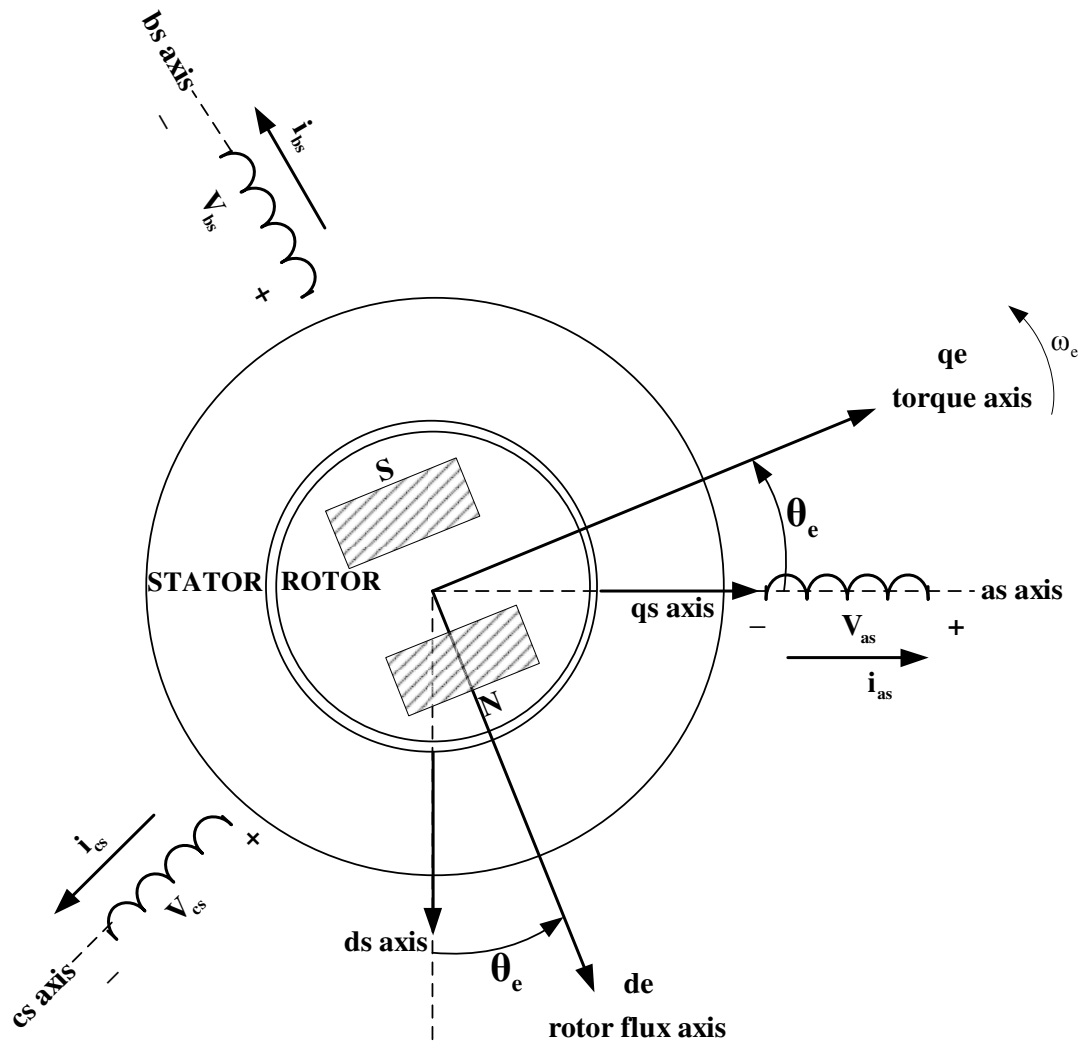
Figure 3.3 Magnetic axes of the three-phase stator windings, stationary frame coordinates and synchronously rotating frame vector coordinates.

The ds, qs axes are two-phase representation of the three-phase variables in the stationary frame, where the de-qe axes are the synchronous frame coordinates rotating with the excitation frequency such that the de axis is fixed to the rotor permanent magnet flux axis and qe axis is orthogonal to it. Since the IPM motor is a synchronous machine, the rotor rotates proportional to the excitation frequency based on equation (2.9) at steady-state. Therefore, the electrical rotor flux angle information can be obtained from a rotor angular position sensor (e.g. encoder) on the shaft of the motor or from estimation algorithms in the sensorless motor drives as realized in this thesis.

Mathematical transformation formulas, which are based on the electrical rotor flux angle θ_e (the angle between the qe-axis of the rotor and magnetic axis of the phase-a), for the transformation of three-phase variables to the synchronous frame variables and the inverse transformations are summarized in Figure 3.4 and given in detail in equations (3.1)-(3.11), where "f" can be stationary or synchronous frame stator/rotor variables. Equations (3.1)-(3.5) are forward transformations while (3.6)-(3.11) are inverse transformations.
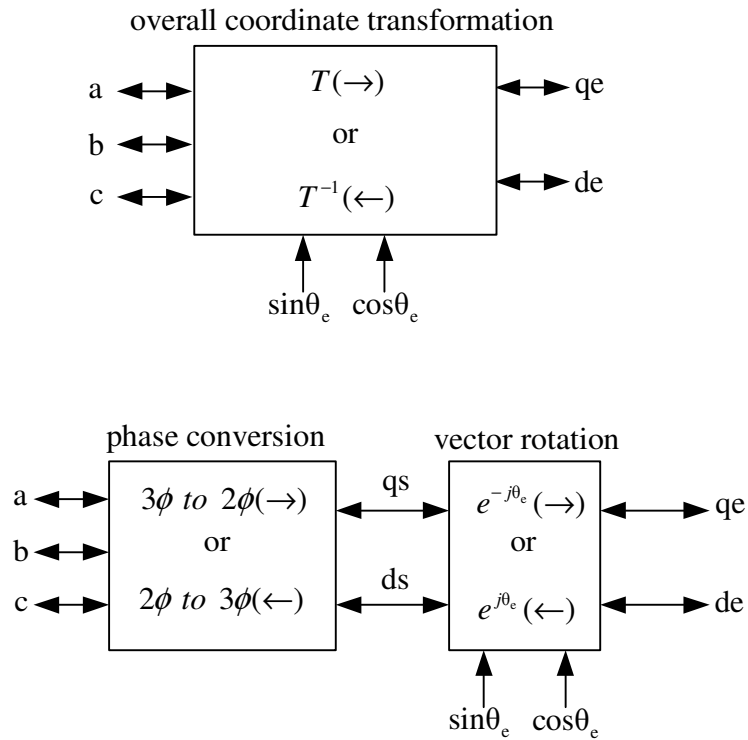
Figure 3.4 Coordinate transformations for vector control.

$$f_q^s = f_a \tag{3.1}$$

$$f_d^s = -\frac{1}{\sqrt{3}}f_a - \frac{2}{\sqrt{3}}f_b \tag{3.2}$$

$$f_q^e = \cos\theta_e f_q^s - \sin\theta_e f_d^s \tag{3.3}$$

$$f_d^e = \sin\theta_e f_q^s + \cos\theta_e f_d^s \qquad (3.4)$$

$$f_{qd}^e = e^{-j\theta_e} f_{qd}^s \qquad (3.5)$$

$$f_a = f_q^s \qquad (3.6)$$

$$f_b = -\frac{1}{2} f_q^s - \frac{\sqrt{3}}{2} f_d^s \qquad (3.7)$$

$$f_c = -\frac{1}{2} f_q^s + \frac{\sqrt{3}}{2} f_d^s = -f_a - f_b \qquad (3.8)$$

$$f_q^s = \cos\theta_e f_q^e + \sin\theta_e f_d^e \qquad (3.9)$$

$$f_d^s = -\sin\theta_e f_q^e + \cos\theta_e f_d^e \qquad (3.10)$$

$$f_{qd}^s = e^{j\theta_e} f_{qd}^e \qquad (3.11)$$

In the above transformations, the vector and scalar variables are related with the scalar to complex number transformation given in (3.12) [40],

$$f_{qd} = f_q - j f_d \qquad (3.12)$$

where f_{qd} represents a generic complex vector (complex number) quantity and j is the imaginary axis unit. Various researchers utilize various notations for the vector transformations (power invariant forms, imaginary axis positive defined form, etc.). Also, the θ_e transformation angle can be defined between the flux axis of the rotor and magnetic axis of the phase a. However, the basic principle of vector control remains the same in all these cases.

Stationary frame voltage equations of the IPM motor, in the ds-qs axes are given in (3.13) - (3.15). The scalar equations can be obtained based on the expansion of these formulas utilizing (3.12),

$$V_{qds}^s = R_s i_{qds}^s + p\lambda_{qds}^s \tag{3.13}$$

$$V_{qs}^s = R_s i_{qs}^s + p\lambda_{qs}^s \tag{3.14}$$

$$V_{ds}^s = R_s i_{ds}^s + p\lambda_{ds}^s \tag{3.15}$$

where

p is the derivative operator,

V_{qds}^s is the stator terminal voltage,

R_s is the stator resistance,

i_{qds}^s is the stator current,

λ_{qds}^s is the flux linkage.

The flux equations in the stationary frame, which depend on the electrical rotor angle θ_e and the saliency of the IPM motor, are given in (3.16) - (3.18),

$$\lambda_{qds}^s = L_{qds}^s i_{qds}^s + \lambda_f^s(\theta_e) \tag{3.16}$$

$$\lambda_{qs}^s = (L_s - \Delta L_s \cos 2\theta_e) i_{qs}^s - \Delta L_s \sin 2\theta_e i_{ds}^s + \lambda_f \sin\theta_e \tag{3.17}$$

$$\lambda_{ds}^s = (L_s + \Delta L_s \cos 2\theta_e) i_{ds}^s - \Delta L_s \sin 2\theta_e i_{qs}^s + \lambda_f \cos\theta_e \tag{3.18}$$

where;

$$L_s = \frac{L_{qs}^e + L_{ds}^e}{2} \tag{3.19}$$

42

$$\Delta L_s = \frac{L_{qs}^e - L_{ds}^e}{2} \tag{3.20}$$

L_{qs}^e is the qe-axis synchronous inductance,

L_{ds}^e is the de-axis synchronous inductance,

λ_f is the permanent magnet flux linkage.

Transformation of the stationary frame equations to the synchronous frame can be made using the formulas (3.1)-(3.11) or utilizing (3.21) and (3.22) directly.

$$f_{qd}^s = f_{qd}^e e^{j\omega_e t} \tag{3.21}$$

$$pf_{qd}^s = p(f_{qd}^e e^{j\omega_e t}) = (p + j\omega_e)f_{qd}^e e^{j\omega_e t} \tag{3.22}$$

Then, the synchronous frame voltage equations (3.13) for the IPM motor become as (3.23).

$$V_{qds}^e = R_s i_{qds}^e + (p + j\omega_e)\lambda_{qds}^e \tag{3.23}$$

When the de-axis lies on the rotor flux (permanent magnet) axis, the synchronous frame flux equations become as (3.24) and (3.25).

$$\lambda_{qs}^e = L_{qs}^e i_{qs}^e \tag{3.24}$$

$$\lambda_{ds}^e = L_{ds}^e i_{ds}^e + \lambda_f \tag{3.25}$$

Substituting the flux equations (3.24) and (3.25) in the voltage equations (3.23), the scalar voltage equations in the synchronous frame are obtained as in (3.26)-(3.27) based on the expansion formula (3.12).

$$V_{qs}^e = R_s i_{qs}^e + L_{qs} p i_{qs}^e + \omega_e L_{ds} i_{ds}^e + \omega_e \lambda_f \qquad (3.26)$$

$$V_{ds}^e = R_s i_{ds}^e + L_{ds} p i_{ds}^e - \omega_e L_{qs} i_{qs}^e \qquad (3.27)$$

By means of the de-qe variables, the electromechanical torque of the IPM motor can be calculated from the general formula of (3.28).

$$T_e = \frac{3}{2} \frac{p}{2} (\lambda_{ds}^e i_{qs}^e - \lambda_{qs}^e i_{ds}^e) \qquad (3.28)$$

Substituting the flux equations (3.24) and (3.25) in the general torque formula (3.28) yields the developed torque in terms of stator currents and magnet flux as in (3.29).

$$T_e = \frac{3}{2} \frac{p}{2} \left[\lambda_f i_{qs}^e + (L_{ds}^e - L_{qs}^e) i_{ds}^e i_{qs}^e \right] \qquad (3.29)$$

Further, the developed torque equation of (3.29) can be expressed as the superposition of the reaction torque and reluctance torque terms as given in (3.30) and (3.31) respectively.

$$T_{reaction} = \frac{3}{2} \frac{p}{2} \lambda_f i_{qs}^e \qquad (3.30)$$

$$T_{reluctance} = \frac{3}{2} \frac{p}{2} (L_{ds}^e - L_{qs}^e) i_{ds}^e i_{qs}^e \qquad (3.31)$$

In summary, vector control is to create the current vector by controlling its spatial angle such that the torque component (I_{qs}^e) is on the torque axis and flux component (I_{ds}^e) is on the flux axis of the motor. In this thesis, I_{ds}^e is always commanded to be zero, i.e. no field weakening operation or MTPA optimization based on the additional reluctance torque is performed, and only I_{qs}^e command is realized, which corresponds to the torque command. Torque control of the motor is realized by

controlling the I_{qs}^e on the torque axis to produce the commanded torque and controlling the I_{ds}^e on the flux axis to be equal to zero, in the synchronous frame; i.e. to create the corresponding three-phase stator currents on the motor and this can be accomplished by a current regulator.

There are various current regulation methods for AC machines such as hysteresis, linear (PI), deadbeat, soft computing based methods, etc. Current regulators can be implemented in the stationary frame or in the synchronous frame. In this thesis, Synchronous Frame Current Regulator (SFCR) employing a linear PI compensator, which is the most suitable current regulator for vector control, is utilized.

3.3.2 The Synchronous Frame Current Regulator (SFCR)

The SFCR [41] operates on the synchronous frame variables, which are DC quantities at steady-state. SFCR does not relate with the three-phase currents, instead it regulates the synchronous frame currents on the synchronous frame, based on the given synchronous frame transformation angle information.

Inputs of the SFCR are the synchronous frame I_{qs}^{e*} (torque) and I_{ds}^{e*} (flux) current commands (coming out of the speed controller and flux level controller), the three-phase motor currents i_a, i_b, i_c used as feedback, the θ_e angle to be used in vector transformations, and DC link voltage level of the inverter used for anti-windup mechanism. The outputs are the three-phase voltage commands to the inverter.

SFCR calculates the synchronous frame I_{qs}^e and I_{ds}^e feedback currents using the three-phase i_a, i_b, i_c currents and the θ_e angle. The error between the commanded currents and the actual current feedback is compensated by a regulator within the SFCR and the output of the compensation is fed to the VSI. SFCR, which is utilized for the vector control of the IPM machine, is shown in Figure 3.5.. Since, torque control of the IPM motor is provided by the vector control theory, which is realized

by the SFCR and the VSI; the SFCR - VSI combination is designated as torque controller in Figure 3.5 and in the following parts.
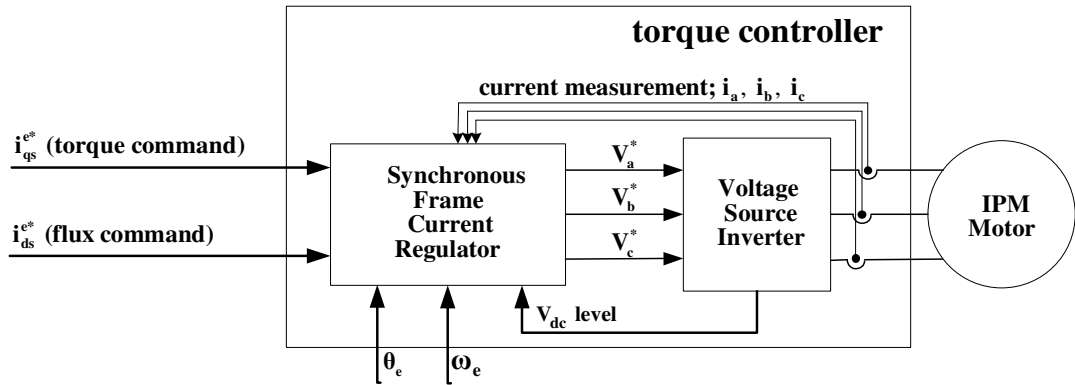
Figure 3.5 Utilization of the SFCR in the vector controlled IPM motor drive.

When the synchronous frame voltage equations of the IPM motor (3.26) and (3.27) are analyzed, it is observed that the IPM motor can be expressed simply as an RL load, when the cross-coupling terms ($\omega_e L_{ds} i_{ds}$, $\omega_e L_{qs} i_{qs}$) and the bemf term ($\omega_e \lambda_f$) are eliminated. Hence, the synchronous frequency (ω_e) is also fed to the SFCR in Figure 3.5 to be used for decoupling of the effects of the cross- coupling terms and bemf terms, which are explained in the following parts. Since the motor can be simplified to an RL load, which has first order lag characteristics and since the SFCR works on the DC quantities on the synchronous frame, the most effective method of current regulation for the SFCR is the linear PI compensator. The PI compensator, including an anti-windup mechanism, compensates for the error between the synchronous frame current commands (I_{qs}^{e*} and I_{ds}^{e*}) and the feedback (I_{qs}^{e} and I_{ds}^{e}) and generates synchronous frame voltage references V_{qs}^{e*} and V_{ds}^{e*}. V_{qs}^{e*} and V_{ds}^{e*} are transformed back to the stationary frame as three-phase voltage command outputs V_{a}^{*}, V_{b}^{*}, V_{c}^{*}, which are fed to the voltage source inverter (VSI).

Here, the VSI works as a voltage amplifier and it produces the commanded voltages at its outputs using the pulse width modulation (PWM) method. PWM method can be

46

of any type (sinusoidal PWM or space vector PWM or near state PWM, etc. [42]. Operating limits and nonlinearities of the VSI will be explained in conjunction with the experimental setup in the related chapter. The block diagram of the SFCR is given in the Figure 3.6.
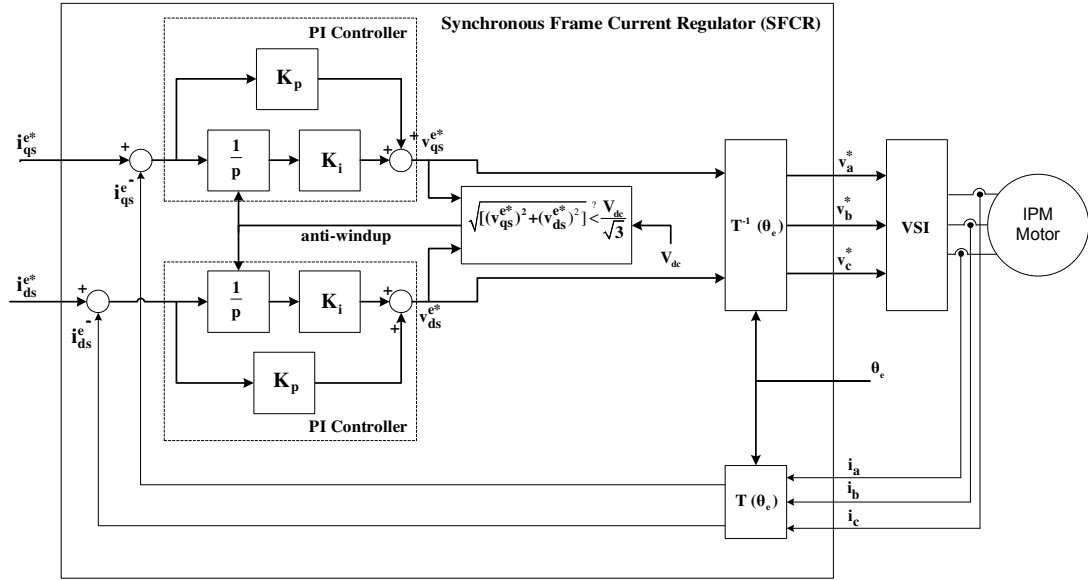
Figure 3.6 Block diagram of the SFCR.

Since the output of the VSI has a saturation limit depending on the DC link voltage level (V_{dc}), outputs of the PI compensators are checked whether the voltage command is realizable or not. An anti-windup mechanism is implemented which stops the "I" (integral) action of the current regulator, depending on the voltage commands and the limits of the VSI, which is related with the DC link level and the PWM method. When the motor operates at very high speeds, the voltage commands goes over the limit of the VSI and saturation occurs. More essential than the anti-windup mechanism, there exist different algorithms, which modify the I_{qs}^{e*} and I_{ds}^{e*} current commands (e.g. for field weakening) or cause overmodulation in the VSI, to operate the motor effectively when the limit of the inverter is reached. The operation in this nonlinear very high speed region is not realized in this thesis since the main scope of the thesis is the sensorless operation, especially at zero and low speed region. However, the DC link voltage level is taken into account within the VSI, and

47

PWM outputs are produced in order to compensate for the changes of the DC link voltage level, which will be explained in the related chapter.

Motor torque control performance depends on the vector control performance. And the vector control is realized by the control of the current vector. Therefore, high performance torque control by the vector control relies on exact rotor flux angle information and on high performance current regulation. The former can be provided by a sensor on the motor or by the sensorless estimation algorithms as in this thesis. The current regulation performance is obtained by implementing effective compensators within the SFCR and by properly operating these compensators. Therefore PI compensators of SFCR are enhanced with additional compensators (cross-coupling and bemf decoupling) based on the fundamental model of the IPM motor. Synchronous frame transformations bring the cross-coupling terms $\omega_e L_{ds} i_{ds}$ to the qe-axis and $\omega_e L_{qs} i_{qs}$ to the de-axis. These cross-coupling terms cause dynamic disturbance to an axis when there is a change of current level on the other axis, especially at high frequency (speed). In order to remove the effects of these cross-coupling, decoupling should be made. Also, back-emf of the motor is seen as $\omega_e \lambda_f$ term on the qe axis, which acts as a disturbance on the qe axis.

Effect of these coupling and disturbance terms can be removed by adding compensation terms for them. This is accomplished by feedforward of the decoupling and disturbance terms to the output of the PI compensators as given in Figure 3.7. [43]-[45].
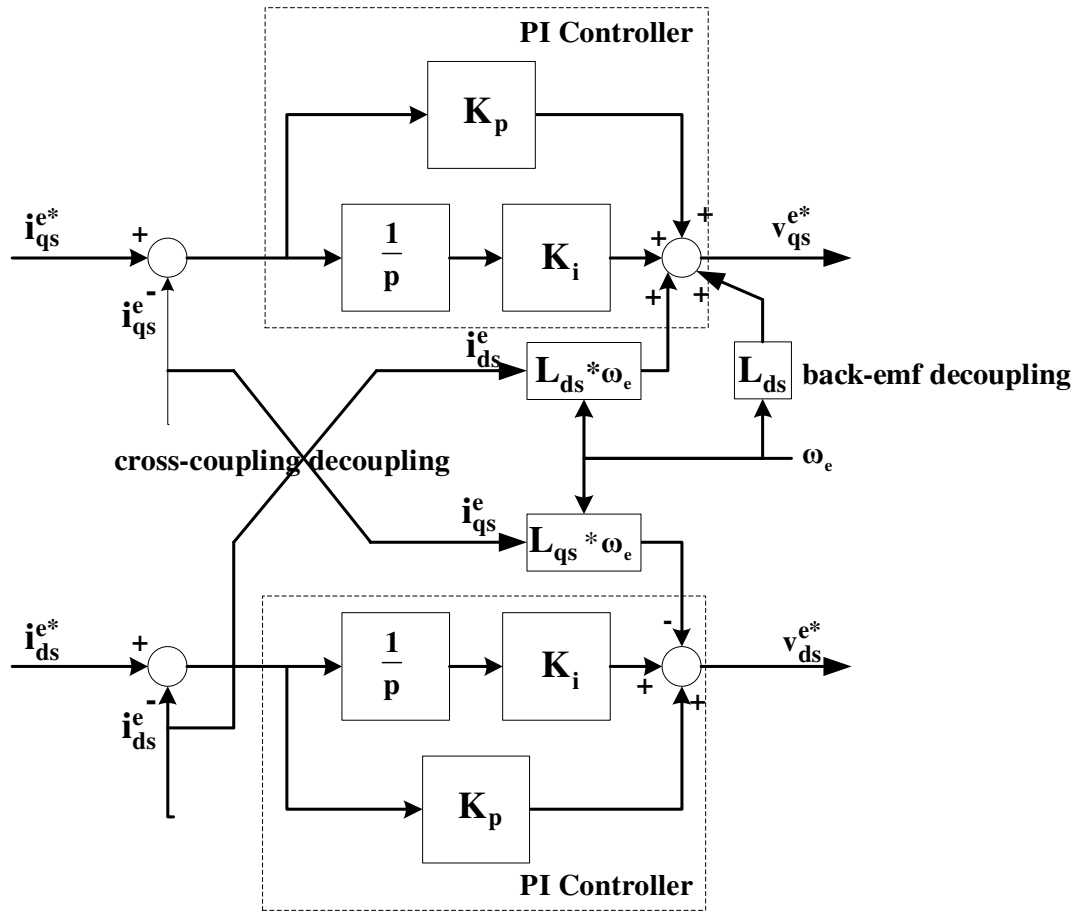
Figure 3.7 Block diagram of SFCR with cross-coupling decoupling.

Decoupling of cross-coupling and disturbance terms rely on the current, inductance, and field flux parameter information. However, parameters of the motors can change during the operation or even may not be known. Also the measurements may be inaccurate. The complex vector synchronous frame current regulator [46], [47] performs the cross-coupling decoupling independent of the motor parameters. This method is not implemented for the IPM motor current, however implemented in the induction motor part of this thesis, which is given in the following chapters.

After implementing the cross-coupling decoupling and back-emf decoupling feedforward terms, IPM motor model is reduced to an RL load (a first order lag system), whose transfer function can be represented as in (3.32)

$$\frac{K_c}{R_s + L_s s} \tag{3.32}$$

The RL load has a pole at the frequency equal to its time constant, R_s/L_s. The well-known and common compensation method for the RL load is the pole-zero cancellation which results in favorable phase and gain margins. Therefore, the K_P and K_I parameters of the PI controller are chosen to create a zero at the same frequency of the RL load. Then, the relation in (3.33) is used for the current regulator PI compensator tuning.

$$\frac{K_I}{K_P} = \frac{R_s}{L_s} \tag{3.33}$$

Tuning of the SFCR aims to improve its bandwidth for high performance current control. As a general rule bandwidth of the SFCR is one tenth of the sampling frequency. In this thesis, properly tuned SFCR bandwidth up to 1 kHz for a 10 kHz sampling frequency could be obtained. However, for the high frequency signal (voltage) injection algorithm implementation, which will be discussed in the next chapter, bandwidth of the SFCR is intentionally decreased by an order of magnitude, in order to prevent the interference between the high frequency injection signal and fundamental frequency signal and obscure the fundamental SFCR operation.

In summary, torque control of the IPM motor is provided by the vector control method. The vector control method needs the rotor flux angle information, which is supplied by the sensorless estimation algorithms within this thesis, and current control is realized by the SFCR and the VSI. As a result, torque control of the motor is accomplished. In some cases, the motor drive may be requested to perform only the torque control of the motor which can be called as torque mode. However, in most of the applications, speed and position control of the motor is requested. Theories of speed and position control are explained in the following sections.

3.4 Speed and Position Control

Most of the applications such as adjustable speed drives (air conditioners, fans, lifts, etc.) or electric vehicles require speed control of the motor and no position control is required. Speed control is realized by a speed feedback which can be provided by a sensor on the motor shaft or by the estimation algorithms as realized in this thesis. Inputs of the speed loop are the speed command and the speed feedback (alternatively estimated speed) and the output is the torque command, which is fed to the torque controller, i.e. vector controller, which is composed of the SFCR and VSI. Block diagram of the speed control is given in Figure 3.8.
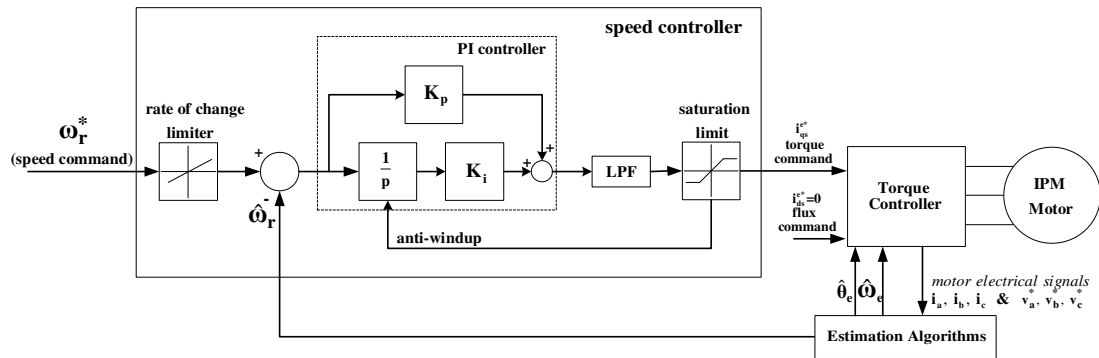
Figure 3.8 Block diagram of the speed control loop with PI controller.

Since the torque of the drive is limited due to motor and/or inverter ratings, the acceleration capability is also limited. The acceleration capability depends on the maximum torque value and the load. Therefore, speed command input of the speed controller is shaped (bounded) by a rate of change limiter. The limit of the rate of change of speed (acceleration) is set by considering the load torque (friction, unbalance, etc.) and the total (load plus rotor) inertia. This can be thought as not to request more acceleration than the drive is able to provide. This shaping prevents the unnecessary build up of speed error. The speed error goes through a PI compensator the output of which is the torque command. High frequency content of the torque command is filtered out with a low pass filter (LPF) to avoid resonance and oscillations at the output, and also to filter the torque commands which are at frequencies higher than the bandwidth of the drive. The torque command is fed

51

through a saturation block which limits the command with the maximum value of the drive torque capability. When the limit of the drive is reached, the anti-windup mechanism stops the build-up of the integral action.

The speed controller is tuned to realize the speed commands with the highest possible bandwidth. However, the speed controller tuned for high performance command tracking may not react to load disturbances very well. If the speed controller PI parameters, K_p and K_I are increased in order to improve the disturbance rejection capability of the drive, then oscillations may occur. The PDFF (Pseudo Derivative Feedback Feedforward) method is implemented for enhancement of the speed control [48], [49] performance in the manner of disturbance rejection while also improving the command tracking performance. The block diagram of the speed control loop with the PDFF controller is shown in Figure 3.9.
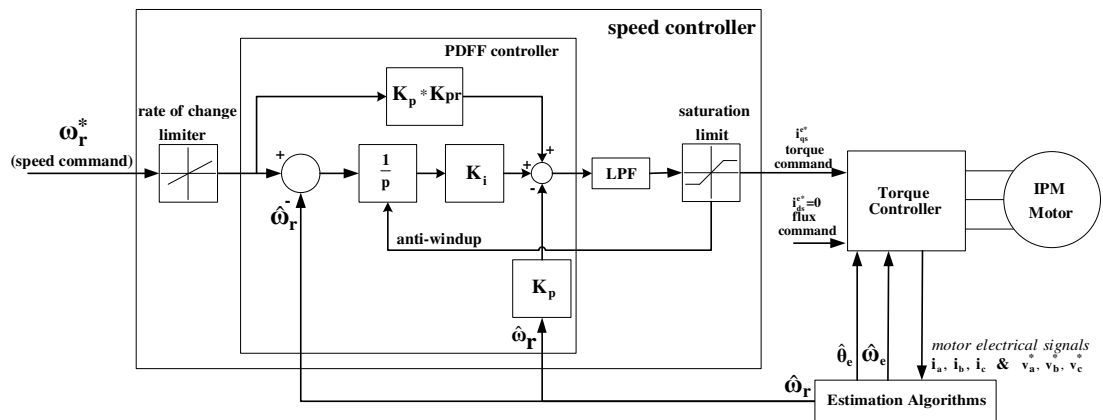
Figure 3.9 Block diagram of the speed control loop with PDFF controller.

The PDFF controller allows for high K_p and K_I gains, which increase the disturbance rejection performance, without causing oscillation at the output. Integral action works as it works in the standard PI control, however proportional action is different. Error between the command and the actual speed is not directly fed to the proportional compensator. The command is scaled by a constant between 0 and 1 and the error between the scaled command and the actual speed is fed to the proportional compensator. Scaling constant is the K_{pr} in the block diagram. When K_{pr} is taken as 0, then the command has no effect on the proportional compensator and for this case

the controller is also called as PDF (Pseudo Derivative Feedback) controller. When K_{pr} is taken as 1, then the PDFF controller is same as the PI controller. The K_{pr} value between 0 and 1 determines the disturbance rejection capability of the controller, such that 0 results in the highest disturbance rejection. There is a trade-off between the command tracking and disturbance rejection characteristic, which is directly related with the K_{pr} constant [48].

In some applications, such as robotics and conveyors, in addition to speed control, angular position control of the motor is also required. Position control is to drive the motor to the requested mechanical angle or to drive the motor with the requested count of turns and to the requested mechanical angle. This means that mechanical position of the motor has to be known and count of the number of turns is required. Position information of the motor can be supplied from a sensor on the motor shaft or from sensorless algorithms as realized in this thesis. Count of the turns can be calculated using the position information.

For high performance position control, cascaded control structure is utilized as; the outer position loop, then the inner motor speed loop, and the inner most torque loop. Block diagram of the position controlled drive system is given in Figure 3.10.
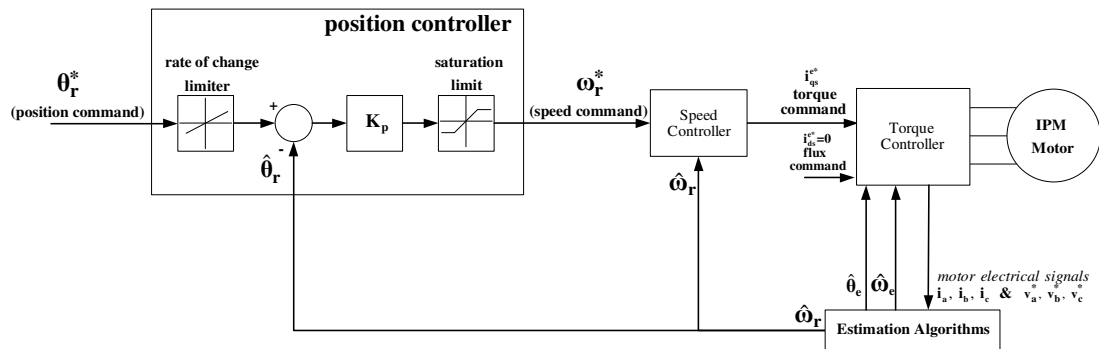
Figure 3.10 Block diagram of the position control loop.

Similar to the speed control loop, command input of the position loop is also shaped by a rate of change limiter since rate of change of the position of the motor (i.e.

speed) is limited with the maximum speed of the drive motor. Only "P" (proportional) type compensator is utilized for the position loop.

In motion control applications, speed control of the motor is highly related to the load attached to the motor. The acceleration limit depends on the load and the tuning of the speed loop is strongly dependent on the load and the disturbance characteristics (magnitude, frequency, etc.). Hence, position control performance, which relies on the speed control, is also dependent on the application. In this thesis, speed loop and position loop tuning are made for the no load case and for loaded (disturbance by the load machine) case by a coupled load machine to the motor, which will be explained in the related chapter. For speed loop tuning, symmetrical optimum [50] and Ziegler Nichols [51] methods, which are the well known methods in the literature, are utilized both for simulations and experimental work.

In summary, motion control applications require three stages of motor control; torque control, speed control, and position control. Torque control is mainly composed of the current control and generally implemented by a power electronics engineer, where the speed control of the motor is performed by the drive engineers and the position control is the task of the servo engineers of the application. In this thesis, torque control is implemented based on the sensorless vector control theory with sensorless estimation of the rotor flux angle. Speed and position estimations of the sensorless algorithms are used for speed and position control of the motor. The aim is to verify that the speed and position estimations of the algorithms can be used for the sensorless motion control application. However, as explained above, high performance speed and position control depends on the load and tuning of the speed and position control loops have to be made in accordance with the application. The following chapter elaborates on the sensorless control of the IPM motor, specifically the rotor flux angle estimation and speed/position estimation methods.

CHAPTER 4

THEORY OF SENSORLESS CONTROL ALGORITHMS FOR THE IPM MOTOR

4.1 Introduction

Sensorless AC drives are employed in motion control applications for robust, cost effective, and efficient solutions. IPM motors are preferred mainly for their high efficiency and high motion quality performance characteristics, in the adjustable speed drive applications and also in the servo applications. In the third chapter, it was shown that performance of the speed/position control of the motor depends on the high performance torque control and for high performance torque control, vector control method is utilized in the AC motor drives. For closed loop speed and position control, encoders or resolvers may be used. Instead of using encoders, the more economical, and in some cases the more reliable sensorless motor drives can be preferred in many applications. Shaft sensorless vector control and sensorless speed/position control of the IPM motor are realized in this thesis. This chapter includes the sensorless rotor flux angle and sensorless speed/position estimation and control algorithms for the IPM motor. The rotor flux angle is estimated and used for vector control; the speed and position are estimated for speed and position control of the IPM motor. The high frequency signal injection method based on the saliency of the IPM motor is utilized for the low and zero speed operation. The fundamental model based flux observer method is utilized for the high and moderate speed range. A hybrid method combining these two algorithms is implemented for the whole speed range operation. The theory of the high frequency signal injection method,

model based flux observer method, and the hybrid method are given in the following sections of this chapter consequently.

4.2 The Saliency Based High Frequency Signal Injection Algorithm

The IPM motor is a synchronous motor with magnetic saliency. The magnetic saliency (spatial anisotropy) of the IPM motor is inherent and speed independent. This physical property allows for the estimation of the rotor flux angle and motor speed even for low and zero speed regions. In the saliency based high frequency signal injection method, saliency of the IPM motor, which is the impedance characteristics of the IPM rotor with respect to the rotor flux axis, is tracked. Hence, the rotor flux axis of the IPM motor is tracked. The estimated rotor flux angle is used for vector control of the IPM motor. Since the IPM motor is a synchronous motor, the mechanical angle and speed of the motor are proportional to the electrical rotor flux angle and speed with the pole pair relation (2.9). Therefore, the electrical synchronous frequency estimation can be used for mechanical speed control and the electrical rotor flux angle estimation can also be used for mechanical angular position control of the IPM motor. The injection and demodulation principles of the saliency based high frequency signal injection algorithm are similar to that of the resolver-to-digital converters. The saliency based high frequency signal injection algorithm uses the motor itself as a resolver [21]. High frequency signals are applied to the motor and the response is analyzed in order to estimate the rotor flux angle and speed/position of the motor.

4.2.1 The Saliency of The IPM Motor

The saliency of the IPM motor, originating from its rotor structure, was discussed in the second chapter and the saliency can be expressed in its fundamental model. The stationary frame voltage and flux linkage equations of the IPM motor were given in

(3.13) - (3.20). The inductance matrix seen from the stationary frame is given in (4.1).

$$L_{qds}^s = \begin{bmatrix} L_s + \Delta L_s \cos 2\theta_e & \Delta L_s \sin 2\theta_e \\ -\Delta L_s \sin 2\theta_e & L_s - \Delta L_s \cos 2\theta_e \end{bmatrix}$$

(4.1)

The effect of the saliency (inductance difference between the two axes of the rotor), is observed as cross-coupling between the qs, ds axes and as dependency of the inductance on the rotor angle θ_e, in the stationary frame inductance matrix. The saliency of the IPM rotor is observed as difference between the impedances of the qe, de axes in the synchronous frame. For zero and low speed, the speed related voltage terms in the synchronous frame voltage equations (3.26)-(3.27), can be neglected since ω_e becomes very small. The voltage equations become as (4.2) and (4.3); and the impedances in two axes can be represented as (4.4) and (4.5).

$$V_{qs}^e = R_s i_{qs}^e + L_{qs} p i_{qs}^e$$

(4.2)

$$V_{ds}^e = R_s i_{ds}^e + L_{ds} p i_{ds}^e$$

(4.3)

$$Z_{qs}^e = R_s + j\omega_{hf} L_{qs}^e$$

(4.4)

$$Z_{ds}^e = R_s + j\omega_{hf} L_{ds}^e$$

(4.5)

When high frequency signals are applied to the IPM motor, R_s can be neglected in (4.4) and (4.5) since at high frequency the reactance terms are dominant. As explained in the second chapter, as a result of the mounting structure of the permanent magnets in the IPM rotor, the reluctance on the qe-axis is lower than the reluctance on the de-axis since there exists permanent magnet material (with low permeability) on the de-axis. Therefore, the inductance on the qe-axis is larger than the inductance on the de-axis and hence the impedance on the qe-axis is larger than the impedance on the de-axis;

57

$$L^e_{qs} > L^e_{ds} \qquad\qquad\qquad\qquad\qquad\qquad (4.6)$$

$$Z^e_{qs} > Z^e_{ds} \qquad\qquad\qquad\qquad\qquad\qquad (4.7)$$

As a result, the impedance of the rotor varies spatially. The (high frequency) impedance is minimum on the de-axis (rotor flux axis) and increases to its maximum on the qe-axis. The saliency of the IPM motor can be easily detected when its impedance characteristics are extracted by applying high frequency voltages or currents and then analyzing the response. For instance, when high frequency voltages are applied to different angles of the rotor covering the whole pole of the rotor, i.e. one electrical pole of the rotor is scanned with a high frequency voltage vector, as in Figure 4.1, the current response gives the shape of the admittance curve, as in Figure 4.1 and 4.2.
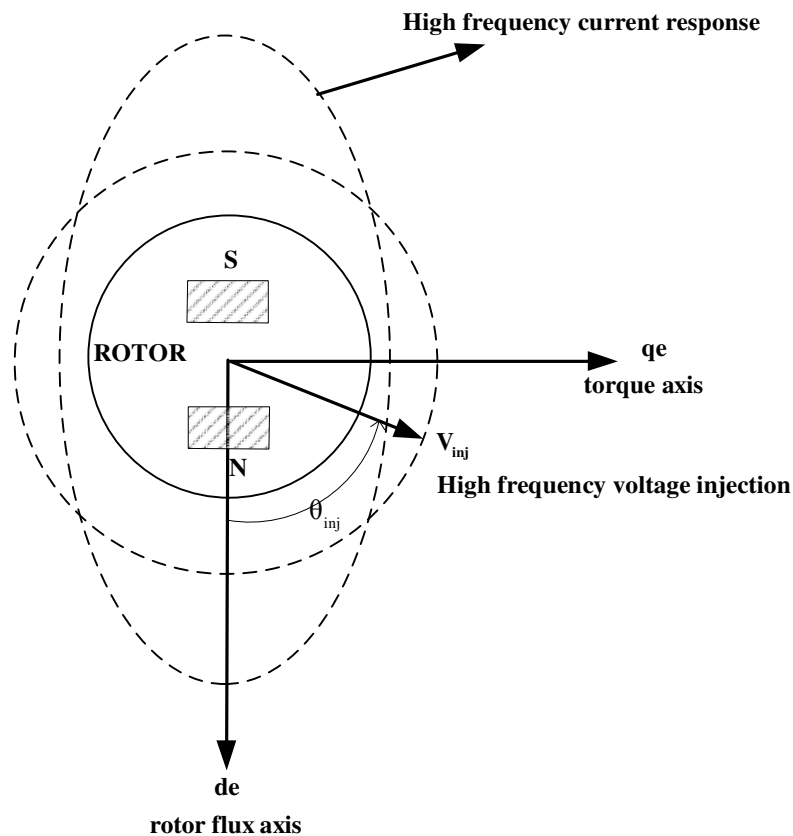
Figure 4.1 Scan of the IPM rotor with high frequency voltage and the induced high frequency current.
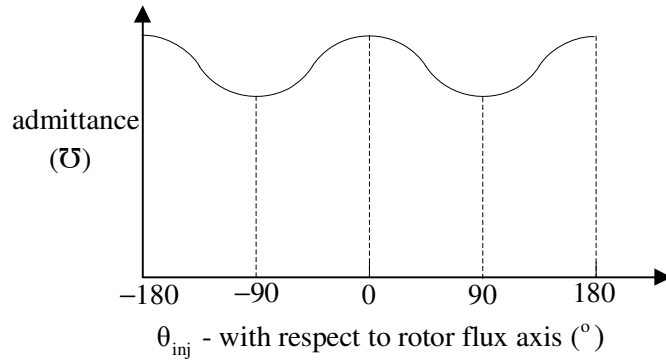
Figure 4.2 Admittance curve (magnetic saliency) of the IPM motor.

When the rotor is stationary with $\theta_e=0°$, the impedance values seen from the stationary frame are as the elliptic curve in Figure 4.3. The impedance ellipse of the rotor rotates with the rotor and can be observed in the synchronous frame.
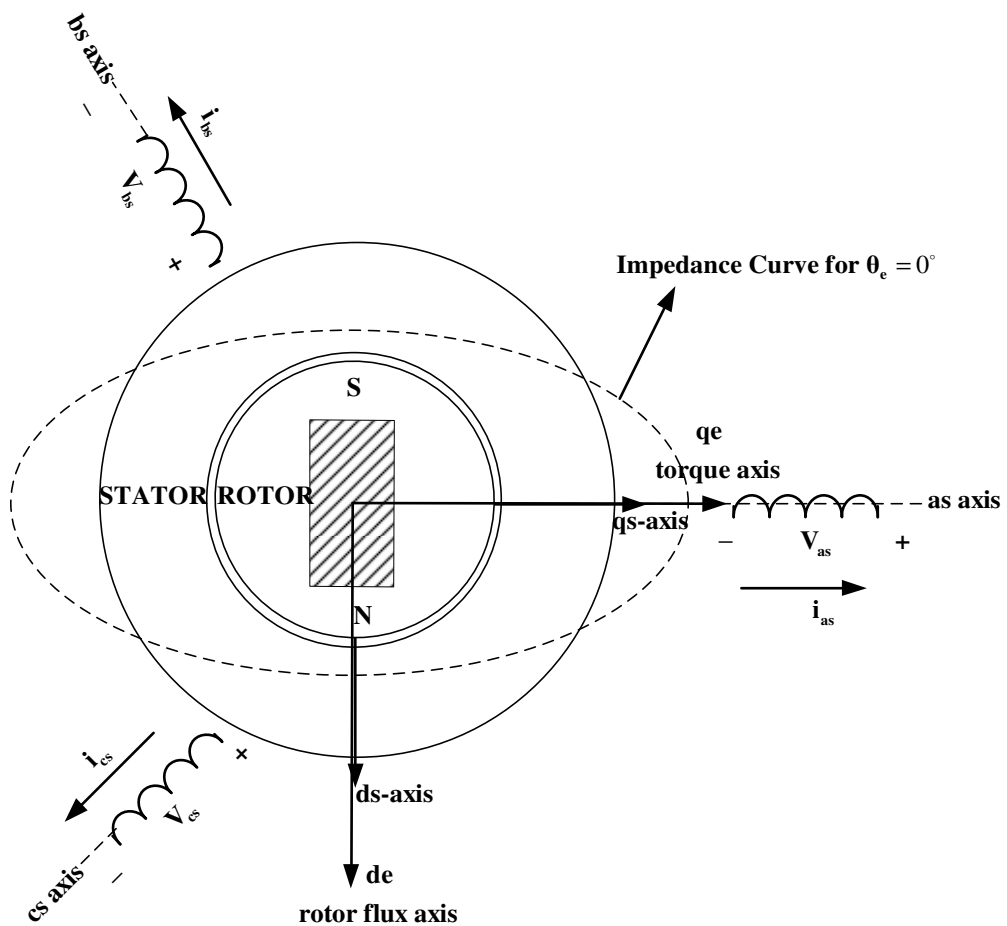
Figure 4.3 Impedance locus (magnetic saliency) of the IPM motor.

59

In Figure 4.4 only high frequency voltages (without any fundamental frequency component excitation) are applied to the phase-a of the IPM motor for three different cases; when the rotor is stationary with $\theta_e=0°$, $\theta_e=45°$, and $\theta_e=90°$. The frequency of the injection voltage is 500 Hz and the magnitude is 75 V peak. The waveforms are simulation results which will be experimentally verified in the related chapter.
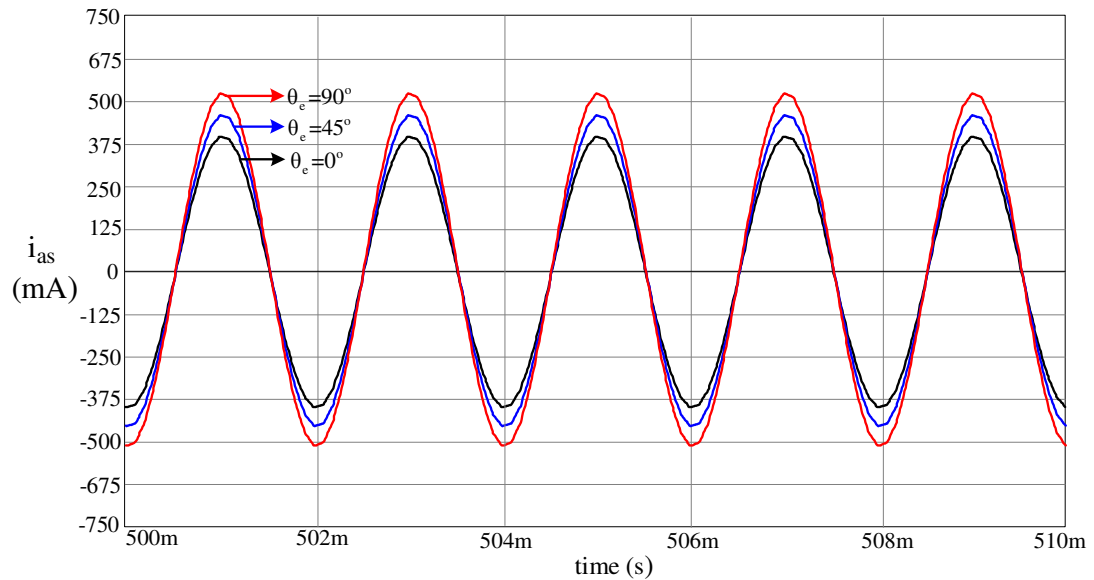
Figure 4.4 Induced high frequency stator phase-a currents for various rotor angle values (ω_r=0 rpm, V_{inj}=75V, f_{inj}=500Hz).

In Figure 4.4, when $\theta_e=0°$, the magnetic axis of phase-a coincides with the qe-axis (torque axis) and injection is made to the qe-axis, which has the highest impedance; hence the induced current has the lowest magnitude for $\theta_e=0°$. When $\theta_e=90°$, magnetic axis of phase-a coincides with the de-axis (rotor permanent magnet flux) and injection is made to the de-axis, which has the lowest impedance; hence the induced current has the highest magnitude for $\theta_e=90°$.

As observed in the Figure 4.1 - Figure 4.4, the minimum impedance (maximum admittance) point of the IPM motor is on the rotor permanent magnet flux axis; and this point rotates with the rotor, and it can be observed in the synchronous frame. When the minimum impedance (maximum admittance) point corresponding to the

rotor flux axis is tracked, then the rotor flux angle is estimated. However, the minimum impedance point may differ from the rotor permanent magnet flux axis for heavy loaded and saturated operation of the motor, which will be discussed for the loading experiments, in the related chapter. These deviations, caused by loading, can be identified off-line as a look-up table, and they can be compensated in the control algorithm through the load current information and by means of the look-up table during the operation [36]. Such compensation is not included in this thesis and left as a future work.

4.2.2 Extraction of The Saliency

In order to extract the saliency of the IPM motor during the operation and to utilize it for estimation purposes, low magnitude high frequency signals are injected to the motor, which are superimposed to the fundamental component signals. Also, there are methods, which do not inject additional high frequency signals, instead utilize the existing PWM ripple for estimations [52]. In the injection method, the high frequency signals are commanded in addition to the fundamental signals within the drive. Therefore, the same inverter and power lines of the motor are utilized for the high frequency signal injection; and the phase variables (voltages/currents) of the motor are composed of both the fundamental and high frequency components. Since the injected high frequency signals have low magnitude, and the reactances become high at high frequency, the injection has negligible effect on the fundamental frequency behavior of the motor. The magnitude and frequency of the injection signal are determined via off-line experiments on the IPM motor for various magnitude and frequency levels. The optimum levels are selected to obtain the maximum saliency information and minimum effect on the fundamental frequency behavior of the motor. Therefore, the injection levels have to be optimized for each motor type/rating/model.

The saliency of the IPM motor can be extracted and utilized by different high frequency signal injection methods. The injected high frequency signal can be

voltage or current. Generally, voltage injection is preferred since high frequency current injection requires a very high bandwidth current regulator. In the high frequency voltage injection method, high frequency voltages are superimposed to the fundamental voltages and the high frequency current response of the motor is used for rotor flux angle (saliency) tracking and estimations. Also, the injection methods differ with respect to how the injection is made. The injection signal can be a rotating vector in the stationary frame [20], [21], short pulses in the stationary frame [54], rotating vectors in the synchronous frame [55], pulsating vectors in the synchronous frame [22], etc. The principle, which is tracking the saliency (impedance characteristic of the rotor) for rotor flux angle estimation, is same for all injection methods; however only the manner of signal injection and the mathematical analysis of the response are different.

In this thesis, synchronous frame pulsating voltage injection method of Ha and Sul [22], [36], [53], [56] is employed, such that a pulsating (AC) high frequency voltage is applied on a specific axis (estimated rotor flux axis) in the synchronous frame. This method starts with an initial estimation of the rotor flux angle, detects the error in the estimation; and via compensating the error continuously, the actual rotor flux axis is tracked. Also, there are other methods which directly estimate the rotor flux angle from the impedance curve. However, the pulsating signal injection method has advantages, such as high dynamic response, less sensitivity to the inverter non-linearity and parameter insensitivity. In this method, high frequency pulsating voltage is injected on the estimated rotor flux axis ($\hat{d}e$-axis) of the motor in the synchronous frame and the current response in the synchronous frame is analyzed for estimation. The pulsating injection voltage is a high frequency AC signal, added to v_{ds}^{e*}, which is the synchronous frame $\hat{d}e$-axis voltage command (DC quantity for steady-state operation) of the synchronous frame current regulator. The block diagram of the high frequency pulsating voltage injection method on the $\hat{d}e$-axis in the synchronous frame is shown in Figure 4.5, where the synchronous frame current regulator in Figure 3.6 is shown as simplified. The resultant stationary frame voltage and current waveforms with the high frequency components superimposed on the fundamental components are also illustrated in the Figure 4.5.

62
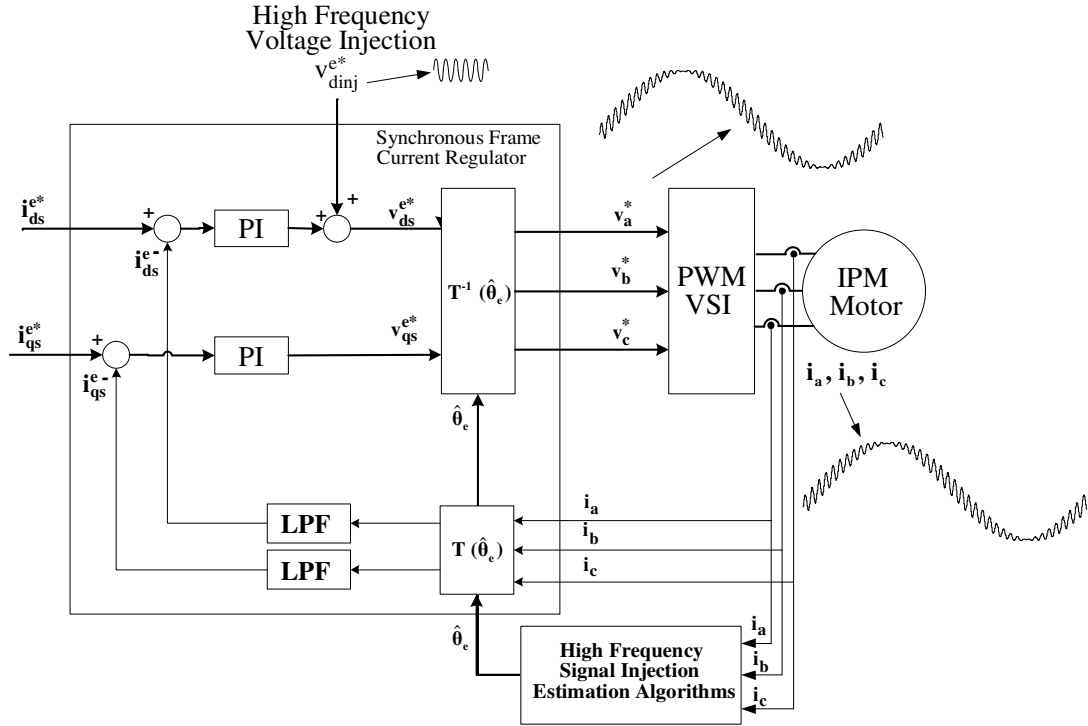
Figure 4.5 High frequency pulsating voltage injection on the $\hat{d}^e$-axis.

The stationary frame transformations of the synchronous frame voltages are given in (4.8) – (4.17) with sample values (V_1, V_2) for the synchronous frame fundamental voltages, which are DC quantities in the synchronous frame at steady-state. The resultant AC voltage on the phase-a is calculated, where ω_{hf} is the frequency of the injected high frequency voltage and the ω_f is the frequency of the fundamental excitation.

$$\theta_f = \omega_f t \tag{4.8}$$

$$V_{dinj}^{e*} = V_{inj}\sin(\omega_{hf}t) \tag{4.9}$$

$$V_{qs}^e = V_1 \tag{4.10}$$

$$V_{ds}^e = V_2 + V_{inj}\sin(\omega_{hf}t) \tag{4.11}$$

$$V_{qs}^s = V_{qs}^e \cos\theta_f + V_{ds}^e \sin\theta_f \tag{4.12}$$

$$V_a = V_{qs}^s \tag{4.13}$$

$$V_a = V_1 \cos\theta_f + [V_2 + V_{inj}\sin(\omega_{hf}t)]\sin\theta_f \tag{4.14}$$

$$V_a = \underbrace{V_1 \cos\theta_f + V_2 \sin\theta_f}_{\text{Fundamental Frequency Component}} + \underbrace{V_{inj}\sin(\omega_{hf}t)\sin\theta_f}_{\text{High Frequency Component}} \tag{4.15}$$

$$\sin x \times \sin y = \frac{\cos(x-y) - \cos(x+y)}{2} \tag{4.16}$$

$$V_{hf} = \underbrace{V_{inj}\sin(\omega_{hf}t)\sin(\omega_f t)}_{\text{High Frequency Component}} = V_{inj}\left[\frac{\cos(\omega_{hf}-\omega_f)t - \cos(\omega_{hf}+\omega_f)t}{2}\right] \tag{4.17}$$

The pulsating voltage vector in the synchronous frame can be considered as two voltage vectors with the same magnitude rotating in opposite directions in the synchronous frame as in Figure 4.6. As a result, the stationary frame high frequency phase voltages are also composed of two components with two different frequencies $(\omega_{hf} - \omega_f)$ and $(\omega_{hf} + \omega_f)$, as expressed in equation (4.17). As expected, the induced high frequency phase currents have the same characteristics. The resulting phase voltage and current waveforms for phase-a are shown in Figure 4.6, where ω_f is equal to 62.8 rad/s (10 Hz) and the injection frequency is 250 Hz with 30 V peak.
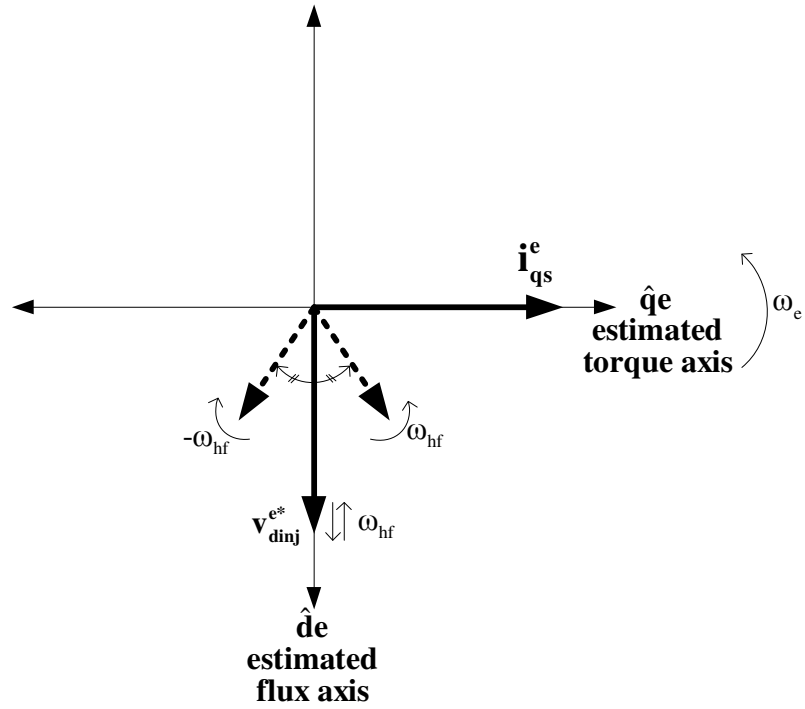
Figure 4.6 Vector diagram for pulsating voltage injection method in the synchronous reference frame.
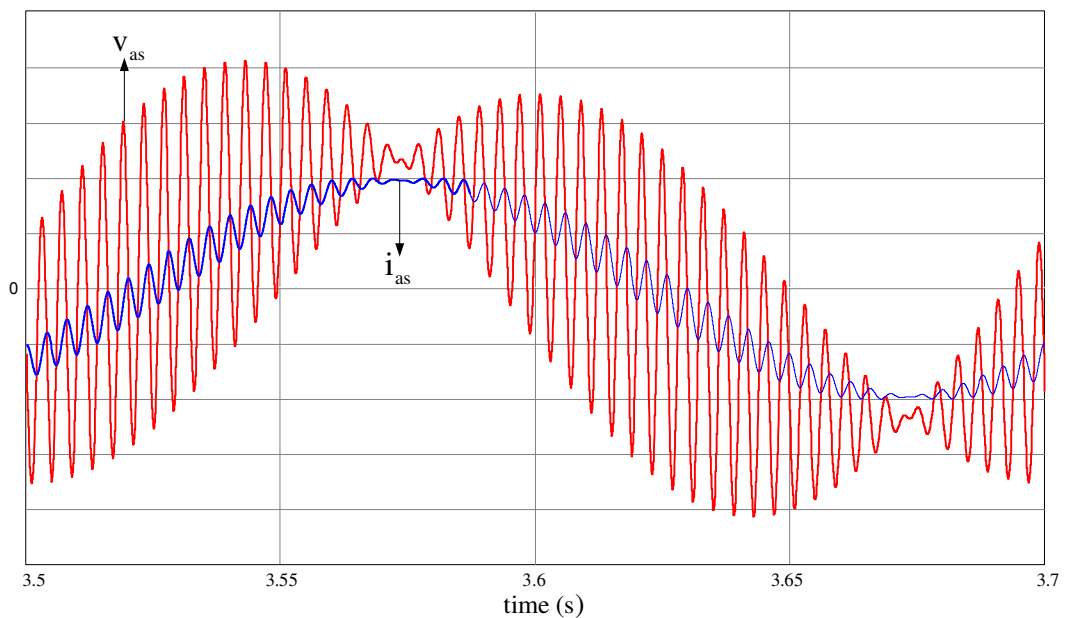
Figure 4.7 Phase-a voltage and current waveforms with 10 Hz fundamental excitation and 250 Hz / 30 V high frequency voltage injection (10V/div, 1A/div).

As seen in equation (4.15) and in Figure 4.7, the resulting high frequency phase voltages and the phase currents have an enveloped waveform. The peaks of the envelope of the injection signal are seen on the zeros of the fundamental component signal and the zeros of the envelope of the injection signal are on the peaks of the fundamental component signal. When the i_{ds}^e current is set to be zero, the fundamental signal, which is only the torque current, is on the estimated torque axis ($\hat{q}e$ -axis) and the injection signal is on the $\hat{d}e$ -axis; and there is spatial 90° between the two axes. In other words, when the fundamental component current vector passes through a phase of the motor, the pulsating injection vector is 90° apart spatially. Since the zero crossing regions of the currents are problematic for the current regulator and the VSI, there are different injection methods, which inject the high frequency signals to the $\hat{q}e$ -axis to prevent non-zero values of injection signal on the zero crossing of the fundamental signal [57]. For DC excitation (zero speed) cases θ_f in (4.15) is constant; hence the high frequency phase currents are not enveloped shaped.

In summary, high frequency pulsating voltage is applied on the estimated rotor flux axis ($\hat{d}e$ -axis) to extract the saliency of the IPM motor. The high frequency voltage is superimposed on the fundamental frequency voltage of the IPM motor; hence the same inverter and power lines are utilized both for fundamental frequency excitation and for high frequency signal injection.

4.2.3 Utilization of The Saliency for Estimation

When the high frequency pulsating voltage vector is injected on the $\hat{d}e$ -axis of the IPM motor, the particular current response, originating from the saliency of the IPM motor, provides useful information for the estimations. When the saliency (impedance curve) of the IPM motor is considered spatially, the curve in Figure 4.8 is obtained, similar to the one in Figure 4.3.
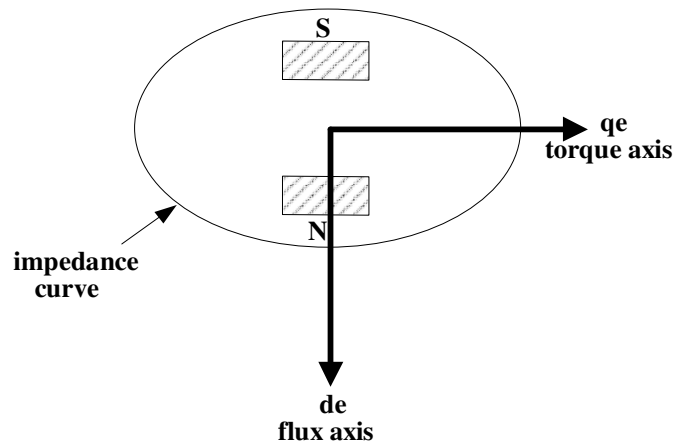
Figure 4.8 The anisotropic impedance curve of the salient pole IPM motor.

For the injection method implemented in this thesis, the injected signal is high frequency voltage and the estimation algorithms utilize the current response of the motor. Hence, instead of the impedance variable, it is better to employ the admittance variable, which is proportional to the current response for the applied constant voltage. Therefore, the saliency of the IPM motor is plotted again as the admittance curve in Figure 4.9, which is similar to the Figures 4.1 and 4.2.
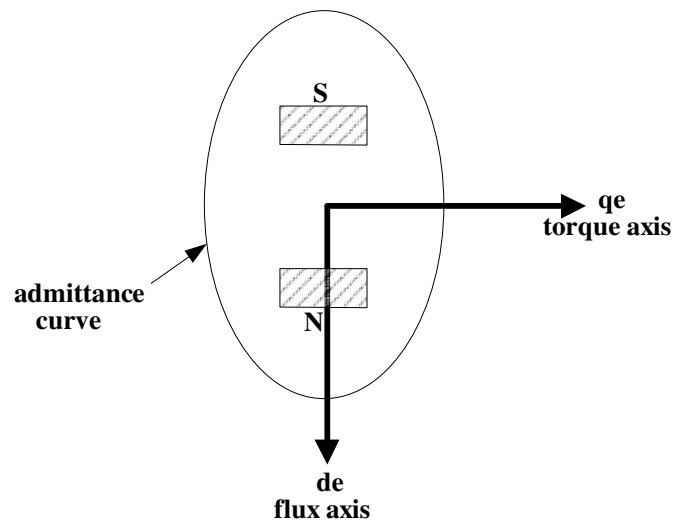
Figure 4.9 The anisotropic admittance curve of the salient pole IPM motor.

The high frequency voltage is injected on the $\hat{d}e$-axis of the motor and the aim is to track the actual flux axis (de-axis), while all the admittance curve and the de, qe, $\hat{d}e$, $\hat{q}e$ axes are rotating (or stalled) with the rotor. The actual and estimated axes, with the injected high frequency voltage vector are shown in the Figure 4.10, omitting the fundamental excitation, which is generally located on the $\hat{q}e$-axis for torque production.
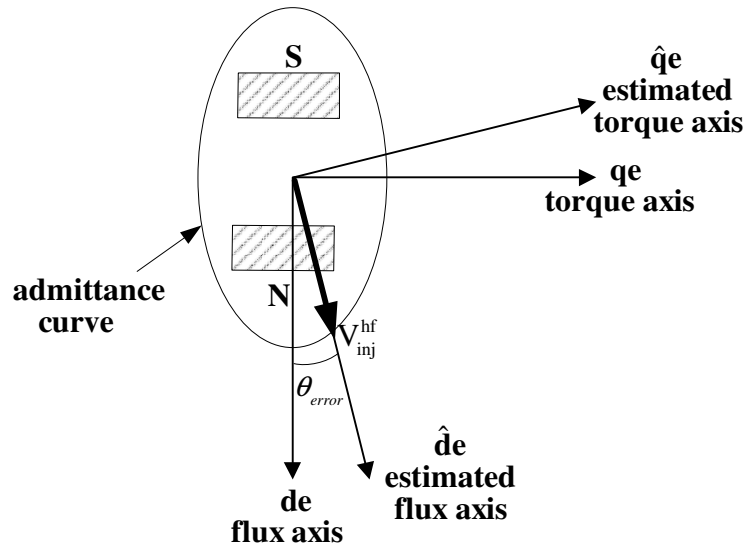
Figure 4.10 Actual and estimated flux and torque axes of the IPM motor.

As seen in Figure 4.10, there can be an error (θ_{error}) between estimated rotor flux axis and actual flux axis, i.e. incorrect estimation of the rotor flux axis. Estimation error is expressed with the equation (4.18),

$$\theta_{error} = \theta_e - \hat{\theta}_e \tag{4.18}$$

where θ_e is the actual rotor (permanent magnet) flux angle (Figure 3.3) and $\hat{\theta}_e$ is the estimated rotor flux angle. If the estimated rotor flux axis is not on the actual flux axis, there will be components of the injected high frequency voltage projected both on the actual flux axis and the actual torque axis. This case is plotted in Figure 4.11.

The permanent magnet material visualization, on which the actual de-axis lies, is omitted in the following figures for visual clearance.
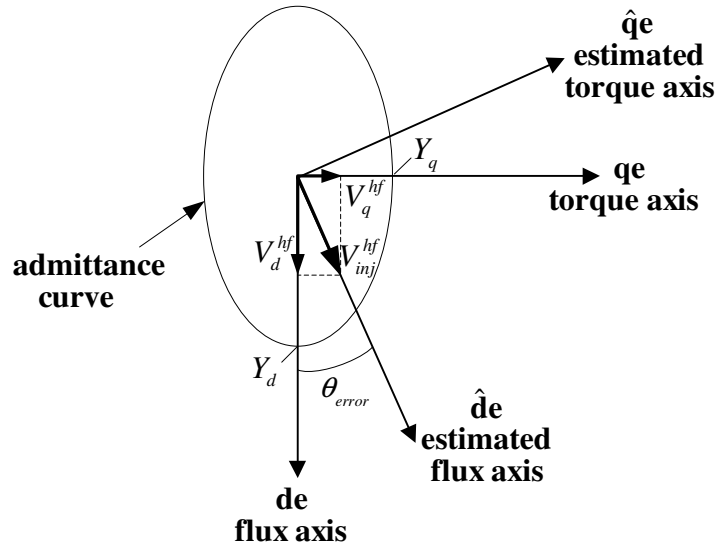
Figure 4.11 Projection of the high frequency injection voltage on the actual flux and torque axes of the IPM motor.

In Figure 4.11, injected high frequency voltage, projects both on the actual flux axis and actual torque axis, and creates high frequency currents. When the high frequency currents on the actual flux axis and actual torque axis are considered, the admittance difference due to the saliency of the IPM motor has a big effect. Since admittances are different in those axes, currents on the actual flux and torque axes are not proportional to the projected voltages. This situation is given in (4.19) and (4.20) and plotted in Figure 4.12. (The current vectors are drawn larger than the voltage vectors just for visual impact)

$$Y_q < Y_d \qquad (4.19)$$

$$\frac{i_q^{hf}}{V_q^{hf}} < \frac{i_d^{hf}}{V_d^{hf}} \qquad (4.20)$$
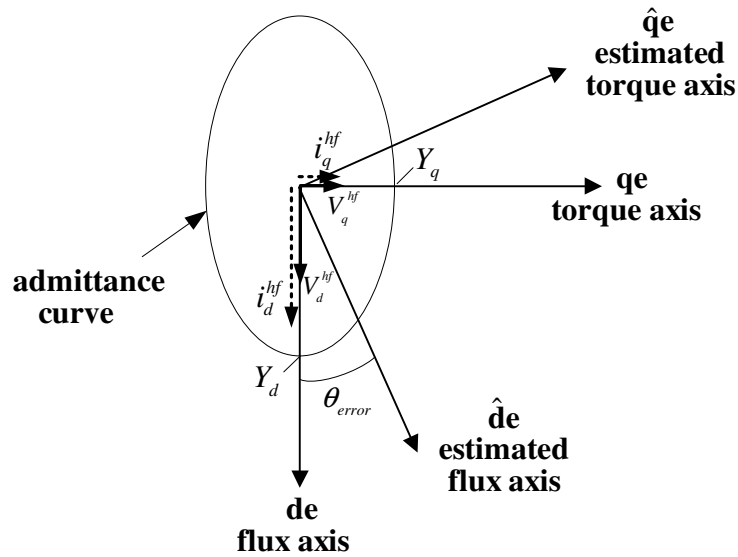
Figure 4.12 High frequency current responses on the actual flux and torque axes of the IPM motor.

Hence, angle of the resulting high frequency current vector is different from the angle of the injected high frequency voltage vector, i.e. high frequency current vector is not on the estimated flux axis where the high frequency injection is made, as plotted in Figure 4.13. It is important to note that this deviation of the high frequency current vector from the injected high frequency voltage vector, is a result of the estimation error and the coupling between the two axes, which is originating from the saliency (admittance difference between two axes) of the IPM motor. If there were no estimation error or there were no saliency, then the high frequency voltage and current vectors will be on the same angle.
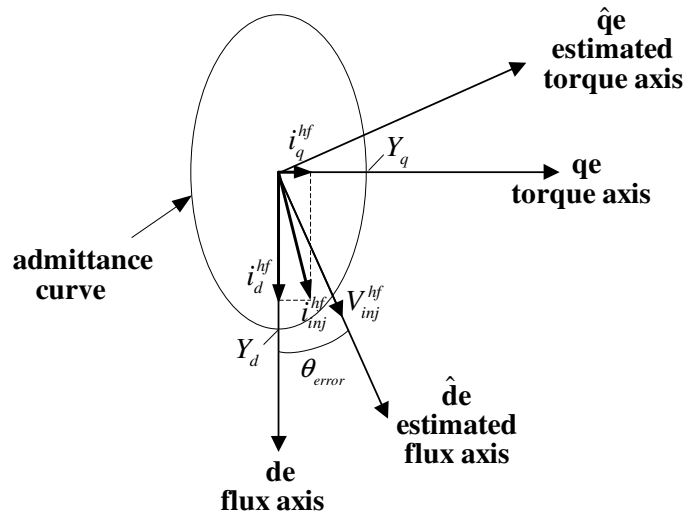
Figure 4.13 High frequency current response of the IPM motor.

As a result, when there is a flux axis estimation error, angle difference occurs between the injected high frequency voltage and the induced high frequency current vectors. This angle difference is the information source of the high frequency signal injection method and the angle difference can be observed at the estimated axes. The projection of the high frequency current vector on the estimated axes is shown in Figure 4.14.
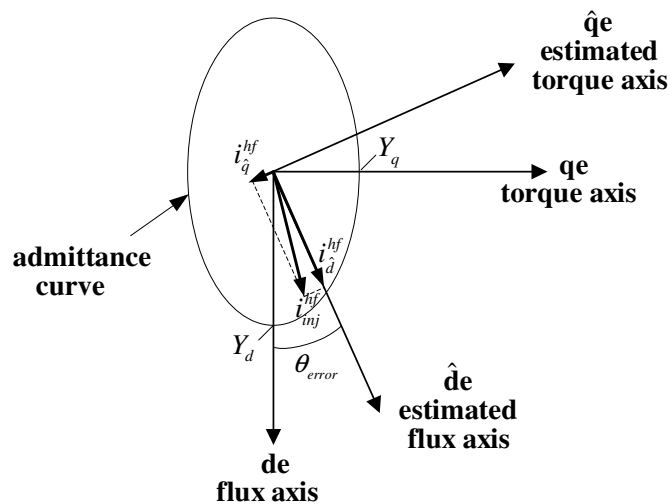
Figure 4.14 Projection of the high frequency current on the estimated flux and torque axes of the IPM motor.

The estimation error results in angle difference between injected high frequency voltage vector and the induced high frequency current vector, and this error is observed as high frequency current component on the q̂e-axis, as shown in Figure 4.14. When there is an estimation error; although the high frequency voltage is injected only to the d̂e-axis, there exists high frequency current component on the q̂e-axis, due to the cross-coupling effect of the saliency. The high frequency signal injection algorithm utilizes this q̂e-axis current component, which exists only when there is an estimation error, to track the rotor flux axis. In the above figures, the estimation error is made to be negative ($\theta_{error}<0°$). The high frequency vectors when the estimation error is positive are shown in the Figure 4.15.
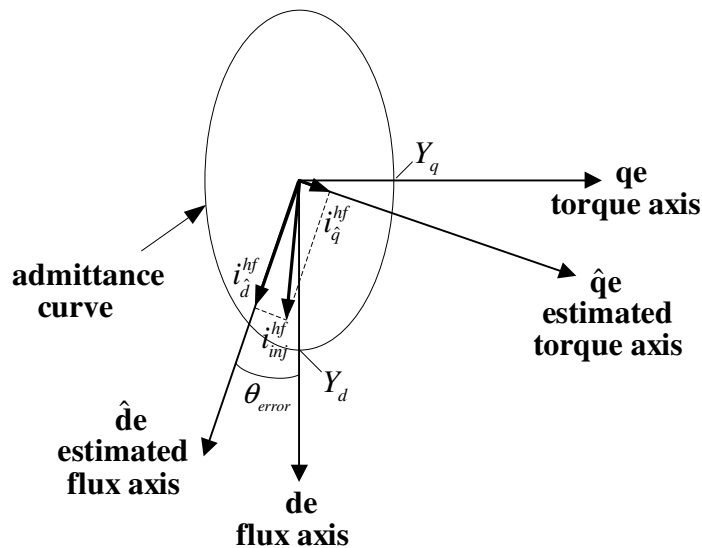
Figure 4.15 High frequency current components on the estimated flux and torque axes of the IPM motor for positive estimation error.

When the estimation error is negative the high frequency current component on the q̂e-axis is negative, as seen in Figure 4.14 and when the estimation error is positive the high frequency current component on the q̂e-axis is positive, as seen in 4.15. When the estimated rotor flux axis is on the actual rotor flux axis (i.e. the estimation is correct), then no projection of the injected voltage drops on the actual torque axis. Therefore, all the high frequency current will be on the estimated flux axis which is

72

same as the actual flux axis and the high frequency current vector is on the same angle of the injected high frequency voltage vector. Also, there is not any high frequency current component on the q̂e -axis. This ideal case, i.e. correct estimation of the rotor flux axis, is plotted in Figure 4.16.
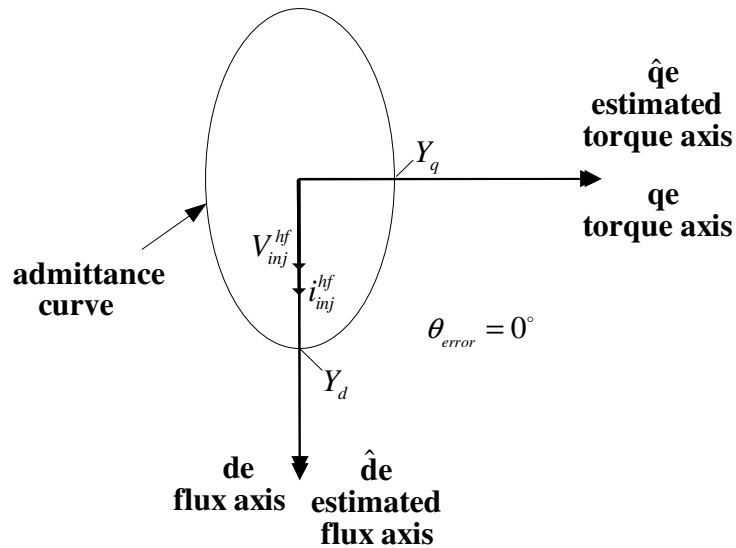
Figure 4.16 High frequency current vector when the estimation error is zero (correct estimation of the rotor flux axis).

In summary, rotor flux axis estimation error can be detected by injecting high frequency pulsating voltage on the d̂e -axis and observing the high frequency current component on the q̂e -axis, whose magnitude is proportional to the estimation error. The estimation can be converged to the actual flux axis by compensating the estimation error signal to zero. In order to compensate the estimation error, magnitude and sign of the high frequency current component on the q̂e -axis has to be measured. Instead of measuring the sign and magnitude of the high frequency current component on the q̂e -axis, pseudo measurement axes are created, which will be explained in the following section.

4.2.4 Detection of The Estimation Error

The high frequency current component on the $\hat{q}e$-axis, which is proportional to the estimation error has very small magnitude and it is a pulsating AC signal in the synchronous frame. Measuring its magnitude requires high current measurement resolution, and measuring its sign is complicated since it is related with the phase of it with respect to the injected high frequency voltage on the $\hat{d}e$-axis. Therefore, pseudo measurement axes are created for the detection of the estimation error, which results in larger high frequency current vector magnitudes to be measured and eliminates the need for detection of the sign of the high frequency current vector. In order to detect the estimation error with its sign and magnitude, two pseudo measurement axes, which are 45° apart from the $\hat{d}e$-axis (injection axis), are created, as shown in the Figure 4.17.
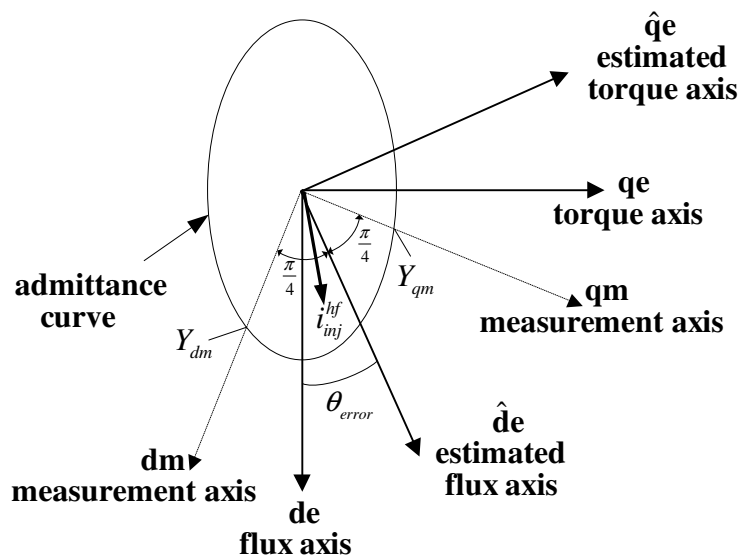
Figure 4.17 Measurement axes for the estimation error detection.

When the projection of the induced high frequency current vector on the measurement axes are considered, it is seen that the difference between the magnitudes of the projected components on the measurement axes is directly proportional to the estimation error. This scheme is given in the Figure 4.18.
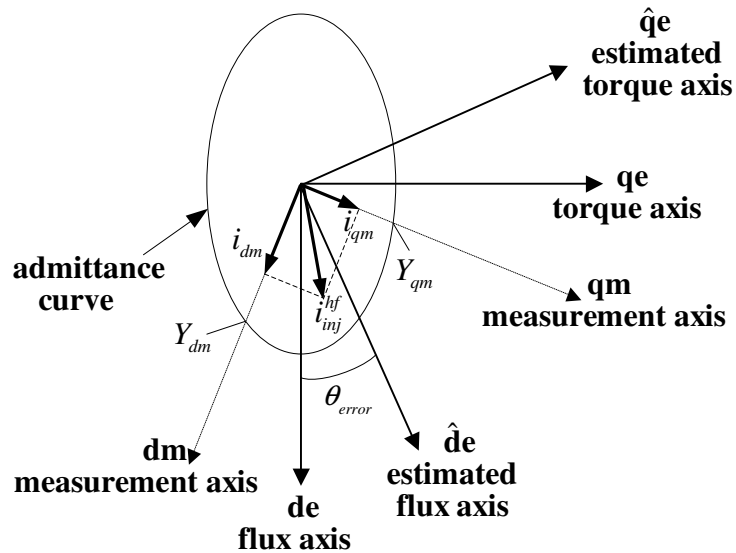
Figure 4.18 Projection of high frequency current vector on the measurement axes.

As seen in the Figure 4.18, if there is an estimation error and as a result the induced high frequency current vector deviates from the injection axis (estimated flux axis), then the magnitudes of the projected components of the high frequency current vector on the measurement axes (qm, dm) are not equal to each other. The difference between the magnitudes of these high frequency current components i_{qm} and i_{dm} is directly proportional to the flux axis estimation error.

$$\theta_{error} = \theta_e - \hat{\theta}_e = K_1 \left(\left| i_{qm} \right| - \left| i_{dm} \right| \right) \tag{4.21}$$

The ideal case when the estimation error is zero, i.e. correct estimation of the rotor flux axis, is plotted in the Figure 4.19.
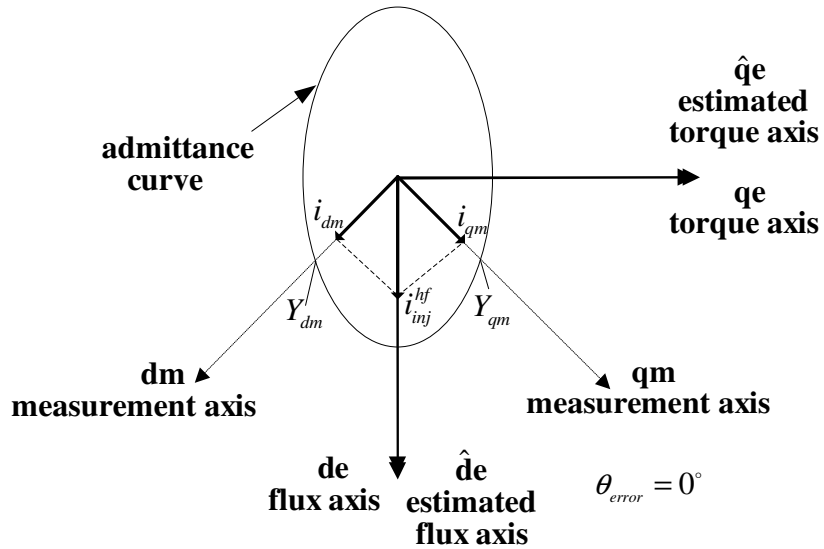
Figure 4.19 Projection of the high frequency current on measurement axes when the estimation error is zero (Correct estimation of the rotor flux axis).

In the above case in Figure (4.19); flux axis estimation error is zero and the magnitudes of the current components on the measurement axes i_{qm} and i_{dm} are equal to each other.

$$\theta_e = \hat{\theta}_e \qquad (4.22)$$

$$\theta_{error} = 0^o \qquad (4.23)$$

$$\left|i_{qm}\right| = \left|i_{dm}\right| \qquad (4.24)$$

In summary, difference between the magnitudes of the high frequency currents on the measurement axes is proportional to the flux axis estimation error. Estimation error can be calculated from the difference of magnitudes of i_{qm} and i_{dm}.

4.2.5 Calculation of The Estimation Error

The estimation error can be calculated from the difference of the magnitudes of the high frequency current components on the pseudo measurement axes, i_{qm} and i_{dm}. In order to calculate the magnitudes of these high frequency current components, the current components on the measurement axes are obtained by the synchronous frame transformations of the stationary frame phase currents with respect to the rotating measurement axes. Stationary frame currents are transformed to the synchronously rotating measurement axes using the transformation equations in (3.1)-(3.11) with the angle of measurement axes $(\hat{\theta}_e - \pi/4)$. Then, the high frequency current components are obtained by utilizing a band pass filter (BPF), which filters out the fundamental frequency current components, which are DC quantities (at steady-state) in the synchronous frame and very high frequency ripples from the transformed currents. The remaining are the high frequency AC currents i_{qm} and i_{dm}. The magnitudes of these high frequency AC currents can be calculated by a signal processing algorithm, which is called as heterodyning. Heterodyning algorithm calculates the magnitude of the specified frequency content of a signal, which can be composed of different frequency components. The scheme for calculation of the difference between the magnitudes of i_{qm} and i_{dm}, i.e. calculation of the estimation error signal is in the block diagram in Figure 4.20.
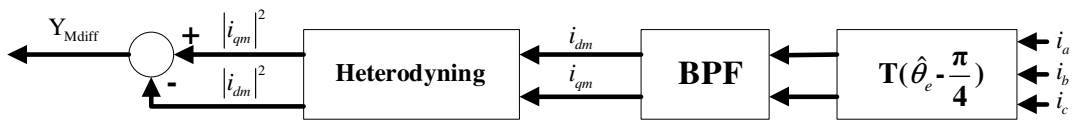
Figure 4.20 Calculation of the estimation error.

Heterodyning algorithm outputs the square of the magnitudes of the high frequency currents i_{qm} and i_{dm}. Diagram and equations for heterodyning algorithm are given in Figures 4.21 and 4.22. Same heterodyning process is applied to i_{dm}, and the square of the magnitude of the high frequency component of i_{dm} is also obtained.
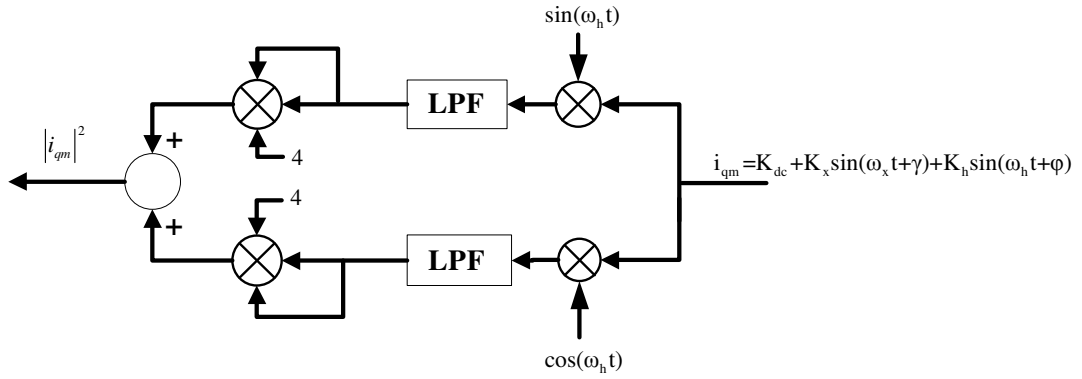
Figure 4.21 The heterodyning process block diagram.

For simplicity i_{qm} is taken to include only the injection frequency component.

$$i_{qm} = K_h \sin(\omega_{hf} t + \varphi) \tag{4.25}$$

$$i_{qm} = K_h \sin(\omega_h t + \varphi)$$

$$i_{qm} = K_h \sin(\varphi)\cos(\omega_h t) + K_h \cos(\varphi)\sin(\omega_h t)$$

$$i_{qm} = K_{h1}\cos(\omega_h t) + K_{h2}\sin(\omega_h t)$$

$i_{qm} \times \sin(\omega_h t)$ $i_{qm} \times \cos(\omega_h t)$

$K_{h1}\cos(\omega_h t)\sin(\omega_h t) + K_{h2}\sin(\omega_h t)\sin(\omega_h t)$ $K_{h1}\cos(\omega_h t)\cos(\omega_h t) + K_{h2}\sin(\omega_h t)\cos(\omega_h t)$

$K_{h1}\sin(2\omega_h t) + K_{h2}\sin^2(\omega_h t)$ $K_{h1}\cos^2(\omega_h t) + K_{h2}\sin(2\omega_h t)$

$K_{h1}\sin(2\omega_h t) + K_{h2}\left(\dfrac{1-\cos(2\omega_h t)}{2}\right)$ $K_{h1}\left(\dfrac{\cos(2\omega_h t)+1}{2}\right) + K_{h2}\sin(2\omega_h t)$

$K_{h1}\sin(2\omega_h t) + \dfrac{K_{h2}}{2} - \dfrac{K_{h2}\cos(2\omega_h t)}{2}$ $\dfrac{K_{h1}\cos(2\omega_h t)}{2} + \dfrac{K_{h1}}{2} + K_{h2}\sin(2\omega_h t)$

LPF   LPF

$\dfrac{K_{h2}}{2}$ $\dfrac{K_{h1}}{2}$

$$\left| i_{qm} \right|^2 = (K_h)^2 = 4x\left(\frac{K_{h1}}{2}\right)^2 + 4x\left(\frac{K_{h2}}{2}\right)^2 = K_{h1}^2 + K_{h2}^2$$

Figure 4.22 Heterodyning process equations.

Heterodyning algorithm outputs the square of the magnitudes of the high frequency currents i_{qm} and i_{dm}. The magnitudes can be calculated by taking the square root of the output signals of the heterodyning process. However these processes increase the complexity unnecessarily. Therefore, the squares of the magnitudes of i_{qm} and i_{dm} are utilized.

The magnitudes of the high frequency current components on the measurement axes are proportional to the admittance values on the measurement axes, Y_{qm} and Y_{dm} in Figures 4.17 – 4.19. Therefore, the difference between the squares of the magnitudes of i_{qm} and i_{dm} is called as admittance difference and designated as Y_{Mdiff} throughout this thesis. The admittance difference signal (Y_{Mdiff}), which is proportional to the estimation error is obtained by the difference between the squares of the magnitudes of i_{qm} and i_{dm} and the unit is A^2.

$$Y_{Mdiff} = (|i_{qm}|^2 - |i_{dm}|^2) = K_3(Y_{qm} - Y_{dm}) \qquad (4.26)$$

$$Y_{Mdiff} = K \times \left(\theta_e - \hat{\theta}_e\right) = K \times \theta_{error} \qquad (4.27)$$

When the admittance curve of the IPM motor in Figure 4.2 is investigated, the admittance difference signal (Y_{Mdiff}) versus estimation error is expected to be as in the curve in Figure 4.23. The admittance difference (Y_{Mdiff}) is proportional to the estimation error for estimation error values less than 45°. Beyond 45° the admittance difference starts to decrease while the estimation error is increasing. For 90° estimation error, the admittance difference is zero, i.e. Y_{qm} is equal to Y_{dm}, as in Figure 4.24. Beyond 90°, the admittance difference changes its sign with respect to the estimation error. This case results in negative feedback for the compensator. When the estimation error is 180° the admittance difference is zero again, i.e. Y_{qm} is equal to Y_{dm}, as in Figure 4.25 and convergence of compensator to this point can occur, which is called as pole skipping. Pole skipping will be discussed in the next

section. This case is originating from the symmetry of the impedance curve for two magnetic poles (N & S) of the IPM rotor.
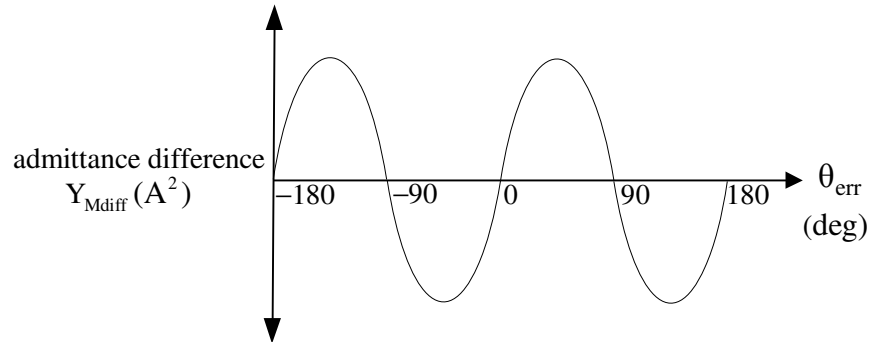
Figure 4.23 Admittance difference versus estimation error.
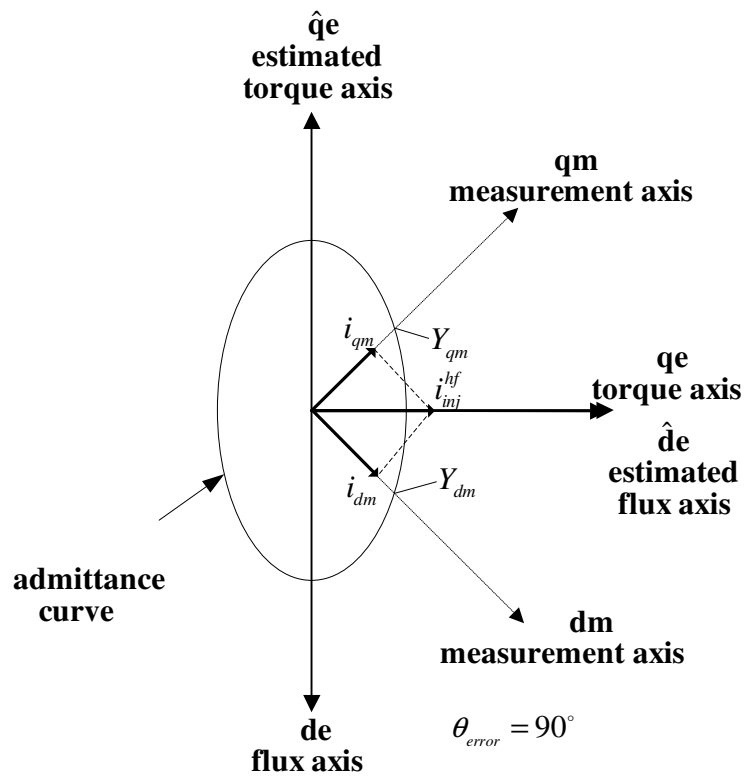
Figure 4.24 High frequency current vectors on the measurement axes when the estimation error is 90°.
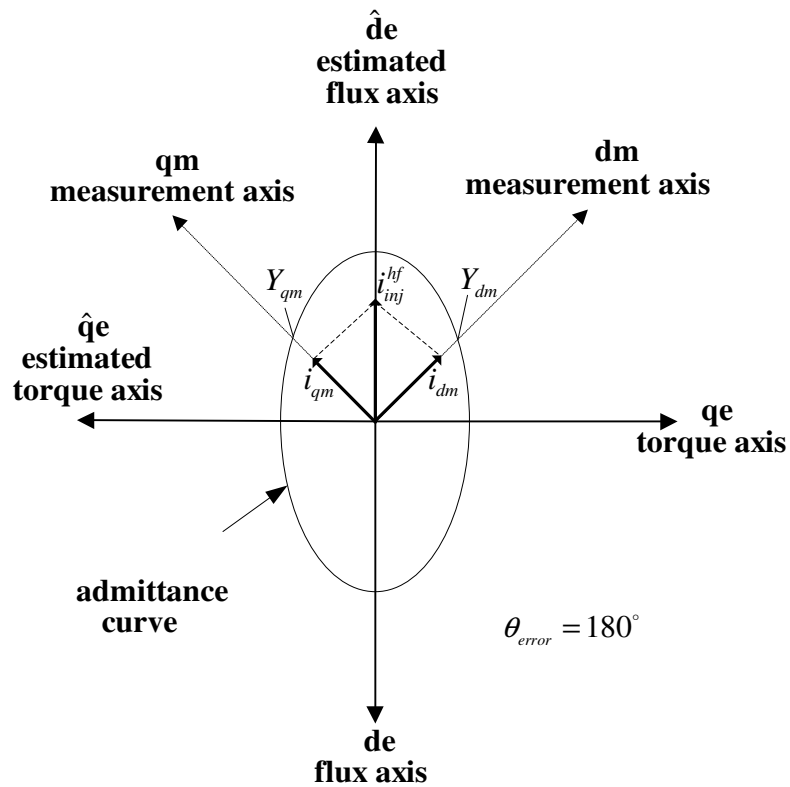
Figure 4.25 High frequency current vectors on the measurement axes when the estimation error is 180° (pole skipping).

In summary, based on the synchronous frame transformations, the BPF, and the heterodyning process, the squares of the magnitudes of the high frequency current components on the measurement axes are calculated. Then, the Y_{Mdiff} signal is calculated by the difference between the squares of the magnitudes of the high frequency current components on the measurement axes. The estimation error is proportional to the admittance difference signal, Y_{Mdiff} and it is fed to the tracker algorithm, which compensates for the estimation error and tracks the actual flux axis. The speed and position of the motor are also derived from the tracker algorithm.

4.2.6 Tracking The Saliency

The estimation error information Y_{Mdiff} is obtained by high frequency pulsating voltage injection on the $\hat{d}e$-axis and then processing the current response of the IPM motor. The estimation error is compensated by the tracker algorithm in order to track the rotor flux axis. As a result, the rotor flux angle is estimated and the IPM motor is closed loop vector controlled. The admittance difference signal (Y_{Mdiff}), which is proportional to the estimation error, can be compensated by a linear PI controller, an on-off controller, or another compensator structure. In this thesis, the linear PI controller is utilized as the compensator mechanism of the tracker, where the block diagram is shown in Figure 4.26.
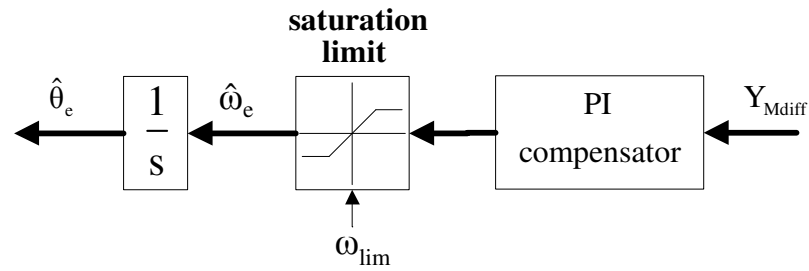
Figure 4.26 Tracker algorithm block diagram.

The compensation mechanism forces the error signal to zero. The output of the compensator is the estimated synchronous frequency ($\hat{\omega}_e$) which is limited by a saturation value ω_{lim} (the maximum speed value for which the high frequency injection method is utilized). The saturation limiting block is omitted in the following figures. The rotor flux axis ($\hat{\theta}_e$) is calculated by integrating the synchronous frequency ($\hat{\omega}_e$). This means that the compensator takes the Y_{Mdiff} signal and by compensating this signal, forces the estimation axis to converge to the actual flux axis. When there is an error, the compensator outputs a correction signal and forces the estimation axis to the actual axis. For instance; when the estimated flux axis goes beyond the actual flux axis ($\hat{\theta}_e > \theta_e$), the output of the estimation error detection

82

algorithm (Figure 4.20) outputs negative value ($Y_{Mdiff} < 0$) and then compensator pulls the estimation axis back to the actual flux axis by decreasing its synchronous frequency ($\hat{\omega}_e$) output. Thus, the estimation error is forced to zero.

In order to track the flux axis by the high frequency signal injection algorithm; vector control (the synchronous frame transformations) has to be performed based on the estimated flux angle. If the loop is not closed by the estimated flux angle ($\hat{\theta}_e$), the compensation of the estimation error does not have any affect and the estimation can not converge to the actual flux axis. The sensorless vector control algorithm for the IPM motor, where the synchronous frame current regulator utilizes the estimated rotor flux angle, based on the high frequency signal injection algorithm, incorporating the estimation error detection and tracker algorithm is shown in Figure 4.27.
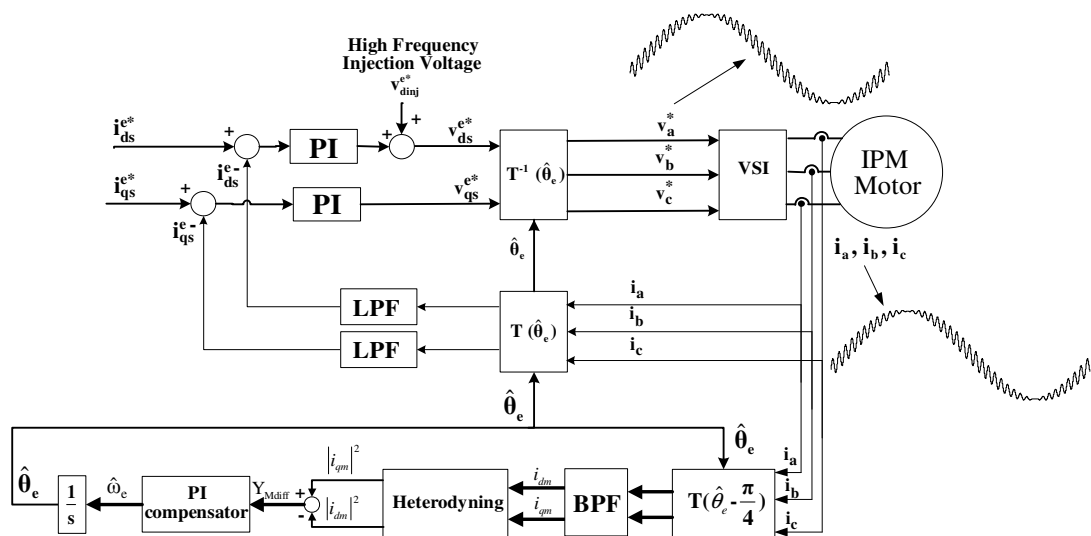
Figure 4.27 Sensorless vector control based on the high frequency signal injection algorithm.

An important point for the tracker is detected when the admittance difference curve in Figure 4.23 is analyzed. It is observed that admittance difference signal is zero for ±90° and ±180° points where the estimation is incorrect, in addition to the 0° point where the estimation is correct. The ±90° points are unstable points and the

compensator does not converge to these points. However, there is another stable convergence point at 180° in addition to the 0° (actual rotor flux axis). If the estimation error goes beyond 90°, then the feedback from the estimation error detection algorithm (Figure 4.20) becomes negative and the tracker converges to the 180°, which is the wrong pole (S pole). This case is called as pole skipping and can be avoided by keeping the estimation error always less than 90° via high gains of the compensator in the tracker.

In summary, the high frequency signal injection method is a combination of an impedance imager and an impedance tracker. The method injects high frequency voltage to the IPM motor; and utilizing the saliency of the IPM motor finds out the error in the estimation, and then compensates for the error to track the actual flux axis.

4.2.7 Speed and Position Estimation by The High Frequency Signal Injection Algorithm

The output of the compensator in the tracker algorithm is the electrical synchronous frequency ($\hat{\omega}_e$) estimation. The mechanical speed of the machine can be deduced from this electrical frequency estimation simply by filtering and using the pole pair relation between the electrical and mechanical frequency (2.9), as shown in Figure 4.28 (a), which is implemented in this thesis. As alternative method; speed can be calculated by taking the derivative of the estimated flux angle, then filtering and using the pole pair relation [58], as shown in Figure 4.28 (b). The derivative of the estimated flux angle can be very noisy for digital implementation. In order to improve the estimation and reduce the noise, the derivative operation can be realized by advanced algorithms such as a PI regulator with integrator feedback [58] or by a Kalman filter.
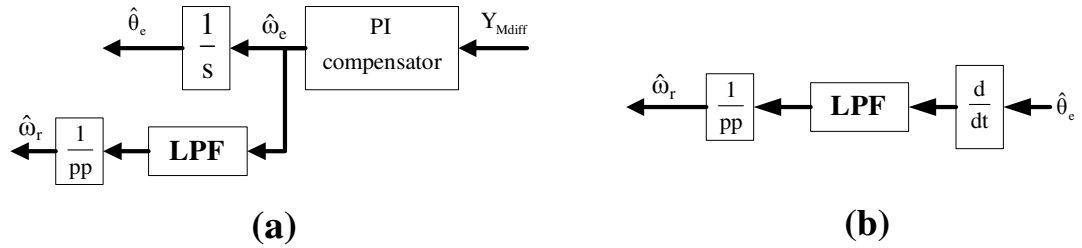
Figure 4.28 Speed estimation from the electrical frequency (a) and via filtering electrical angle (b) based on the high frequency signal injection method.

Similar to the estimation of the flux angle, in order to achieve the correct speed estimation, vector control loops (the synchronous frame transformations) have to be performed based on the estimated flux axis. In other words, the speed can be estimated only if the flux axis is tracked with the high frequency signal injection algorithm.

The mechanical angular position information of the IPM motor can be easily obtained from the estimated rotor flux angle since the flux angle and the mechanical angle of the IPM motor is related with the pole pair equation (4.28).

$$\theta_{mech} = \frac{\theta_{elect}}{pp} \tag{4.28}$$

Mechanical position control can be provided starting from the initial estimated position of the motor, using the flux angle information, the pole pair equation, and count of the number of electrical periods. Sensorless vector control and sensorless speed and position control based on the high frequency signal injection algorithm is in Figure 4.29.
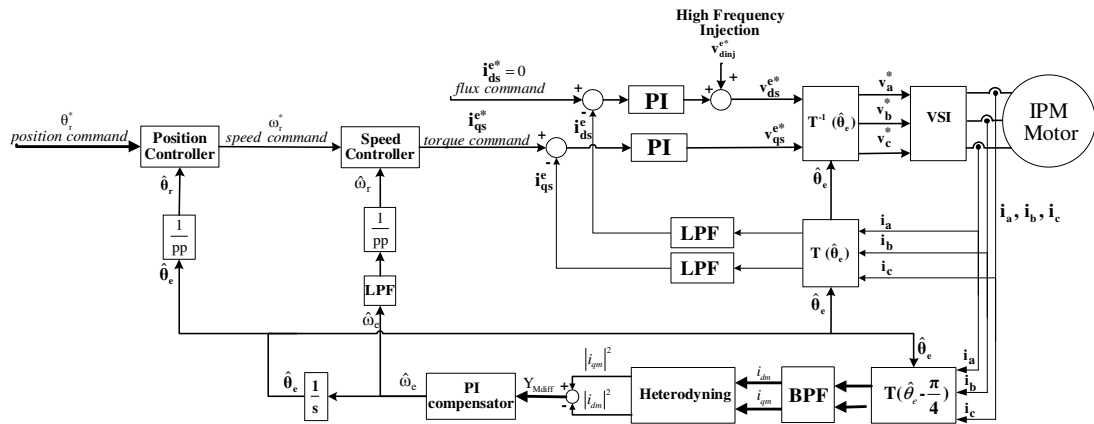
Figure 4.29 Sensorless position and speed control based on the high frequency signal injection method.

4.2.8 Speed Command Feedforward Method for The Tracker Algorithm

The PI compensator in the tracker has high gains to track the flux axis with high dynamic performance, to respond to the disturbances, and to avoid pole skipping. Due to the high gains, there can be oscillations in the estimations, which are designated as chattering [28], and the oscillation of the estimated signals cause oscillations in torque response, and speed/position output of the IPM motor. In order to improve the dynamic and steady-state performance of the high frequency signal injection algorithm, various methods are developed in the literature [28], [55], [27]. These methods generally utilize the estimation of a fundamental model based algorithm as a feedforward term to the saliency based high frequency signal injection algorithm, which compensates for the estimation error of the fundamental model based algorithm. These methods are generally employed only for low and zero speed operation, since at the high speed region the injection method is not utilized and fundamental model based algorithms perform well.

In this thesis, the dynamic and steady-state performance of the high frequency signal injection algorithm is improved by a method which is based on the feedforward of the speed command to the tracker algorithm. The speed command feedforward method can only be used if the speed and/or position control of the motor is realized.

For the applications where only the torque control of the motor is implemented, the speed command does not exist, hence the speed command feedforward method can not be used. For the torque control applications, standard tracker algorithm with the PI compensator is used.

Since the tracker algorithm works as a Phase Locked Loop (PLL) method, which locks the estimated flux angle to the actual rotor flux angle, its steady-state performance can be improved by a feedforward term. Then, the compensator reacts only to the deviations from the feedforward term. Hence, dynamic and especially the steady-state performance of the tracker are improved. The block diagram of the speed command feedforward method is shown in the Figure 4.30.
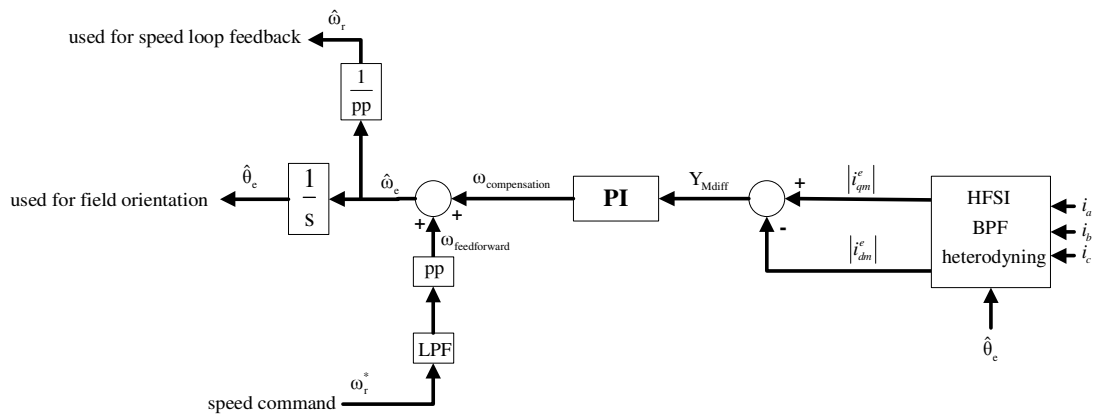
Figure 4.30 Tracker algorithm with speed command feedforward method.

The speed command feedforward method is based on the idea that the motor will rotate with the commanded speed and the speed of the motor can be used as a forward estimation of the flux speed. When the motor actually rotates with the commanded speed, the estimation is provided almost completely by the feedforward term and the compensator reacts for small estimation error caused by deviation from the speed command. For the transient (acceleration/ deceleration) and heavy loading conditions in which the actual motor speed is not same as the commanded speed, the PI compensator reacts and compensates for the estimation error as in the standard method. Speed estimation is still derived from the electrical synchronous frequency

($\hat{\omega}_e$) output of the compensator with the feedforward term as in the Figure 4.30. Using the speed command feedforward method, gains of the PI compensator are tuned easier than the standard method, which includes only a PI. Additionally, smooth torque, speed, and position control are obtained, especially at steady-state. The full block diagram of sensorless vector control and sensorless position/speed control, based on the high frequency signal injection algorithm with the speed command feedforward method is given in Figure 4.31.

Figure 4.31 Sensorless position and speed control based on the high frequency signal injection algorithm with the speed command feedforward method.

4.2.9 Summary of The High Frequency Signal Injection Algorithm

Saliency based high frequency signal injection algorithm is utilized for low and zero speed torque, speed, and position control of the IPM motor. A pulsating voltage is applied to the estimated rotor flux axis ($\hat{d}e$-axis) of the motor to detect the estimation error, and then the estimation error is compensated by a tracker algorithm. As a result, the rotor flux angle, motor speed and motor position are estimated. For the speed/position control applications, a speed command feedforward method is developed to improve the tracking and the estimation performance; hence the torque, speed, position control performance are improved.

For the high frequency voltage injection method, in order to prevent the interference of induced high frequency currents with the fundamental frequency operation of the inverter, the synchronous frame current regulator is modified. Controller gains of the current regulator and cut-off frequency of the low pass filter on the feedback path of the current regulator are decreased. Hence, a very low bandwidth current regulator is designed. As a result, the torque, speed and, position control bandwidth of the drive are decreased. Nevertheless, sensorless AC drives are preferred since they have low maintenance problems and low cost. For high dynamic performance applications, AC drives with shaft sensors are employed.

Another drawback of the high frequency signal injection algorithm is reported as the torque ripple due to high frequency injection. The torque ripple also causes oscillations and sound noise. However, for pulsating voltage injection on the $\hat{d}e$-axis method, torque ripple is almost negligible, since the flux of the permanent magnet is not influenced by such a low magnitude injection. Low magnitude torque ripple exists due to the reluctance torque component, which is created due to the high frequency current on the $\hat{d}e$-axis, as will be shown with the simulations in the related chapter.

In summary, the saliency based high frequency signal injection algorithm performs successfully for sensorless torque/speed/position control of the salient pole IPM motor for low and zero speed regions. However, the high frequency signal injection algorithm injects additional voltages, hence requests more voltage from the limited source of the VSI. Therefore, for moderate and high speed regions, where high voltages are needed due to high back emf values, the high frequency signal injection algorithm is not executed to utilize the VSI effectively. For moderate and high speed regions, fundamental model based flux observer methods perform well, which will be discussed in the next section.

4.3 Fundamental Model Based Flux Observer Algorithm

Sensorless control for the IPM motor based on the fundamental model is a well-known issue, on which there has been research continuing for many years [8], [30]. State observers using the fundamental model of the IPM motor have been developed and improvement is continuing for better performance [31], [32]. Fundamental model based observers, which work as detection of the back-emf of the motor, depend on the mathematical equations and parameters of the motor, and estimates the unknown states (rotor flux angle, speed, etc.) using the motor model and the known states.

The flux is an observable state variable of the fundamental model of the IPM motor at high speeds. For a typical AC drive, the stator currents are measured and the stator voltages are measured or can be calculated from the voltage commands to the VSI based on the DC link measurement, within the drive. Hence, the flux and then the flux angle can be estimated using the input variables (stator voltages) and the measured states (stator currents) and the fundamental model parameters of the IPM motor. For the moderate and high speed region, fundamental model based flux observers are developed, and successfully implemented in the literature [30] and utilized in the practical commercial motor drive applications. However, since the flux estimation depends on the known state variables and the motor parameters, any error in those variables or parameters cause erroneous estimation. The known state variables can include errors (for instance the stator voltages can be calculated with errors due to the nonlinearity of the VSI) and the known parameters of the motor can be incorrect or can change during the operation (for instance stator resistance changes with the temperature), and as a result the flux can be estimated with error. Also, at zero speed, the back-emf of the IPM motor becomes negligible and the flux is unobservable for the fundamental model at low and zero speed. Additionally, at low and zero speed the voltage drop on the stator resistance becomes dominant; hence any error in the stator resistance parameter, causes large estimation error. Adaptive observers, which compensate for the errors, based on the corrections from the measured states, are developed in order to decrease the sensitivity to state

variable and parameter errors, especially for low and zero speed region [31]. However, sensorless control based on the fundamental model can not be utilized for low and zero speed region, even with the adaptive methods. Nonetheless, fundamental model based observers provide reliable estimations at high speed.

In this thesis, sensorless control of the IPM motor at high speed is realized by the fundamental model based flux observer of Wu and Slemon, which calculates the flux linkage space vector via sensing and processing the stator currents and stator voltages to calculate the emf space vector; and then integrates the emf space vector [30]. The major drawback of the method, which is the drift in the integration is solved by appropriate compensation algorithms. Since, sensorless control of the IPM motor at low and zero speed is realized successfully by saliency based high frequency signal injection method in this thesis, adaptive mechanisms are not utilized in the fundamental model based algorithm to improve the low speed performance.

4.3.1 Flux Estimation Based on The IPM Motor Model

Stationary frame equations of the IPM motor were given in (3.13) – (3.20). The voltage equation (4.29) can be utilized to calculate stator flux linkage.

$$V_{qds}^s = R_s i_{qds}^s + \frac{d}{dt} \lambda_{qds}^s \qquad (4.29)$$

The stator flux linkage vector can be calculated from the measured/calculated stator currents and voltages with the integration process below;

$$\lambda_{qds}^s = \int_{t_0}^{t} \underbrace{\left[V_{qds}^s - R_s i_{qds}^s \right]}_{\text{emf vector}} dt \qquad (4.30)$$

$$\lambda_{qs}^s = \int_{t_0}^{t} \left[V_{qs}^s - R_s i_{qs}^s \right] dt \qquad (4.31)$$

$$\lambda_{ds}^{s} = \int_{t_0}^{t} \left[V_{ds}^{s} - R_s i_{ds}^{s} \right] dt \qquad (4.32)$$

The space angle of the stator flux can be calculated from the real and imaginary parts by;

$$\theta_s = \tan^{-1}\left(\frac{\lambda_{qs}^{s}}{\lambda_{ds}^{s}} \right) \qquad (4.33)$$

The vector diagram for the flux linkage vectors, stator flux linkage and the rotor permanent magnet flux, λ_{df}^{e} is given in Figure 4.32.
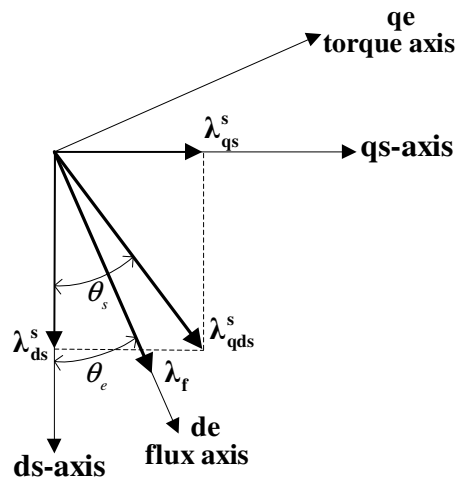
Figure 4.32 Flux vectors for the IPM motor.

The synchronous frame stator flux linkage equations for the IPM motor are given below.

$$\lambda_{qs}^{e} = L_{qs}^{e} i_{qs}^{e} \qquad (4.34)$$

$$\lambda_{ds}^{e} = L_{ds}^{e} i_{ds}^{e} + \lambda_f \qquad (4.35)$$

92

The vector diagram based on the flux linkage equations is in the Figure 4.33, where $i_{ds}^e \neq 0$ in order to provide a general solution.
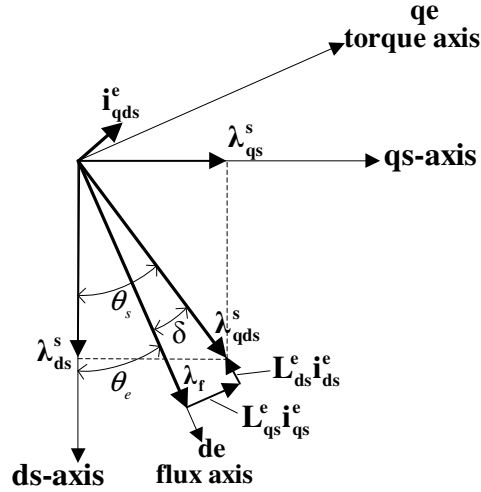
Figure 4.33 Flux linkage vector diagram for the IPM motor.

The rotor flux angle θ_e, which is the angle of the rotor permanent magnet is required for vector control and mechanical speed/position feedback derivation. The angle between the stator flux vector and the rotor permanent magnet flux vector can be calculated using the synchronous frame load angle equation in (4.36) [38].

$$\delta = \tan^{-1}\left(\frac{L_q i_{qs}^e}{L_d i_{ds}^e + \lambda_f}\right) \tag{4.36}$$

The synchronous frame currents i_{qs}^e, i_{ds}^e are available within the drive as feedback for the synchronous frame current regulator; and the permanent magnet flux linkage λ_f is a known motor parameter or can be easily extracted by tests on the motor. The rotor flux angle θ_e can be calculated from the stator flux vector angle and the load angle based on the equation (4.37).

$$\theta_e = \theta_s - \delta \tag{4.37}$$

93

As a result, the rotor flux angle is estimated using the motor terminal voltages, currents, the synchronous frame current variables, and the permanent magnet flux linkage value. The fundamental model based flux observer algorithm solely involves integration. Parameter errors, parameter changes during the operation, measurement/calculation error of the currents/voltages, and any offset (e.g. transient offsets) result in drift of the integration. The drift is compensated by a method calculating the drift value in the integration and compensating the drift if required. The drift compensation method is discussed in the following section.

4.3.2 Initial Value for The Integrators

Generally and in this thesis, the fundamental model based flux observer algorithm is started to be operated after the motor reaches a moderate speed, since the method can not be used stably for low and zero speed. In this thesis, initial start up (low and zero speed operation) of the motor is realized by the saliency based high frequency signal injection algorithm and the model based observer starts execution (integration) after the motor reaches steady state. Therefore, the initial value for the stator flux linkage is needed to be used as the integration initial value [59], and these initial values are provided based on the information of the rotor flux angle (rotor position) at the instant when the integration starts. In this thesis, the initial rotor flux angle information is provided by the saliency based high frequency signal injection algorithm since the rotor flux angle is estimated by the injection algorithm at low speed before the fundamental model based flux observer starts. Based on the known initial rotor flux angle and the equations below, initial stator flux linkage values are calculated and the integration for the stator flux linkage starts with the initial values.

$$\lambda^s_{qs}(t_0)=\lambda_f \sin(\theta_e)_{t_o} + L^e_{qs}i^e_{qs}\cos(\theta_e)_{t_o} \tag{4.38}$$

$$\lambda^s_{ds}(t_0)=\lambda_f \cos(\theta_e)_{t_o} - L^e_{ds}i^e_{ds}\sin(\theta_e)_{t_o} \tag{4.39}$$

4.3.3 Integration Drift Compensation

Fundamental model based flux observer is mainly composed of integration and the integration process has always been a problematic issue. Parameter estimation errors or parameter changes during the operation, offset due to transients or offsets in the measured variables within the motor drive (such as current transducer offset), quantization errors of the digital implementation cases, incorrect initial value calculations, etc. can cause drift of the integration and the estimation becomes incorrect. Moreover, the estimation can diverge resulting in unstable operation. Additionally, the drift causes oscillation in the rotor flux angle estimation and the oscillation reflects to the speed estimation, which is based on the rotor flux angle. Therefore, drift of the integration has to be avoided.

Drift of the integration can be calculated continuously during the operation [30] and can be compensated for by an appropriate algorithm. Drift of the integration is calculated based on the idea that, at steady-state the locus of the flux linkage space vector is a circle symmetrical about the origin, as in the Figure 4.34.
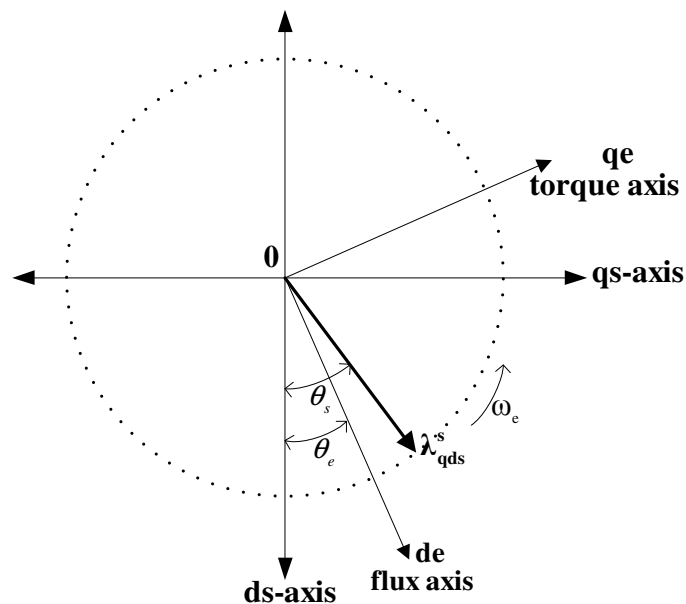
Figure 4.34 Locus of the stator flux linkage vector without drift.

If any drift occurs, the center of the locus of the flux linkage drifts by the amount of the drift in the integrators as in the Figure 4.35.
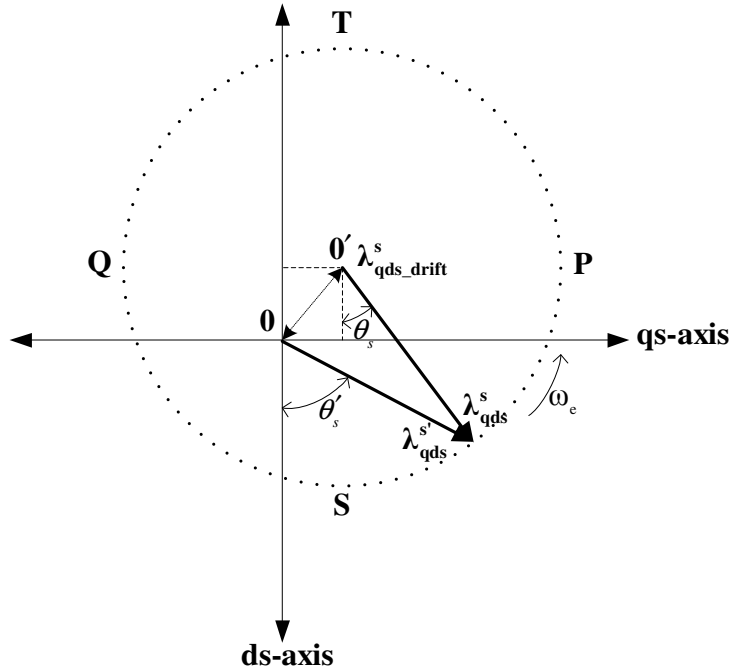
Figure 4.35 Locus of the stator flux linkage vector with drift.

As observed in the Figure 4.35, when drift occurs, the stator flux linkage vector and its angle are incorrectly estimated. If the drift increases beyond a level, than the estimations diverge and the sensorless control can not be performed stably. Drift (offset) of the integration can be calculated based on the idea that the locus of the flux vector has to be symmetric about the origin, which is correct at steady-state. Then, origin of the drifted locus, the $\mathbf{0'}$ point can be derived from the maximum and minimum values of the flux vector; P, Q, T, S in Figure 4.35. The drift in two axes can be found separately by the equations (4.40) and (4.41) below.

$$\lambda^s_{qs\_drift} = \left(\frac{\lambda^s_{qs\_max}(P) + \lambda^s_{qs\_min}(Q)}{2} \right) \qquad (4.40)$$

$$\lambda^s_{ds\_drift} = \left(\frac{\lambda^s_{ds\_max}(T) + \lambda^s_{ds\_min}(S)}{2} \right) \qquad (4.41)$$

In order to reach the maximum and minimum values, the flux linkage estimation in two axes has to be continuously checked for a time duration, larger than one electrical period. Since the electrical period depends on the speed of the motor, the time duration for drift calculation is adapted with the motor speed feedback. The drift of the integration is compensated by the drift compensation algorithm which checks for the value of the calculated drift and compensates for the drift if increases beyond a limit value. The drift compensation is realized by subtracting the calculated offset values from the estimated flux linkage in two axes. Subtraction is performed separately on each axis, when the flux linkage is equal to or nearly zero on the other axis in order to avoid step changes in the estimated stator flux angle. After the drift compensation is made, the drift is continued to be calculated by maximum and minimum values of the flux linkage estimation.

Sensorless vector and speed control of the IPM motor at high speed based on the flux observer algorithm is given in the block diagram in Figure 4.36.
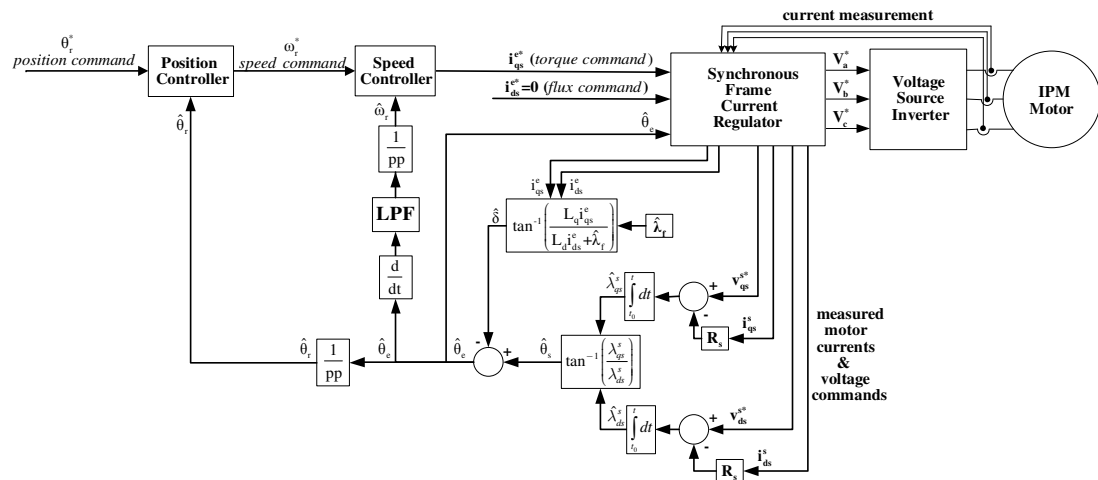
Figure 4.36 Sensorless vector control and speed control based on the flux observer algorithm.

4.3.4 Summary of The Fundamental Model Based Flux Observer Algorithm

At high speed, the rotor flux angle of the IPM motor is estimated by the fundamental model based flux observer algorithm, which estimates the stator flux linkage by the

integration of the back-emf voltages and then rotor flux angle using the load angle information. The initial value for the integration is supplied from the high frequency signal injection algorithm which works at low speed. The major problem of the observer, which is the drift of the integration, is solved by a drift compensation algorithm. Rotor flux angle estimation is used for the vector control of the IPM motor. Also, mechanical position of the rotor can be calculated from the rotor flux angle based on the pole pair relation. Motor speed feedback is derived from the rotor flux estimation by simply taking the derivative of the rotor flux angle, and then filtering it to attenuate the ripple and noise in the derivative. Since derivative of the rotor flux angle gives the electrical speed, the mechanical speed is calculated based on the pole pair relation.

4.4 Hybrid Theory for The Whole Speed Range Operation

Saliency based high frequency signal injection algorithm is utilized for the low and zero speed operation of the IPM motor. For the moderate and high speed range, the fundamental model based flux observer method is employed. Both of these methods perform successfully in separate speed regions. For the whole speed range sensorless operation these two methods are implemented together and seamless transition between the two methods is provided. In this thesis, the hybrid method is mainly composed of the transition algorithms for smooth speed control of the IPM motor when a switching occurs from one algorithm to the other. Switching to an estimation algorithm depends on the estimated speed feedback. The main flow diagram for the hybrid method is shown in Figure 4.37.
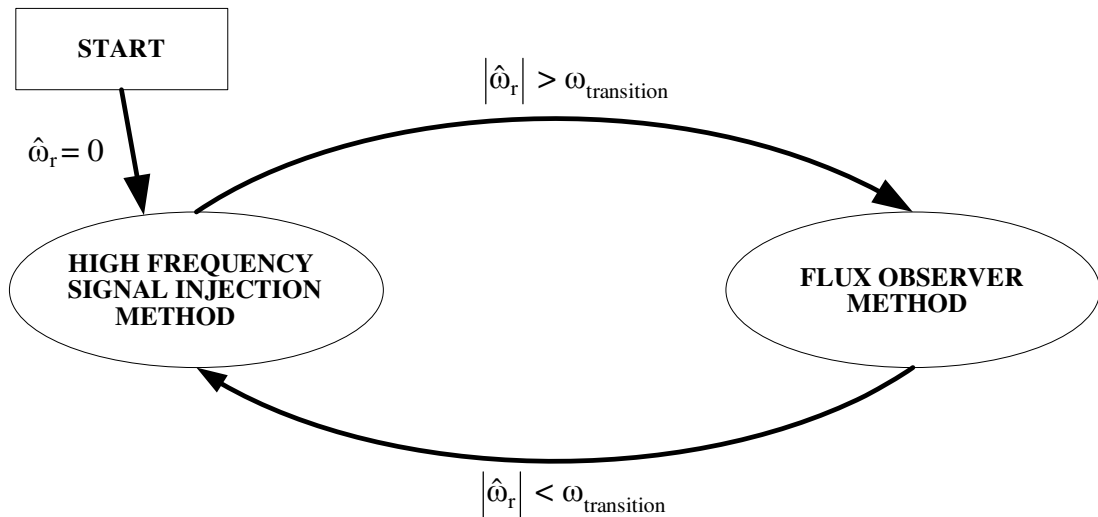
Figure 4.37 Hybrid method flow diagram.

4.4.1 Transition Conditions

The sensorless control of the IPM motor starts with the high frequency signal injection algorithm. The rotor flux angle and the motor speed are estimated with the high frequency signal injection algorithm. If the motor speeds up to set level ($\omega_{\text{lim-obs}}$) where the flux observer works stably, then the flux observer is started to be executed. When a higher set speed value (ω_{obs}) is reached, which is set to be the transition level, the rotor flux angle and the motor speed feedback are switched to the estimations of the flux observer method. Sensorless control of the IPM motor is provided by the flux observer method at moderate and high speeds. In order to use the VSI effectively, the injection voltage is decreased after speed becomes higher than a set level (ω_{lim1}) and finally injection is ceased when the speed reaches higher speed level (ω_{lim2}). Therefore, the high frequency signal injection algorithm is turned off at high speeds.

When the motor decelerates to the speed level ω_{lim2}, the injection voltage is slowly increased and fully applied when the motor decelerates to the speed level ω_{lim1}. When the motor enters the low speed region ($<\omega_{\text{inj1}}$), the rotor flux angle feedback is used from the estimation of the high frequency signal injection algorithm. The last

99

estimation of the flux observer is used for the initial condition of the injection algorithm since the rotor flux angle is calculated by the integration of the rotor flux speed (ω_e). When the estimated rotor flux angle of the high frequency signal injection method is used, the tracker of the injection algorithm estimates the speed successfully and then the speed feedback is closed via the speed estimation of the injection algorithm when the motor decelerates to ω_{inj2}. When the motor speed becomes smaller than the $\omega_{lim-obs}$ level, after which the observer can not work stably, the observer is turned off in order to stop the integration for stator flux linkage.

During the transition between the two methods, parameters of the synchronous frame current regulator and the speed/position control loops are adapted since the tuning of the controllers for the methods is different. For instance, when the high frequency injection is made, the bandwidth of the current regulator has to be lowered. Also, the speed estimation of the flux observer method can be oscillatory due to the small drifts in the integration and the derivative operator.

The initial position of the motor is successfully detected with the high frequency signal injection algorithm if the estimation error is not larger than electrical 90°. If the error is larger than 90°, then the tracker of the injection algorithm would converge to the wrong pole of the motor. Therefore an initial rotor position detection algorithm is required, however it is not in the scope of this thesis and left as future work. If the motor is started when the rotor flux angle is between electrical -90° and 90°, the estimation converges to the rotor flux angle.

Also there are advanced hybrid methods, which make use of the two methods at the same time [28], [55], [27]. These methods are developed especially for the low speed region, where both the injection and the flux observer methods can work. Via advanced hybrid methods, estimation of the two algorithms are combined as a sensor fusion and the performance of the estimation is improved. As a simplest hybrid method the information from two algorithms can be used in a well known feedforward structure. The rotor flux angular speed information can be given directly as feedforward while the error information from the high frequency signal injection

is used to compensate the error and to force the estimation from the observer to converge to the actual rotor flux axis. The schematic of this simple hybrid structure is shown in the figure below.
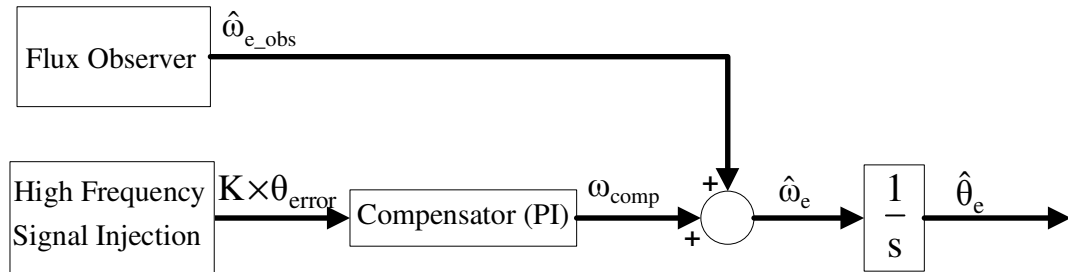
Figure 4.38 Simple hybrid structure by feedforward of the estimation from the flux observer.

In this thesis, the low speed performance is improved by the speed command feedforward method for the tracker of the injection algorithm. More improvement is left as a future work to improve the flux observer algorithm with adaptive mechanisms and fusion of the two estimations at the same time.

CHAPTER 5

SIMULATION RESULTS OF THE SENSORLESS CONTROL ALGORITHMS

5.1 Simulation Model

In order to verify the theory of sensorless control algorithms for the IPM motor, computer simulations are conducted utilizing the Ansoft SIMPLORER simulation program [60]. The program is a graphic window based power electronic circuit simulator. In this simulation program, in the schematic window, the power electronic circuit is constructed by picking, placing, and connecting the circuit components and the control blocks. Control of the power circuit is performed by programming control and/or equation blocks accordingly. After the circuit schematic is created and the simulation parameters are entered, simulations can be conducted. Selected waveforms such as voltage, current, speed, and torque waveforms are illustrated by the graphic view window. The conducted simulation results are evaluated by the analysis tools of the day-postprocessor window.

For the simulations, the permanent magnet synchronous motor model of the SIMPLORER is used with the parameters given in Table 5.1, which is the same of the IPM motor used in the laboratory experiments. The model utilized within the simulation is based on the fundamental model of the IPM motor with linear mathematical equations. The high frequency response of the IPM motor, such as the skin effect and the non-linearities such as the magnetic saturation, which can be observed experimentally, are not included within the simulations. The saliency of the IPM motor is represented with the different entries for the L_d an L_q.

The estimation and control algorithms are coded in the equation editor of SIMPLORER which is executed with the same sampling frequency of the real-time implementation (10 kHz); hence discrete time processing is obtained. The simulation is executed with a small enough simulation step size of 10μs. The IPM motor is supplied from the ideal voltage sources instead of Pulse Width Modulated Voltage Source Inverter, in order decrease the simulation time. So, ideal voltage source is used in the simulations discarding the inverter nonlinearities such as deadtime and PWM ripple. Since the algorithms are verified by experiments in the next chapter, simulation deficiencies can be neglected.

Table 5.1 The IPM motor parameters

YASKAWA VARISPEED-686SS SSR1-42PBFN-L	
	Manufacturer Information
Rated Power	2.2 kW
Rated Voltage	368 V rms
Rated Frequency	72.5 Hz
Rated Current	4.1 A rms
Power Factor	0.93
Rated Speed	1450 rpm
Rated Torque	14.5 Nm
Pole	6
r_1	2.656 Ω
L_d	46.42 mH
L_q	60.32 mH
$K_e\,(\lambda_f)$	579.4 mWb
$\Delta\Theta$	-7.6

When the parameters of the IPM motor, which is utilized in the simulations and experiments, in Table 5.1 are used in the torque equation (3.29), the numerical torque constant can be calculated in the following.

$$T_e = \frac{3}{2}\frac{6}{2}\left[0.5794i_{qs}^e + (0.04642-0.06032) \times i_{ds}^e \times i_{qs}^e\right] = \underbrace{2.6073 \times i_{qs}^e}_{\text{reaction torque}} - \underbrace{0.06255 \times i_{ds}^e \times i_{qs}^e}_{\text{reluctance torque}} \quad (5.1)$$

In this thesis, i_{ds}^e is always commanded to be zero; hence the reluctance torque is zero. Positive reluctance torque is obtained when i_{ds}^e is negative (for positive i_{qs}^e), which is also realized for field weakening operation. However, as obvious from (5.1), the saliency torque of the selected IPM motor is small and its torque is negligible. Therefore, selecting $i_{ds}^e = 0$ provides control simplicity and does not result in any noticeable performance loss. When the rotor flux angle is estimated with high accuracy (i.e. estimation error of less than 10°), vector control condition is satisfied and the torque output of the IPM motor becomes proportional to the i_{qs}^e current with the equations in (5.2) and (5.3). Although the i_{ds}^e current is commanded to be zero in the synchronous frame current regulator, there exists high frequency current on the estimated de-axis since the high frequency injection is made on this axis. This high frequency i_{ds}^e current results in high frequency reluctance torque, i.e. torque ripple at the output, which will be investigated in the simulation results.

$$T_e = K_t \times i_{qs}^e \quad (5.2)$$

$$K_t = 2.6073 \ \frac{Nm}{A} \quad (5.3)$$

The rated current of the IPM motor utilized in this thesis is 4.1 A rms as given in Table 5.1, which results in 5.8 A peak current. Therefore, for the vector control case, the rated torque of the motor is calculated from (5.3) to be 15 Nm, which is

approximately equal to the steady-state value given in the nameplate of the IPM motor in Table 5.1. Generally permanent magnet synchronous motors have a high peak torque capability for limited duty cycle, which is set by the current rating of the stator windings, thermal specifications of the motor, magnetic saturation and demagnetization issues, etc. In this thesis, peak current of the motor is limited to be 10 A for short transient periods.

5.2 Simulation Results of The High Frequency Signal Injection Algorithm

The high frequency signal injection algorithm is employed for low and zero speed operation. The rotor flux angle is estimated and used for vector control, and the speed estimation of the high frequency signal injection algorithm is used as the feedback for the sensorless speed control loops. Since the saliency of the IPM motor exists in its fundamental model as different entries for L_d and L_q, the saliency based high frequency signal injection algorithm can be simulated using the motor model of the SIMPLORER. The magnitude and frequency of the injected high frequency signal are determined via experimental tests on the IPM motor, which will be shown in the next chapter. The injection voltage magnitude is selected to be 75 V peak and the frequency as 500 Hz. In the following simulations the sensorless vector control and sensorless speed control of the IPM motor is realized based on the high frequency signal injection algorithm as given in Figure 4.31. The controller parameters for the simulation of the high frequency signal injection algorithm, based on the block diagram in Figure 4.31, are given in Table 5.2.

Table 5.2 Parameters used within the high frequency signal injection simulation

Synchronous Frame Current Regulator	K_p	7.5
	K_I	930
	LPF on the feedback path	2nd order with 100 Hz cut-off frequency
High Frequency Signal Injection Algorithm	Injection Frequency	500 Hz
	Injection Voltage	75 V
	BPF	4th order wide band-pass with 100 Hz low cut-off and 2500 Hz high cut-off frequencies
	LPF within the heterodyning	2nd order with 20 Hz cut-off frequency
	K_P of the compensator	5000
	K_I of the compensator	250
Speed Controller	K_{pr}	0.5
	K_p	0.08
	K_I	1
Position Controller	K_p	20

5.2.1 Acceleration from Zero Speed and Step Load at Constant Speed Operation

In Figures 5.1-5.13, ramp speed acceleration with 200 rpm magnitude is commanded while the motor is at zero speed and a 50% (7.5 Nm) of rated torque is applied as step load torque at t=1 s after the motor reaches steady-state constant speed of 200 rpm. In Figure 5.1 the speed command (black), actual speed (red), and estimated speed (blue), by which the speed loop is closed, are shown. In Figure 5.2 the applied load torque is shown, where the rate of change of the applied load torque is limited such that the step 50% load torque is applied in 10 ms. In Figure 5.3, the commanded torque current i_{qs}^{e*} (red) and the actual torque current i_{qs}^{e} (blue), which is calculated

106

based on the estimated rotor flux angle, are shown to imply the performance of the synchronous frame current regulator. The oscillations of the commanded torque current is a result of high gains of the speed loop, which is designed to meet both high performance command tracking and high performance (load torque) disturbance rejection requirements. In Figure 5.4 the estimated rotor flux angle is given, which will be verified by the Figure 5.5 showing the error in the estimation of the rotor flux angle. In Figure 5.5 (a), the error in the estimation of the rotor flux angle is shown, where the output of the estimation error detection algorithm, calculated as in Figure 4.20, that is the admittance difference signal (Y_{Mdiff}) is shown in Figure 5.5 (b). As observed in Figure 5.5 (a), rotor flux angle estimation is accurate with error of less than $10°$; and for such estimation error values, the admittance difference signal (Y_{Mdiff}) is proportional to the estimation error as expected in equation (4.27). In Figure 5.6, the synchronous frame rotor flux axis current (i_{ds}^e), which is calculated based on the estimated rotor flux angle, is shown to imply that the synchronous frame current regulator keeps it at zero level, where there is high frequency component due to the injection on this axis. The effect of this high frequency current component on the reluctance torque and the output torque ripple will be represented in the following figures. In Figure 5.7, the electromagnetic torque output of the IPM motor is shown, which is obtained from the motor model of the SIMPLORER software, to verify the performance of the vector control operation, such that the torque output is proportional to the torque current (i_{qs}^e), which was given in Figure 5.3, with the torque equation of (5.3). The phase-a current is given in Figure 5.8, where the magnified waveforms of the phase-a current for no-load and loaded time periods are given in Figure 5.9 and 5.10, respectively. As observed in Figures 5.9-5.10, the peak magnitude of the high frequency component in the phase-a current is same for both the no-load and loaded operations, since the injected high frequency voltage magnitude and frequency are not changing. In Figures 5.11 and 5.12 the high frequency current ripple in the i_{ds}^e current due to the injection and the resultant torque ripple at the output due to the reluctance torque are shown both for no-load (a) and loaded (b) cases. Since the reluctance torque value is proportional to both the i_{ds}^e and i_{qs}^e currents as given in (5.1) and the magnitude of the ripple of the i_{ds}^e current is

107

constant (for constant injection voltage and frequency level); the magnitude of the torque ripple, which is due to the reluctance torque, is directly proportional to the i_{qs}^e current. Hence, the ratio of the magnitude of the output torque ripple to the average torque output is always constant. From the Figures 5.11 and 5.12, the ripple of the i_{ds}^e current has a peak of 0.5 Amperes and the torque ripple at the output seems to be 2.25 %. The quantization in the i_{ds}^e waveform in Figures 5.11 and 5.12 is a result of discrete time processing (with 10 kHz) within the simulation. In Figure 5.13, the speed command feedforward method for the tracker algorithm (Figure 4.30) is investigated. The speed command is used as a pre-estimation for the synchronous speed, thus for the rotor flux angle. For the steady-state periods, the feedforward term almost provides all the synchronous speed estimation and the compensator does not react. For the transient acceleration and loading periods, the command can not be exactly realized and the actual speed deviates from the command; therefore the pre-estimation of the command feedforward term becomes incorrect, which results in error in the rotor flux angle estimation as shown in Figure 5.5 (a). However, the rotor flux angle estimation error is detected by the detection algorithm and the compensator reacts to the error, as shown in Figure 5.13. The sum of the feedforward and the compensation terms is the estimated synchronous speed as in Figure 4.30, which is almost same as the actual synchronous speed. In summary, the synchronous speed, hence the mechanical speed and the rotor flux angle of the IPM motor are estimated with high accuracy and the closed loop sensorless control is performed.
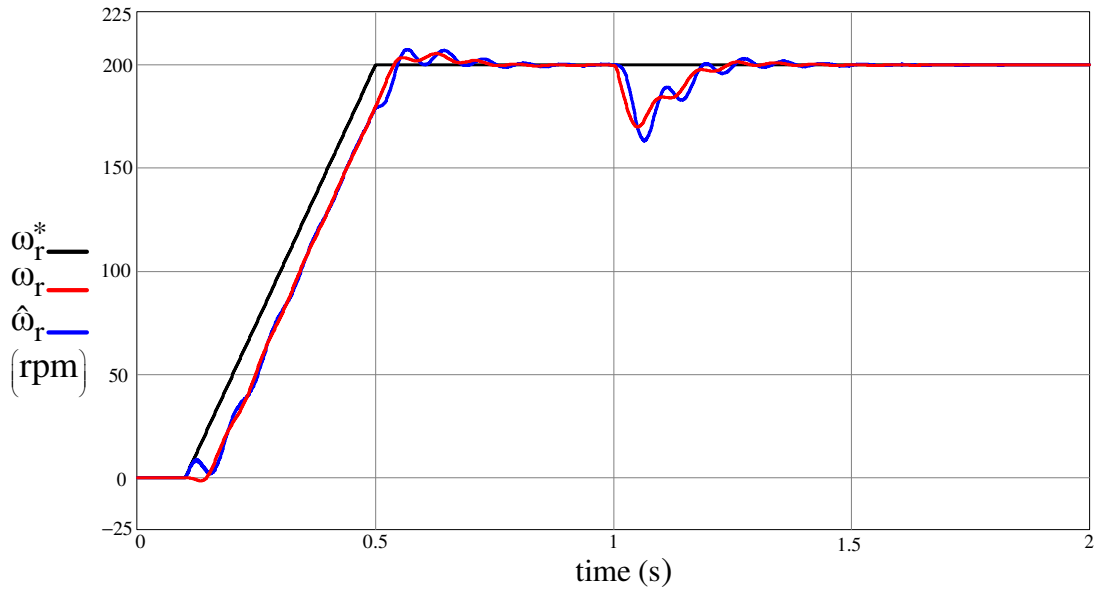
Figure 5.1 Speed command (black), actual speed (red), estimated speed (blue) for acceleration from 0 rpm to 200 rpm under no-load followed by a 50% step load at constant 200 rpm operation.
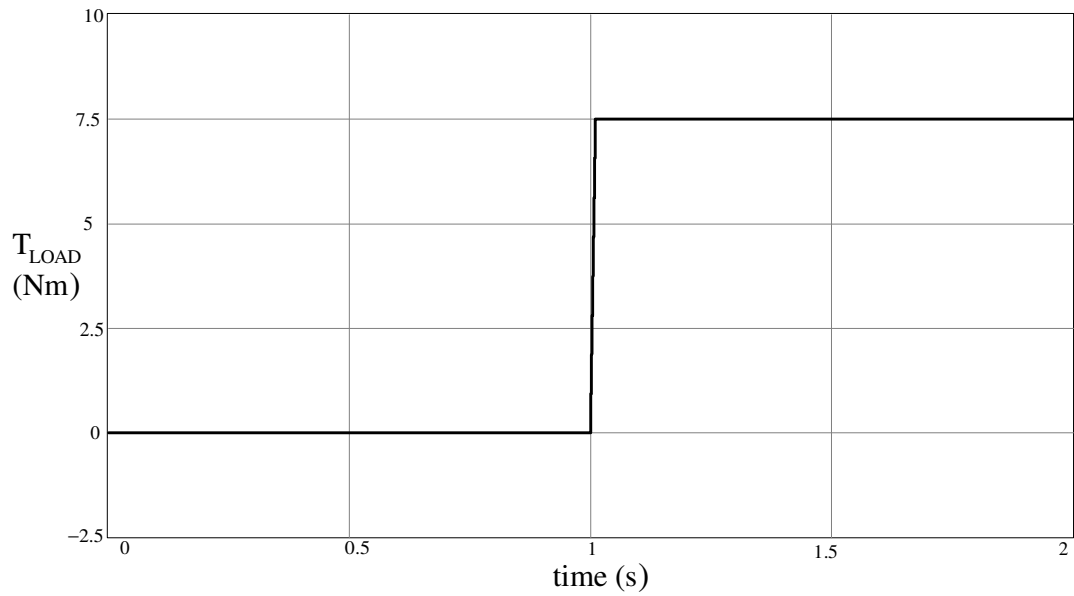
Figure 5.2 The applied load torque value for acceleration from 0 rpm to 200 rpm under no-load followed by a 50% step load at constant 200 rpm operation.

109
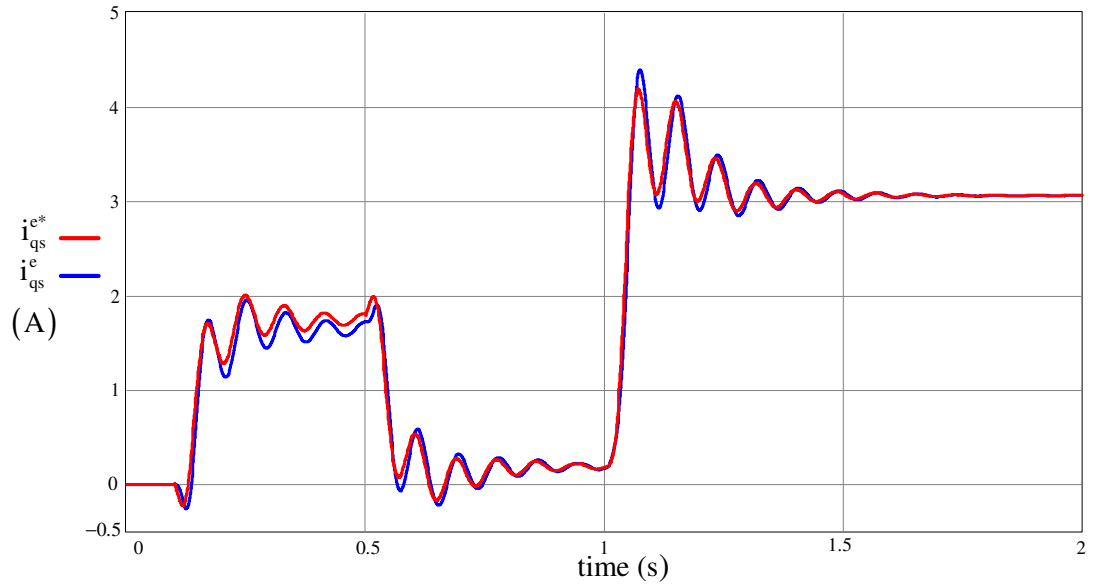
Figure 5.3 Synchronous frame torque axis current command (i_{qs}^{e*}) and actual i_{qs}^{e} current for acceleration from 0 rpm to 200 rpm under no-load followed by a 50% step load at constant 200 rpm operation.
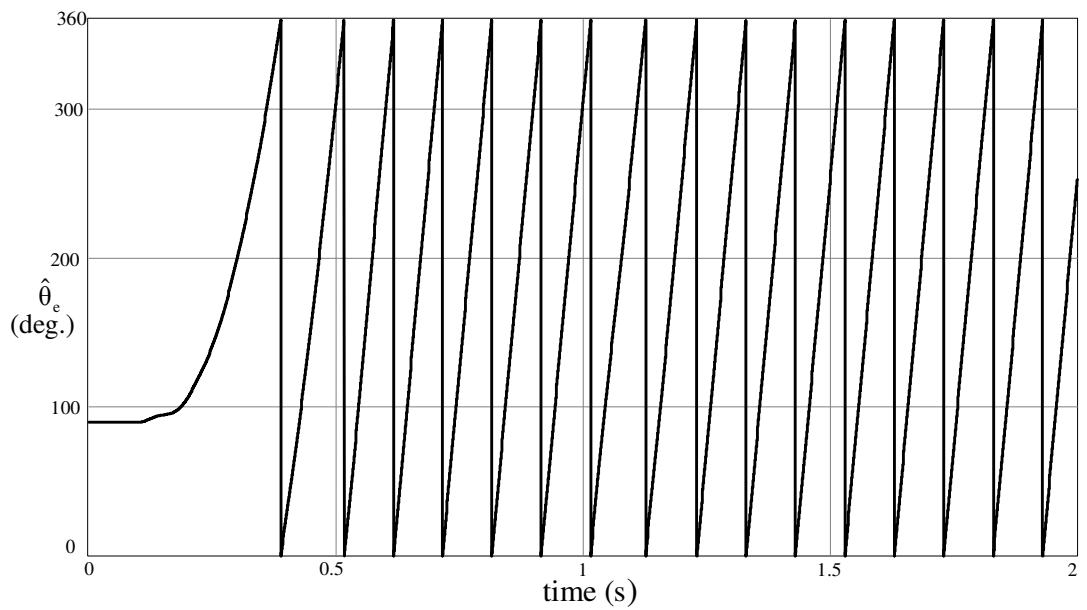
Figure 5.4 Estimated rotor flux angle for acceleration from 0 rpm to 200 rpm under no-load followed by a 50% step load at constant 200 rpm operation.
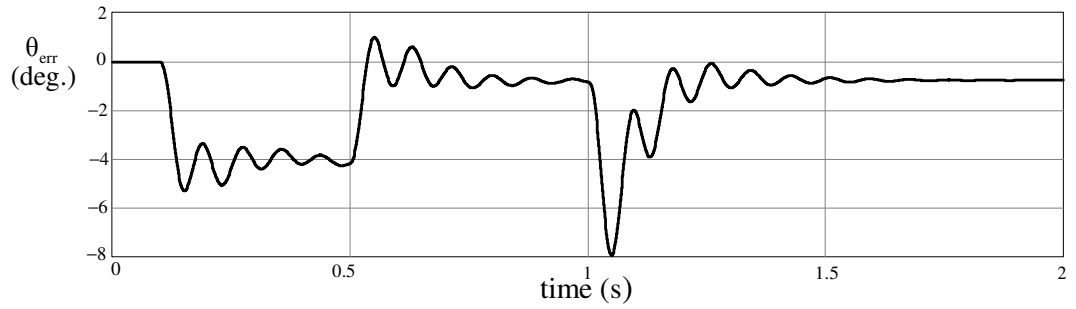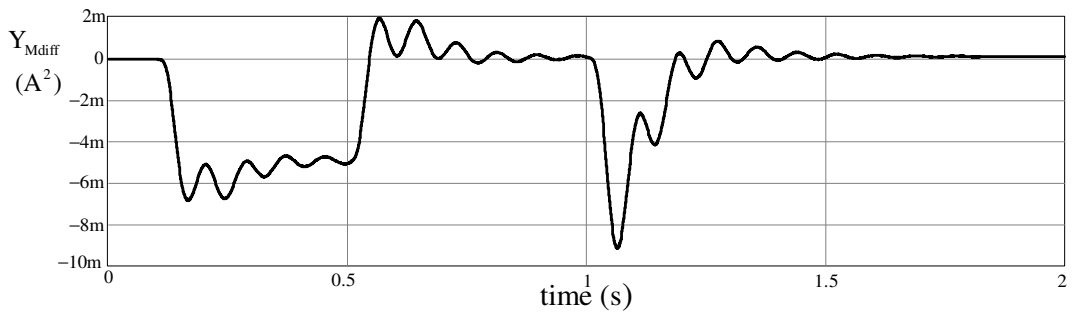
Figure 5.5 Estimation error of rotor flux angle (a) and the admittance difference output of the estimation error detection algorithm (b) for acceleration from 0 rpm to 200 rpm under no-load followed by a 50% step load at constant 200 rpm operation.
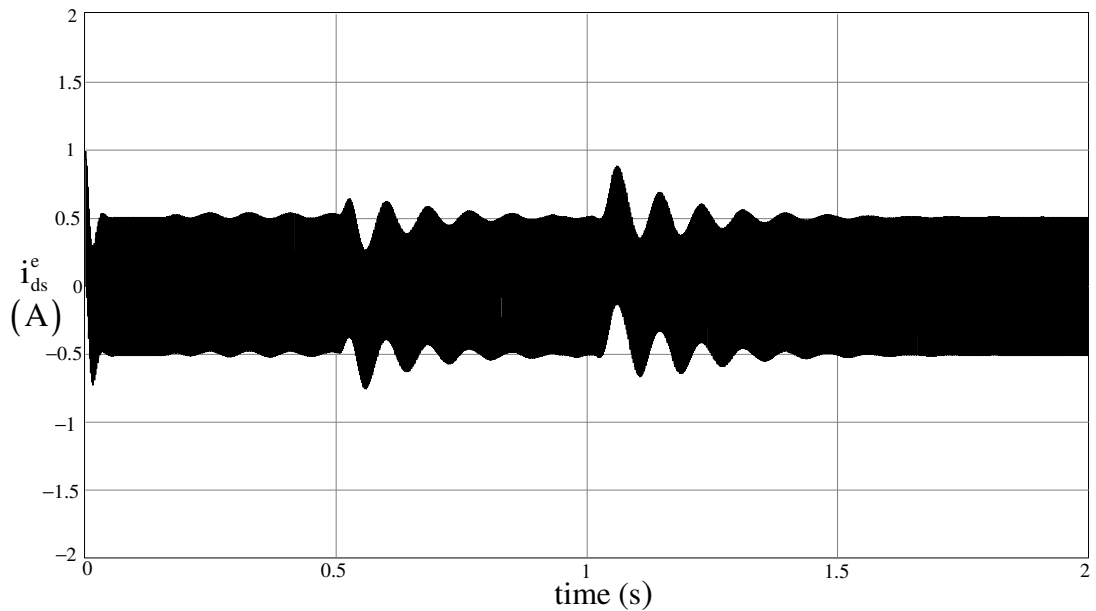
Figure 5.6 Synchronous frame flux axis current (i_{ds}^e) for acceleration from 0 rpm to 200 rpm under no-load followed by a 50% step load at constant 200 rpm operation.
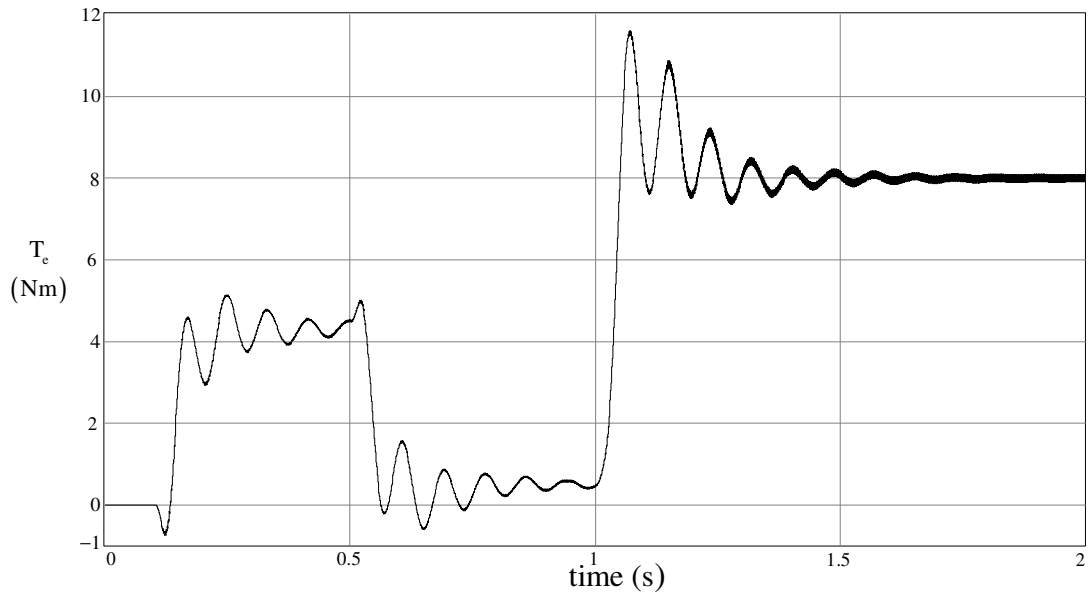
Figure 5.7 Electromagnetic torque output of the IPM motor for acceleration from 0 rpm to 200 rpm under no-load followed by a 50% step load at constant 200 rpm operation.
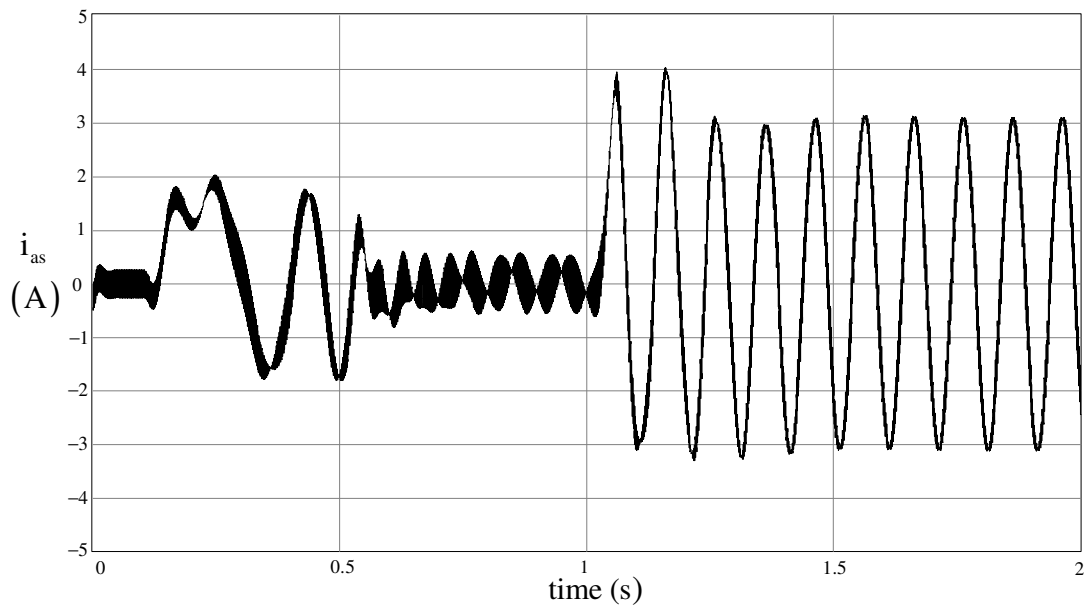
Figure 5.8 Phase-a current waveform for acceleration from 0 rpm to 200 rpm under no-load followed by a 50% step load at constant 200 rpm operation.
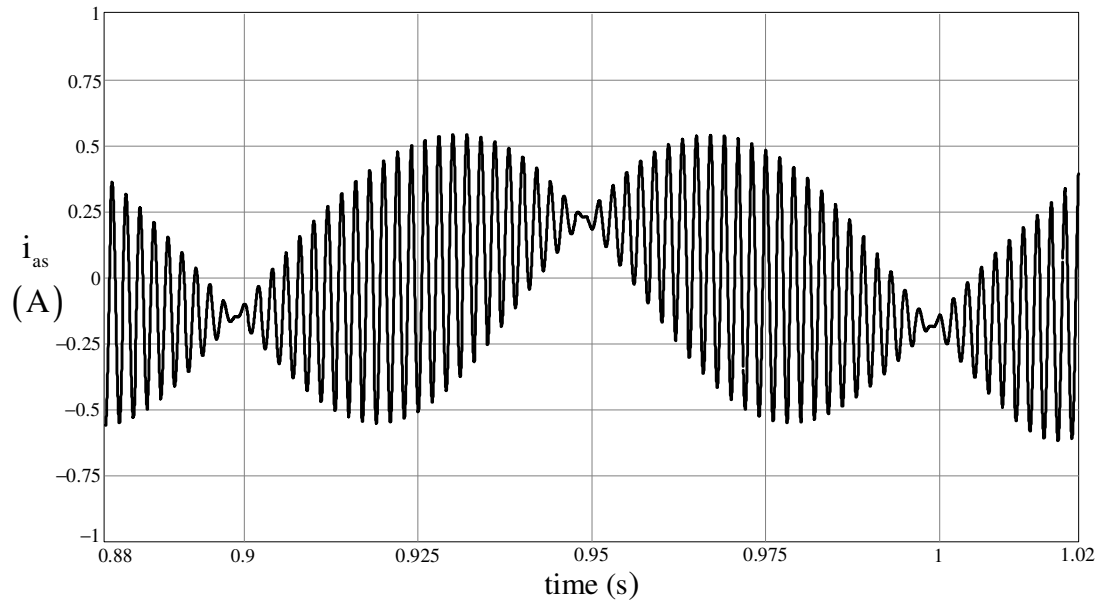
Figure 5.9 Zoom of phase-a current for no-load case for acceleration from 0 rpm to 200 rpm under no-load followed by a 50% step load at constant 200 rpm operation.
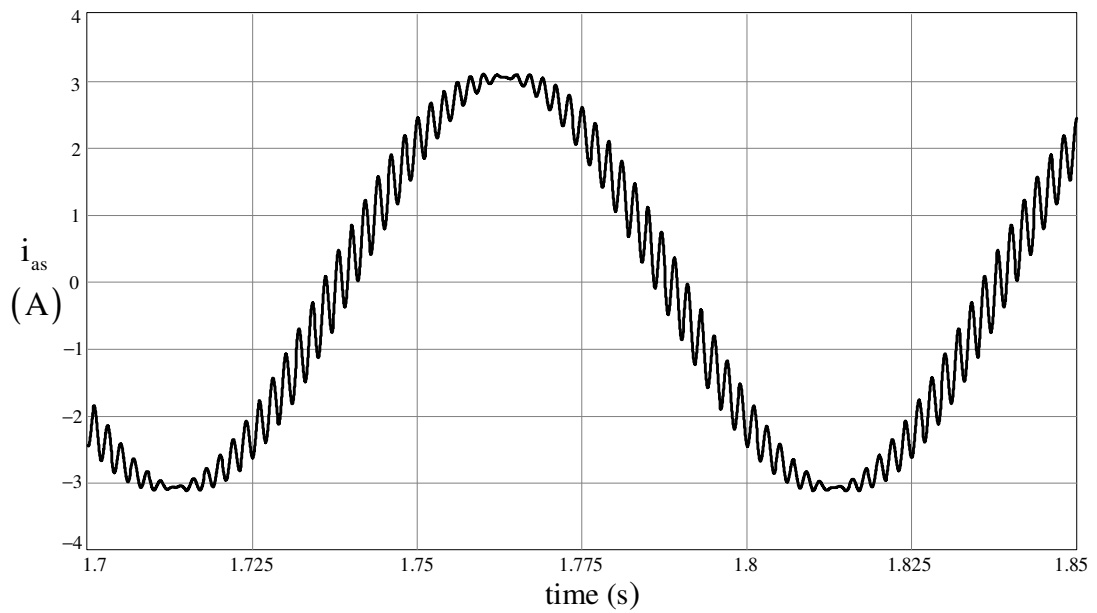
Figure 5.10 Zoom of phase-a current for loaded case for acceleration from 0 rpm to 200 rpm under no-load followed by a 50% step load at constant 200 rpm operation.

113
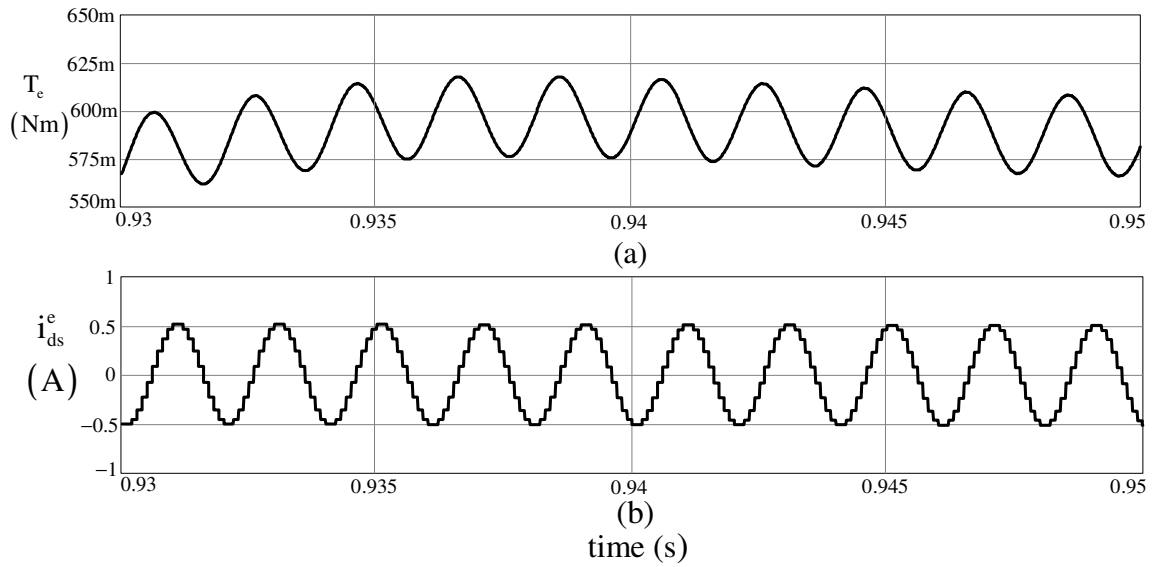
Figure 5.11 High frequency ripple in i_{ds}^e current (a) and the torque ripple (b) for no-load case for acceleration from 0 rpm to 200 rpm under no-load followed by a 50% step load at constant 200 rpm operation.
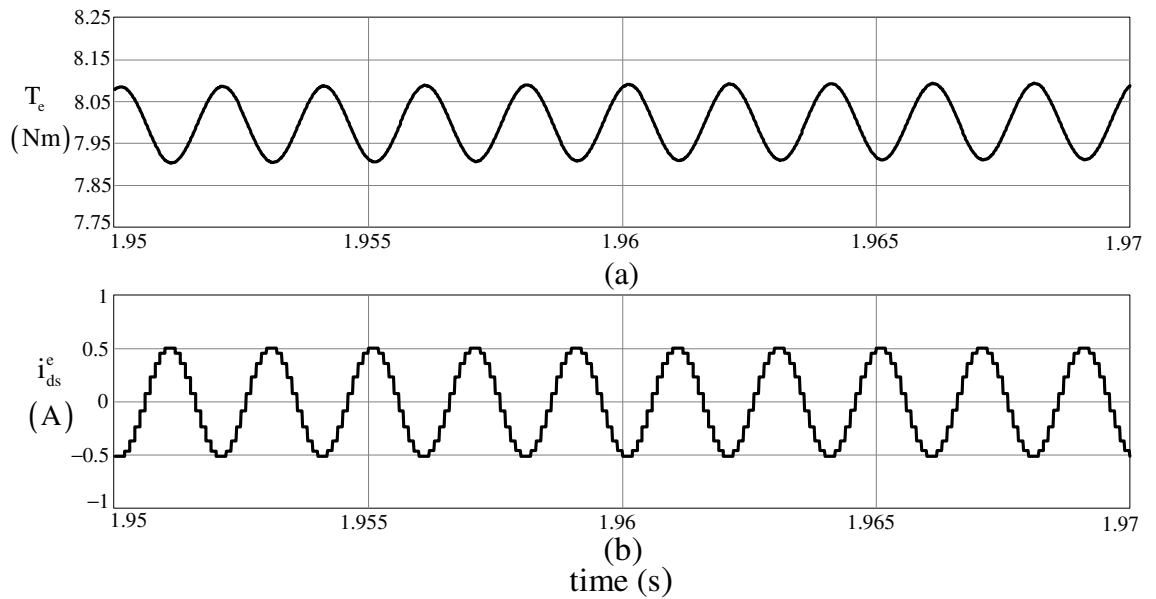
Figure 5.12 High frequency ripple in i_{ds}^e current (a) and the torque ripple (b) for loaded case for acceleration from 0 rpm to 200 rpm under no-load followed by a 50% step load at constant 200 rpm operation.
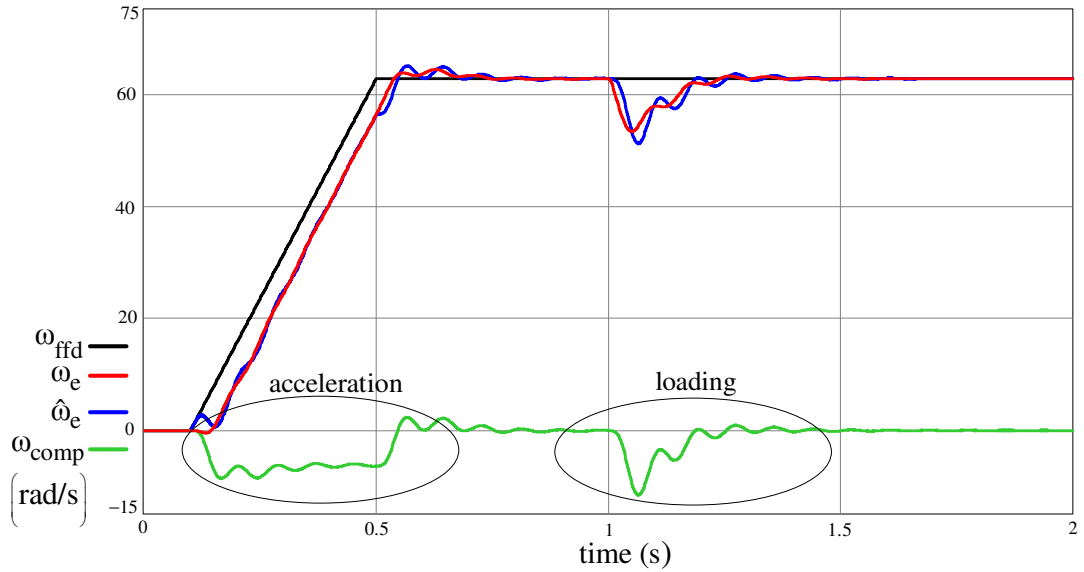
Figure 5.13 Command feedforward (black), actual synchronous frequency (red), estimated synchronous frequency (blue), output of the compensator of the tracker (green) for acceleration from 0 rpm to 200 rpm under no-load followed by a 50% step load at constant 200 rpm operation.

5.2.2 Trapezoidal Speed Profile Operation Under No-Load

In Figures 5.14-5.18, trapezoidal speed profile command for both directions is realized with no-load. In Figure 5.14 the speed command (black), actual speed (red), and estimated speed (blue), by which the speed loop is closed, are shown. In Figure 5.15, the commanded torque current i_{qs}^{e*} is shown. In Figure 5.16 the estimated rotor flux angle is given, where the error in the estimation of the rotor flux angle is given in Figure 5.17. The rotor flux angle estimation error is found to be less than 5°. In Figure 5.18, the electromagnetic torque output of the IPM motor, which is proportional to the commanded torque current with equation (5.3), is shown.
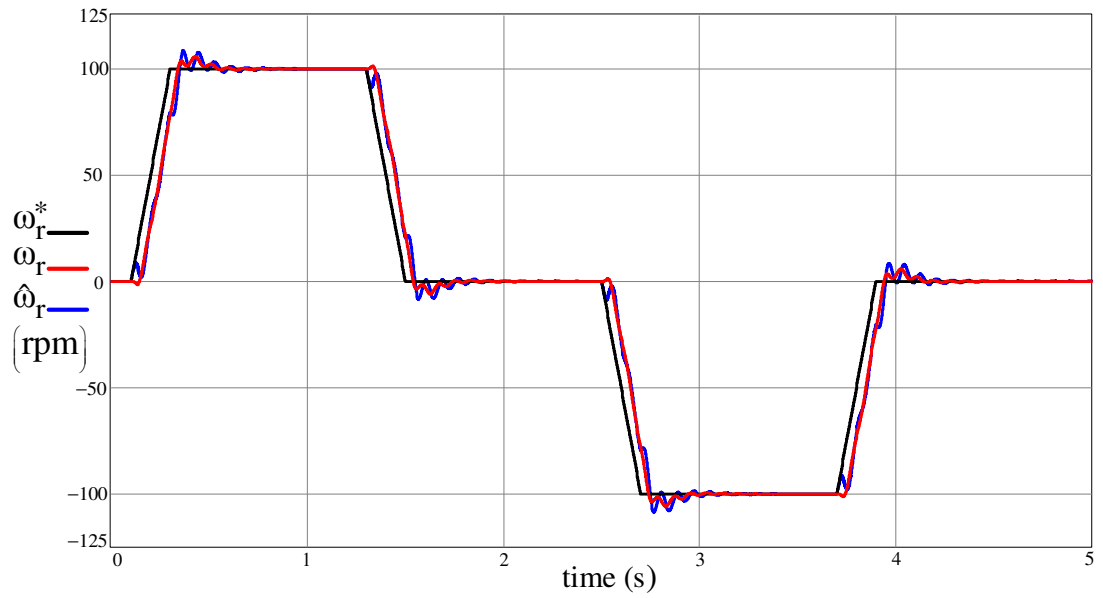
Figure 5.14 Speed command (black), actual speed (red), estimated speed (blue) for trapezoidal ±100 rpm speed profile operation under no-load.
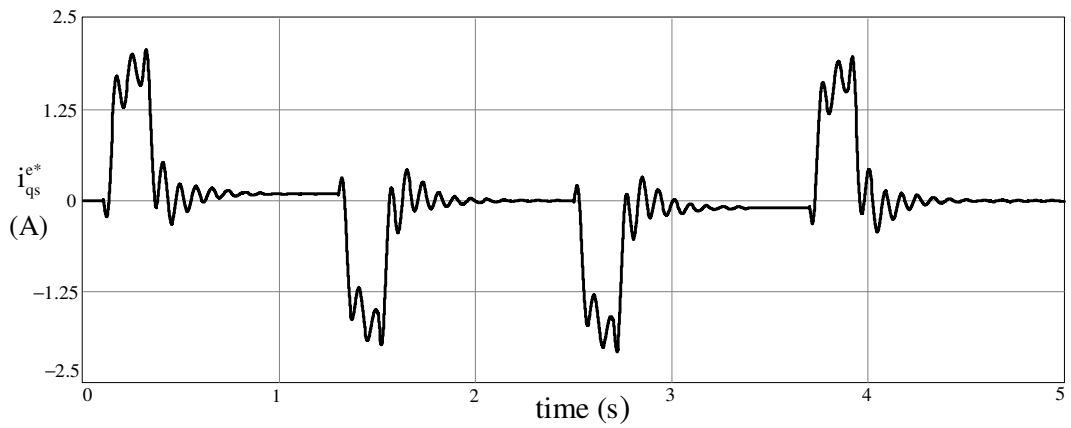
Figure 5.15 Synchronous frame torque axis current command (i_{qs}^{e*}) for trapezoidal ±100 rpm speed profile operation under no-load.
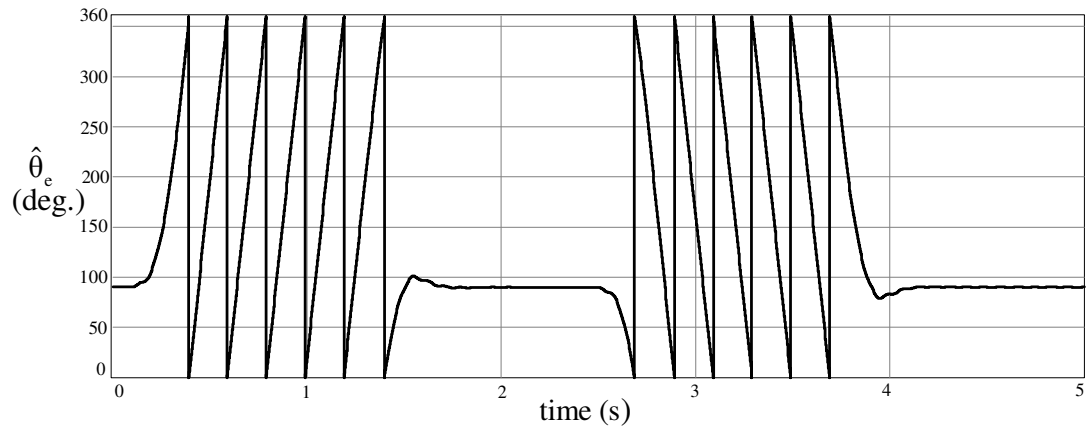
Figure 5.16 Estimated rotor flux angle for trapezoidal ±100 rpm speed profile operation under no-load.
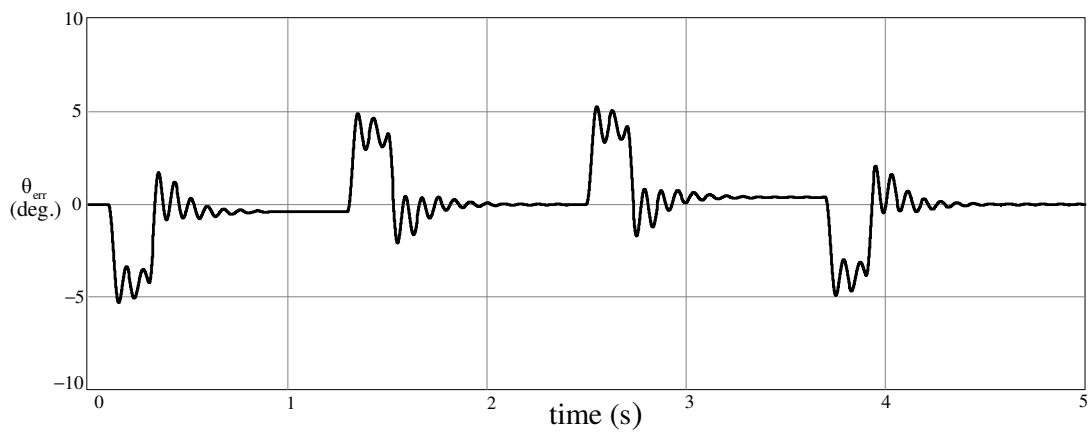
Figure 5.17 Estimation error of rotor flux angle for trapezoidal ±100 rpm speed profile operation under no-load.
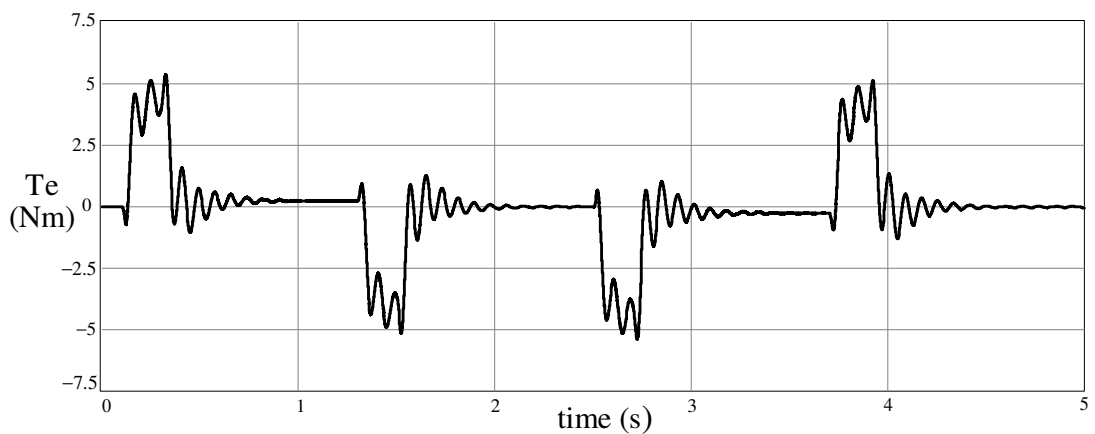
Figure 5.18 Electromagnetic torque output of the IPM motor for trapezoidal ±100 rpm speed profile operation under no-load.

117

5.2.3 Step Load at Zero Speed Operation and Acceleration Under Load

In Figures 5.19-5.25, 100% of rated torque is applied as step load torque at t=0.5 s when there is zero speed command and acceleration to 150 rpm is realized under constant 100% load. In Figure 5.19 the speed command (black), actual speed (red), and estimated speed (blue), by which the speed loop is closed, are shown. The applied load torque is shown in Figure 5.20, where the rate of change of the applied load torque is limited such that the step 100% load torque is applied in 20 ms. In Figure 5.21, the commanded torque current i_{qs}^{e*} is shown. In Figure 5.22 the estimated rotor flux angle is given, where the error in the estimation of the rotor flux angle is given in Figure 5.23. The rotor flux angle estimation error is found to be less than $15°$. In Figure 5.24, the electromagnetic torque output of the IPM motor, which is proportional to the commanded torque current with the equation (5.3), is shown. The phase-a current waveform is given in Figure 5.25.
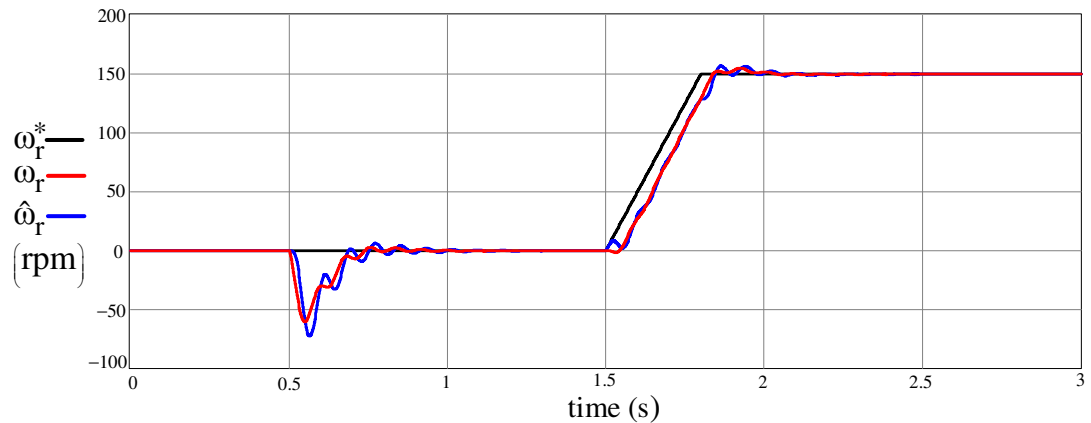
Figure 5.19 Speed command (black), actual speed (red), estimated speed (blue) for 100% step load at zero speed followed by an acceleration to 150 rpm under 100% load.
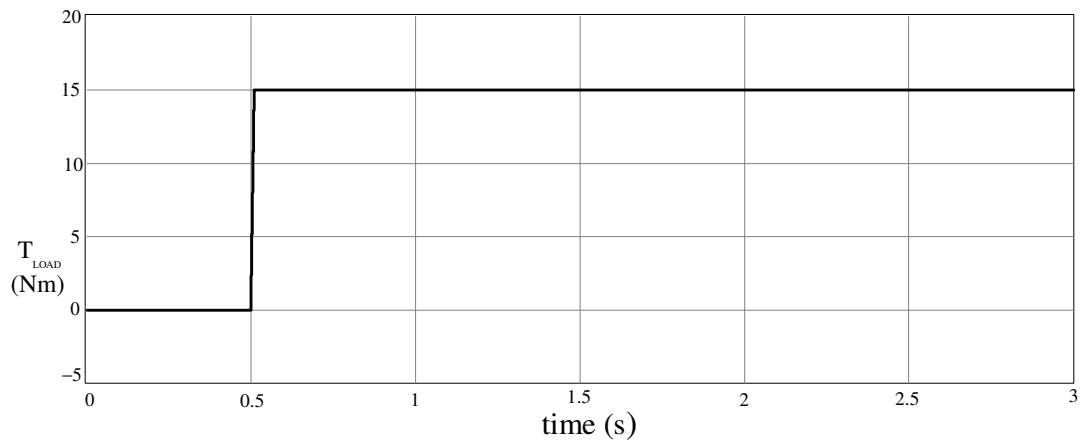
Figure 5.20 The applied load torque value for 100% step load at zero speed followed by an acceleration to 150 rpm under 100% load.
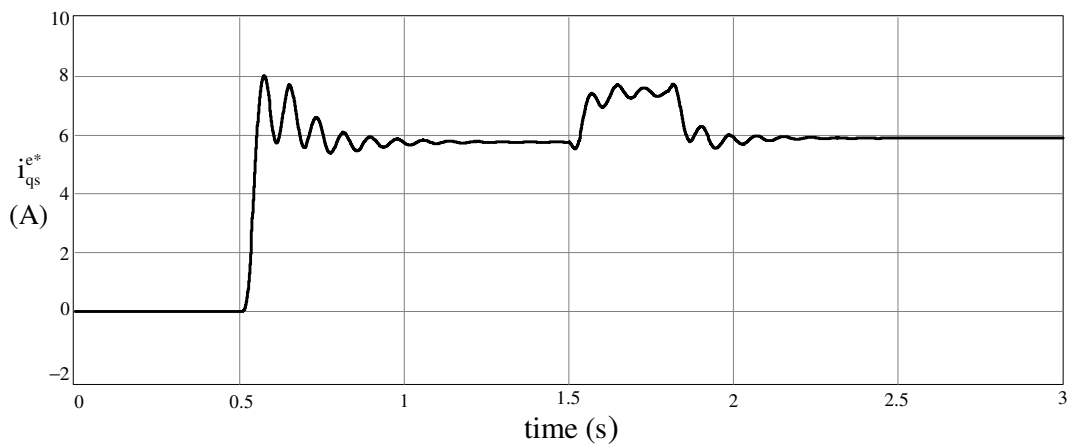
Figure 5.21 Synchronous frame torque axis current command (i_{qs}^{e*}) for 100% step load at zero speed followed by an acceleration to 150 rpm under 100% load.
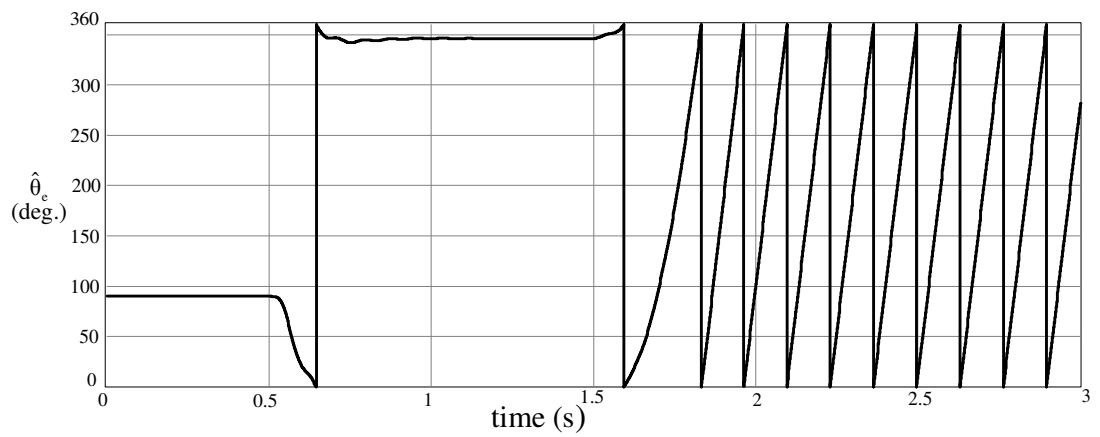
Figure 5.22 Estimated rotor flux angle for 100% step load at zero speed followed by an acceleration to 150 rpm under 100% load.
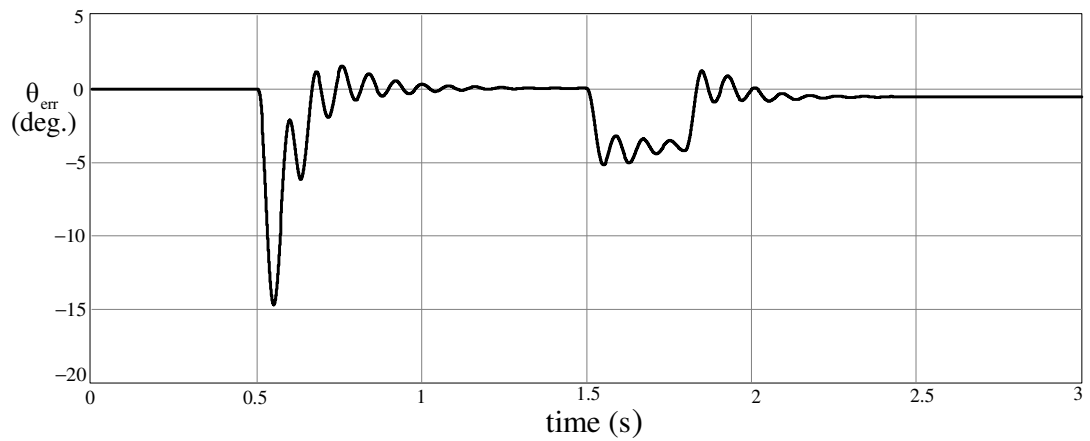
Figure 5.23 Estimation error of rotor flux angle for 100% step load at zero speed followed by an acceleration to 150 rpm under 100% load.
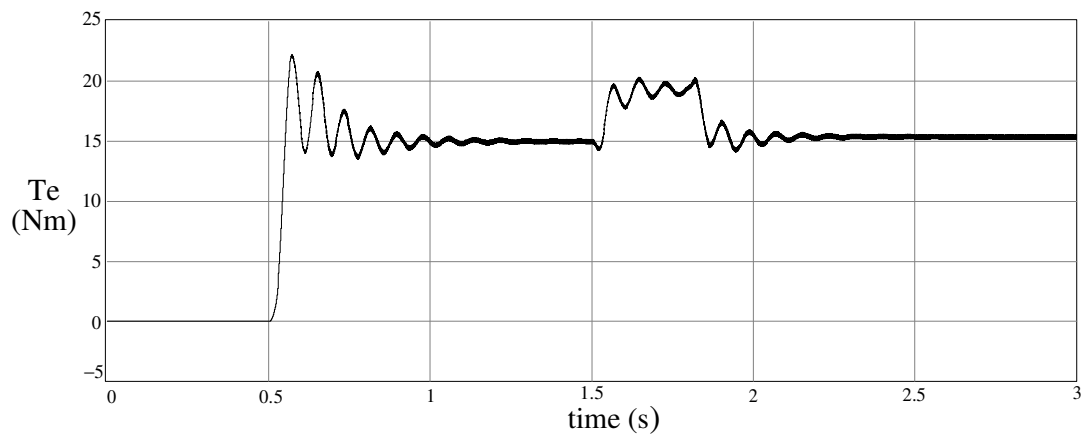
Figure 5.24 Electromagnetic torque output of the IPM motor for 100% step load at zero speed followed by an acceleration to 150 rpm under 100% load.
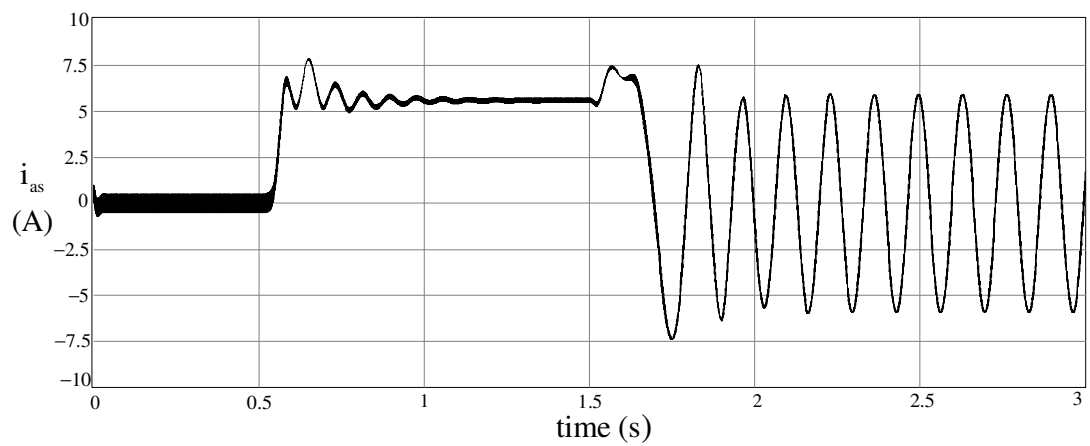
Figure 5.25 Phase-a current waveform for 100% step load at zero speed followed by an acceleration to 150 rpm under 100% load.

5.3 Simulation Results of The Flux Observer Algorithm

The fundamental model based flux observer algorithm is utilized for medium and high speed operation. In the following simulations, sensorless vector control and speed control of the IPM motor are realized with the flux observer algorithm as given in Figure 4.36. The controller parameters for the simulation of the fundamental model based flux observer algorithm, based on the block diagram in Figure 4.36, are given in Table 5.3.

Table 5.3 Parameters used within the flux observer simulation

Synchronous Frame Current Regulator	K_p	75
	K_I	9300
	LPF on the feedback path	2nd order with 1 kHz cut-off frequency
Speed Controller	K_{pr}	0.5
	K_p	0.04
	K_I	0.4
Position Controller	K_p	20

5.3.1 Acceleration Under No-Load and Step Load at Constant Speed Operation

In Figures 5.26-5.32 ramp speed command with 500 rpm magnitude is given when the IPM motor is rotating with 250 rpm and a 50% (7.5 Nm) of rated torque is applied as step load at t=1.5 s after the motor reaches steady-state constant speed of 500rpm. In Figure 5.26 the speed command (black), actual speed (red), and estimated speed (blue), by which the speed loop is closed, are shown. The applied load torque is shown in Figure 5.27, where the rate of change of the applied load torque is limited such that the step 50% load torque is applied in 10 ms. In Figure 5.28, the commanded torque current i_{qs}^{e*} is shown. In Figure 5.29 the estimated rotor flux angle is given, where the error in the estimation of the rotor flux angle is given in Figure

5.30. The rotor flux angle estimation error is found to be less than 1.5°. In Figure 5.31, the electromagnetic torque output of the IPM motor, which is proportional to the commanded torque current with the equation (5.3), is shown. The phase-a current waveform is given in Figure 5.32.
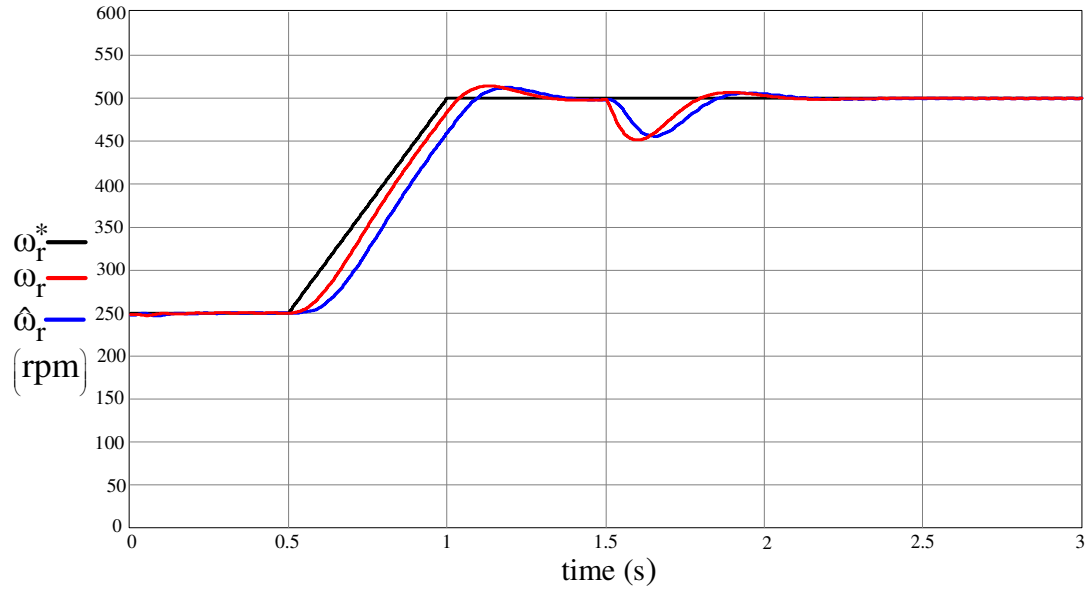
Figure 5.26 Speed command (black), actual speed (red), estimated speed (blue) for acceleration from 250 rpm to 500 rpm under no-load followed by a 50% step load at constant 500 rpm operation.
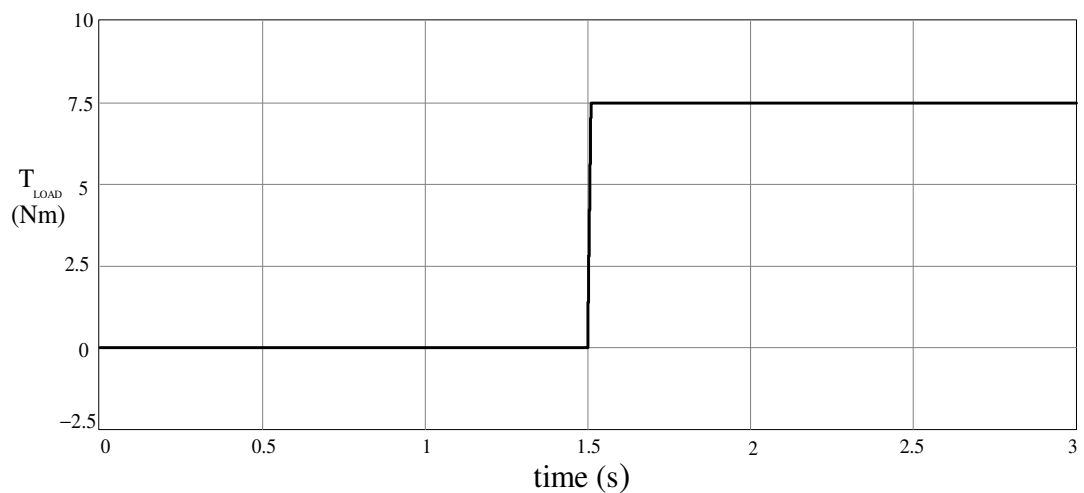
Figure 5.27 Step 50 % load torque for acceleration from 250 rpm to 500 rpm under no-load followed by a 50% step load at constant 500 rpm operation.

123
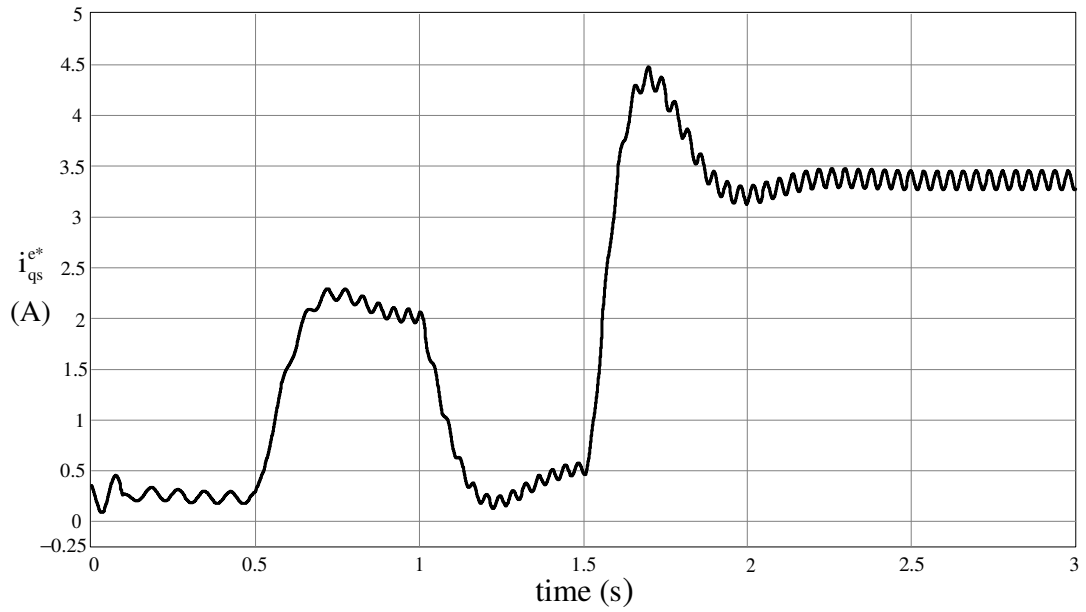
Figure 5.28 Synchronous frame torque axis current (i_{qs}^e) command for acceleration from 250 rpm to 500 rpm under no-load followed by a 50% step load at constant 500 rpm operation.
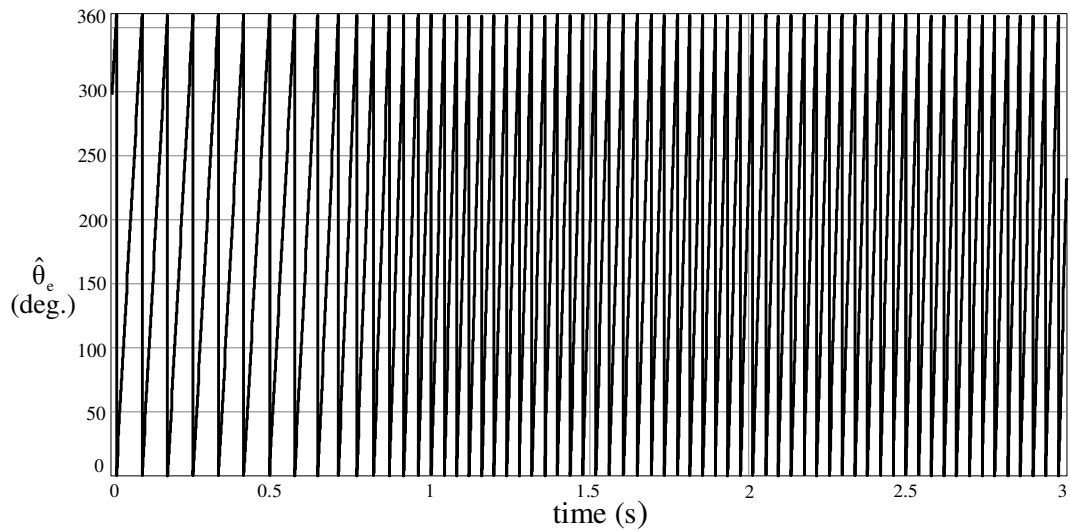
Figure 5.29 Estimated rotor flux angle for acceleration from 250 rpm to 500 rpm under no-load followed by a 50% step load at constant 500 rpm operation.
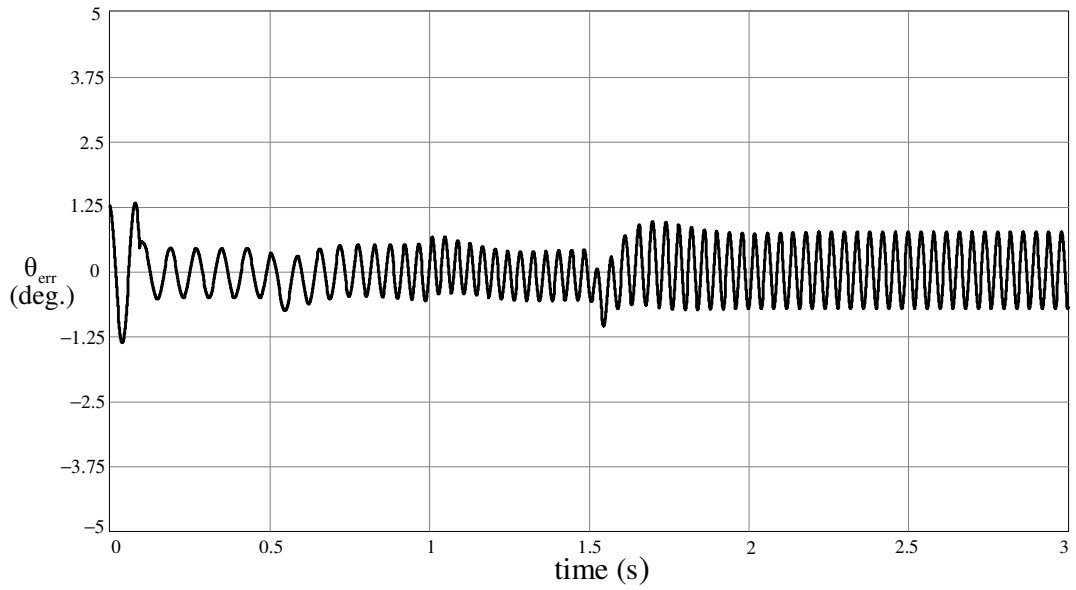
Figure 5.30 Estimation error of rotor flux angle for acceleration from 250 rpm to 500 rpm under no-load followed by a 50% step load at constant 500 rpm operation.
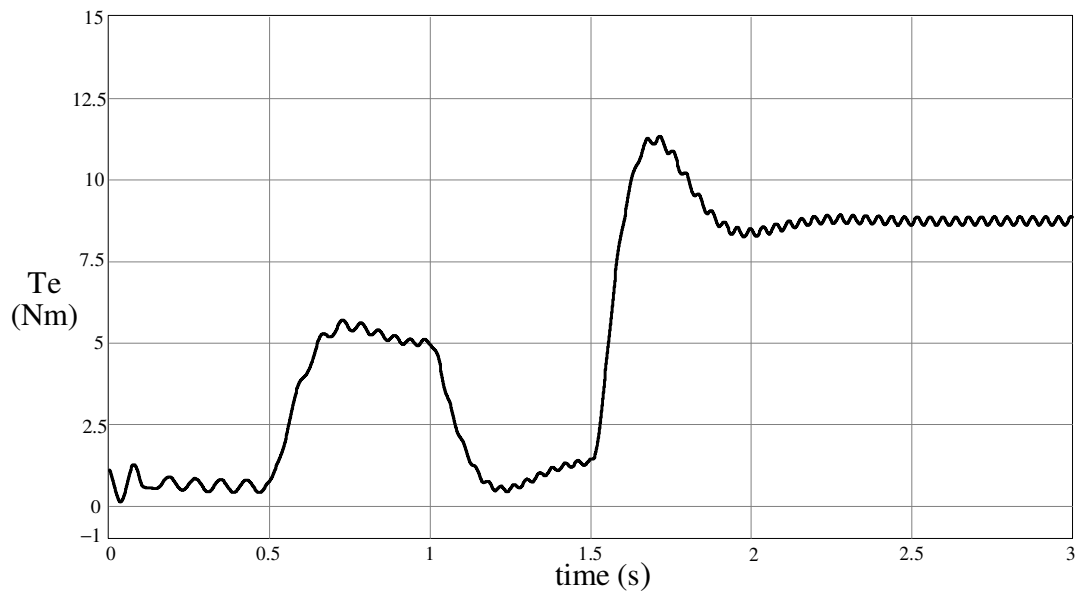
Figure 5.31 Electromagnetic torque output of the IPM motor for acceleration from 250 rpm to 500 rpm under no-load followed by a 50% step load at constant 500 rpm operation.
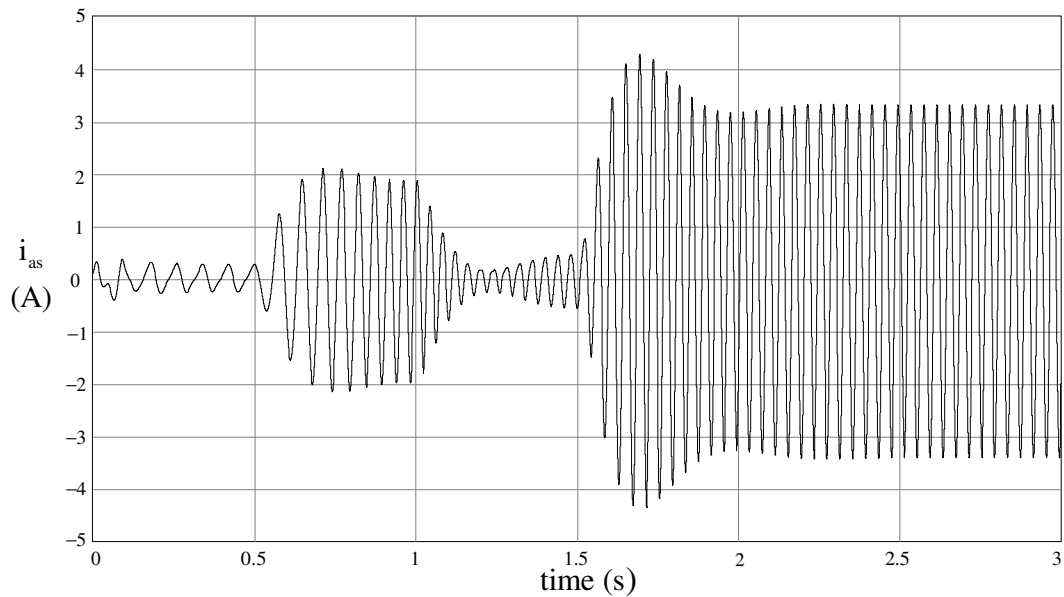
Figure 5.32 Phase-a current waveform for acceleration from 250 rpm to 500 rpm under no-load followed by a 50% step load at constant 500 rpm operation.

5.3.2 Step Load at Constant Speed Operation

In Figures 5.26-5.32 100% of rated torque is applied as step load torque between t=1 s and t=2 s while constant 500 rpm speed is commanded. In Figure 5.26 the speed command (black), actual speed (red), and estimated speed (blue), by which the speed loop is closed, are shown. The applied load torque is shown in Figure 5.27, where the rate of change of the applied load torque is limited such that the step 100% load torque is applied in 20 ms. In Figure 5.28, the commanded torque current i_{qs}^{e*} is shown. In Figure 5.29 the estimated rotor flux angle is given, where the error in the estimation of the rotor flux angle is given in Figure 5.30. In Figure 5.31, the electromagnetic torque output of the IPM motor, which is proportional to the commanded torque current with the equation (5.3), is shown. The phase-a current waveform is given in Figure 5.32.

126
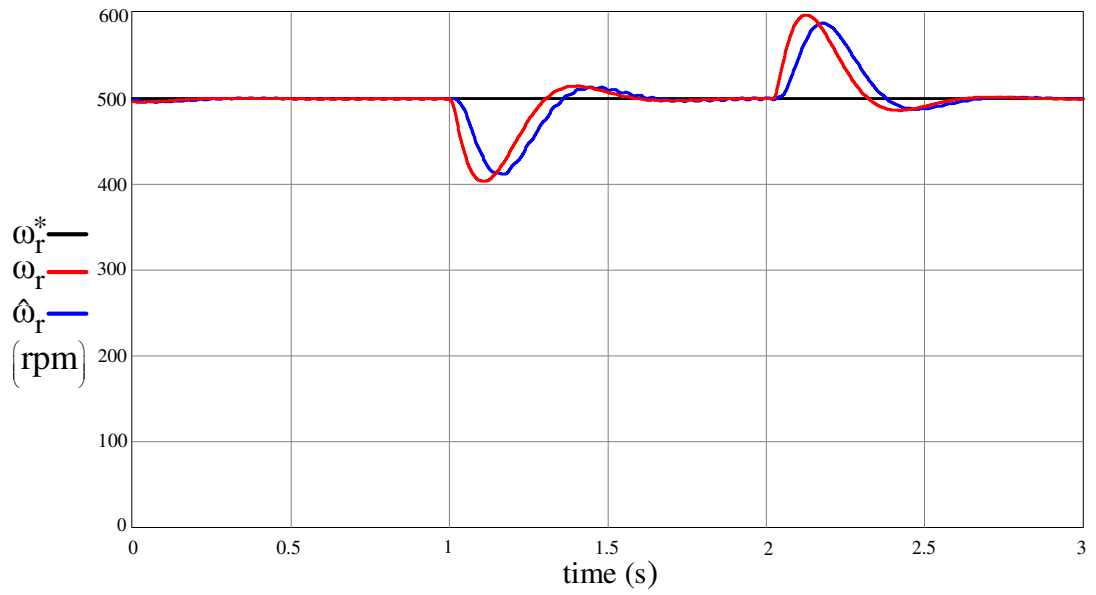
Figure 5.33 Speed command (black), actual speed (red), estimated speed (blue) for 100% step load at constant 500 rpm operation.
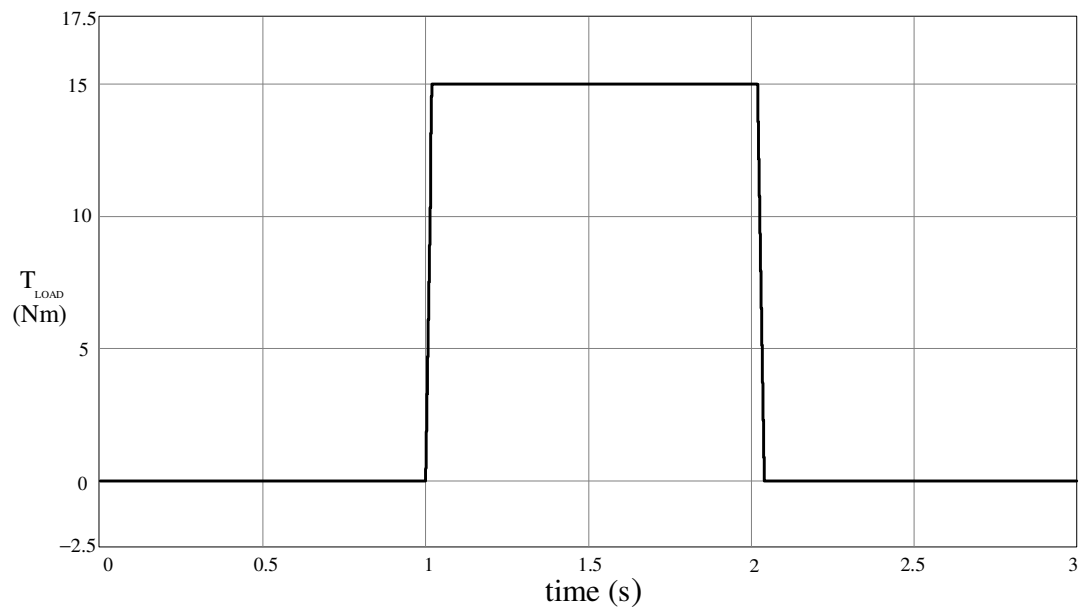
Figure 5.34 The applied load torque value for 100% step load at constant 500 rpm operation.
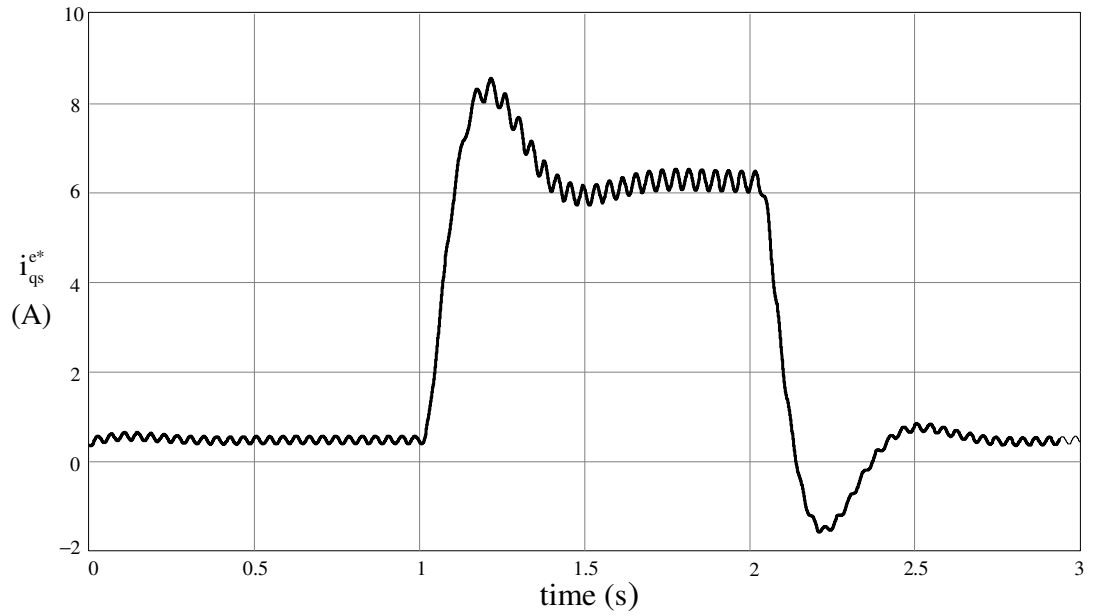
Figure 5.35 Synchronous frame torque axis current command (i_{qs}^{e*}) for 100% step

load at constant 500 rpm operation.
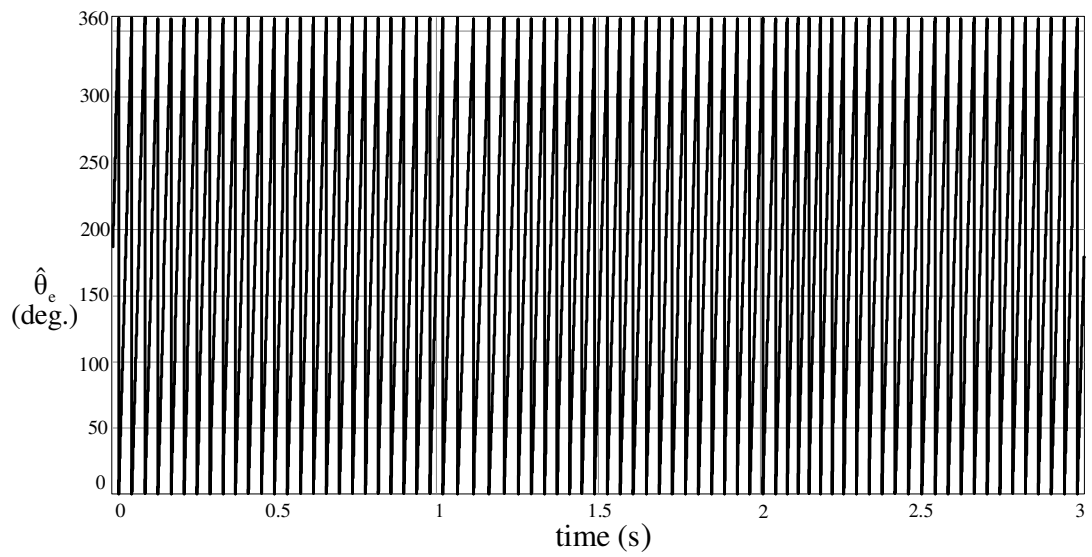
Figure 5.36 Estimated rotor flux angle for 100% step load at constant 500 rpm
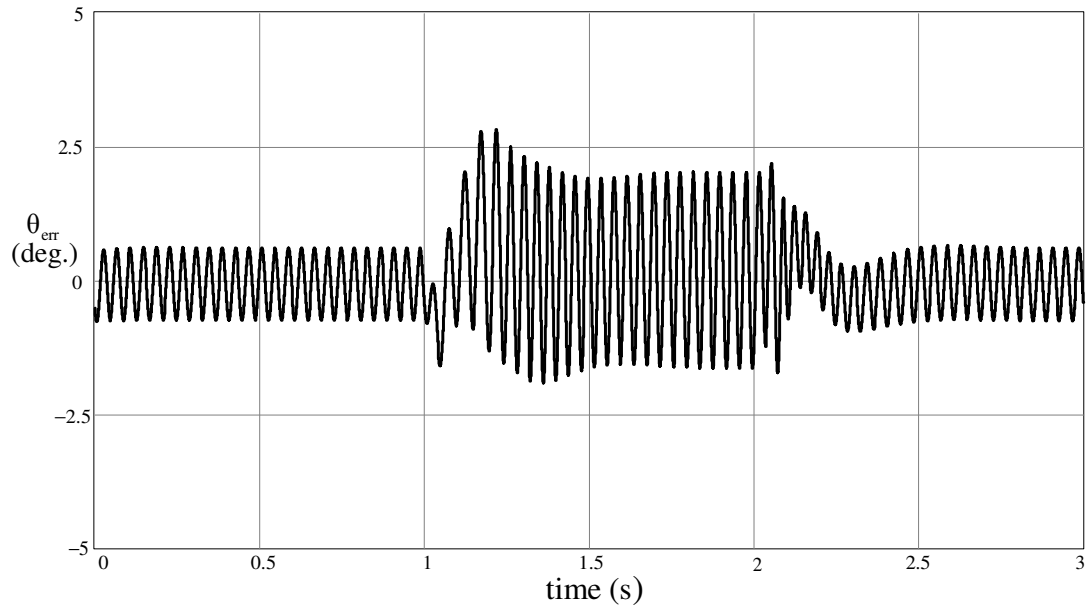
operation.

Figure 5.37 Estimation error of rotor flux angle for 100% step load at constant 500 rpm operation.
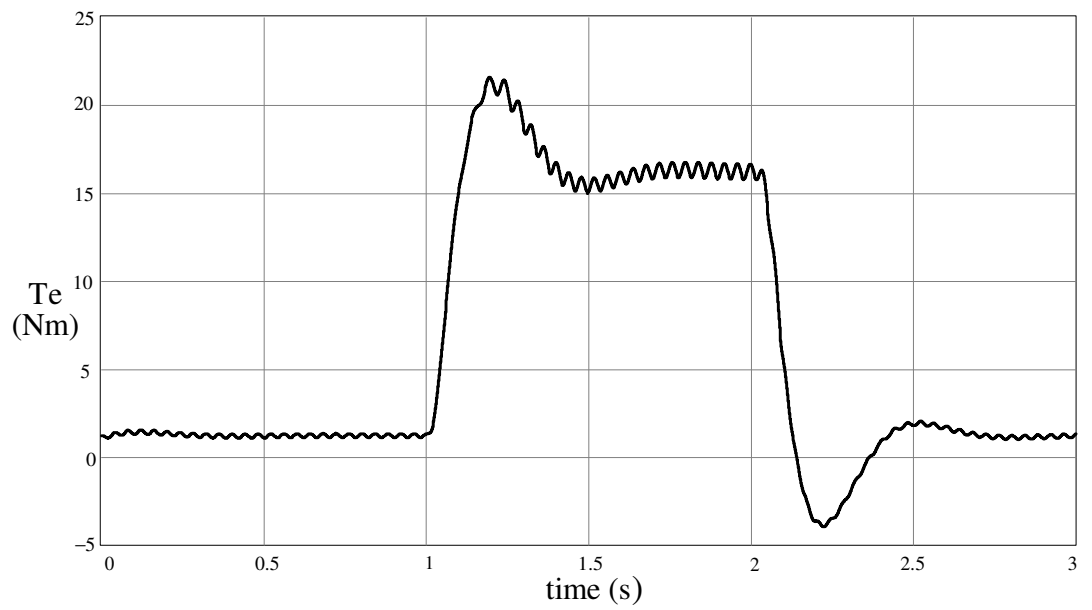
Figure 5.38 Electromagnetic torque output of the IPM motor for 100% step load at constant 500 rpm operation.
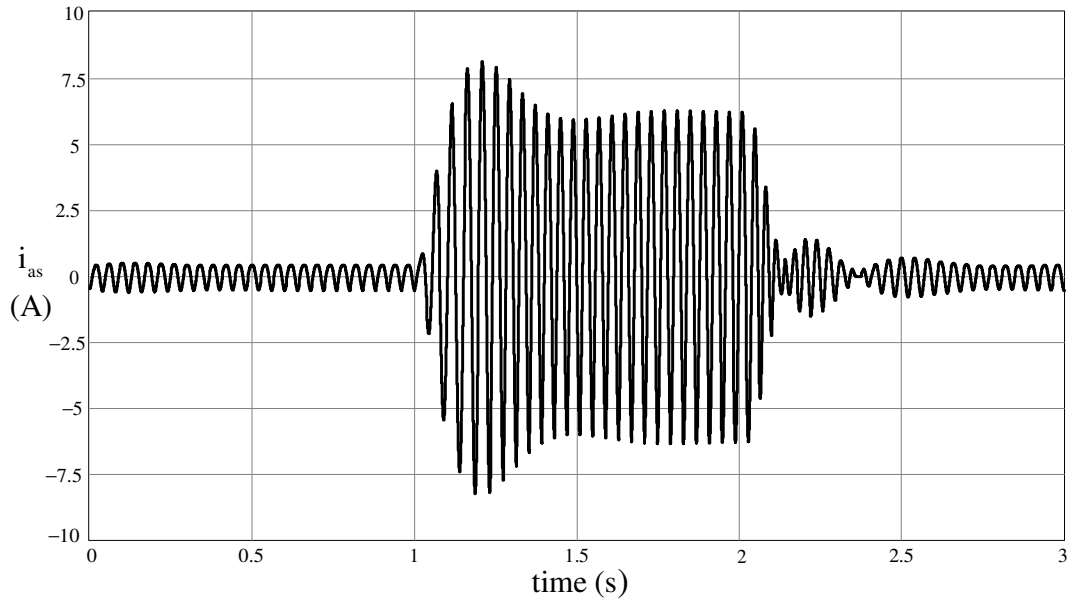
Figure 5.39 Phase-a current waveform for 100% step load at constant 500 rpm operation.

5.3.3 Drift in Stator Flux Estimation

In Figures 5.40-5.43, the IPM motor is modeled with motor parameters different than the parameters which are used within the observer algorithm; and the drift compensation algorithm is not executed in order to observe the effect of the parameter error on the drift of the integration in the observer algorithm. The stator resistance of the IPM motor model in the simulation is increased to 2.956 Ω while the original value of 2.656 Ω is used within the observer algorithm. This can be thought as increase of the stator resistance due to temperature rise which can be encountered in practice. Additionally, the outputs of the ideal voltage sources within the simulator are scaled down by 0.95 to simulate the non-linearity of the VSI. In Figure 5.40 and 5.41 estimated stator flux linkages on the qs and ds axes are shown. Since the estimated parameters within the observer are incorrect and the drift is not compensated, drift of the integration occurs, which results in large error of the rotor flux angle estimation (i.e. divergence) as shown in Figure 5.42; and also oscillation in the speed estimation as in Figure 5.43.

130
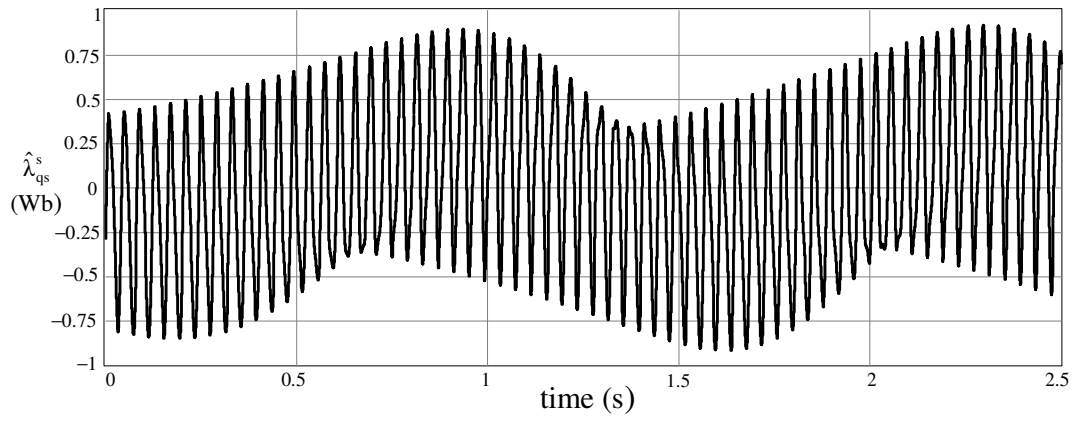
Figure 5.40 Estimated stator flux linkage on qs-axis for observer with incorrect
parameters without drift compensation.
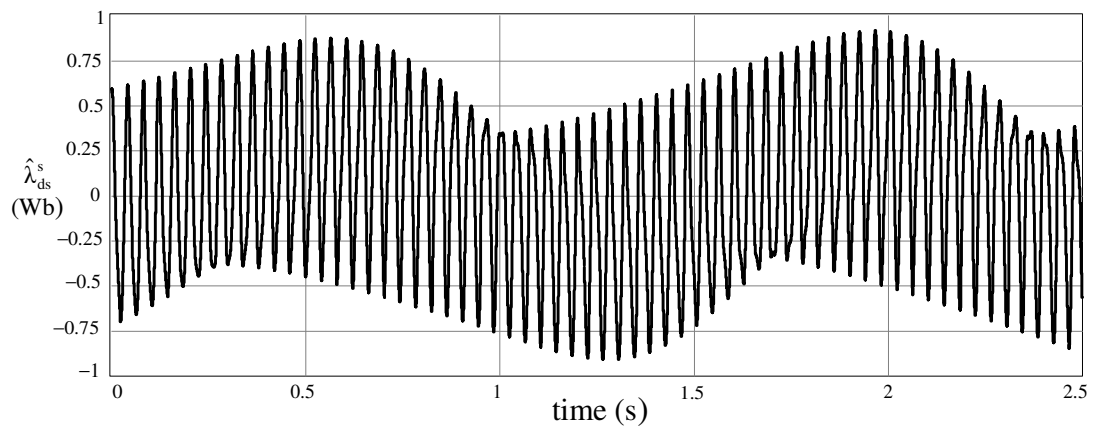
Figure 5.41 Estimated stator flux linkage on ds-axis for flux observer with incorrect
parameters without drift compensation.

131
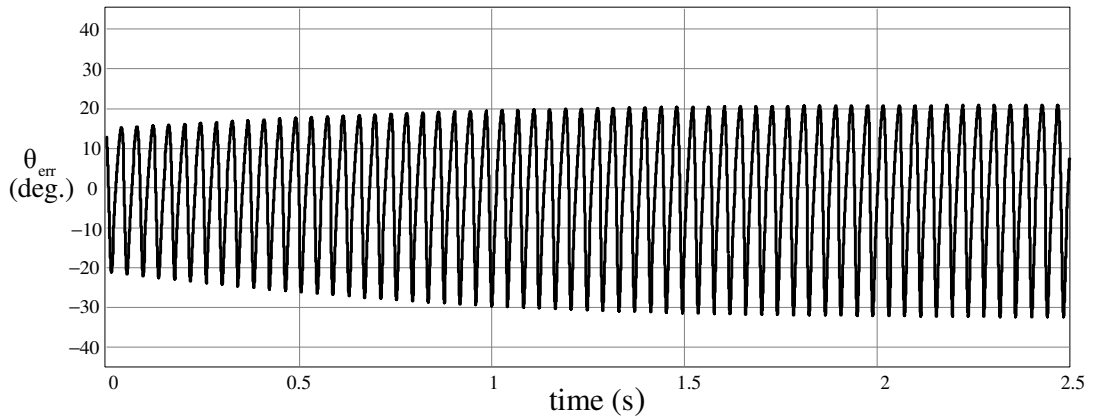
Figure 5.42 Estimation error of rotor flux angle for flux observer with incorrect parameters without drift compensation.
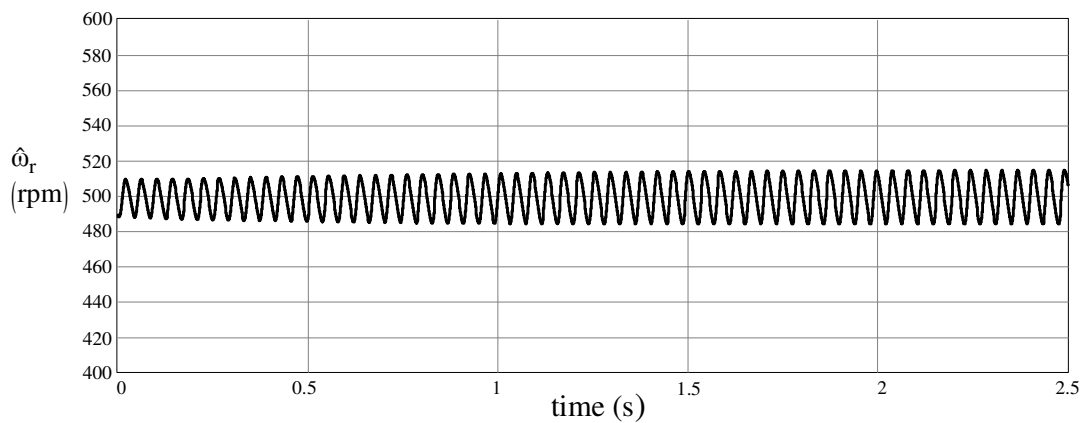
Figure 5.43 Estimation of motor speed for flux observer with incorrect parameters without drift compensation.

5.3.4 Compensation of Drift in Stator Flux Estimation

In Figures 5.44-5.47, the IPM motor is modeled with motor parameters different than the parameters which are used within the observer algorithm; and the drift compensation algorithm is executed in order to prevent the effect of parameter error on the drift of the integration in the observer algorithm. The stator resistance of the IPM motor model is increased to 2.956 Ω while the original value of 2.656 Ω is used within the observer algorithm. This can be thought as increase of the stator resistance due to temperature rise which is mostly encountered in practice. Additionally, the

132

outputs of the ideal voltage sources within the simulator are scaled down by 0.95 to simulate the non-linearity of the VSI. In Figure 5.44 and 5.45 estimated stator flux linkages on the qs and ds axes are shown. Although the assumed parameters within the observer are incorrect, the drift of the integration for stator flux linkage estimation is avoided since it is compensated continuously. As a result; the rotor flux angle estimation is accurate with error of less than 2.5° as shown in Figure 5.46 and also oscillation in the speed estimation is less than 2.5 rpm as in Figure 5.47.
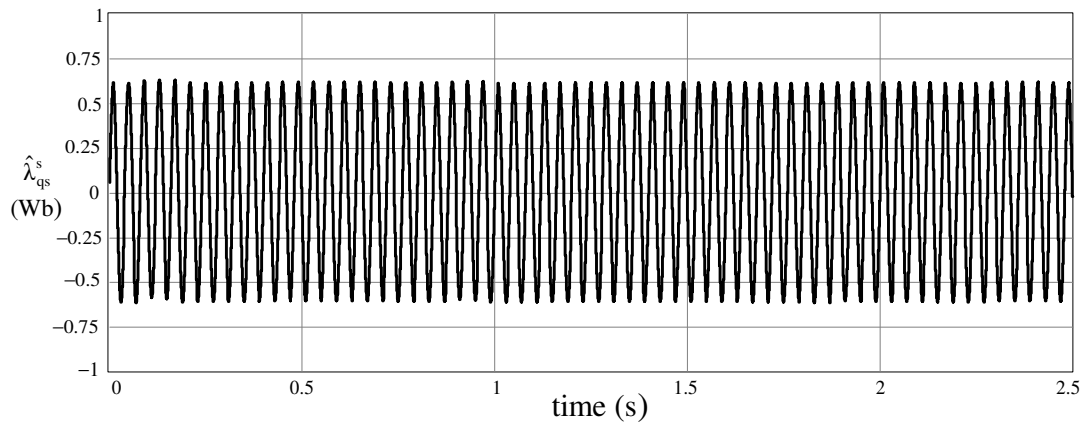
Figure 5.44 Estimated stator flux linkage on qs-axis for observer with incorrect parameters with drift compensation.
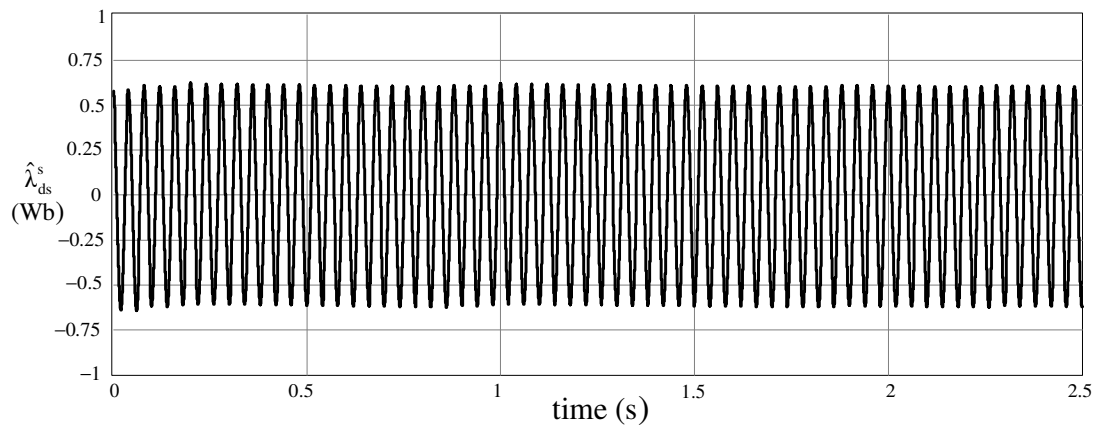
Figure 5.45 Estimated stator flux linkage on ds-axis for flux observer with incorrect parameters with drift compensation.

133
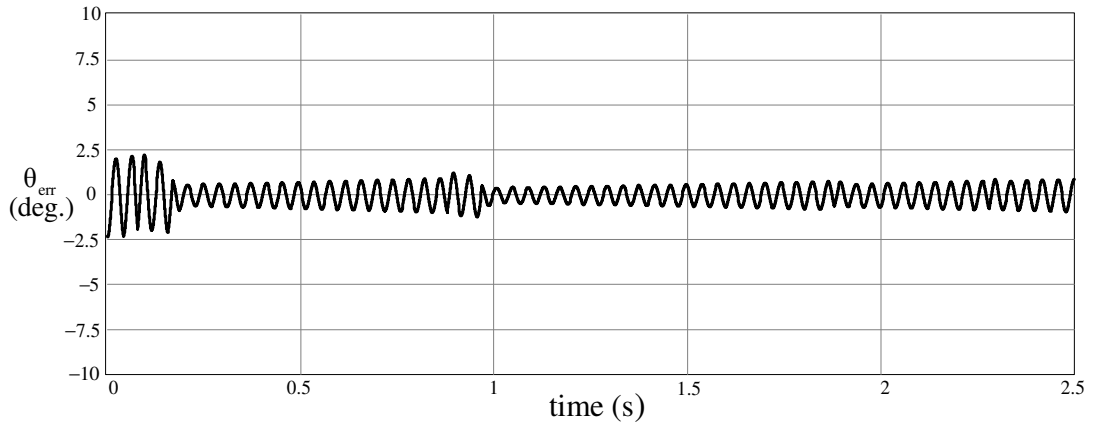
Figure 5.46 Estimation error of rotor flux angle for flux observer with incorrect parameters with drift compensation.
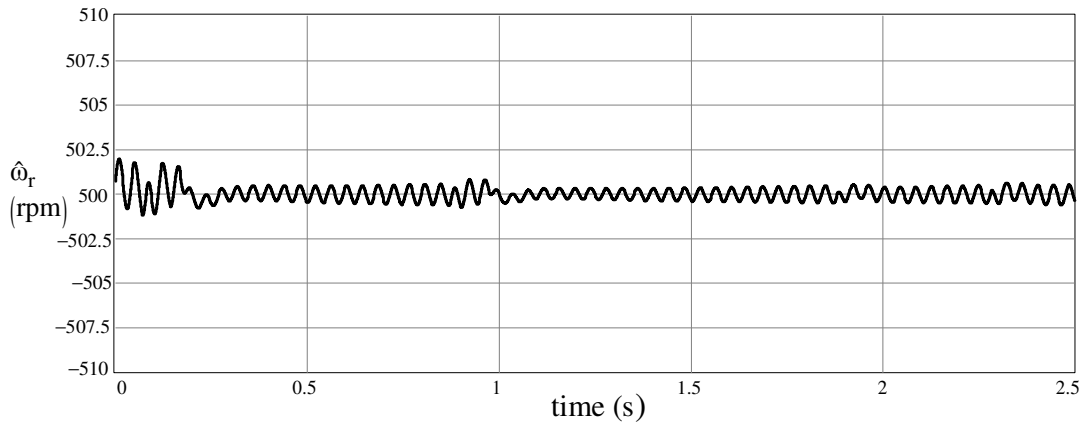
Figure 5.47 Estimation of motor speed for flux observer with incorrect parameters with drift compensation.

5.4 Simulation Results of The Hybrid Algorithm

The hybrid algorithm is the combination of the two estimation methods; the high frequency signal injection method and the fundamental model (back emf detection) based flux observer; such that the high frequency signal injection algorithm is utilized for zero and low speed and transition occurs to the fundamental model (back emf detection) based flux observer algorithm when the motor reaches the medium

speed range. The most important attribute of the hybrid algorithm is the seamless transition between the two estimation methods during speed change. The vector control and speed control loops are closed by the estimations of high frequency signal injection algorithm up to 150 rpm. Above 150 rpm estimations of the flux observer algorithm is used for sensorless vector control and speed control. Beyond 300 rpm, injection of high frequency voltage injection is gradually ceased since it is not utilized.

5.4.1 Trapezoidal Speed Profile Operation for Wide Speed Range with No-Load

In Figures 5.48-5.55, the trapezoidal speed command is realized from zero speed to 500 rpm based on the hybrid method. In Figure 5.48 the speed command (black), actual speed (red), and estimated speed (blue), by which the speed loop is closed, are shown. In Figure 5.49, the commanded torque current i_{qs}^{e*} is shown. In Figure 5.50 the estimated rotor flux angle is given, where the error in the estimation of the rotor flux angle is given in Figure 5.51. The rotor flux angle estimation error is found to be less than $15°$. In Figure 5.52, the electromagnetic torque output of the IPM motor, which is proportional to the commanded torque current with the equation (5.3), is shown. The phase-a current is given in Figure 5.53. The magnified waveform of the phase-a current for the transition period from high frequency signal injection to flux observer algorithm is given in Figure 5.54 and for the transition period from flux observer to high frequency signal injection algorithm is given in Figure 5.55. As observed in Figure 5.48, Figure 5.50, and Figure 5.51 seamless speed control and rotor flux angle estimation is provided for transition periods. The high frequency injection is gradually ceased when the motor reaches 300 rpm speed.
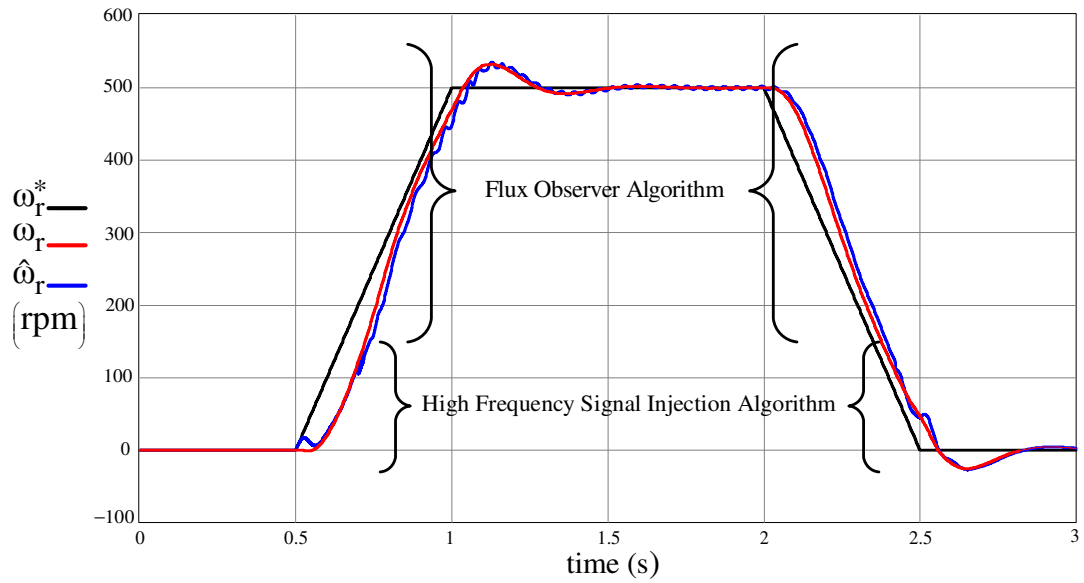
Figure 5.48 Speed command (black), actual speed (red), estimated speed (blue) for trapezoidal 0 rpm to 500 rpm speed profile operation under no-load.
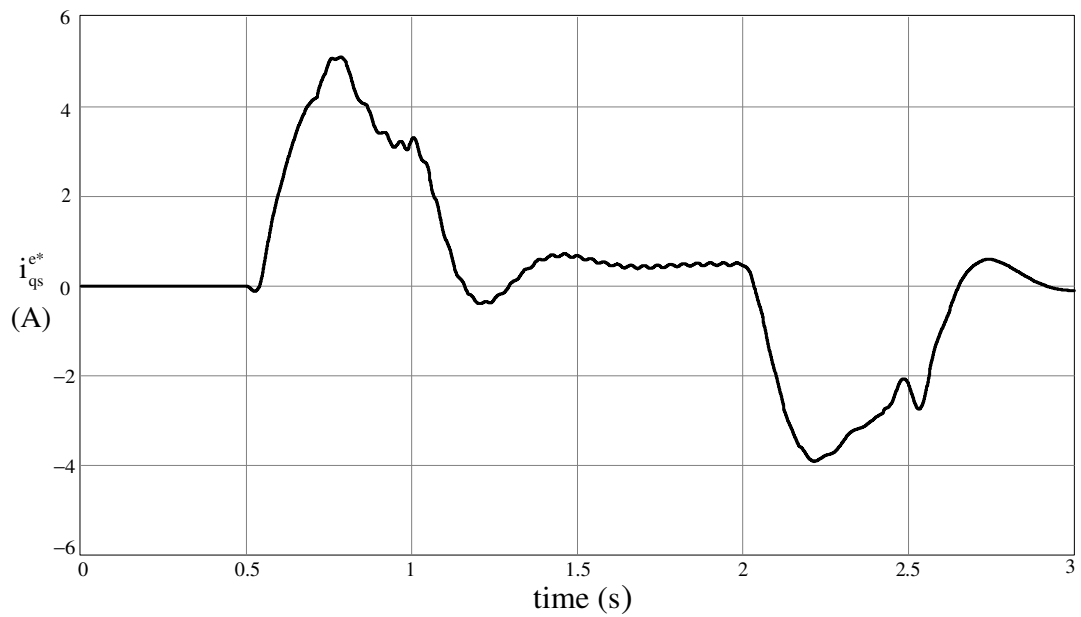
Figure 5.49 Synchronous frame torque axis current command (i_{qs}^{e*}) for trapezoidal 0 rpm to 500 rpm speed profile operation under no-load.

136
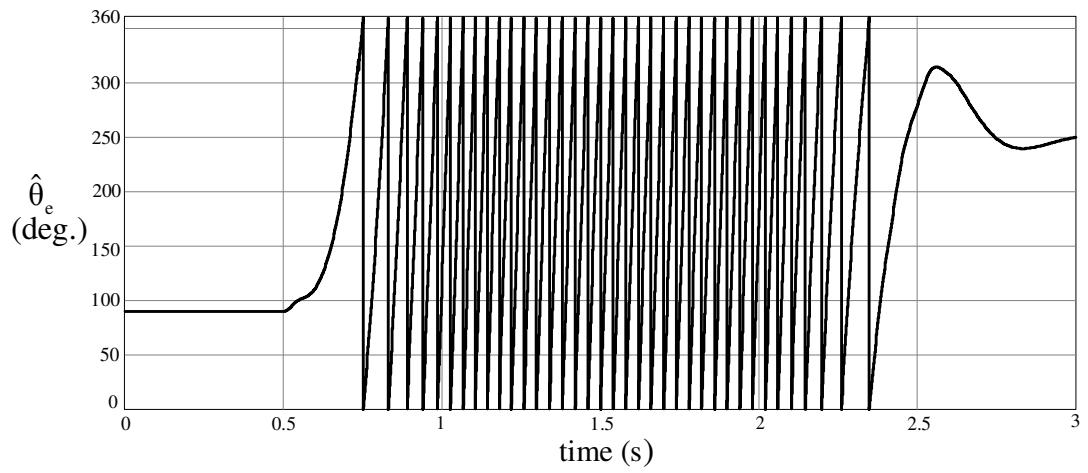
Figure 5.50 Estimated rotor flux angle for trapezoidal 0 rpm to 500 rpm speed profile operation under no-load.
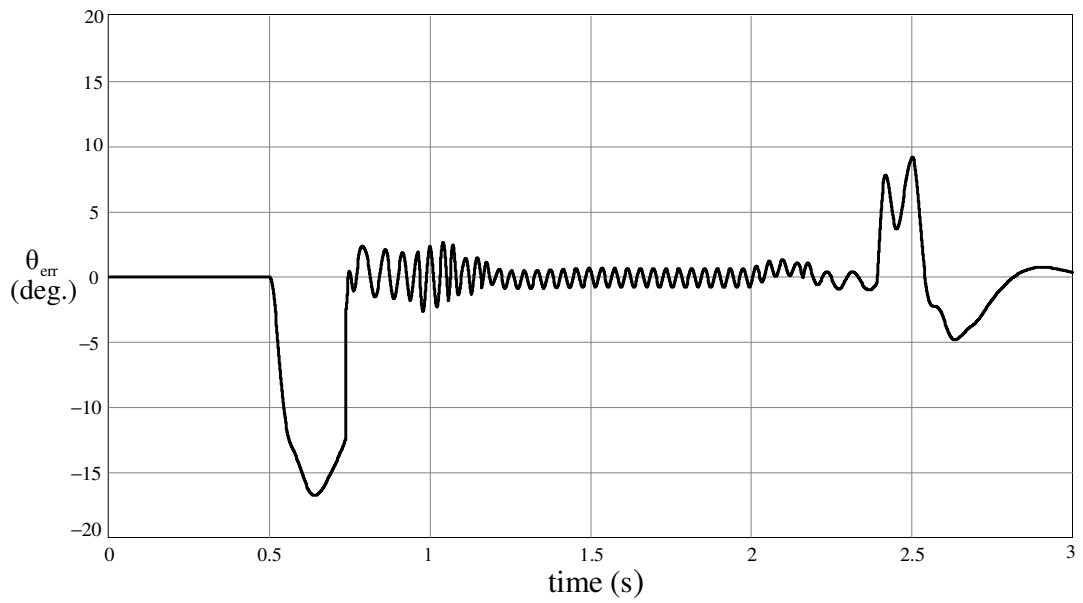
Figure 5.51 Estimation error of rotor flux angle for trapezoidal 0 rpm to 500 rpm speed profile operation under no-load.
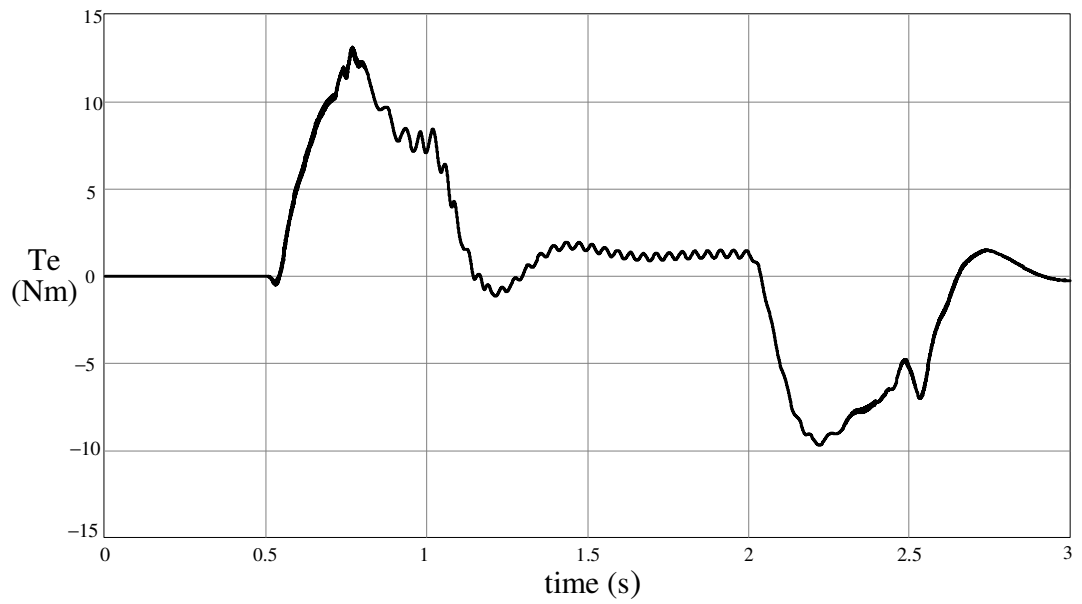
Figure 5.52 Electromagnetic torque output of the IPM motor for trapezoidal 0 rpm to 500 rpm speed profile operation under no-load.
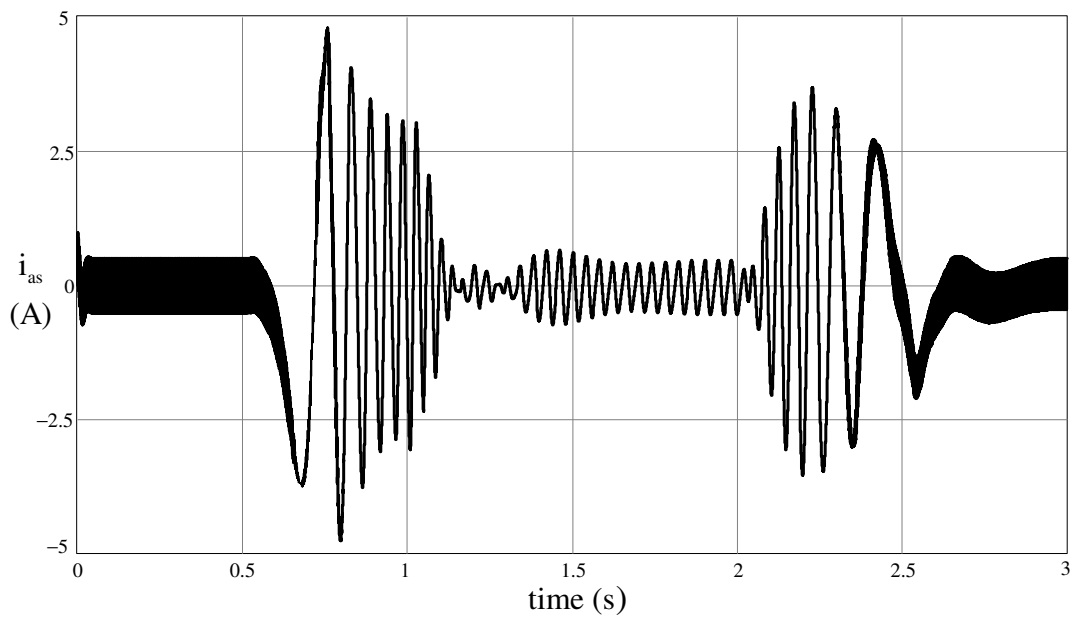
Figure 5.53 Phase-a current waveform for trapezoidal 0 rpm to 500 rpm speed profile operation under no-load.

138
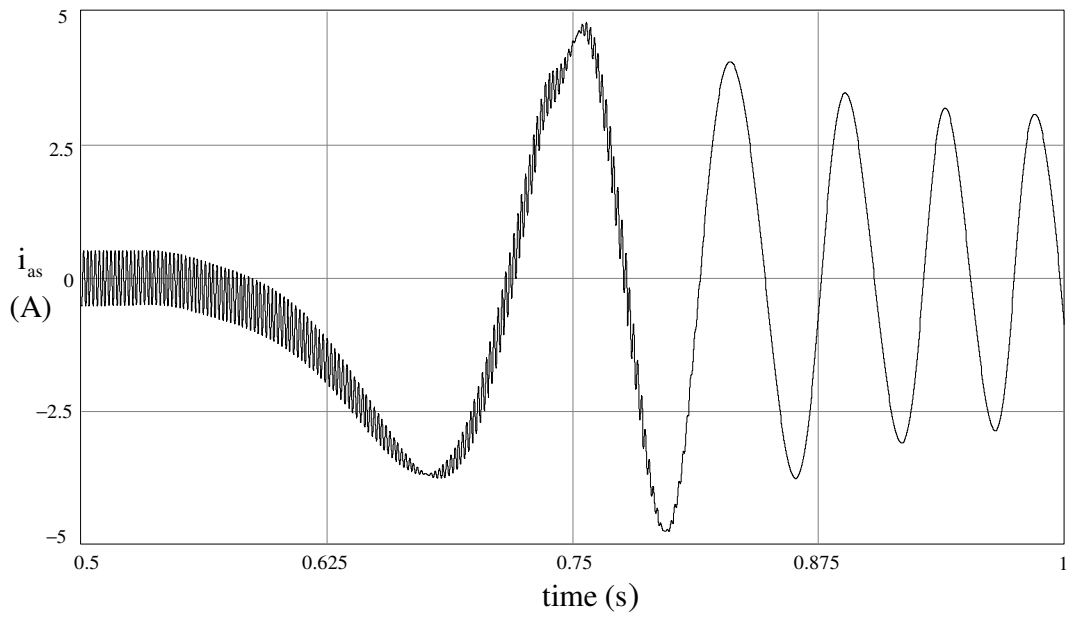
Figure 5.54 Zoom of the phase-a current at transition stage during acceleration for trapezoidal 0 rpm to 500 rpm speed profile operation under no-load.
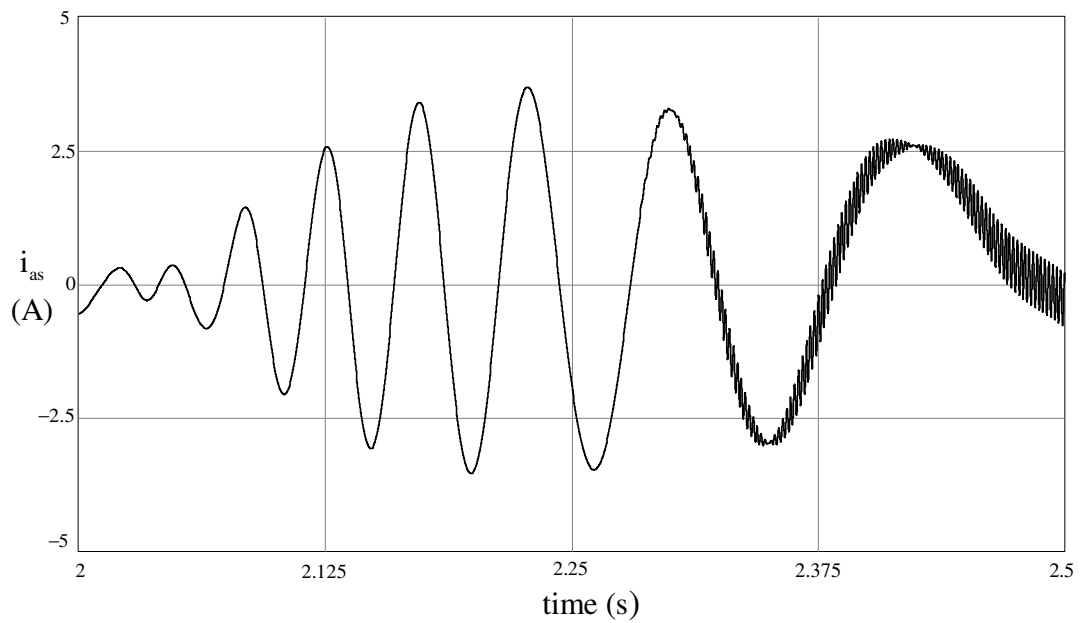
Figure 5.55 Zoom of the phase-a current at transition stage during deceleration for trapezoidal 0 rpm to 500 rpm speed profile operation under no-load.

139

5.4 Conclusion of The Simulation Results

Simulation of the sensorless control algorithms; the saliency based high frequency signal injection algorithm and the fundamental model based flux observer algorithm, and the hybrid algorithm are conducted with the SIMPLORER simulation tool.

The saliency of the IPM motor is provided by the saliency existing in the fundamental model of the IPM motor as different entries for L_d and L_q. Therefore, the high frequency characteristics and the non-linearities, which are encountered in practice, can not be modeled. However, the saliency of the model provided the simulation of the saliency based high frequency signal injection algorithm, such that he estimation error detection algorithm produces the admittance difference signal, which is proportional to the estimation error, based on the saliency of the IPM motor. The IPM motor is sensorless vector controlled based on the estimation of the rotor flux angle and the sensorless speed control is provided via the speed estimation of the high frequency signal injection algorithm. The performance the synchronous frame current regulator is investigated by observing the commanded synchronous frame current commands, the synchronous frame current response, and the torque output. The torque ripple due the high frequency signal injection is investigated and found to be less than 3% of the average torque. The speed command feedforward method is investigated both for steady-state and transient and it is shown that with the use of the speed command feedforward method, the compensator within the tracker only reacts to small errors during the transient operation and pre-estimation for the rotor flux angle is provided by the speed command feedforward for the steady-state operation. The sensorless speed control performance based on the high frequency signal injection algorithm is investigated both for no-load and loaded operation, and it is shown that the sensorless control is provided even at zero speed under loaded conditions while estimating the rotor flux angle with an error of less than 15°.

The simulation of the fundamental model based flux observer algorithm is conducted for sensorless control at medium and high speed range. Sensorless speed control of

the IPM motor based on the flux observer is investigated both for no-load and loaded operation. The rotor flux angle is estimated with an error of less than 3° even under loaded conditions, since flux observer algorithm is based on the ideal (i.e. correct) motor parameters and the voltage source inverter is modeled as ideal. However, the flux observer algorithm is also simulated with parameter errors and non-ideal voltage source inverter in order to simulate the practical conditions as much as possible. The drift of the integration within the flux observer is shown for the case with parameter error, and it is shown that the drift compensation algorithm performs well in the presence of drift. The speed estimated by the derivative of the estimated rotor flux angle is shown to be accurate and the actual speed of the IPM motor tracks the speed command.

The hybrid method combining the two algorithms is simulated for the sensorless control of the IPM motor for the whole speed range. The transition from one algorithm to the other algorithm during the speed change is provided depending on the estimated speed. It is shown that seamless transition, without oscillation in the actual speed and with accurate estimation of the rotor flux angle, is realized based on the transition algorithms of the hybrid method.

The estimation and control algorithms of the simulation model, which are coded in the equation editor of the SIMPLORER, provided the convenience for experimental implementation of the algorithms on the DSP platform based on the C language. The experimental results of the sensorless control algorithms are given in the next chapter.

CHAPTER 6

EXPERIMENTAL RESULTS OF THE SENSORLESS CONTROL ALGORITHMS

6.1 Experimental Setup

For the purpose of conducting the laboratory experiments, a two-level three-phase voltage source inverter and a motor test bench are built at METU, Electrical and Electronics Engineering Department, in the Electrical Machines and Power Electronics Laboratory. The experimental system diagram is illustrated in Figure 6.1. The AC line voltage is fed to the drive through a three-phase variable transformer in order to control the DC-link voltage of the inverter and also avoid inrush currents (there is no pre-charge circuit in the drive). A three-phase circuit breaker is connected for system protection. This circuit-breaker also allows interrupting the input voltage of the rectifier manually. In the experimental setup, the three-phase AC input voltage is rectified by a Semikron SKD30/12 diode bridge rectifier which has a voltage rating of 1200 Volts and a current rating of 30 Amperes. Between the rectifier and the DC link, a 20 A semiconductor fast fuse is inserted for system protection. The rectified DC voltage is filtered via two series connected 2200 µF electrolytic capacitors, with 450 V voltage rating. In order to discharge the DC-link capacitors when system is shut down, and also to provide voltage balancing among the series connected capacitors, a 30 kΩ discharging resistor with 10W power ratings is connected in parallel to each capacitor.
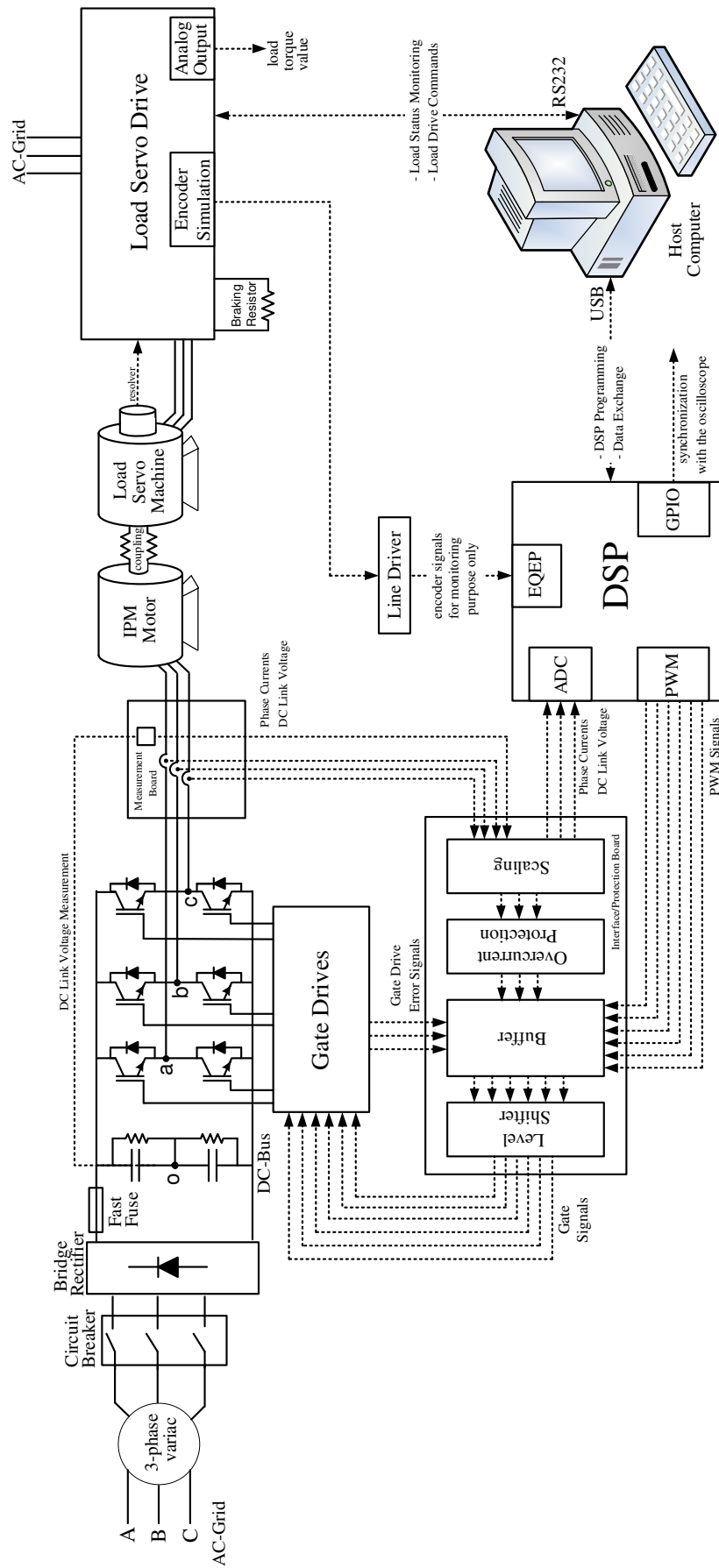
Figure 6.1 Experimental drive system hardware and the control diagram.

The VSI is built from three Semikron SKM75GB123D dual-pack IGBT modules. The voltage and the current ratings of the IGBT modules are 1200 V and 75 A respectively. The current rating is selected far higher then the rated current of the system and the motor, used in the experiments, in order to minimize the risk of burn out of the IGBT switches. Semikron Skyper 32 Pro gate-drive modules are utilized to drive the IGBT switches. These gate drive modules have internal overcurrent protection such that they generate a fault signal when the collector-emitter voltage (V_{CE}) of the IGBT is too high in conduction state (In IGBT switches when a high current is flowing, the V_{CE} of the corresponding switch rises, so called the desaturation or desat condition). The gate resistor value is 22 Ω which corresponds to approximate rise and fall times of 200 ns. In order to measure the output phase currents and the DC Link voltage level, the LEM LA25 P/SP1 current transducers and the LEM LV25-P voltage transducer are utilized in the measurement board. The phase currents and DC link voltage signals from the measurement board are fed to the interface/protection board for the purpose of scaling of these signals to appropriate levels (0V/3V) for the Analog to Digital Converter (ADC) of the Digital Signal Processor (DSP), which uses these signals as feedback for the control algorithms. The scaled phase current signals are also utilized for additional overcurrent protection in the interface/protection board, such that when any of the phase currents goes over a limit value, an error signal is fed to the hardware buffer on the interface/protection board. The overcurrent limit value is adjustable with potentiometers on the interface/protection board. Error signals from the overcurrent protection circuitry or from the gate drives disable the hardware buffer, which transfers the PWM signals from the DSP to the level shifter circuitry. When an error occurs, the output of the buffer is disabled; hence the "0" logic is applied to all top and bottom switches of the inverter legs to disable the VSI for protection. The level shifter circuitry converts the PWM digital logic signals (0V/3.3V) of the DSP to the signals compatible for the gate drive inputs (0V/15V). In the experimental set-up, for the control of the IPM motor via the VSI, the eZdsp F2808 starter kit [61] is utilized, which includes a Texas Instruments TMS320F2808 fixed-point DSP with peripheral units such as ADC, Enhanced PWM (EPWM), Enhanced Quadrature Encoder Pulse (EQEP), General Purpose Input Output (GPIO).

The required PWM pulse patterns are generated using the F2808DSP, and the PWM frequency is set to 5 kHz where control algorithms are executed with double update, i.e. with 10 kHz sampling frequency. DC Bus voltage is held around 500Volts, however DC link voltage is measured continuously by the DSP and ripples are taken into account within the control algorithms. There is a deadtime of 3.8 µseconds, which is generated within the EPWM module of the DSP and the effect of the deadtime is compensated by a standard deadtime compensation method (modification of duty cycle depending on the current direction), which is discussed in the following section.

The F2808 DSP is programmed via its software Code Composer Studio [62] using C Language through the host computer, which is connected to the DSP via its USB port. Commands for the control algorithm are entered through the watch window of the Code Composer Studio. On-line visualization of selected variables in the running code is possible using the graph window. Logging of variables in the memory of the DSP and then downloading them to the PC via Code Composer Studio software is used for experiment results. Since the memory of the DSP is limited, data stored in the DSP is limited but it is adequate for the experiments. For instance, values for two variables can be stored for 5 seconds with 100 Hz sampling rate. The stored data in the memory of the DSP is downloaded to the host computer and the experimental results are analyzed and graphed by the MATLAB Software [63], which is represented in the following sections. Also, a digital output from the GPIO port of the DSP is utilized during the experiments, for synchronization of the data logged within the DSP and the oscilloscope, which is used for phase current and load torque observation and logging, by triggering the oscilloscope at the same time of the logging within the DSP.

A servo system manufacture of Kollmorgen is used as load machine in the motor test bench. 3.6 kW, 3600 rpm, 10 Nm Kollmorgen surface mount permanent magnet servo motor AKM54N with resolver feedback and integrated mechanical fail-safe brake; and its inverter drive S620 along with a 1200W external braking resistor (dynamic brake) provide the necessary load torque. Since it is a sensored servo

system, it has the capability of producing the commanded torque with high performance. Additionally, speed and position control capability of the load servo system is sometimes utilized to rotate the IPM motor externally. The commands for the load servo drive are given through the RS232 interface of the S620 unit via the user interface software of the Kollmorgen drive and the status of the S620 is observed via the same software on the host computer. The actual load current (i.e. load torque) value within the load servo drive S620 is supplied from its analog output interface. This analog load torque value is observed and logged on the oscilloscope during the experiments. Additionally, the S620 provides the angular position of the load servo machine, which is obtained from the resolver, as converted to differential incremental encoder signals with index (zero position); and the encoder signals are used as the actual position information of the IPM motor for monitoring purposes. The encoder output of S620 is set to be 1024 lines/rev. Incremental encoder's differential signals are adapted to the DSP with a line driver board, which converts the differential encoder signals (+15V/-15V) to the single ended signals (0V/3.3V). The encoder signals are captured by EQEP (Enhanced Quadrature Encoder Pulse) module of the F2808 DSP board [64]. The actual position of the IPM motor is provided by this encoder feedback in order to verify the rotor flux angle estimation algorithms and the speed of the IPM motor is calculated via taking the derivative of the encoder position signals in order to verify the rotor speed estimation algorithms. The derivative of the encoder position signals is taken with 1 kHz sampling frequency and a moving average algorithm is utilized to filter the noise due to digital derivative. As a result, the resolution for the calculated speed is around 1.5 rpm and the bandwidth is 100 Hz, which is adequate for verification of the speed estimation and sensorless speed control algorithms. A picture of the experiment setup is given in Figure 6.2.
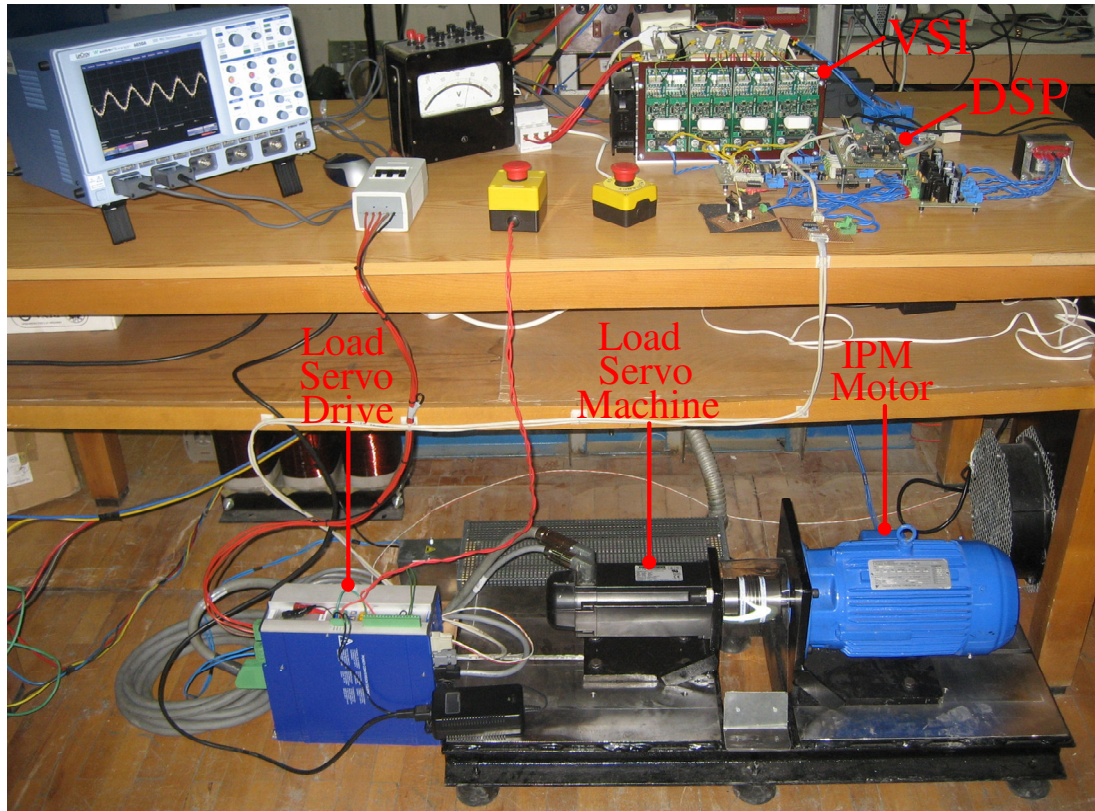
Figure 6.2 Laboratory experimental setup.

6.1.1 PWM Signal Generation and Dead-Time Compensation

In the experimental setup, the PWM signals are generated by the EPWM unit of the Texas Instruments TMS320F2808 fixed-point DSP chip which has an on chip digital hardware PWM module with flexible programmability. During this process instead of the direct voltage vector PWM implementation, the scalar PWM implementation approach is utilized such that the PWM pulses are generated by comparing a reference signal with a triangular carrier signal. The PWM signals are generated by the enhanced PWM (EPWM) unit of the 2808 DSP [65]. The EPWM unit includes an internal counter which corresponds to the triangular carrier signal for comparison with the reference. The carrier signal counts up and down; and both when the carrier signal reaches zero (underflow) or the full value (period) an interrupt is given (double update). When the interrupt is given, the duty cycles of the phase switch signals are calculated. The analog phase current measurements by the LEM LA25

P/SP1 current transducers are converted to digital signals by the A/D converter of the eZdsp F2808 starter kit. With the phase current measurements, the polarity information of the phase currents are obtained and this polarity information is considered in the compensation of the effects of the dead-time. According to the polarities of the phase currents, the calculated duty cycles of the phase switch signals (i.e. the output of the control algorithms) are modified for each half of the PWM triangular carrier signal period. After the calculation of the duty signals of the phase switch signals, the comparator registers of the EPWM are set accordingly to give the defined pulse pattern of the selected PWM method. Experimental results for the effect of the deadtime on the phase current waveform and the Fast Fourier Transform (FFT) of the phase current showing its harmonic content are shown in Figure 6.3 and the results of the deadtime compensation method are shown in Figure 6.4. In this experiment, VSI is utilized to drive an induction machine with sinusoidal voltage with constant peak magnitude of 60 V at 10 Hz.
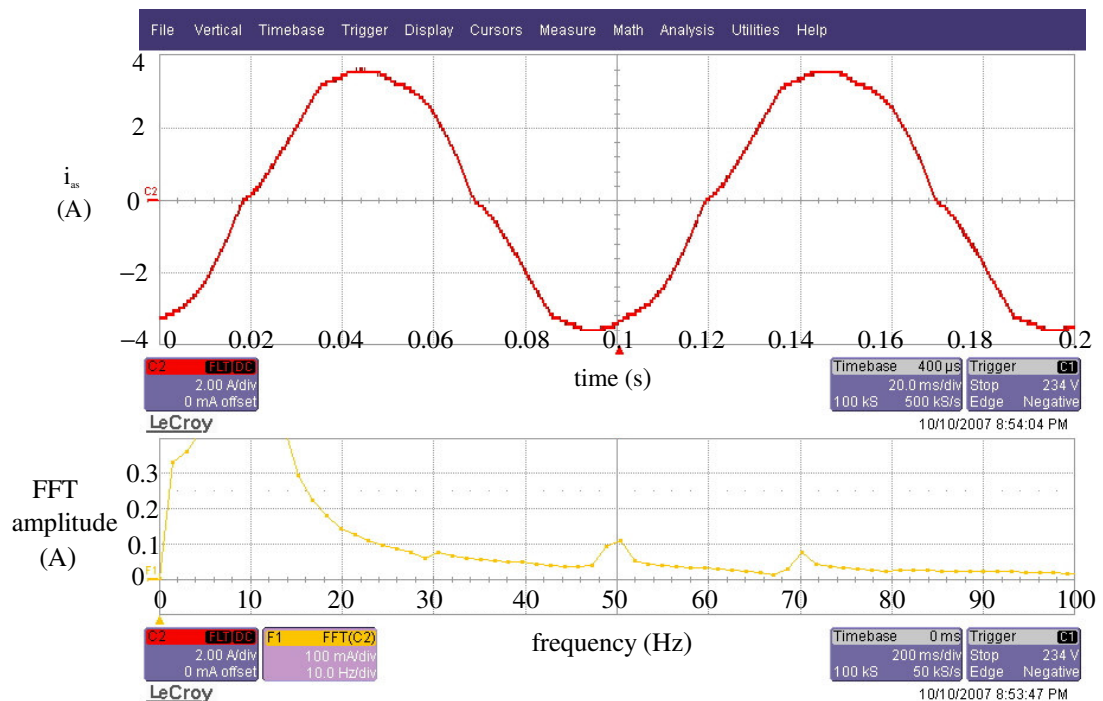
Figure 6.3 The phase current waveform (red) and the FFT of the phase current (yellow) without dead-time compensation.
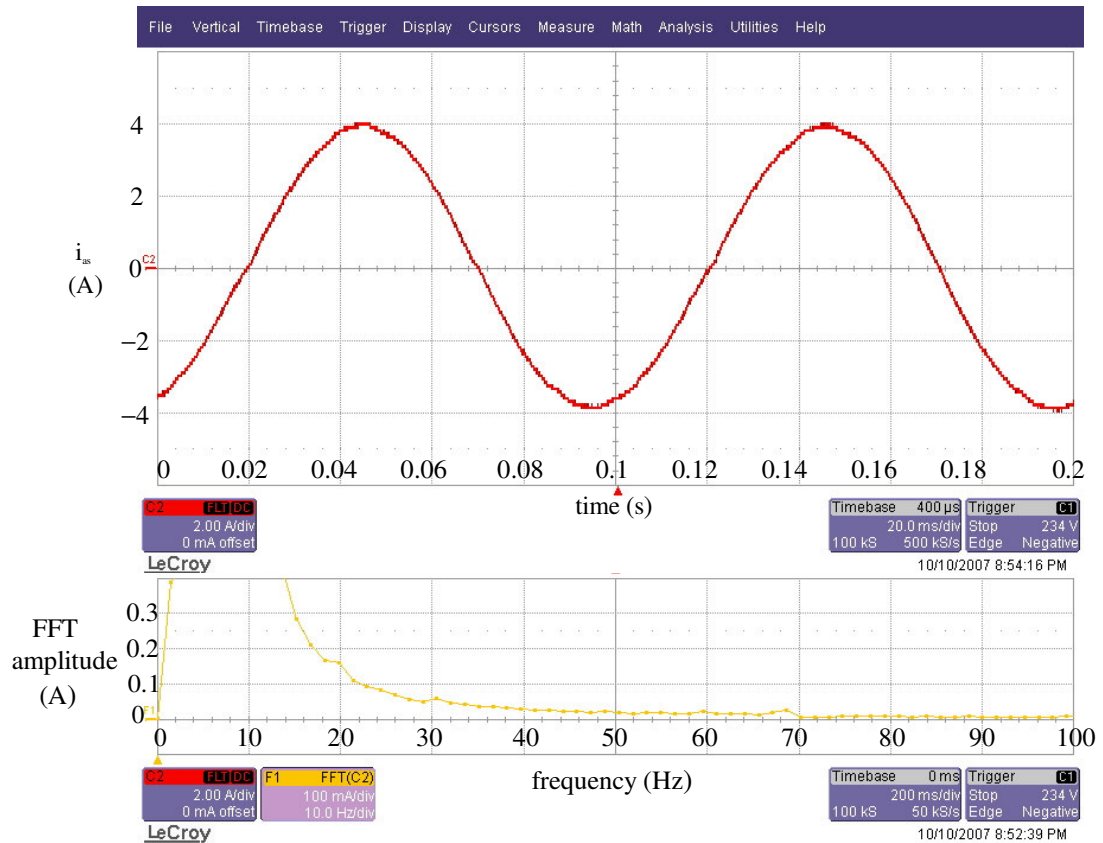
Figure 6.4 The phase current waveform (red) and the FFT of the phase current (yellow) with dead-time compensation.

Due to the dead-time, output voltage of the VSI can not be constructed as a pure sinusoidal and 6xn±1 (n=1, 2…) harmonics of the fundamental frequency exist in the output voltage; hence in the phase current. As observed in Figure 6.3, there exists fifth and seventh harmonics which correspond to 50Hz and 70Hz for 10Hz fundamental frequency. However, the effect of dead-time is compensated by the dead-time compensation algorithm and almost pure sinusoidal phase current waveform without the fifth and seventh harmonics is obtained as shown in Figure 6.4. The dead-time compensation method is vital especially for the low speed operating range as the applied voltages are small and the dead-time results in significant deviation of the output voltages from the commanded values.

6.1.2 Voltage Source Inverter Output Voltage Characteristics

For both the flux observer and high frequency signal injection algorithms, deterministic system characteristics become very important. Linearity of the VSI, which is one of the most critical elements of the real plant, is considered in detail because the phase voltages applied to the motor terminals are not measured directly; instead they are calculated based on the DC Link voltage measurement and the reference voltages. Reference voltages can not be constructed exactly by the VSI due to the non-linearity of the VSI. Although the dead-time effect is almost compensated by the dead-time compensation method, still there can be problems around the zero crossing of the phase currents since detection of the polarity of the current at zero crossing can be difficult due to the PWM ripple and noise. Moreover, the nonlinearity due to the IGBT voltage drops, measurement error, etc. exist within the VSI. In order to investigate the voltage linearity of the VSI, an induction machine in the laboratory is driven open loop via V/f method and the relation between the referenced peak voltage magnitude and the peak value output voltages are plotted in Figure 6.5, in conjunction with the ideal voltage source characteristics.
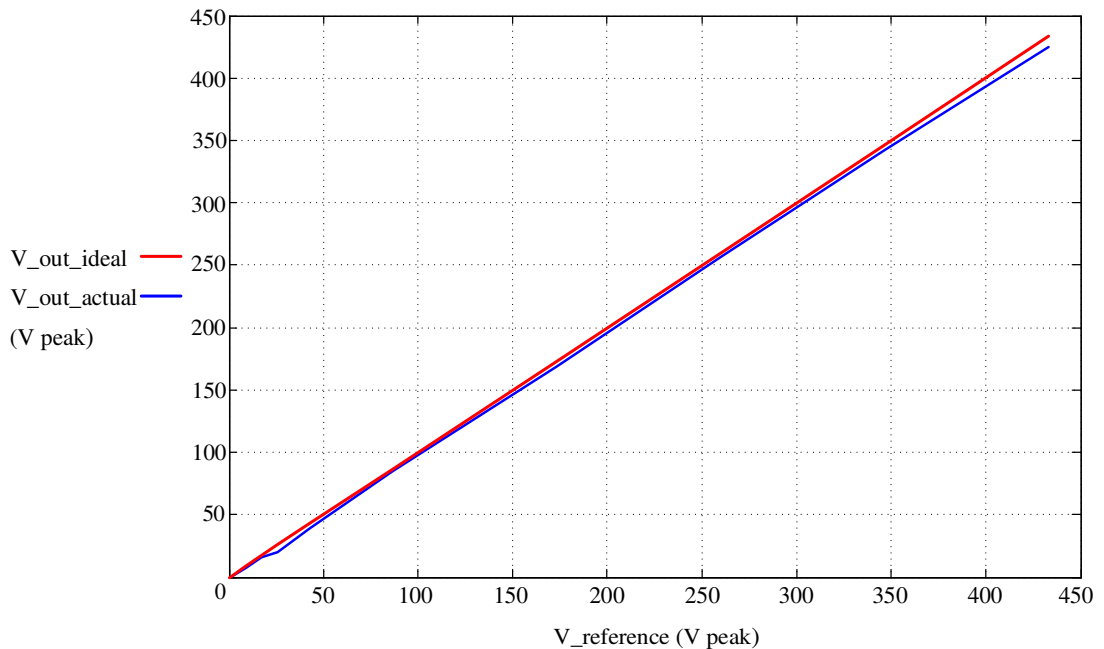
Figure 6.5 Voltage source inverter linearity characteristics - the ideal output voltage (red), the actual output voltage (blue) versus reference voltage.

Although the output voltage characteristics of the VSI seem to be satisfactory, in order to improve the response, compensation of the loss and nonlinearity should be accomplished. This issue is very important for the flux observer algorithm, especially at medium speed range, because reference voltages are taken as the input values for the model. However, the high frequency signal injection algorithm is less sensitive to the voltage source inverter nonlinearity, because the difference between the current response on the measurement axes is observed, and same voltage is applied on both measurement axes even the actual voltage is not realized exactly as commanded.

6.2 Experimental Results of The High Frequency Signal Injection Algorithm

The saliency based high frequency signal injection algorithm is utilized for sensorless vector control at zero and low speed region, and speed and position of the IPM motor is closed loop controlled based on the speed and position estimation of the control high frequency signal injection algorithm. In section 6.2.1, the saliency of the IPM motor and the effect of the injection voltage and frequency level are investigated experimentally. The saliency of the IPM motor is shown and optimum values for the injection voltage magnitude and frequency are determined via tests on the IPM motor. In section 6.2.2, the utilization of the saliency for estimation error detection is observed and the steady-state performance of the estimation error detection algorithm is analyzed. In section 6.2.3, the dynamical analysis of the estimation error detection algorithm is performed via creating dynamic estimation errors externally and observing the admittance difference output of the estimation error detection algorithm. In section 6.2.4, step response and steady-state performance of the rotor flux angle tracking algorithm is investigated by starting the high frequency signal injection algorithm with initial estimation error. In section 6.2.5 dynamic analysis for the rotor flux angle tracker is performed via rotating the IPM motor dynamically and observing the rotor flux angle estimation. In sections 6.2.6 to 6.2.11, sensorless motion control of the IPM motor is performed for various operations and load conditions. The rotor flux angle is tracked by the tracker and also the speed of the motor is estimated within the tracker. For the speed and position

151

control experiments, the control diagram in Figure 4.31 is realized; i.e. the rotor flux angle, motor speed, and motor position feedback are estimated by the high frequency signal injection algorithm and motor is closed loop sensorless controlled. Additionally, in section 6.2.9, the speed command feedforward method is investigated for heavy loading (external braking) operation. The parameters used within the experimental implementation of the high frequency signal injection algorithm are given in Table 6.1.

Table 6.1 Parameters used within the high frequency signal injection experiments

Synchronous Frame Current Regulator	K_p	7.5
	K_I	930
	LPF on the feedback path	2nd order with 100 Hz cut-off frequency
High Frequency Signal Injection Algorithm	Injection Frequency	500 Hz
	Injection Voltage	75 V
	BPF	4th order wide band-pass with 100 Hz low cut-off and 2500 Hz high cut-off frequencies
	LPF within the heterodyning	2nd order with 20 Hz cut-off frequency
	K_P of the compensator	2000
	K_I of the compensator	100
Speed Controller	K_{pr}	0.5
	K_p	0.012
	K_I	0.2
Position Controller	K_p	20

6.2.1 Saliency Characterization of The IPM Motor

The saliency of the IPM motor can be observed as impedance difference seen from the stator side with respect to the rotor angle. In Figure 6.6, investigation of the saliency of the IPM motor is accomplished, similar to the simulation analysis in Figure 4.4. Only high frequency voltages (without any fundamental excitation) are applied experimentally to phase-a of the IPM motor for three different rotor angles; when the rotor is stationary with $\theta_e=0°$, $\theta_e=45°$, and $\theta_e=90°$. The frequency of the injection voltage is 500 Hz and the magnitude is 75 V peak.

In Figure 6.6, when $\theta_e=0°$, magnetic axis of phase-a coincides with the qe-axis (Figure 3.3) and injection is made to the qe-axis, which has the highest impedance; hence the induced current has the lowest magnitude for $\theta_e=0°$. When $\theta_e=90°$, magnetic axis of phase-a coincides with the de-axis (rotor permanent magnet flux) and injection is made to the de-axis, which has the lowest impedance; hence the induced current has the highest magnitude for $\theta_e=90°$.

The impedance values of the IPM motor in de and qe axes at high frequency (500 Hz) can be calculated from the current response in Figure 6.6. The impedance on the de-axis, when $\theta_e=90°$ in Figure 6.6, is found to be 136 Ω, which corresponds approximately to the reactance value of the inductance on de-axis ($L_d=46mH$) at 500 Hz. The impedance on the qe-axis, when $\theta_e=0°$ in Figure 6.6, is found to be 250 Ω, which corresponds to more than the reactance value of the inductance on qe-axis ($L_q=60mH$) at 500 Hz. The increase of the impedance on the qe-axis is due to the skin effect at high frequency. Thus, the saliency ratio of the IPM motor increases to 0.456, as given in Table 2.2, when high frequency signal injection is applied to the IPM motor, where its saliency ratio at the fundamental frequency is 0.23.
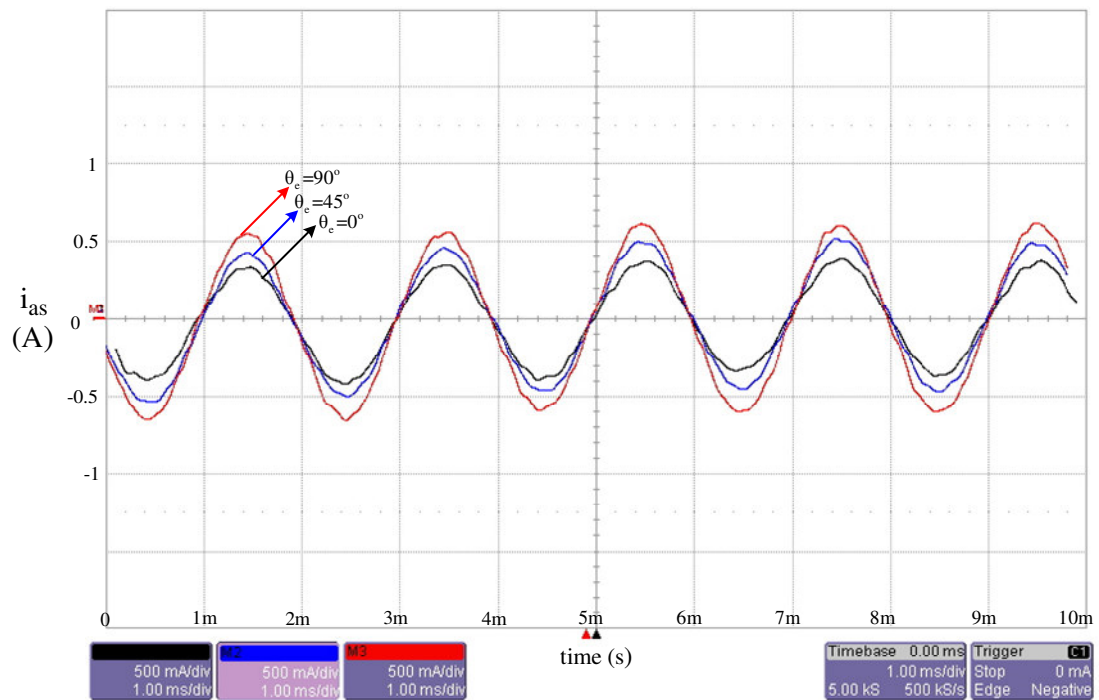
Figure 6.6 Induced high frequency phase-a currents for various rotor angles (ω_r=0 rpm, V_{inj}=75 V, f_{inj}=500 Hz).

The saliency of the IPM motor is also extracted by scanning the rotor with a high frequency voltage vector, i.e. high frequency voltage is applied on one pole of the IPM motor, as in Figure 4.2, when the motor is stalled. The frequency and the magnitude of the high frequency voltage are selected to be 500 Hz and 75 V, respectively. The magnitude of the high frequency current response of the IPM motor ($\left|i_{\hat{d}}^{hf}\right|$ in Figure 4.14) is recorded for every injection angle and the resultant curve for the magnitudes of the high frequency current response corresponding to the admittance characteristics of the IPM motor is drawn in Figure 6.7. The experimental admittance curve of the IPM motor is found to be almost identical with its theoretical curve in Figure 4.2.

154
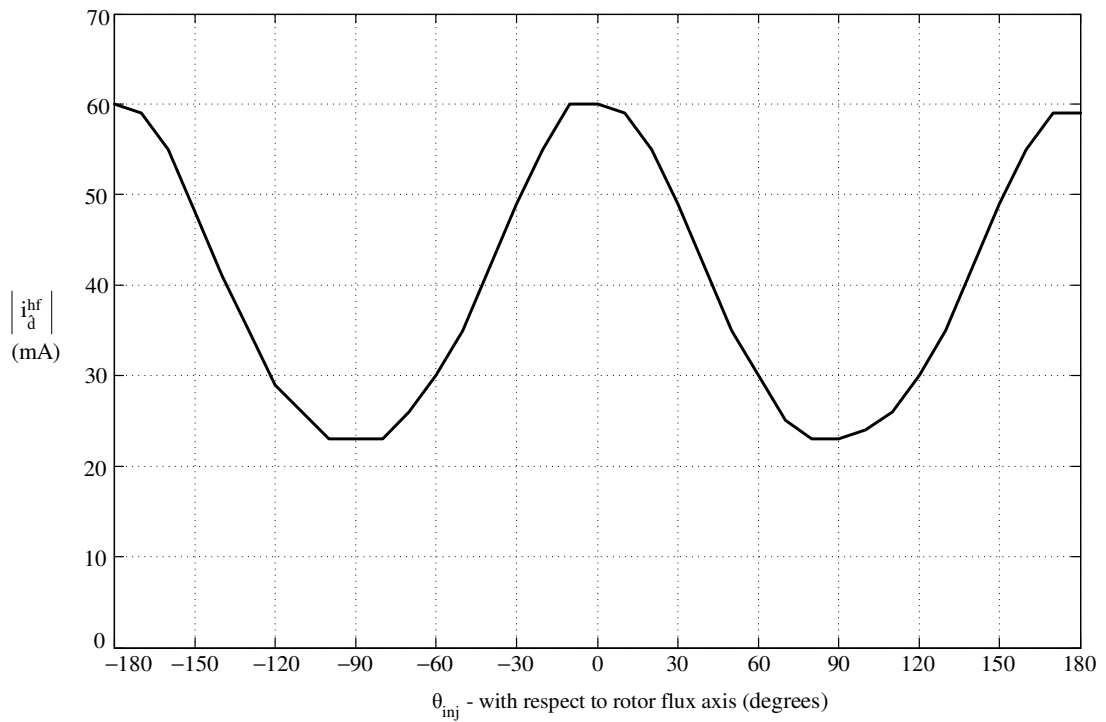
Figure 6.7 Spatial admittance (saliency) curve of the stalled IPM motor (ω_r=0 rpm, V_{inj}=75 V, f_{inj}=500 Hz).

In order to find the optimum injection voltage and frequency level, tests with different levels of injection voltage magnitude and frequency are performed on the IPM motor. High frequency responses of the IPM motor for different injection frequencies with constant injection voltage magnitude of 100 V are given in the Figure 6.8. In Figure 6.9, admittance curve of the IPM motor is drawn for various injection voltage levels, where the injection frequency is held constant at 500 Hz.
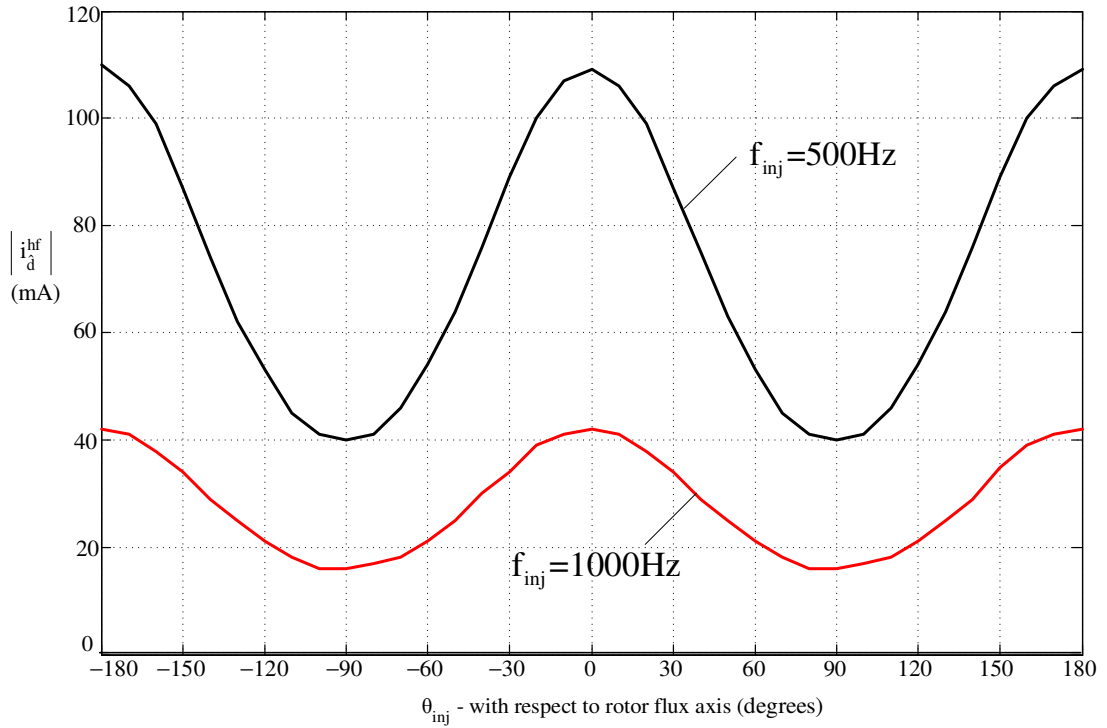
Figure 6.8 Saliency curve of the stalled IPM motor ($\omega_r=0$ rpm) with 100 V injection for 500 Hz injection frequency (black) and for 1000 Hz injection frequency (red).
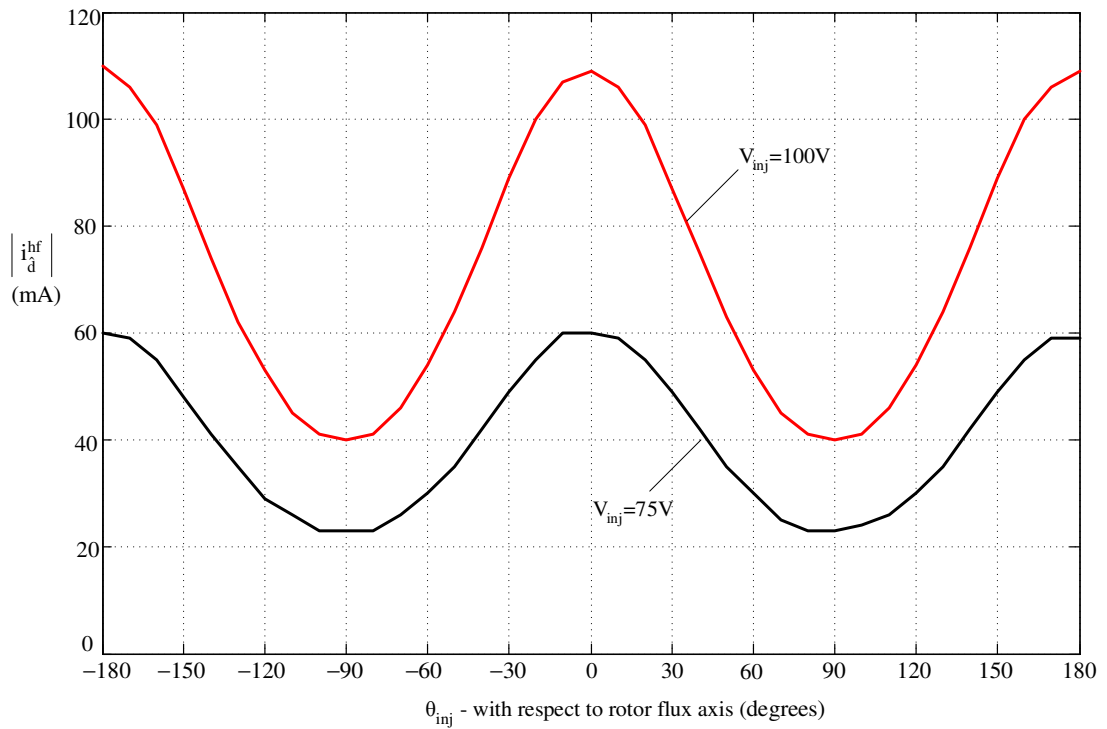
Figure 6.9 Saliency curve of the stalled IPM motor ($\omega_r=0$ rpm) with 500 Hz injection frequency for 75 V injection voltage (black) and for 100 V injection voltage (red).

The saliency curves of the IPM motor, while it is stalled and rotating with 50 rpm, are given in Figure 6.10.
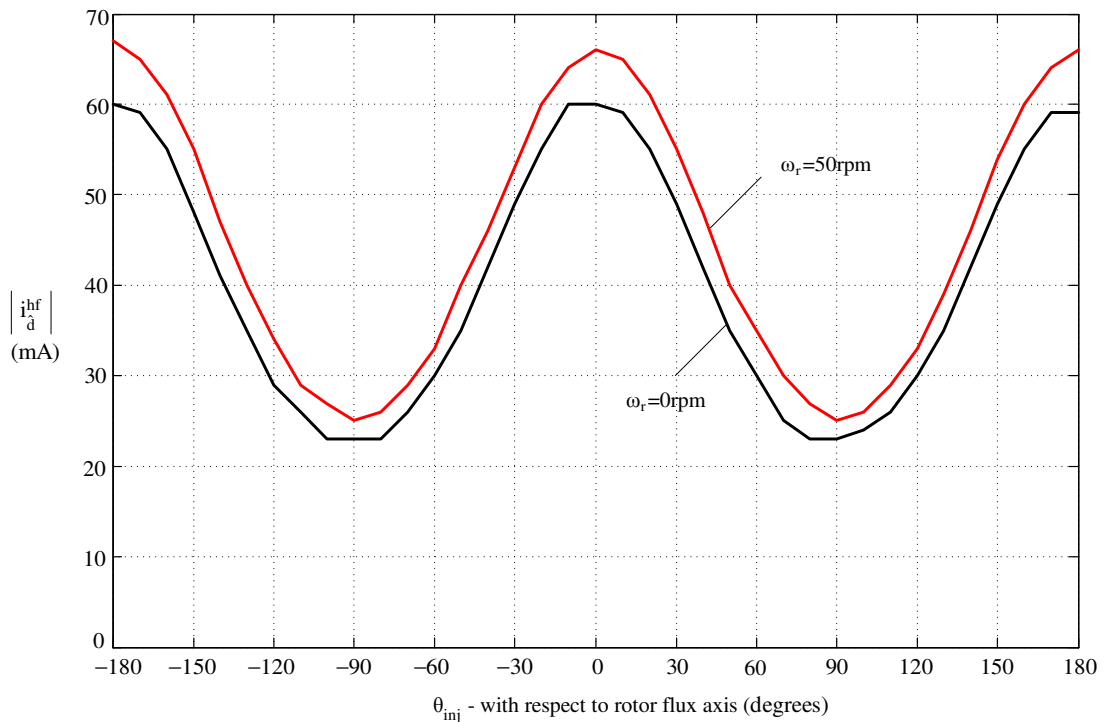
Figure 6.10 Spatial admittance (saliency) curve of the IPM motor with 75 V and 500 Hz injection signal for stalled rotor (black) and for the rotor at 50 rpm (red).

It is observed that the IPM motor has significant saliency characteristics, which can be used for the estimation purposes. The frequency of the injection is selected to be 500 Hz since more saliency is caught with this frequency and the injection voltage level is held at 75 V in order not to create significant high frequency current on the motor.

6.2.2 Estimation Error Detection

In order to detect the estimation error, high frequency pulsating voltage is applied to the estimated rotor flux axis in the synchronous frame. The high frequency response of the IPM motor includes information about the estimation error based on the

saliency of the IPM motor. As shown in Figure 4.14 and Figure 4.15; when there is an estimation error, a high frequency current component is observed on the estimated q-axis ($\hat{q}e$-axis), even the injection is made on the estimated d-axis ($\hat{d}e$-axis). The experimental analysis of this case is performed by observing the phase currents on the scope. In this case, the fundamental components of the current is held at zero by commanding $i^{e*}_{ds}=0$ and $i^{e*}_{qs}=0$; and only high frequency signal injection is made. The estimated rotor flux angle is forced (coded) to be zero ($\hat{\theta}_e = 0°$) in the control algorithm software in order to create estimation error via rotating the rotor externally. When the synchronous frame transformations are made with $\hat{\theta}_e = 0°$, the phase-a becomes equal to i^e_{qs}, which is the synchronous frame $\hat{q}e$-axis current. Therefore for $\hat{\theta}_e = 0°$, the current component on the $\hat{q}e$-axis can be observed on the phase-a, and the current component on the $\hat{d}e$-axis can be observed on the phase-b and phase-c. In order to observe the effect of saliency and the estimation error, first the motor is held at electrically zero angle ($\theta_e = 0°$), such that the estimation is correct. This case is given in the Figure 6.11. Since there is no estimation error, no high frequency current component is observed on the $\hat{q}e$-axis, which is phase-a in Figure 6.11. Then, an estimation error is created by rotating the motor externally to electrical 45°. In this case high frequency current is created on the $\hat{q}e$-axis, as in Figure 6.12.
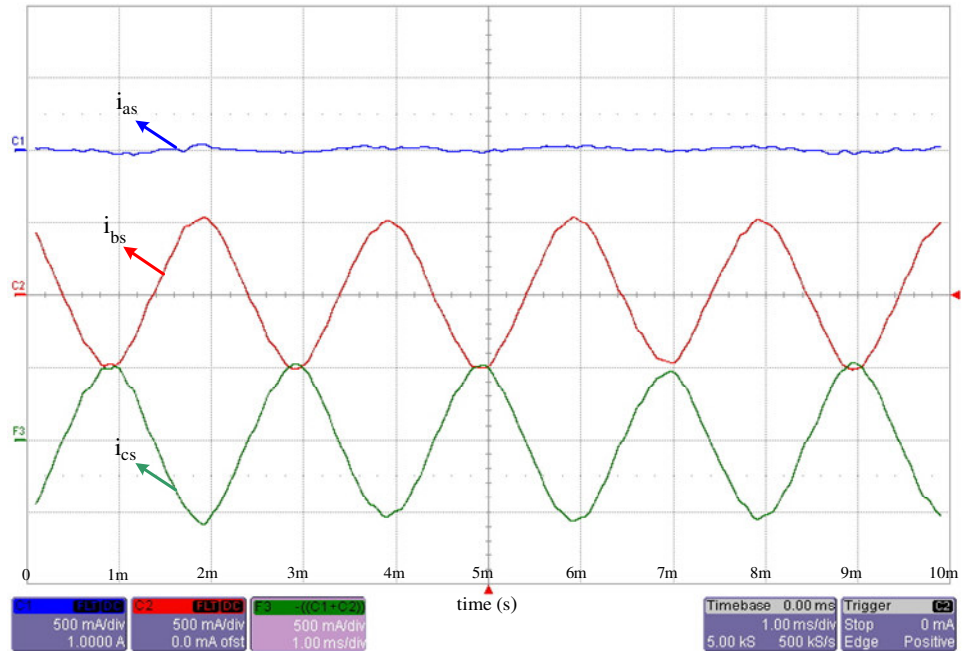
Figure 6.11 Phase-a (blue), phase-b (red) and phase-c (green) currents for correct estimation of rotor flux angle ($\hat{\theta}_e = 0°$, $\theta_e = 0°$, $\theta_{err} = 0°$, ω_r=0, V_{inj}=75 V, f_{inj}=500 Hz, vertical axis scale:500 mA/div).
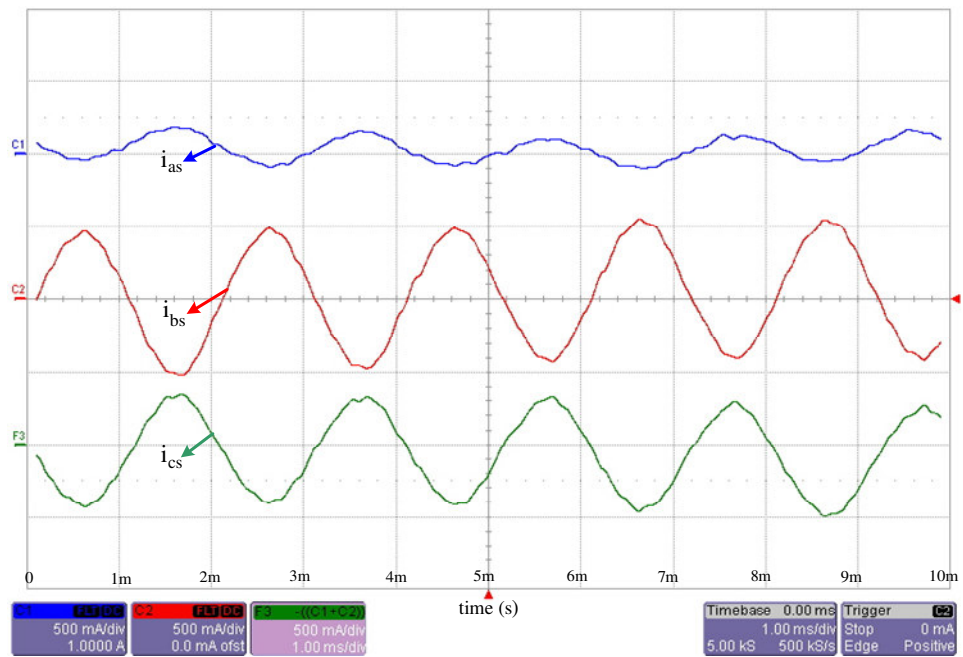
Figure 6.12 Phase-a (green), phase-b (red) and phase-c (yellow) currents for erroneous estimation of rotor flux angle ($\hat{\theta}_e = 0°$, $\theta_e = 45°$, $\theta_{err} = 45°$, ω_r=0, V_{inj}=75 V, f_{inj}=500 Hz, vertical axis scale:500mA/div).

159

In Figure 6.12 estimation error is positive ($\theta_e - \hat{\theta}_e = 45°$); hence the induced high frequency current deviates from the $\hat{d}e$-axis, as in Figure 6.13 similar to Figure 4.15. As a result of this deviation, magnitude of the phase-b current, which is negative of phase-a and phase-c currents, becomes larger than the magnitude of the phase-c current, as observed in Figure 6.12.
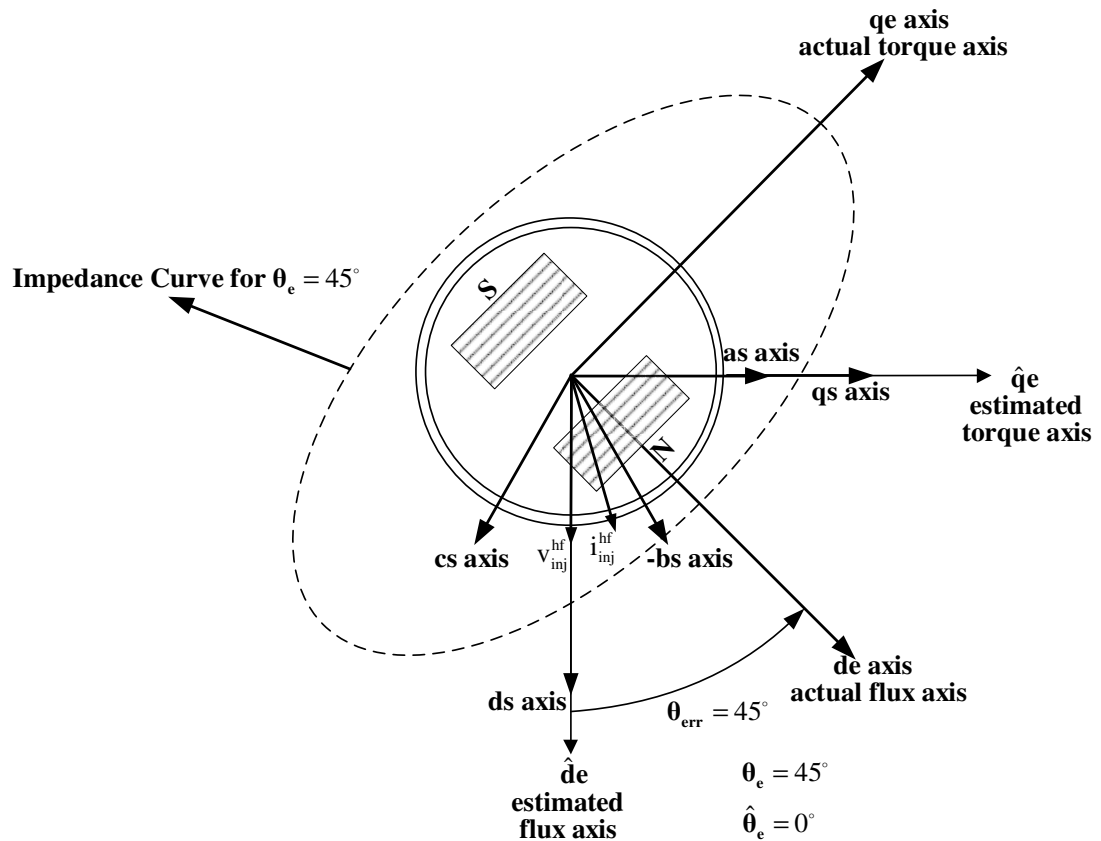
Figure 6.13 Synchronous and stationary frame axes for estimation error of 45°.

The estimation error is deduced from the induced high frequency current component on the $\hat{q}e$-axis, which is observed as the difference between the magnitudes of the current components on the measurement axes (Figure 4.18). The admittance error signal (Y_{Mdiff}), which is proportional to the estimation error is calculated by the band pass filtering and heterodyning algorithms as given in the block diagram of Figure 4.20. The experimental admittance difference signal is recorded for every estimation error angle and plotted with respect to the estimation error in Figure 6.14.
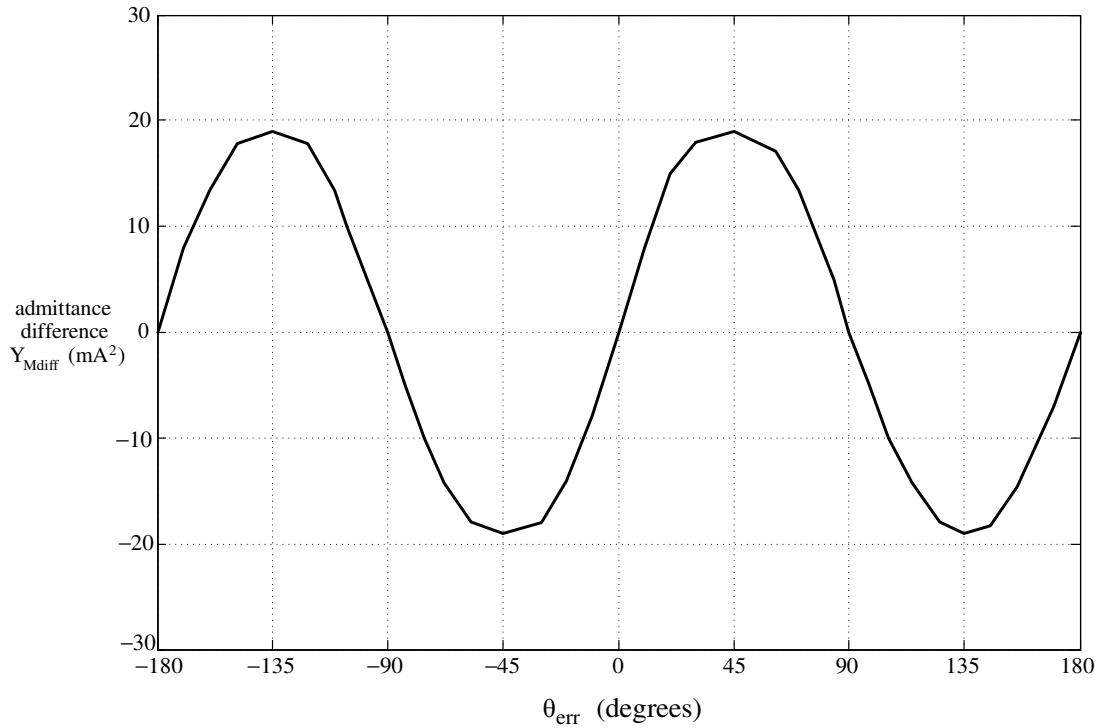
Figure 6.14 Admittance difference signal (Y_{Mdiff}) versus estimation error (θ_{err}).

As seen from in Figure 6.14, admittance difference is zero when the estimation is correct ($\theta_{err} = 0°$) and admittance difference signal is almost linearly proportional to the estimation error when error is less than 45°. When there is an estimation error, it is observed as the admittance difference signal; and it is expected that the tracker algorithm compensates for the error to converge to the actual rotor flux angle. The admittance difference signal becomes negative of the error when the error goes beyond 90°. Hence, if the error goes beyond 90°, pole skipping, which will be investigated in the following sections, occurs.

6.2.3 Dynamics of The Estimation Error Detection Algorithm

The estimation error detection algorithm is based on the band-pass filtering and heterodyning algorithms given in the block diagram of Figure 4.20. When there is an estimation error, it is observed as difference between the magnitudes of the currents

on the measurement axes. The rate of the change of the magnitudes of the currents on the measurement axes, hence the rate of the change of the admittance difference signal is dependent on the cut-off frequencies of the low-pass filters within the heterodyning algorithm, given in Figure 4.21. Hence, the dynamics of the estimation error detection algorithm is mostly dependent on the low-pass filters within the heterodyning algorithm. In this thesis, the low-pass filters of the heterodyning algorithm are designed as second order filters with 20 Hz cut-off frequencies. Hence, the estimation error detection algorithm is expected to response with a bandwidth of 20 Hz. Dynamics of the estimation error detection algorithm are investigated by creating estimation error artificially and observing the output (Y_{Mdiff}) of the estimation error detection algorithm. In Figures 6.15 and 6.16, the estimated rotor flux angle is forced (coded) to be zero ($\hat{\theta}_e = 0°$) in the control algorithm software in order to create estimation error via rotating the rotor externally. The IPM rotor is rotated externally around electrical $0°$ with magnitudes less than $45°$ via commanding sinusoidal position motion tasks to the load servo drive. Hence, estimation error is created with different frequencies.

As observed in Figures 6.15 and 6.16, the output of the estimation error detection algorithm (Y_{Mdiff}) is proportional to the estimation error since the error magnitude is always less than $45°$; however, there exists some delay when the estimation error changes with 6.25 Hz. It is expected that the estimation error detection algorithm can respond up to 20 Hz, however the error could not be created with such frequency. Nevertheless, it is observed that, the algorithm responds well up to 6 Hz. The dynamic performance of the estimation error detection algorithm is adequate for tracking the rotor flux angle with high performance. The tracker algorithm, which compensates for the error is investigated in the next section.
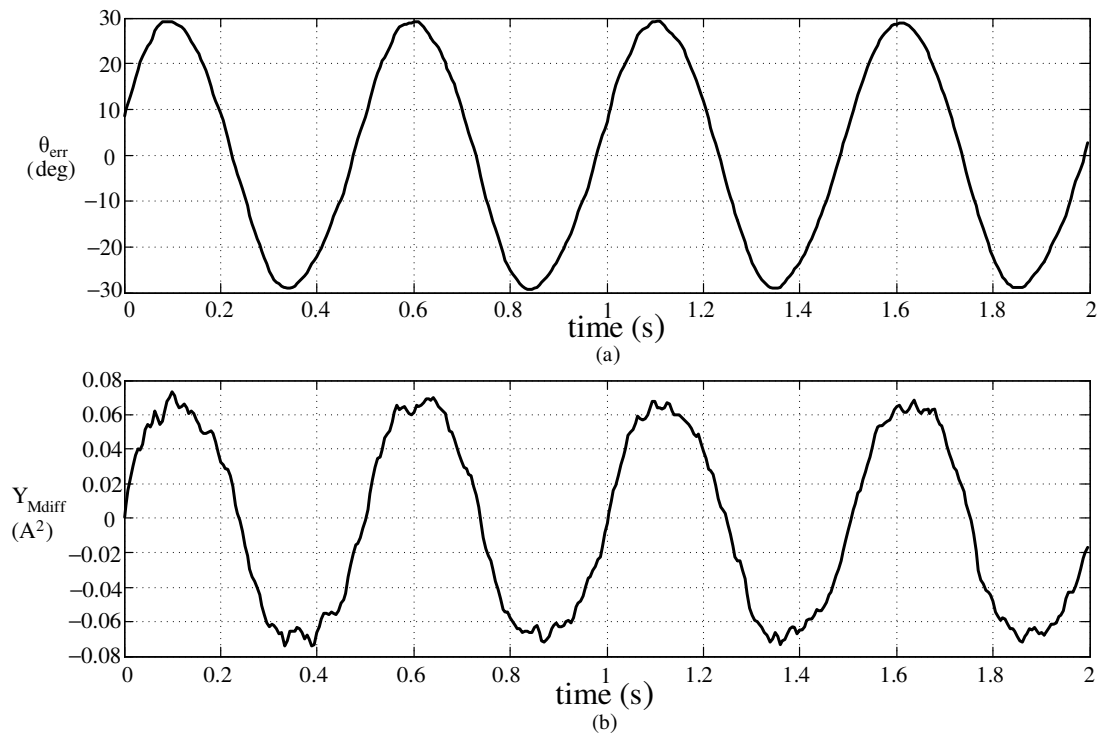
Figure 6.15 Estimation error at 2 Hz (a) and the output of the estimation error detection algorithm (Y_{Mdiff}) (b).
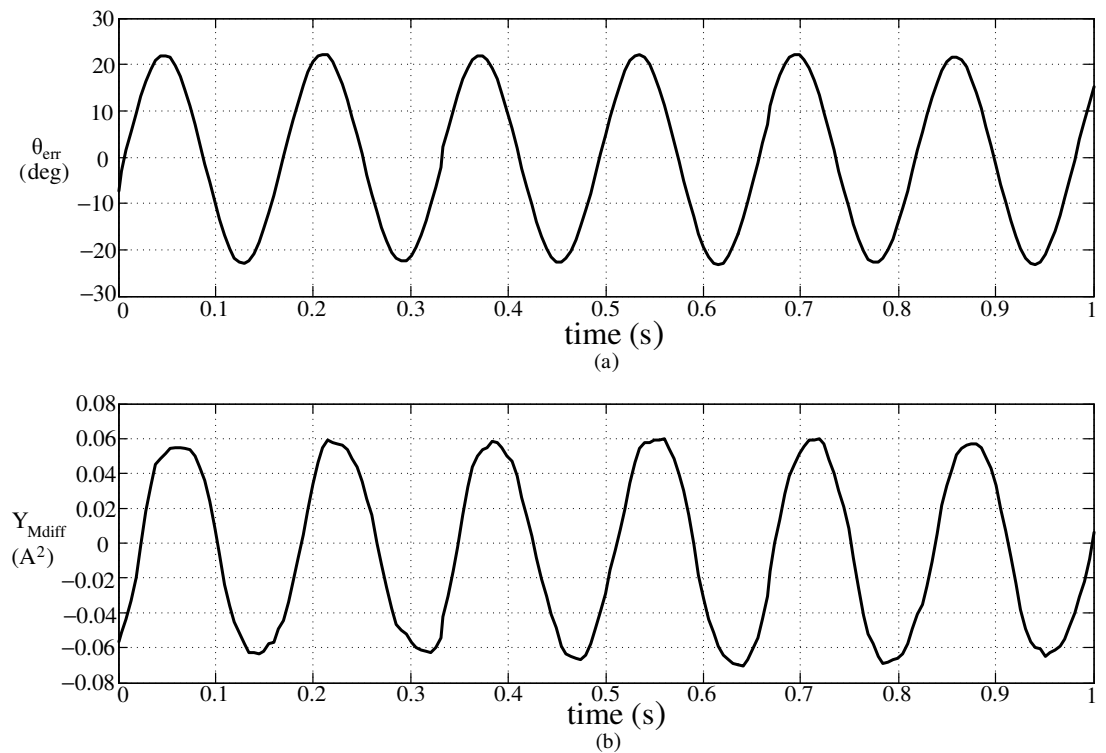
Figure 6.16 Estimation error at 6.25 Hz (a) and the output of the estimation error detection algorithm (Y_{Mdiff}) (b).

163

6.2.4 Compensation of The Estimation Error and Tracking The Rotor Flux Axis

The admittance difference signal, which is proportional to the estimation error, is fed to the tracker algorithm, which involves the compensator; and rotor flux angle calculated from the tracker is used for transformations of the closed loop vector control. When the estimation error is compensated, the estimated flux axis converges to the actual flux axis. In this section, the experimental results for the convergence of the tracker are shown for step estimation error and its steady-state performance is also investigated. The high frequency signal injection algorithm is started when there is estimation error of 45°and 90° in Figures 6.17 and 6.18, respectively; and it is illustrated that the tracker converges to the actual rotor flux angle in both cases. In Figures 6.17-6.19, the injection is also started at t=0. Therefore, the admittance difference signal is observed with a delay, and the step response includes both the step response of the estimation error detection algorithm and the step response of the tracker algorithm.
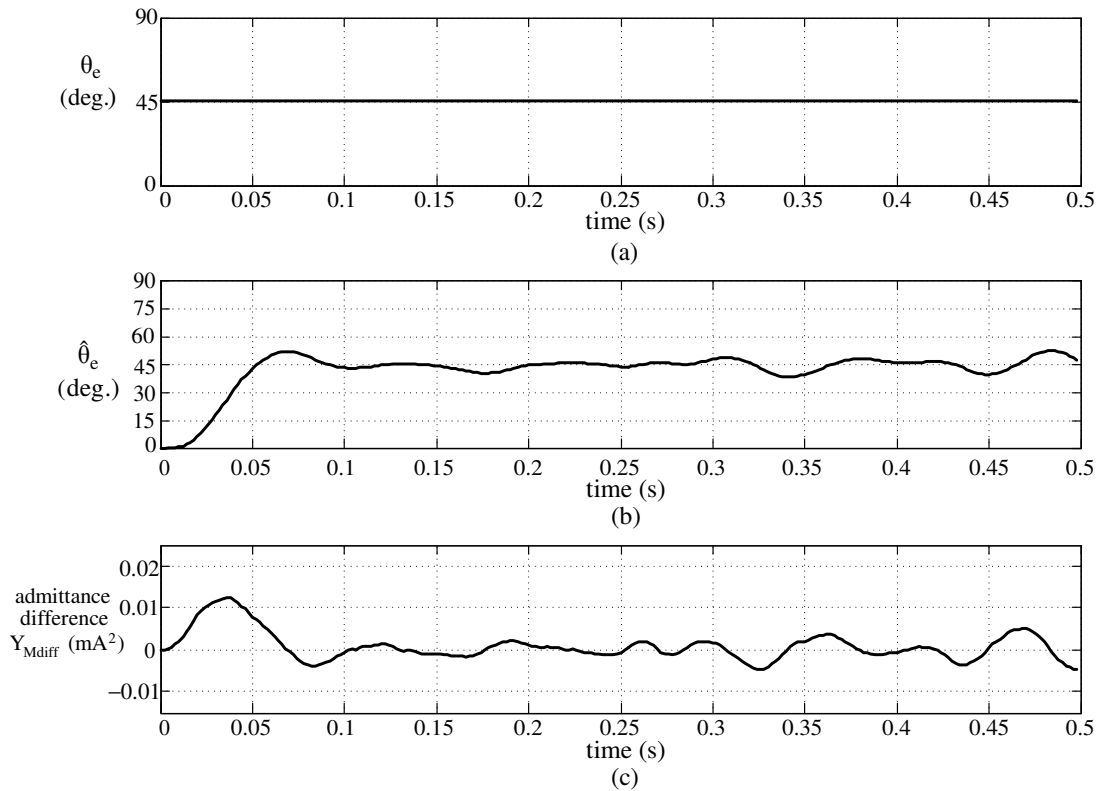
Figure 6.17 Convergence of the tracker with 45° estimation error input; actual rotor flux angle (a), estimated rotor flux angle (b), admittance difference signal (c).

164
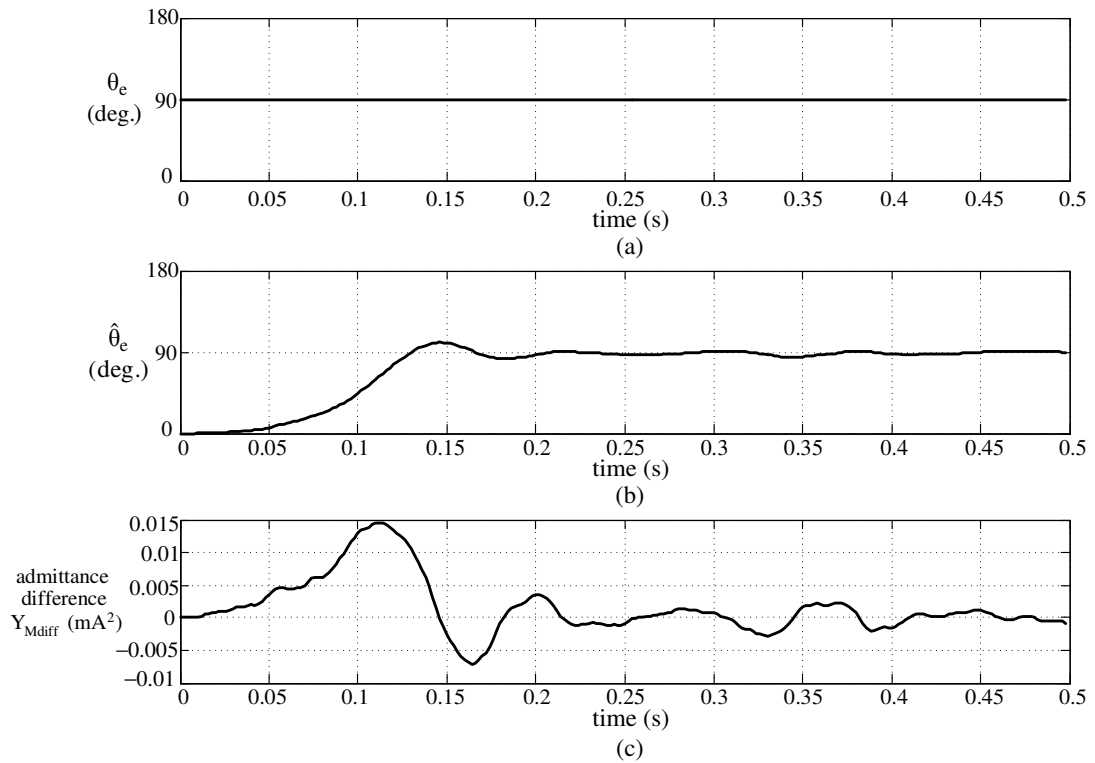
Figure 6.18 Convergence of the tracker with 90° estimation error input; actual rotor flux angle (a), estimated rotor flux angle (b), admittance difference signal (c).

In Figure 6.19, the tracker is started with 135° of initial estimation error. Since the estimation error is larger than 90°, the admittance difference signal is negative, although the estimation error is positive (Figure 6.14). Therefore, the tracker compensates for the negative admittance difference signal and converges to the -45° instead of 135°, with 180° error. This case is called as pole skipping, which can be avoided by preventing the estimation error to be larger than 90°.
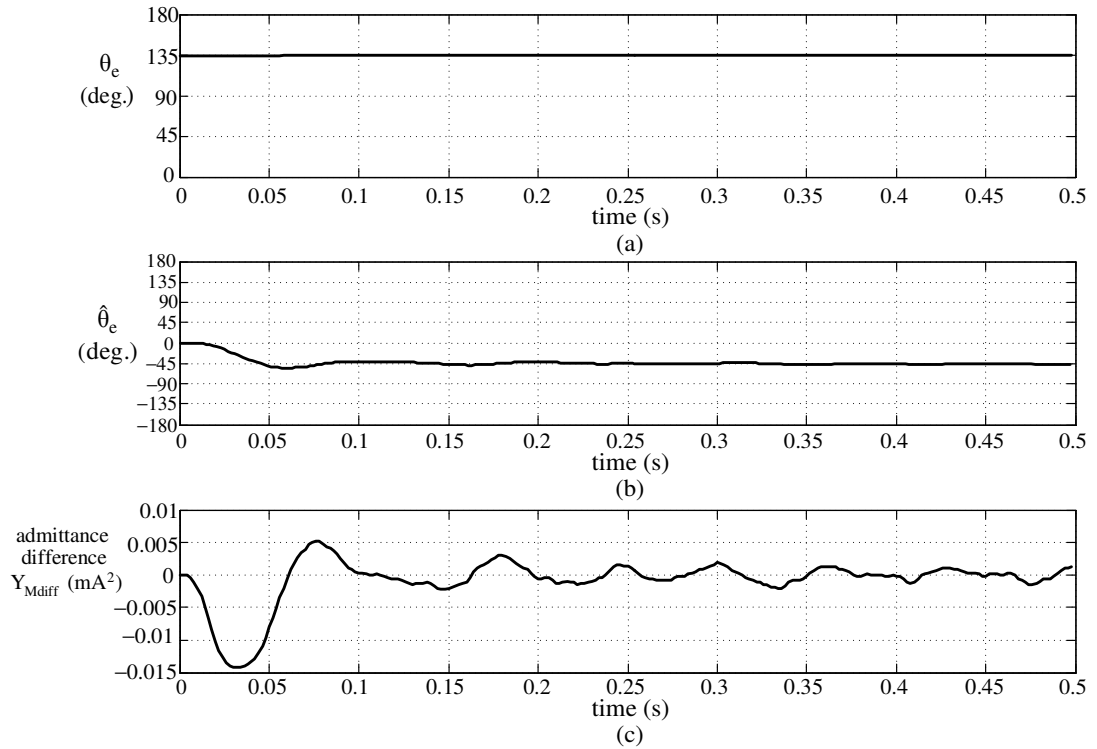
Figure 6.19 Pole skipping of the tracker with 135° estimation error input; actual rotor
flux angle (a), estimated rotor flux angle (b), admittance difference signal (c).

6.2.5 Dynamics of The Rotor Flux Axis Tracking Algorithm

The dynamic performance of the tracker algorithm is based on the compensator
within the tracker and on the performance of the estimation error detection algorithm.
In this thesis, the tracker algorithm is also improved by the speed command
feedforward method. The dynamic analysis of the estimation error detection
algorithm was given in section 6.2.3, and the bandwidth of the estimation error
detection algorithm is expected to be 20 Hz depending on the low-pass filters within
the heterodyning algorithm. In Figures 6.20 – 6.23, the IPM motor is driven in torque
mode, such that the speed loop is not executed, and only the vector control based on
the estimated rotor flux angle is accomplished. However, any torque command is not
realized, and only the dynamic performance of the rotor flux angle estimation by the
tracker algorithm is investigated. The IPM rotor is rotated externally around
electrical 0° with magnitudes less than 180° via commanding sinusoidal position

166

motion tasks to the load servo drive. Hence, the actual rotor flux angle is varied with different frequencies and the rotor flux angle estimation of the tracker algorithm is observed. For the experiments of this section, where the results are given in Figures 6.20 – 6.23, the speed command feedforward method has no effect since the motor is driven in torque mode without any speed command. The rotor flux angle is estimated by the tracker which involves only the compensator. However, as explained in the fourth chapter, with the use of the speed command feedforward method, the steady-state response of the tracker is improved and the gains of the compensator can be tuned for better transient response.

As observed in Figures 6.20 – 6.23, the rotor flux angle can be tracked (estimated) with a bandwidth of 3 Hz. The estimated rotor flux angle is used for the vector control and also for the mechanical position control. The speed estimation derived from the tracker is not dynamically analyzed, however the accuracy and dynamic response of the speed estimation is observed in the motion control experiments in the following sections.
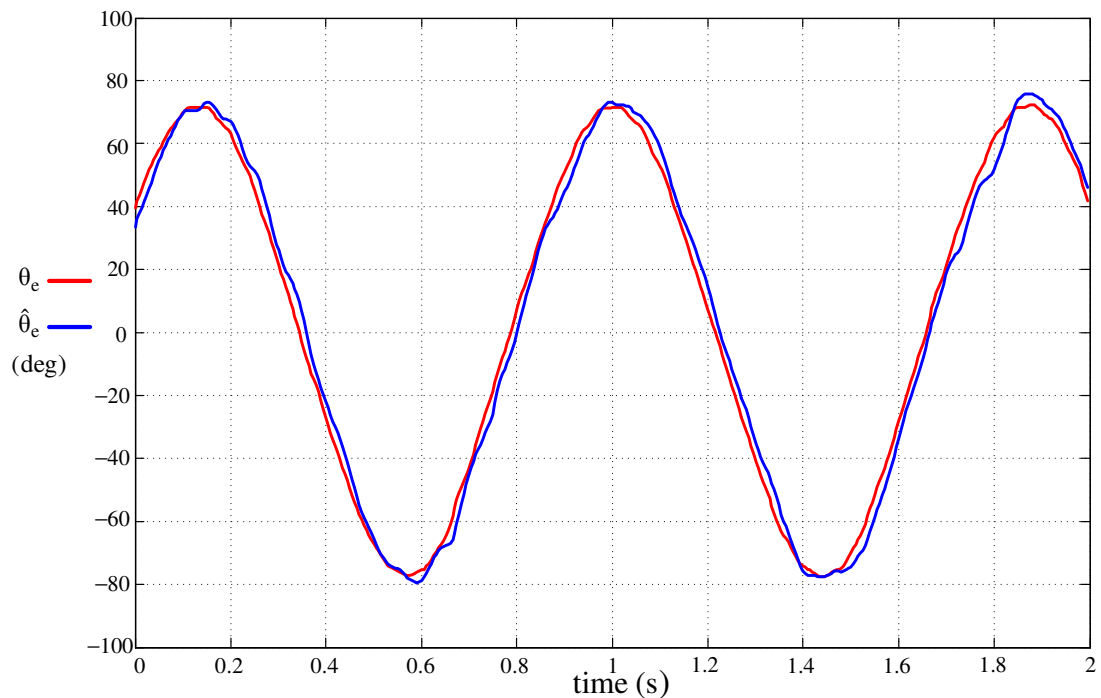
Figure 6.20 The actual rotor flux angle at 1 Hz (red) and the estimated rotor flux angle (blue).

167
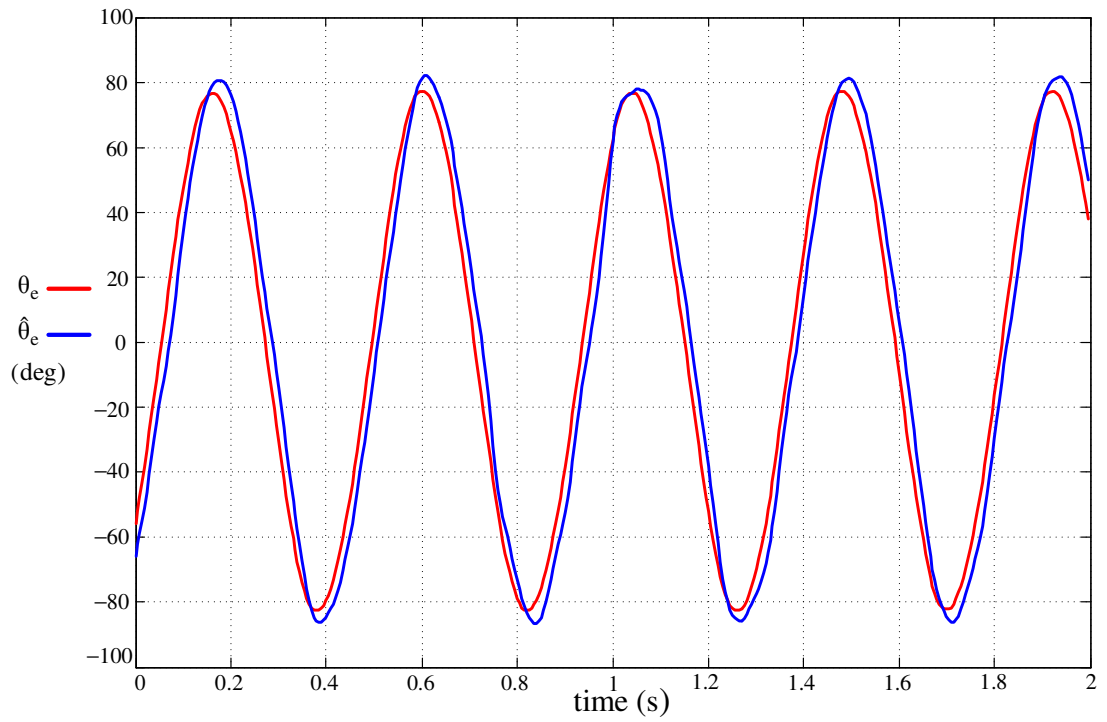
Figure 6.21 The actual rotor flux angle at 2 Hz (red) and the estimated rotor flux angle (blue).
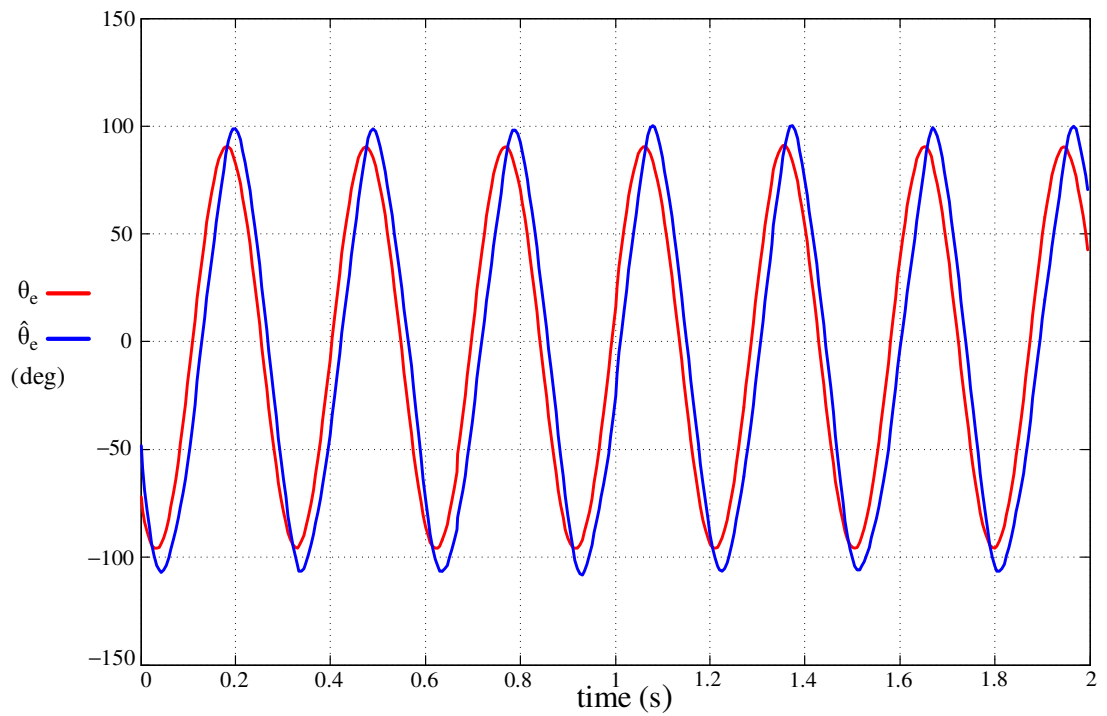
Figure 6.22 The actual rotor flux angle at 3 Hz (red) and the estimated rotor flux angle (blue).

168
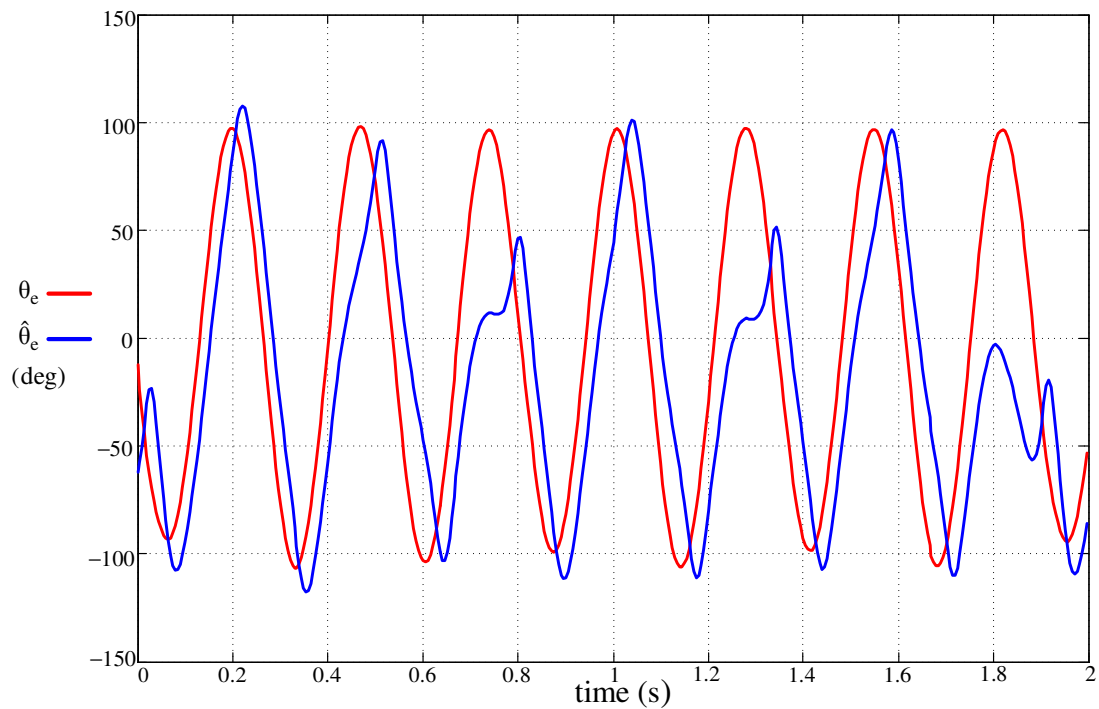
Figure 6.23 The actual rotor flux angle at 3.5 Hz (red) and the estimated rotor flux angle (blue).

6.2.6 Trapezoidal Speed Profile Under No-Load

In Figure 6.24, sensorless vector control and sensorless speed control based on the high frequency signal injection algorithm are performed. Trapezoidal speed profile command with 100 rpm magnitude for both directions is given to the speed controller. In Figure 6.24, the commanded, actual, and estimated speeds are shown with the actual and estimated rotor flux angles.
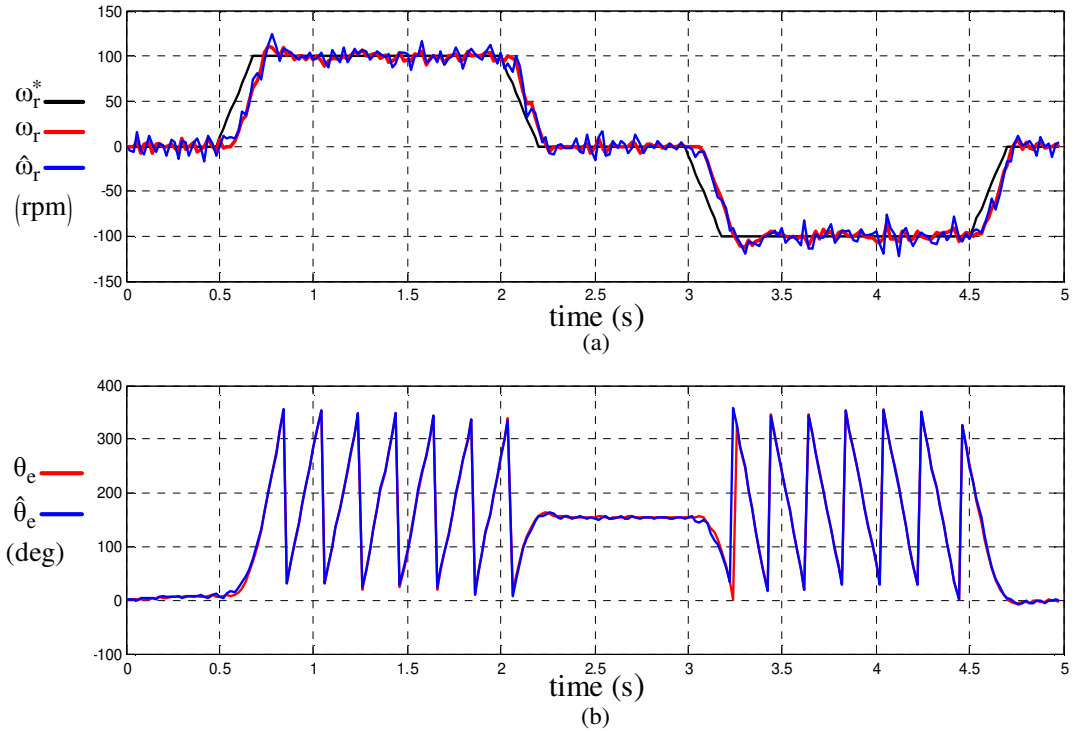
Figure 6.24 The speed command ω_r^* (black), the actual speed ω_r (red), the estimated speed $\hat{\omega}_r$ (blue) (a); the actual rotor flux angle θ_e (red), the estimated rotor flux angle $\hat{\theta}_e$ (blue) (b) for trapezoidal speed profile command under no-load.

6.2.7 Step Load at Zero Speed Operation

In Figure 6.25 – 6.27, sensorless vector control and sensorless speed control based on the high frequency signal injection algorithm are performed. Step load torque of 50% is applied to the motor while zero speed is commanded. In Figure 6.25; commanded, actual, estimated speeds and the difference between the actual rotor flux angle and the estimated rotor flux angle are shown. In Figure 6.25, the applied load torque, which is obtained from the analog output of the load servo drive, is shown. In Figure 6.27, the phase currents are shown, where the high frequency ripples are the result of the high frequency signal injection and the low frequency ripples are due to the ripples of the rotor (as observed in Figure 6.25 (a)).
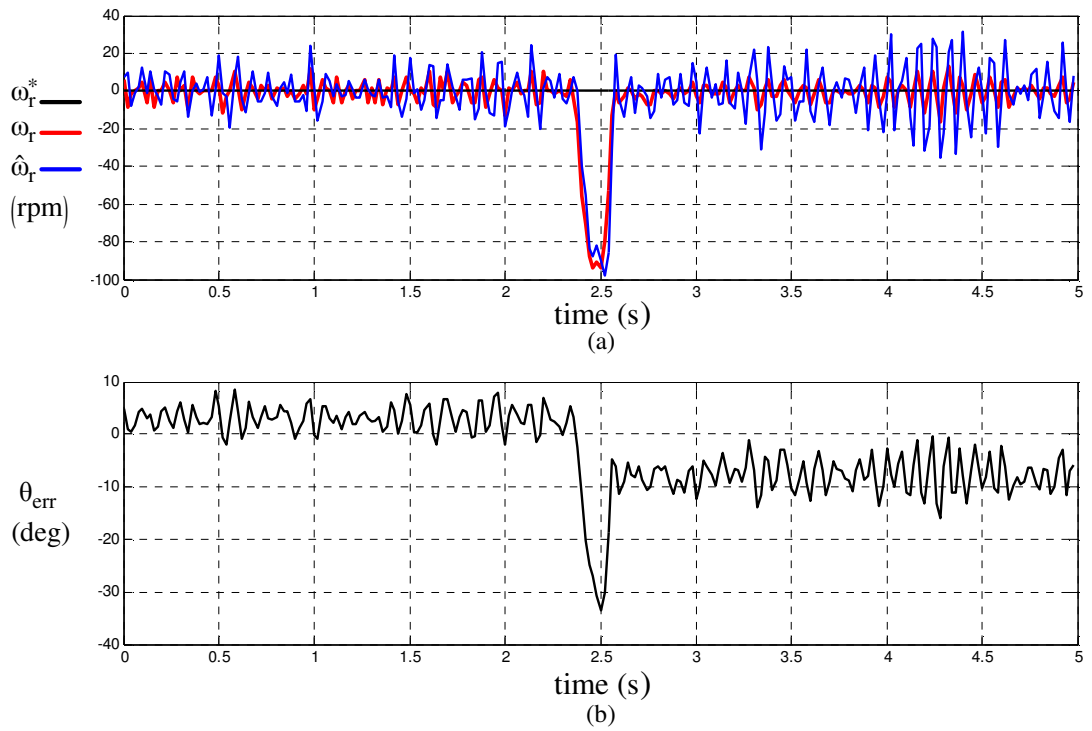
Figure 6.25 The speed command ω_r^* (black), the actual speed ω_r (red), the estimated speed $\hat{\omega}_r$ (blue) (a); rotor flux angle estimation error (θ_{err}) (b) for 50% step load at zero speed operation.
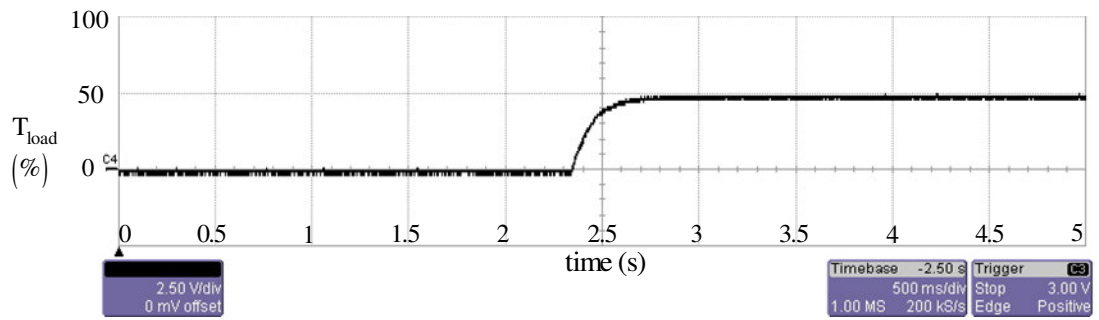
Figure 6.26 Applied load torque for 50% step load at zero speed operation.
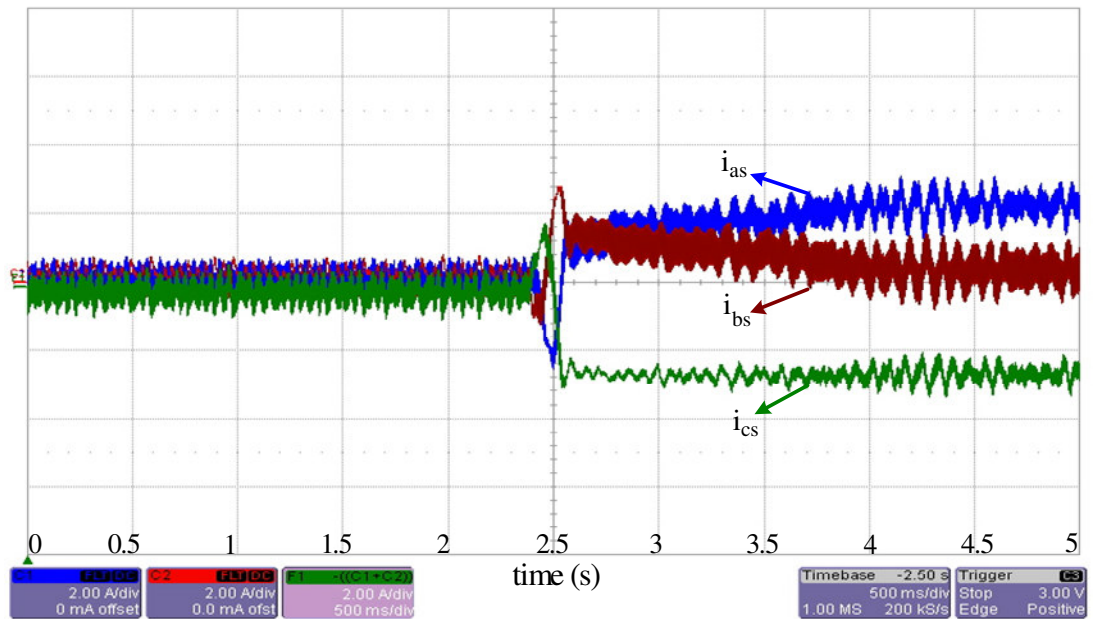
Figure 6.27 Phase-a current (blue), phase-b current (red), phase-c current (green) for 50% step load at zero speed operation (y-axis: 2A/div).

6.2.8 Acceleration Under Constant Load

In Figure 6.28 – 6.30, sensorless vector control and sensorless speed control based on the high frequency signal injection algorithm are performed. Acceleration command from 0 rpm to 150 rpm is given to the speed controller while the motor is under constant 100% load torque. In Figure 6.28 commanded, actual, estimated speeds and the difference between the actual rotor flux angle and the estimated rotor flux angle are shown. In Figure 6.29, phase-a current is shown where the high frequency ripples are the result of the high frequency signal injection and the low frequency ripples for the time period between 0 and 2.5 seconds are due to the ripples of the rotor (as observed in Figure 6.28 (a)). In Figure 6.30, zoom of the phase-a current, when the motor reaches 150 rpm speed, is shown.

172
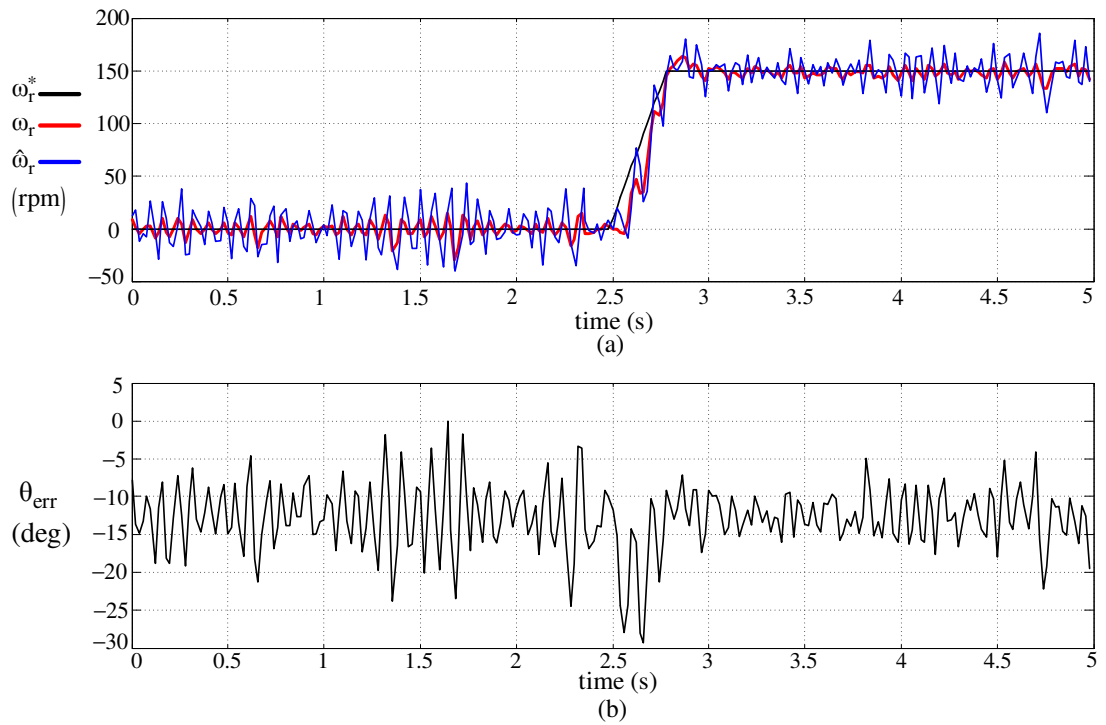
Figure 6.28 The speed command ω_r^* (black), the actual speed ω_r (red), the estimated speed $\hat{\omega}_r$ (blue) (a); rotor flux angle estimation error (θ_{err}) (b) for acceleration to 150 rpm under 100% constant load.
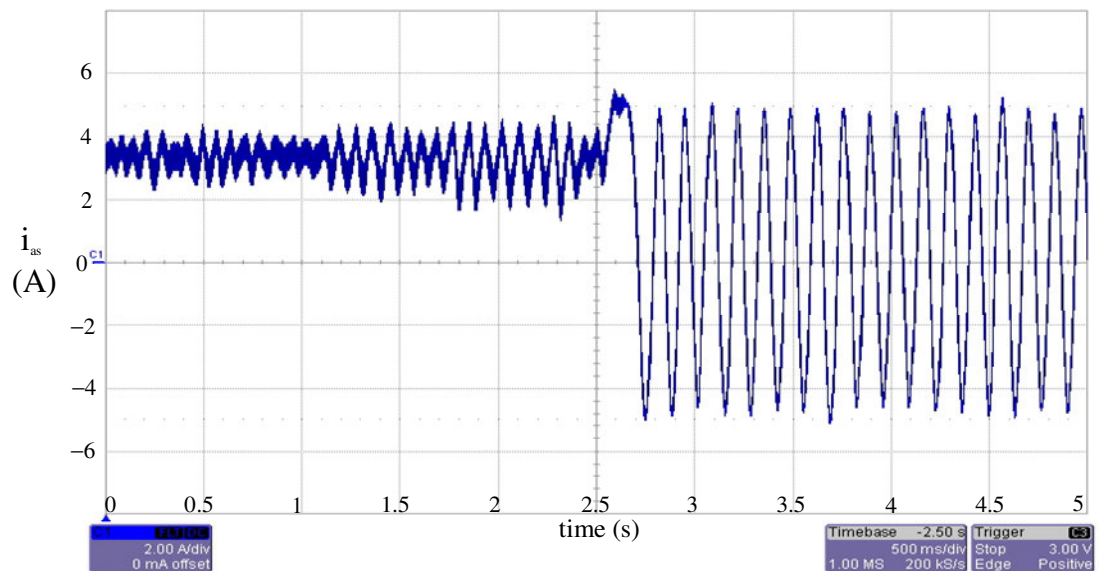
Figure 6.29 Phase-a current for acceleration to 150 rpm under 100% constant load.
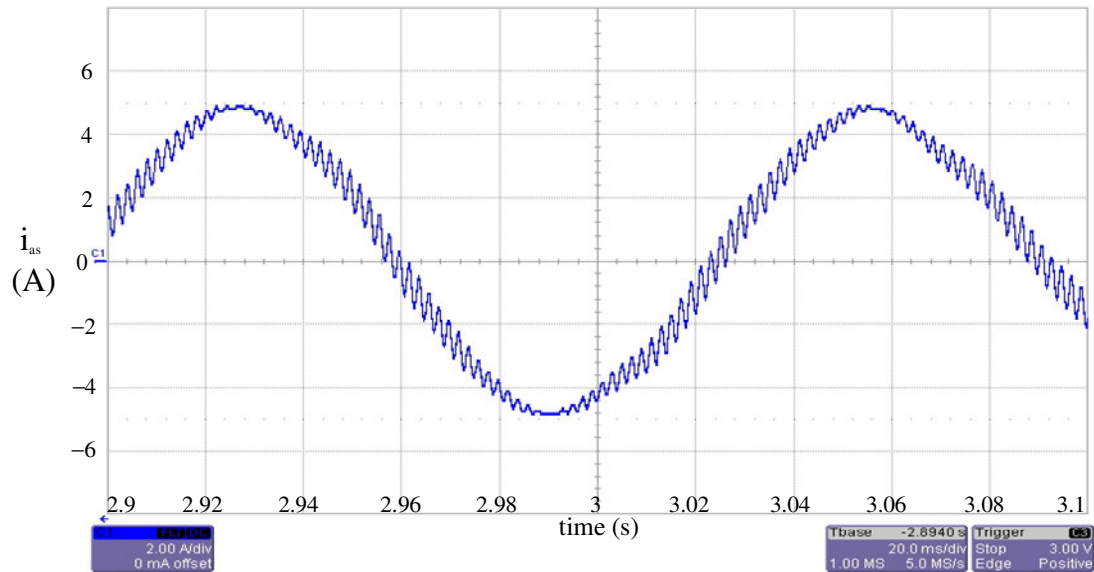
Figure 6.30 Zoom of phase-a current for acceleration to 150 rpm under 100% constant load.

In Figures 6.25 (b) and 6.28 (b), there is estimation error, which is created and consistent with loading. This is the result of deviation of the admittance (impedance) curve of the rotor with the torque current. When, high torque currents exist, the maximum admittance point of the rotor is deviated from the permanent magnet axis due to the saturation effect. The estimation error becomes negative, which means that the maximum admittance point deviates slightly towards the torque axis, where the torque current is created, as shown in Figure 6.31. In Figure 6.31, the tracker converges to the maximum admittance point; however the maximum admittance point is not the actual rotor flux axis (permanent magnet axis) due to the loading effect. Therefore, the rotor flux angle is estimated with a small error of less than 15° even for full load operation as shown in Figure 6.28 (b). This estimation error, which is proportional to the torque current value, can be compensated by a look-up table using the torque current value during the operation. Development of such a compensation algorithm is beyond the scope of this thesis.
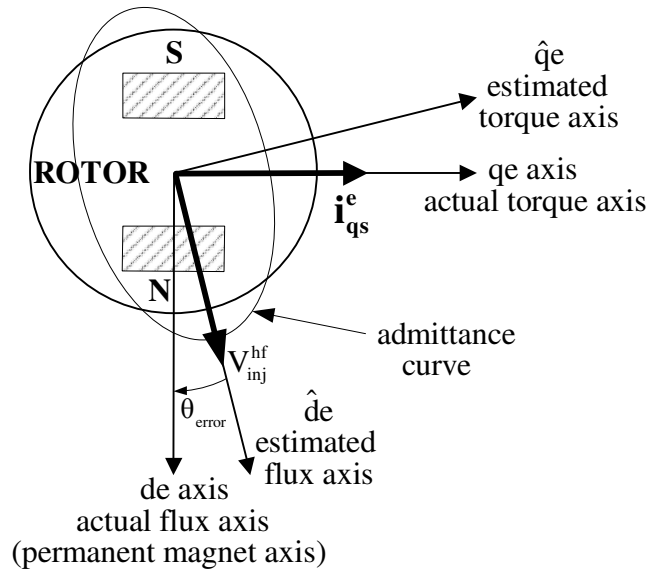
Figure 6.31 Deviation of the admittance curve with loading.

6.2.9 Investigation of Speed Command Feedforward Method via Lock of Rotor

In Figure 6.32, speed command feedforward method in Figure 4.30 is investigated. The IPM motor is commanded with a speed of 100 rpm and it is locked by the mechanical brake of the load machine while it is rotating. Even the speed command is not realized due to heavy loading (braking), the compensator output (ω_{comp}) provides the necessary correction term for the feedforward speed (ω_{ffd}) and the estimated speed ($\hat{\omega}_e$) tracks the actual speed (ω_e).
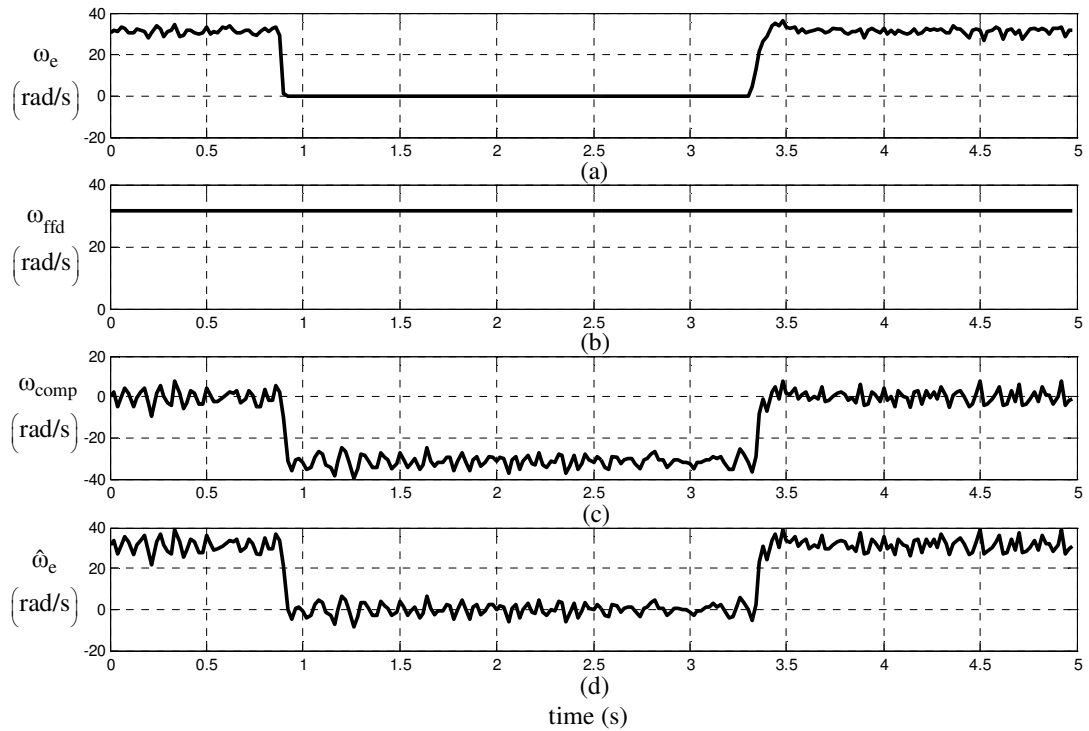
Figure 6.32 Investigation of the speed command feedforward method for lock of the motor via brake with 100 rpm speed command.

6.2.10 Trapezoidal Position Profile Under No-Load

In Figure 6.33, sensorless vector control and sensorless speed and position control based on the high frequency signal injection algorithm are performed. Trapezoidal position command profile with 200° magnitude is given to the position controller and the position of the IPM motor is closed loop controlled by the estimated position feedback of the high frequency signal injection algorithm. In Figure 6.33 commanded, actual, estimated rotor angles and the difference between the actual rotor angle and the estimated rotor angle are shown with the actual and estimated speeds.
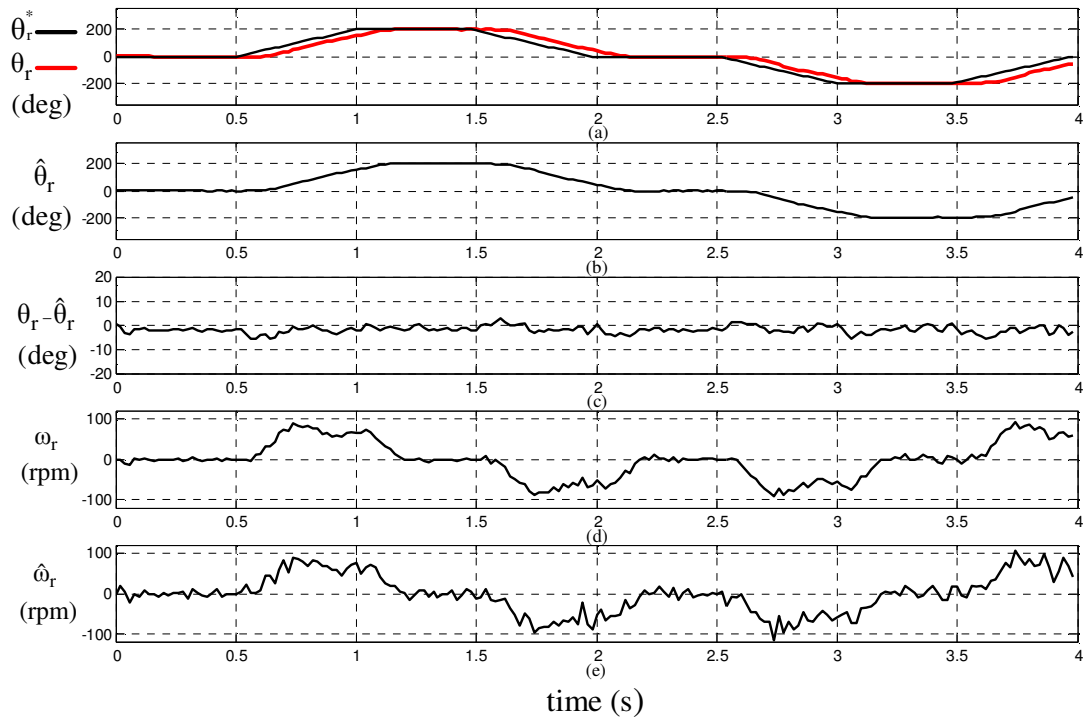
Figure 6.33 The position command θ_r^* (black), the actual position θ_r (red) (a); the estimated position $\hat{\theta}_r$ (blue) (b); the difference between the actual position and the estimated position (c); the actual speed w_r (d); the estimated speed $\hat{w}_r$ (e) for trapezoidal position profile command under no-load.

6.2.11 Step Load at Zero Position Operation

In Figures 6.34 – 6.36, sensorless vector control and sensorless speed and position control based on the high frequency signal injection algorithm are performed. Zero degree (0°) position command is given to the position controller and then step load is applied. In Figure 6.34 commanded, actual, estimated rotor angles and the difference between the actual rotor angle and the estimated rotor angle are shown with the actual and estimated speeds. In Figure 6.35, the applied load torque, which is obtained from the analog output of the load servo drive, is shown. In Figure 6.36, the phase currents are shown, where the high frequency ripples are the result of the high frequency signal injection and the low frequency ripples are due to the ripples of the rotor (as observed in Figure 6.34).

177
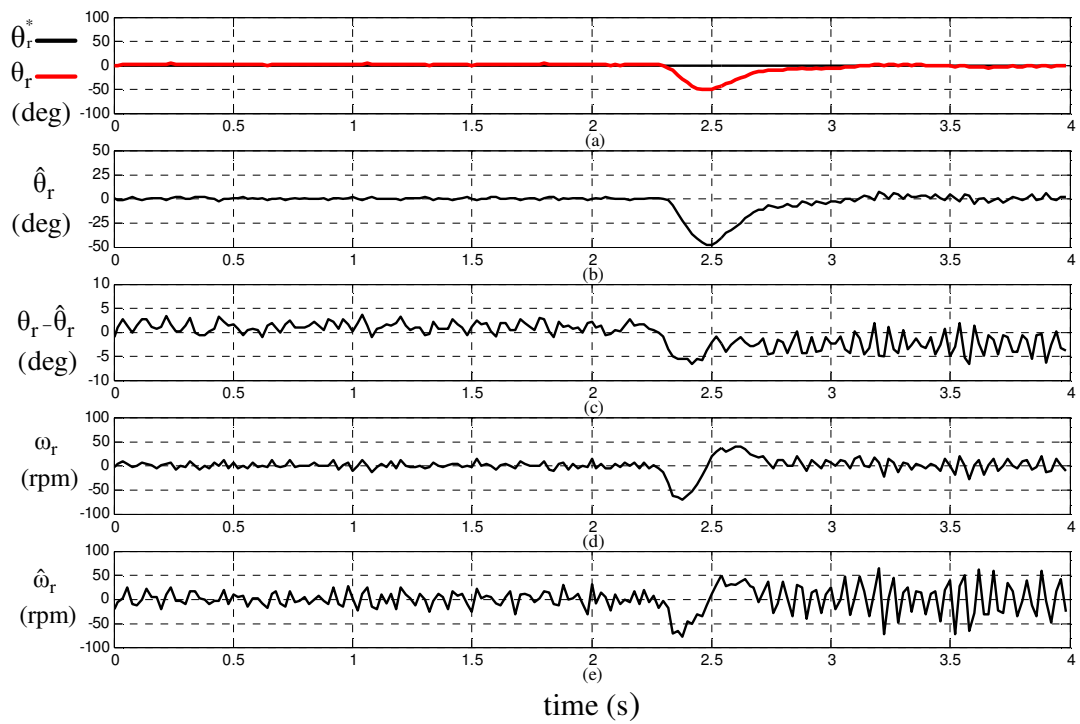
Figure 6.34 The position command θ_r^* (black), the actual position θ_r (red) (a); the estimated position $\hat{\theta}_r$ (blue) (b); the difference between the actual position and the estimated position (c); the actual speed w_r (d); the estimated speed $\hat{w}_r$ (e) for 50% step load at zero position operation.
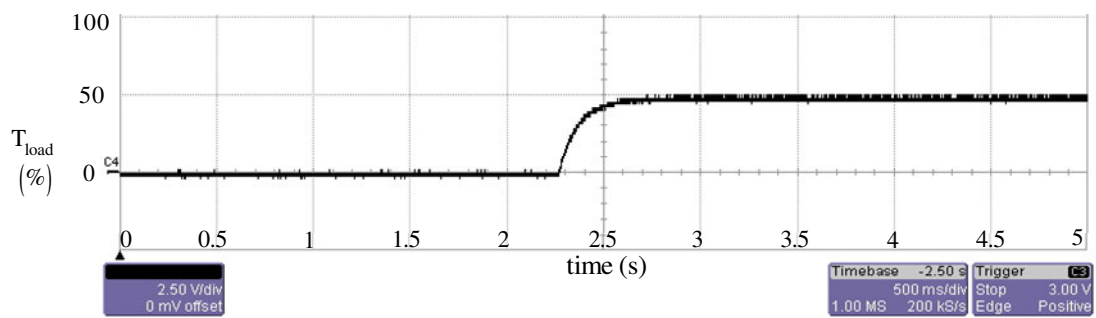
Figure 6.35 Applied load torque for 50% step load at zero position operation.
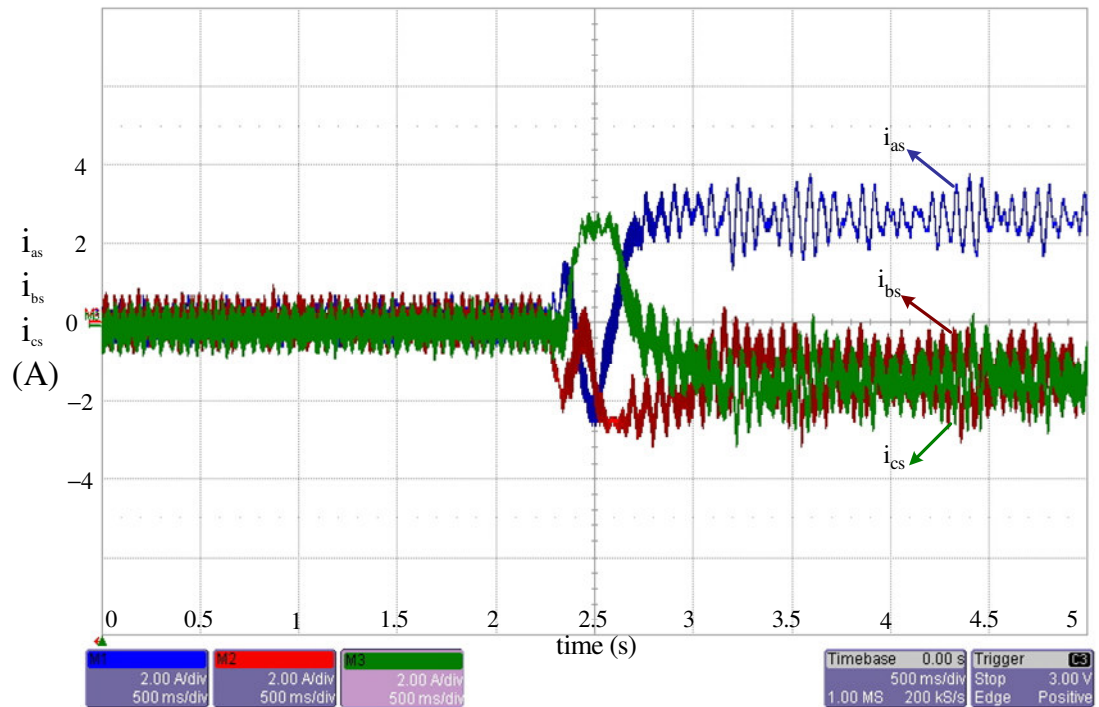
Figure 6.36 Phase-a current (blue), phase-b current (red), phase-c current (green) for 50% step load at zero position operation (y-axis: 2A/div).

6.3 Experimental Results of The Flux Observer Algorithm

The fundamental model based flux observer method is experimentally investigated for sensorless vector control and sensorless speed control of the IPM motor for moderate and high speed regions. Vector control of the IPM motor is performed via the rotor flux angle estimation of the flux observer, and the speed feedback is also provided by the estimation of the flux observer, as in Figure 4.36. The parameters used within the experimental implementation of the flux observer algorithm are given in Table 6.2.

Table 6.2 Parameters used within the flux observer experiments

Synchronous Frame Current Regulator	K_p	75
	K_I	9300
	LPF on the feedback path	2nd order with 1 kHz cut-off frequency
Speed Controller	K_{pr}	0.5
	K_p	0.08
	K_I	0.01
Position Controller	K_p	20

6.3.1 Acceleration Under No-Load

In Figure 6.37, sensorless vector control and sensorless speed control based on the fundamental model based flux observer algorithm are performed. Speed command of the motor is increased from 250 rpm to 500 rpm. In Figure 6.37, commanded, actual, estimated speeds and the difference between the actual rotor flux angle and the estimated rotor flux angle are shown.
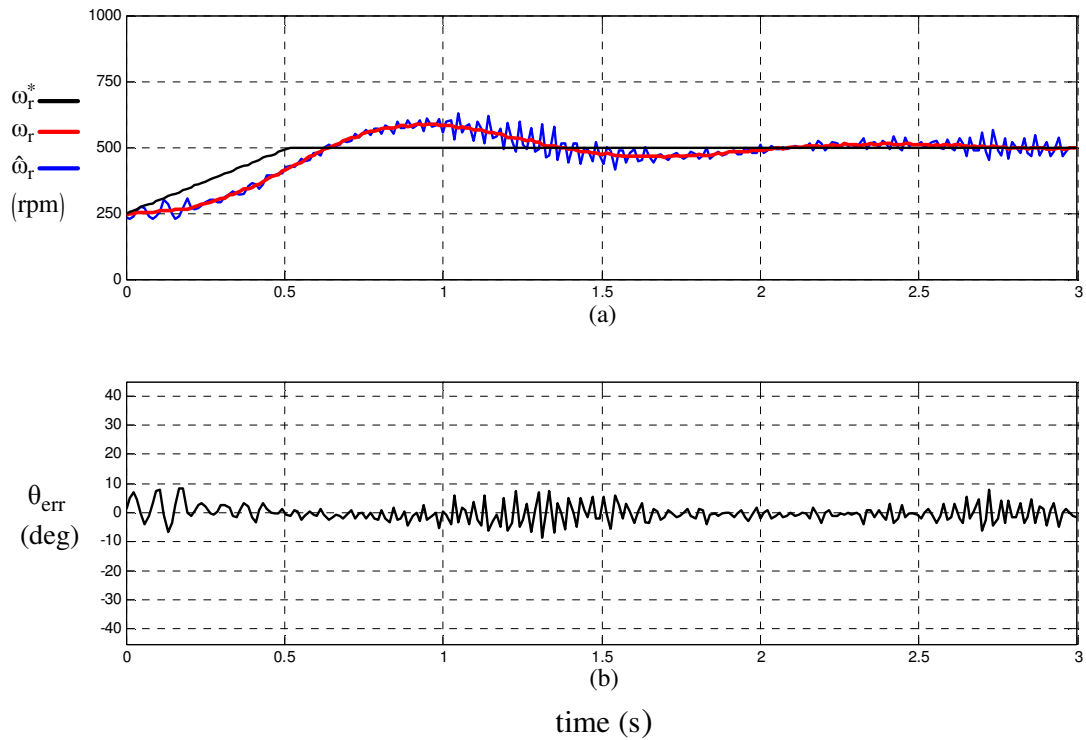
Figure 6.37 The speed command ω_r^* (black), the actual speed ω_r (red), the estimated speed $\hat{\omega}_r$ (blue) (a); rotor flux angle estimation error (θ_{err}) (b) for acceleration from 250 rpm to 500 rpm under no-load.

6.3.2 Step Load at Constant Speed Operation

In Figure 6.38, sensorless vector control and sensorless speed control based on the fundamental model based flux observer algorithm are performed. Step load torque of 25% is applied to the motor while constant 500 rpm is commanded to the speed controller. In Figure 6.38 commanded, actual, estimated speeds, the applied load torque, and the difference between the actual rotor flux angle and the estimated rotor flux angle are shown.
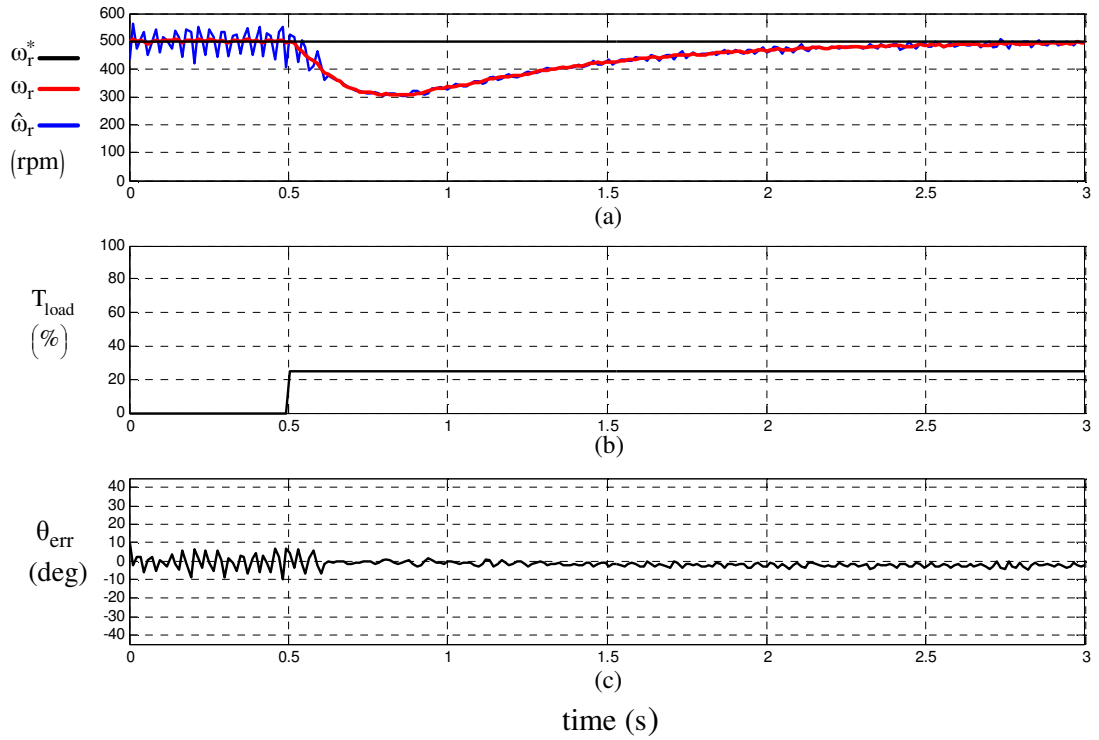
Figure 6.38 The speed command ω_r^* (black), the actual speed ω_r (red), the estimated speed $\hat{\omega}_r$ (blue) (a); rotor flux angle estimation error (θ_{err}) (b) for 25% step load with constant 500 rpm speed operation.

6.4 Experimental Results of The Hybrid Algorithm

The hybrid algorithm is the combination of the two estimation methods; the high frequency signal injection method and the flux observer. The major important point of the hybrid algorithm is the seamless transition between the two estimation methods while there is a speed change. The vector control and speed control loops are closed by the rotor flux angle and speed estimations of the high frequency signal injection algorithm up to 150 rpm; and above 150 rpm estimations of the flux observer algorithm are used for sensorless vector control and sensorless speed control, as given in 4.37. Beyond 300 rpm, injection of high frequency voltage is ceased since it is not utilized for medium and high speed regions.

6.4.1 Acceleration for Wide Speed Range Under Constant Load

In Figures 6.39 - 6.41, sensorless vector control and sensorless speed control based on the hybrid algorithm are performed. Acceleration from zero speed to 750 rpm is performed based on the hybrid algorithm while the motor is under constant 50% load. In Figure 6.39, commanded, actual, estimated speeds, and the difference between the actual rotor flux angle and the estimated rotor flux angle are shown. In Figure 6.40, the phase currents are shown. In Figure 6.41, zoom of the phase-b current is shown for the transition period. The injection of high frequency voltage is ceased gradually when the motor reaches 300 rpm, as shown in Figure 6.41.
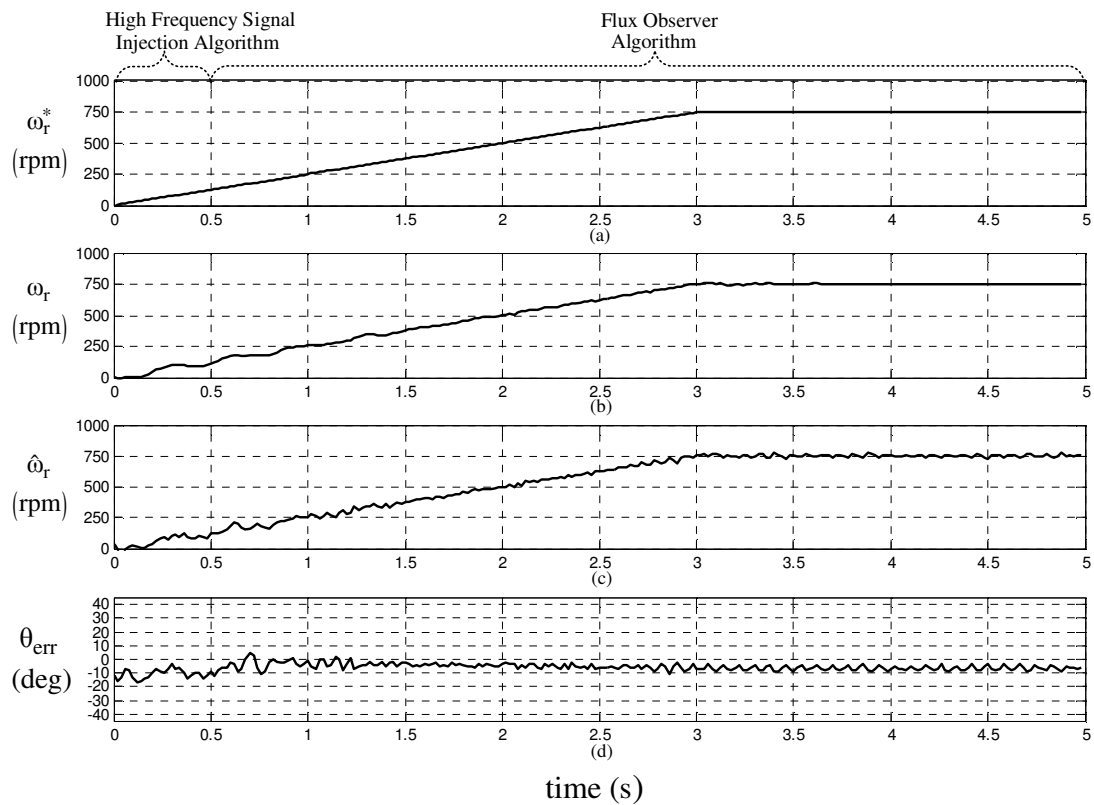
Figure 6.39 The speed command ω_r^* (a); the actual speed ω_r (b); the estimated speed $\hat{\omega}_r$ (c); rotor flux angle estimation error (θ_{err}) (d) for acceleration to 750 rpm under 50% constant load.
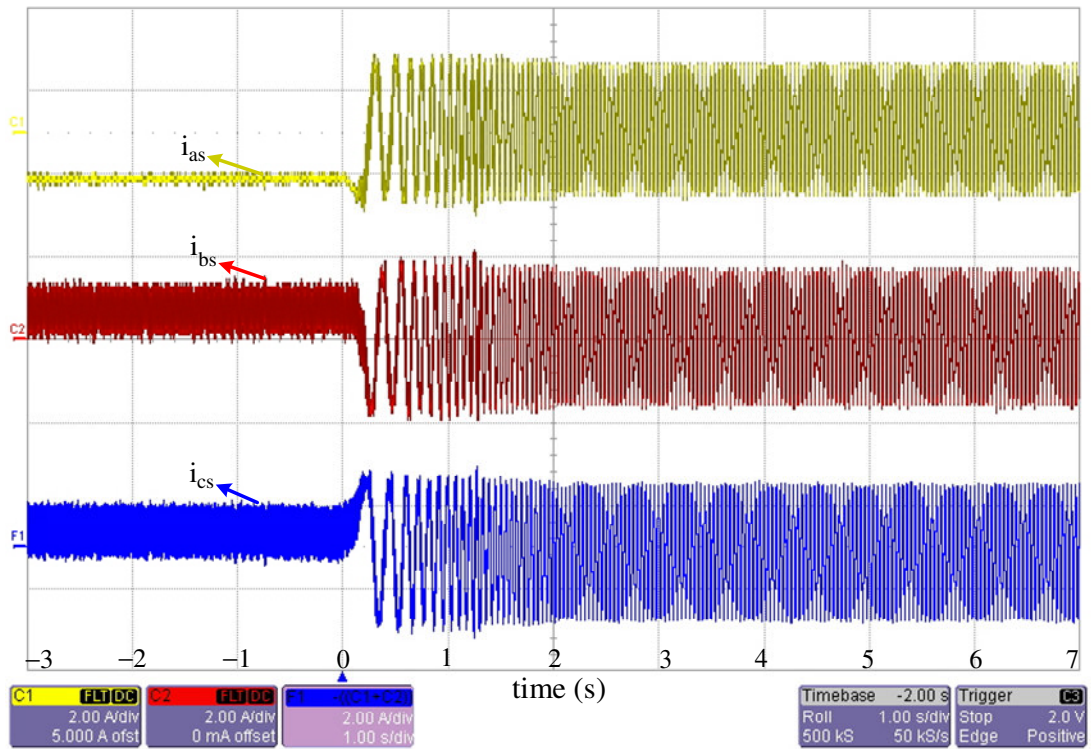
Figure 6.40 Phase-a current (yellow), phase-b current (red), phase-c current (blue)

for acceleration to 750 rpm under 50% constant load.
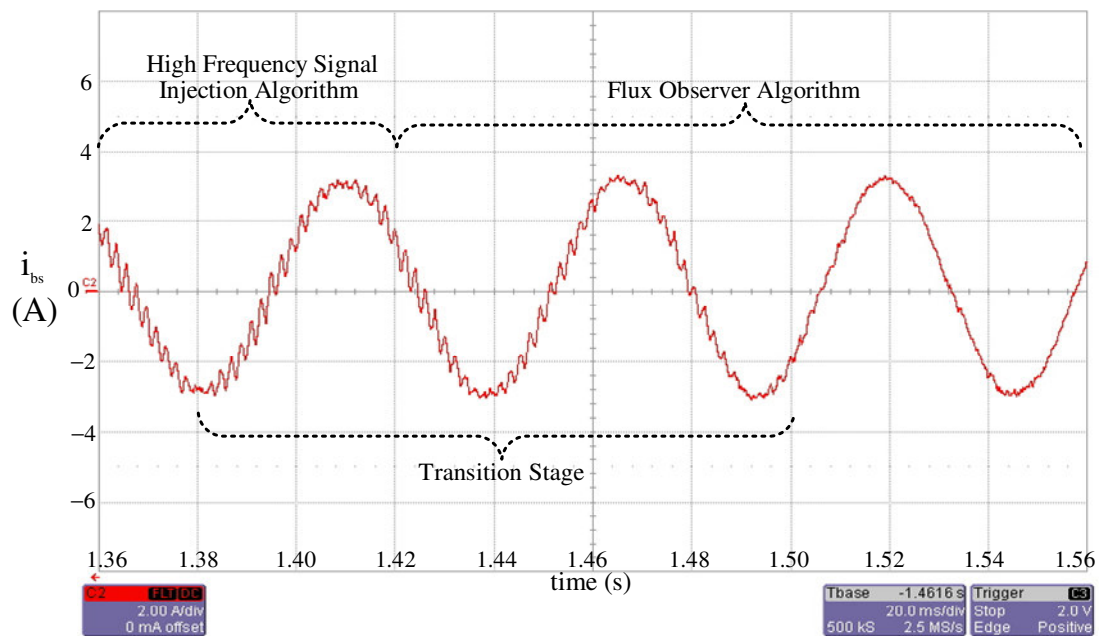
Figure 6.41 Zoom of the phase-b current waveform during transition stage for

acceleration to 750 rpm under 50% constant load.

6.4.2 Speed Reversal Under No-Load

In Figure 6.42, sensorless vector control and sensorless speed control based on the hybrid algorithm are performed. Speed reversal from 500 rpm to -500 rpm is performed. In Figure 6.42, commanded, actual, estimated speeds, and the difference between the actual rotor flux angle and the estimated rotor flux angle are shown.
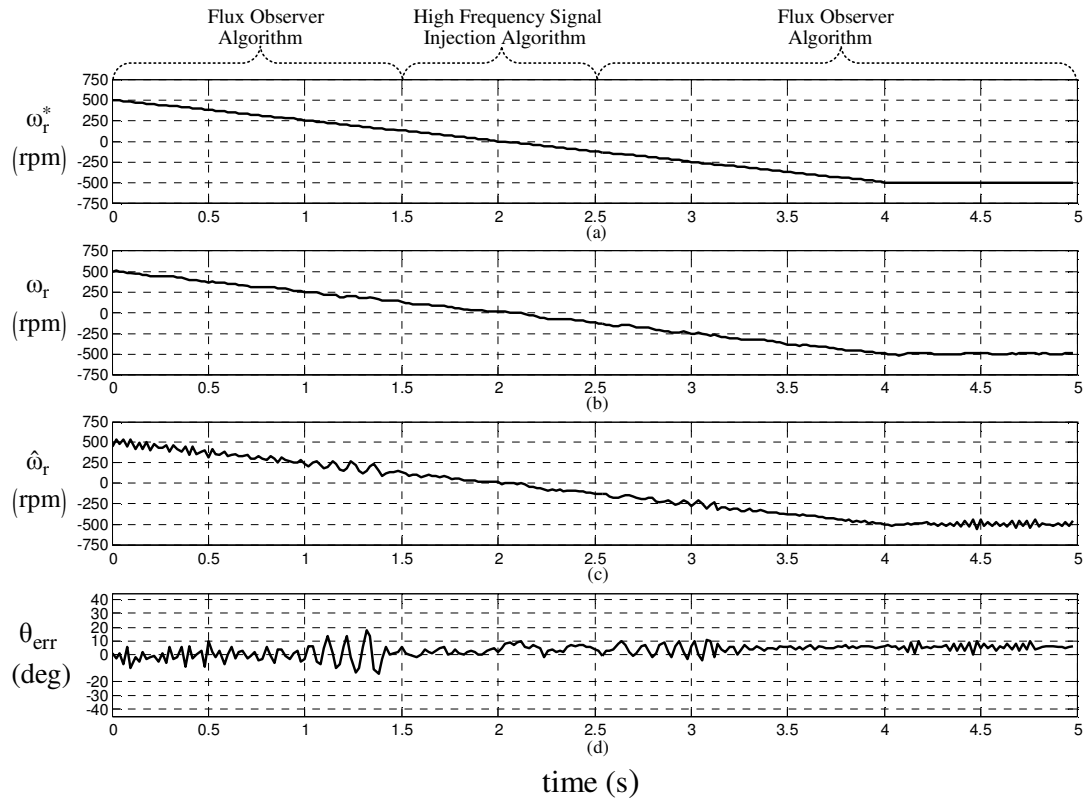
Figure 6.42 The speed command ω_r^* (a); the actual speed ω_r (b); the estimated speed $\hat{\omega}_r$ (c); rotor flux angle estimation error (θ_{err}) (d) for speed reversal from 500rpm to -500rpm under no-load.

6.5 Conclusion of The Experimental Results

The experimental implementation of the sensorless control algorithms is performed in the laboratory on the experimental setup, which includes a DSP based PWM-VSI and the IPM motor coupled to the load servo machine on the motor test bench. The

performance of the PWM-VSI is analyzed in the name of voltage linearity, and the effect of the dead-time on the phase-current and result of the dead-time compensation method are shown. The motion control simulations of the sensorless control algorithms are experimentally verified, and similar results of the simulations are obtained within the experimental analysis.

The saliency of the IPM motor and the saliency characteristics for various injection frequency and voltage level are extracted experimentally. The high frequency current component on the estimated q-axis, is shown to be zero when the there is not any estimation error and non-zero when there is an estimation error. The admittance difference signal output of the estimation error detection algorithm is shown to be proportional to the estimation error for estimation error values of less than 45°. The steady-state and dynamic performance of the estimation error detection algorithm is analyzed, and the bandwidth of the estimation algorithm is found to be directly proportional to the cut-off frequency of the low-pass-filters within the heterodyning algorithm. The step response, steady-state response, and dynamic performance of the tracker algorithm, which compensates the estimation error and estimates the rotor flux angle, is analyzed. The pole skipping condition, which is due to the symmetry of the N&S poles, is experimentally realized. The bandwidth of the tracker, in the name rotor flux angle estimation, is shown to be 3 Hz. Sensorless speed control and position control of the IPM motor are performed both for no-load and loaded cases and it is shown that the speed and position of the IPM motor are closed loop controlled based on the high frequency signal injection algorithm, even for zero speed operation. The rotor flux angle is estimated with an error of less than 10° for no-load operation, where it is estimated with an error of 15° for 100% loaded operation due to the saturation effect of loading. Speed of the IPM motor is estimated with high accuracy and the speed of the IPM motor is close loop controlled with a ripple magnitude of less than 20 rpm based on the estimated speed. The position of the IPM motor is estimated and close loop controlled with an error of less than 5° and ripple of less than 10°, even under loaded operation, based on the estimated position information.

The fundamental model based flux observer algorithm is implemented and utilized for sensorless control of the IPM motor at medium and high speed region. The speed of the IPM motor is closed loop controlled based on the flux observer algorithm, even under loading conditions. The command tracking and disturbance rejection performance of the speed control loop based on the flux observer algorithm is analyzed. The rotor flux angle is estimated with an error of less than 10° even under loaded operation. The speed of the IPM motor is estimated with high accuracy and the ripple on the actual speed of the IPM motor is less than 10 rpm both for no-load and loaded operations.

The hybrid method combining the two estimation algorithms for whole speed range is implemented and speed of the IPM motor is closed loop controlled based on the hybrid algorithm both for no-load and loaded operation. Seamless transition from one algorithm to the other is performed, where the speed of the IPM motor is smoothly increased or decreased even for the transition periods and under constant load.

CHAPTER 7

APPLICATION OF THE SENSORLESS CONTROL ALGORITHMS TO THE INDUCTION MOTOR

7.1 Introduction

The two sensorless control algorithms; the saliency based high frequency signal injection algorithm [22] and a fundamental model based adaptive flux observer algorithm [15] are also implemented for the induction motor, in this thesis. The saliency based high frequency signal injection algorithm is basically the same as the algorithm implemented for the IPM motor. However, the fundamental model based flux observer algorithm for the induction motor is of a model reference adaptive system (MRAS) type with an adaptive speed estimation law. The vector control and speed control principles, which are discussed in the third chapter, are the same for the induction motor. The rotor flux oriented vector control theory, which is utilized and implemented for the IPM motor, is also implemented for the induction motor. The rotor flux angle is estimated by the sensorless control algorithms and used for the synchronous frame transformations and the mechanical speed estimation is used for the sensorless speed control of the induction motor. The synchronous frame current regulator, whose parameters are tuned for the induction motor, is utilized for the vector control of the induction motor.

There exist two main differences of the induction motor from the IPM motor. The induction motor is asynchronous, where the IPM motor is synchronous, and the field of the induction motor is created by the induced rotor currents due to the external excitation, where the rotor field of the IPM motor is inherent due to the permanent

magnets without any rotor currents. Since the induction motor is asynchronous, the mechanical speed of the induction motor is not same as the synchronous speed (excitation frequency) such that there exists slip frequency between the excitation frequency and the speed of the rotor, as given in (7.1) below. Since the induction motor does not involve permanent magnets for field flux, the flux axis current command (i_{ds}^{e}) is realized for the creation of the rotor field (flux) of the induction motor.

$$\omega_e = \omega_r + \omega_s \tag{7.1}$$

where,

ω_e is the synchronous frequency,

ω_r is the rotor frequency,

ω_s is the slip frequency.

The rotor flux angle of the induction motor is not directly related with the mechanical speed; however the rotor flux angle can be calculated based on the synchronous speed (excitation frequency) with the equation (7.2).

$$\theta_e = \int \omega_e dt \tag{7.2}$$

For the induction motor, the vector control (field orientation) can be implemented in two different ways; direct field orientation and indirect field orientation, depending on the way the rotor flux angle is obtained [40]. For the direct field orientation, the rotor flux angle is obtained directly. For instance; the fundamental model based flux observer algorithms solve the fundamental motor model and directly output the rotor flux angle, or the high frequency signal injection algorithm tracks the rotor flux angle and directly outputs the rotor flux angle, as implemented for the IPM motor. In the indirect field orientation method, the synchronous frequency (ω_e) of the motor is obtained, from the rotor frequency (ω_r) and the slip frequency (ω_s), as in (7.1); and the rotor flux angle is obtained by integrating the synchronous frequency (ω_e) as in (7.2). For the vector control of the induction motor in this thesis, the direct field

orientation is utilized with the high frequency signal injection algorithm and the indirect field orientation is utilized with the speed adaptive flux observer algorithm.

For the indirect vector control theory, the rotor speed (ω_r) is obtained from the rotor speed estimation of the sensorless control algorithm (it can be obtained from a shaft sensor for the applications using a sensor). The slip frequency is obtained from the slip relation, which gives the slip frequency satisfying the rotor flux oriented vector control conditions, given in (7.3) [40].

$$\omega_s = \frac{r_r}{L_r} \frac{i_{qs}^e}{i_{ds}^e} \tag{7.3}$$

where,

r_r is the rotor resistance,

L_r is the rotor self inductance.

The slip frequency, which satisfies the vector control conditions, is obtained based on the synchronous frame de and qe axes currents and the rotor time constant. Therefore, the rotor parameters used for the slip relation are critical for correct field orientation. There are adaptive schemes for parameter estimation of the induction motor; however such parameter estimation schemes are not included in this thesis.

As discussed in the first chapter, the fundamental model based estimation algorithms can not be utilized for sensorless control of the AC motors at the low and zero speed region. Therefore, similar to the IPM motor, the fundamental model based flux observer algorithm is implemented for medium and high speed region, and the saliency based high frequency signal injection algorithm is implemented for low and zero speed regions, for sensorless control of the induction motor. In the following section, the implementation of the high frequency signal injection algorithm for the sensorless vector control is given. The saliency based high frequency signal injection algorithm estimates the rotor flux angle directly, thus direct field orientation control is realized. In the next section, the implementation of a speed adaptive flux observer,

which estimates both the rotor flux angle and the motor speed, is given. The motor speed estimation of the speed adaptive flux observer is utilized in the indirect field orientation and also utilized for the sensorless speed control of the induction motor.

7.2 High Frequency Signal Injection (HFSI) Method for The Induction Motor

The induction motor possesses a symmetrical rotor without any spatial anisotropy; therefore it is a non-salient pole motor in its nature. However, artificial saliency can be created in the induction motor. The saliency of the induction motor arises due to the saturation of the leakage inductances on the flux axis by the rotor flux [53]. Also, there are different methods, which modify the mechanical rotor structure of the induction motor and create the saliency by modifying the rotor slot openings of the induction motor [21]. These methods are not preferred since they require specially treated motors for saliency based sensorless control. The saliency of the induction motor, which is saturation consequent, can be observed by injecting high frequency signal to the motor besides the fundamental excitation, same as the high frequency signal injection method implemented for the IPM motor. The rotor flux angle and speed of the motor are estimated via the high frequency signal injection method based on the saliency of the induction motor.

7.2.1 Saliency of the Induction Motor

Source of the saliency of the induction motor is mainly the saturation of the motor in the flux axis with the rotor flux and another source is slightly the skin effect [53]. The main idea involves the differences of the leakage inductances and resistances at high frequency between the de (flux) and qe (torque) axes of the induction motor.

The well known synchronous frame voltage equations of the induction motor for rotor flux oriented case ($\lambda_{qr}^e = 0$) are given in (7.4) – (7.5).

191

$$v_{ds}^e = \left(r_s + p\sigma L_s + p\frac{r_r L_m^2}{L_r(r_r + pL_r)} \right) i_{ds}^e - \omega_e \lambda_{qs}^e \tag{7.4}$$

$$v_{qs}^e = \left(r_s + p\sigma L_s \right) i_{qs}^e - \omega_e \lambda_{ds}^e \tag{7.5}$$

$$L_s = L_m + L_{ls} \tag{7.6}$$

$$L_r = L_m + L_{lr} \tag{7.7}$$

$$r_s' = r_s + \left(\frac{L_m}{L_r} \right)^2 r_r' \tag{7.8}$$

$$\sigma = 1 - \frac{L_m^2}{L_s L_r} \tag{7.9}$$

where

v_{ds}^e, v_{qs}^e stator de-axis and qe-axis voltages,

i_{ds}^e, i_{qs}^e stator de-axis and qe-axis currents,

$\lambda_{ds}^e, \lambda_{qs}^e$ stator de-axis and qe-axis flux linkages,

p, derivative operator,

r_s, r_r stator and rotor resistances,

L_s, L_r stator and rotor self inductances,

L_m mutual inductance,

σ leakage coefficient,

$L_{\sigma s}$ stator transient inductance,

τ_r rotor time constant,

ω_e synchronous frequency (rotational speed of the rotor flux).

192

For the high frequency signal injection method $\omega_h \gg \omega_e$, where ω_h is the frequency of the injected high frequency signal. Thus, voltage equations can be rewritten as in (7.10) and (7.11) while taking $p = j\omega_h$.

$$v_{ds}^e = \left(r_s + j\omega_h \sigma L_s + j\omega_h \frac{r_r L_m^2}{L_r(r_r + j\omega_h L_r)} \right) i_{ds}^e \tag{7.10}$$

$$v_{qs}^e = \left(r_s + j\omega_h \sigma L_s \right) i_{qs}^e \tag{7.11}$$

The stator voltage is composed of the fundamental and high frequency components as in (7.12) and (7.13)

$$V_{ds}^e = V_{ds1}^e + \tilde{v}_{ds}^e = V_{ds1}^e + V_{ds}^e \sin(\omega_h t) \tag{7.12}$$

$$V_{qs}^e = V_{qs1}^e + \tilde{v}_{qs}^e = V_{qs1}^e + V_{qs}^e \sin(\omega_h t + \varphi) \tag{7.13}$$

, where the "~" sign corresponds to the high frequency components.

For high frequencies $r_r + j\omega_h L_r$ can be approximated as $j\omega_h L_r$, since ω_h is quite large. Then voltage equations at high frequency become as (7.14) and (7.15).

$$\tilde{v}_{ds}^e \approx \left(r_s + r_r \frac{L_m^2}{L_r^2} + j\omega_h \sigma L_s \right) \tilde{i}_{ds}^e \equiv \tilde{Z}_d \tilde{i}_{ds}^e \tag{7.14}$$

$$\tilde{v}_{qs}^e \approx \left(r_s + j\omega_h \sigma L_s \right) \tilde{i}_{qs}^e \equiv \tilde{Z}_q \tilde{i}_{qs}^e \tag{7.15}$$

Due to the skin effect at high frequency, the value of rotor resistance, r_r in (7.14) becomes much larger than its value at the fundamental frequency. Therefore, there is a difference between the resistances when the high frequency signal injection is made on the de-axis or on the qe-axis, such that resistance is lower for qe-axis. This analysis proves that;

$r_d > r_q$ (7.16)

The rotor flux, which is created on the de-axis, saturates the region of qe-axis windings. Due to the saturation, the leakage inductance seen by the qe-axis windings becomes low. However, leakage inductance seen by the de-axis winding is high since no saturation exists in that region, as given in Figure 7.1. Therefore, leakage inductance seen by the de-axis is higher than the leakage inductance of the qe-axis. This analysis proves that;

$X_d > X_q$ (7.17)
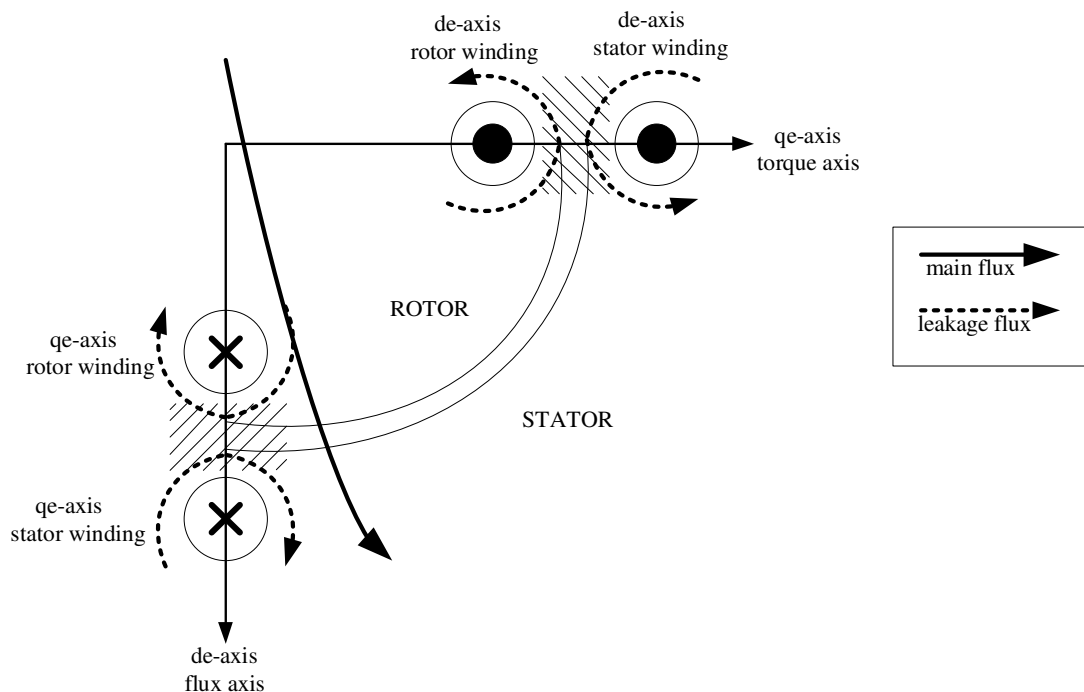
Figure 7.1 Saturation of the induction motor.

In summary, the impedance on the real flux axis (de-axis) is higher than the impedance on the orthogonal torque axis (qe-axis) when high frequency signal injection is made.

$Z_d > Z_q$ (7.18)

$$Y_q > Y_d \qquad\qquad\qquad (7.19)$$

As a result, the induction motor behaves as a salient-pole motor when high frequency signal injection is applied and the minimum admittance point is on the rotor flux axis. This minimum admittance point can be tracked, thus the rotor flux angle can be estimated. The only difference between the saliency of the induction motor and the saliency of the IPM motor is such that the admittance is minimum on the de-axis, where the admittance was maximum on the de-axis for the IPM motor. The impedance curve of the induction motor is given in Figure 7.2.
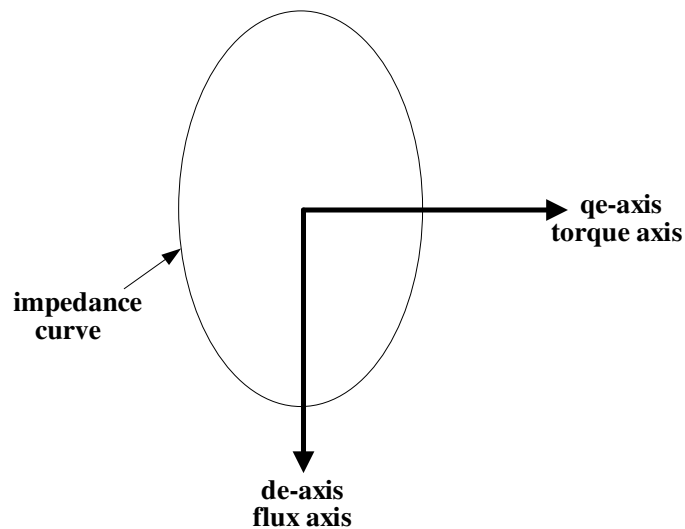
Figure 7.2 Impedance curve of the induction motor showing its magnetic saliency.

7.2.2 Sensorless Control of The Induction Motor with The HFSI

The method of fluctuating high frequency voltage injection on the flux axis in the synchronous frame (de-axis) [22] is utilized for the estimation of the rotor flux angle of the induction motor, which is also implemented for the IPM motor. The estimation error detection and the tracker principles are the same for the induction motor. The only difference is that the estimation error signal, which is called as admittance difference (Y_{Mdiff}), is obtained by the difference of the magnitude of the high frequency current component i_{dm} than the magnitude of the high frequency current

component i_{qm}, where it was the converse for the IPM motor. The formula for the admittance difference signal is given in (7.20) and (7.21).

$$Y_{Mdiff} = (\left|i_{dm}\right|^2 - \left|i_{qm}\right|^2) = K_{Y1}(Y_{dm} - Y_{qm}) \tag{7.20}$$

$$Y_{Mdiff} = K_{Y2} \times \left(\theta_e - \hat{\theta}_e\right) = K_{Y2} \times \theta_{error} \tag{7.21}$$

The rotor flux angle is estimated via compensating the estimation error signal and tracking the minimum admittance point of the rotor of the induction motor. The synchronous speed of the induction motor is calculated based on the synchronous speed (ω_e) estimation of the tracker, similar to the IPM motor. However, the mechanical speed is not directly related with the synchronous speed since the induction motor is asynchronous. The mechanical rotor speed is deduced from the synchronous speed (ω_e) based on the slip relation (7.3) and equation (7.1). The sensorless rotor flux angle estimation and vector control, and the sensorless speed estimation and speed control algorithms for the induction motor, based on the high frequency signal injection algorithm are given in Figure 7.3.
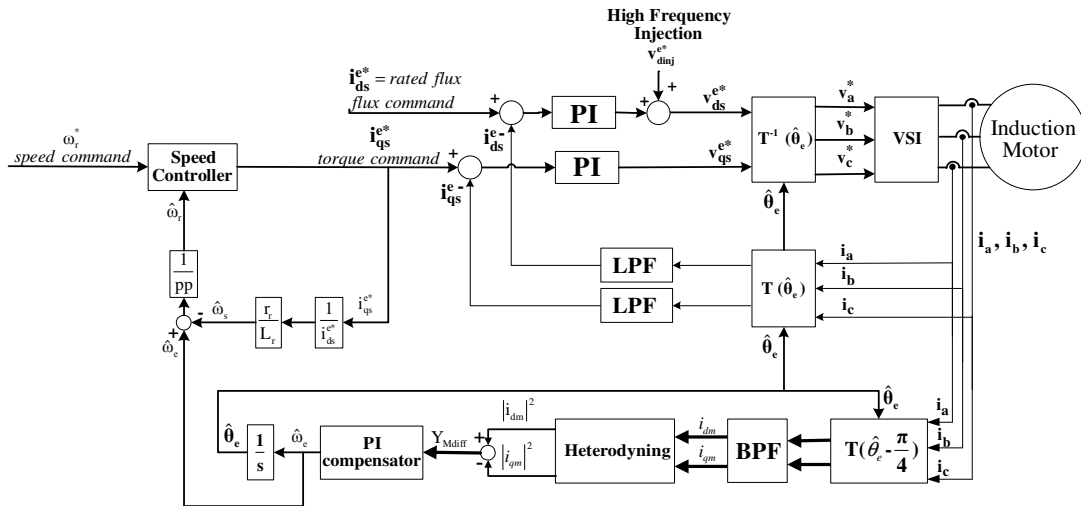
Figure 7.3 Sensorless control of the induction motor with the high frequency signal injection algorithm.

Since the induction motor's fundamental model is non-salient (no different entries for L_d and L_q), simulation of the saliency based high frequency signal injection algorithm can not be conducted with the tools like SIMPLORER or MATLAB, which include the fundamental model of the induction motor. Electromagnetic Finite Element Method (FEM) analysis can be conducted to investigate electromagnetic response and saliency of the induction motor or the high frequency characteristics of the induction motor can be mathematically modeled within the simulation tools SIMPLORER or MATLAB. Moreover, FEM simulation of the induction motor can be combined with the control algorithms implemented within SIMPLORER or MATLAB. However, simulation of the high frequency signal injection method for the induction motor is beyond the scope of this thesis. Experimental investigation of the saliency of the induction motor and implementation of the sensorless control algorithms based on the high frequency signal injection method are given in the following section.

7.2.3 Experimental Results of The HFSI Algorithm with The Induction Motor

7.2.3.1 Experimental Setup for The Induction Motor

For the experiments, a standard closed slot induction motor, whose parameters are given in Table 7.1, is utilized. Motor parameters are obtained by tests (locked rotor and no load tests) in the laboratory and also obtained from the manufacturer.

For monitoring the actual speed of the induction motor, an incremental encoder manufacture of Thalheim (ITD-20-A-4-1024-H-NI with 1024 lines/rev (4096 pulses/rev) and an index signal) is mounted on the fan side of the induction motor. The same drive with the F2808 DSP and the motor test bench are utilized during the experiments of the induction motor. The picture of the experimental setup of the induction motor coupled with the load servo drive is in Figure 7.4.

Table 7.1 The induction motor parameters

SIEMENS 1LA7113-4AA		
	Test Results	**Manufacturer Information**
Rated Power		4 kW
Rated Voltage		400V
Rated Current		8.2A
Power Factor		0.83
Rated Speed		1440 rpm
Rated Torque		26.5 Nm
Pole		4
Rs	1.7 Ω	1.77 Ω
Rr'	0.54 Ω	1.23 Ω
Lls	7 mH	7.9 mH
Llr'	7 mH	15.8 mH
Lm	140 mH	172 mH
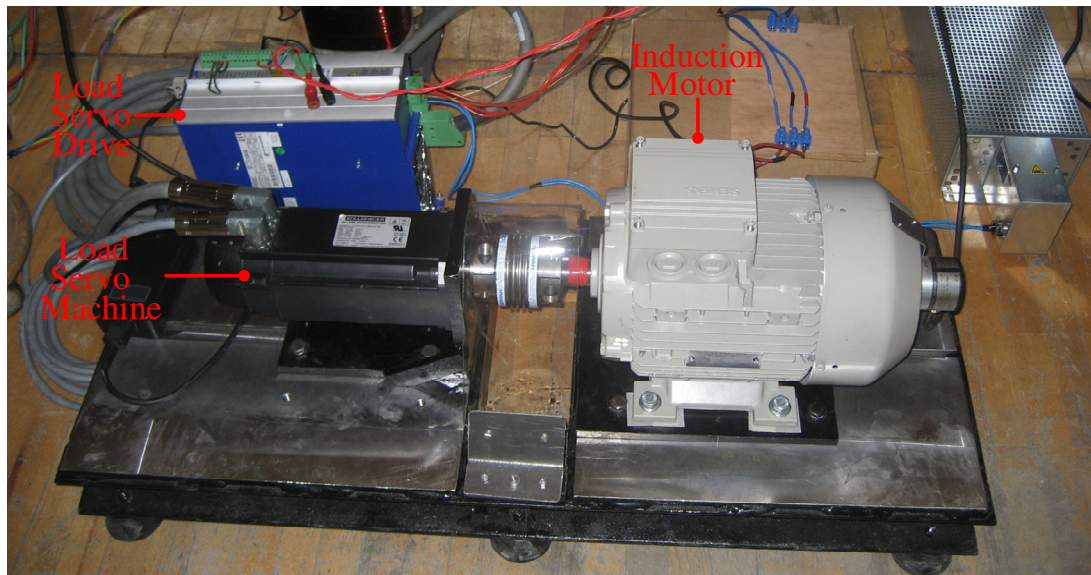
Figure 7.4 Experimental setup for the induction motor.

During the experiments, the rated flux current reference of 6 Amperes (peak) is commanded resulting in a flux linkage level of 1 Wb, as calculated in (7.22).

$$\lambda_r = L_m \times i_{ds}^{e*} = 177 \text{ mH} \times 6 \text{ A} = 1.062 \text{ Wb} \tag{7.22}$$

7.2.3.2 Saliency Characterization of The Induction Motor

Similar to the IPM motor, the saliency of the induction motor is investigated via applying high frequency voltages to the different rotor angle values. However, since the saliency of the induction motor does exist only when it is excited, the saliency is investigated while the motor is excited with fundamental component and the rotor flux is created. The saliency characteristics of the induction motor is investigated for various injection frequency and voltage level and the injection frequency and voltage level are selected to be 500 Hz and 75 V, respectively. The admittance characteristic of the induction motor, which is obtained by the scan of the motor with high frequency voltages, is given in Figure 7.5. In Figure 7.5, the actual rotor flux angle is obtained by the indirect field orientation, based on the speed feedback from the encoder. The admittance characteristic is investigated for no-load and loaded operation of the induction motor, in order to observe the loading effect. As seen in Figure 7.5, the admittance is minimum on the rotor flux axis, for no-load operation. However, for the loaded motor condition, the minimum admittance point is deviated due to the loading effect, similar to the IPM motor.
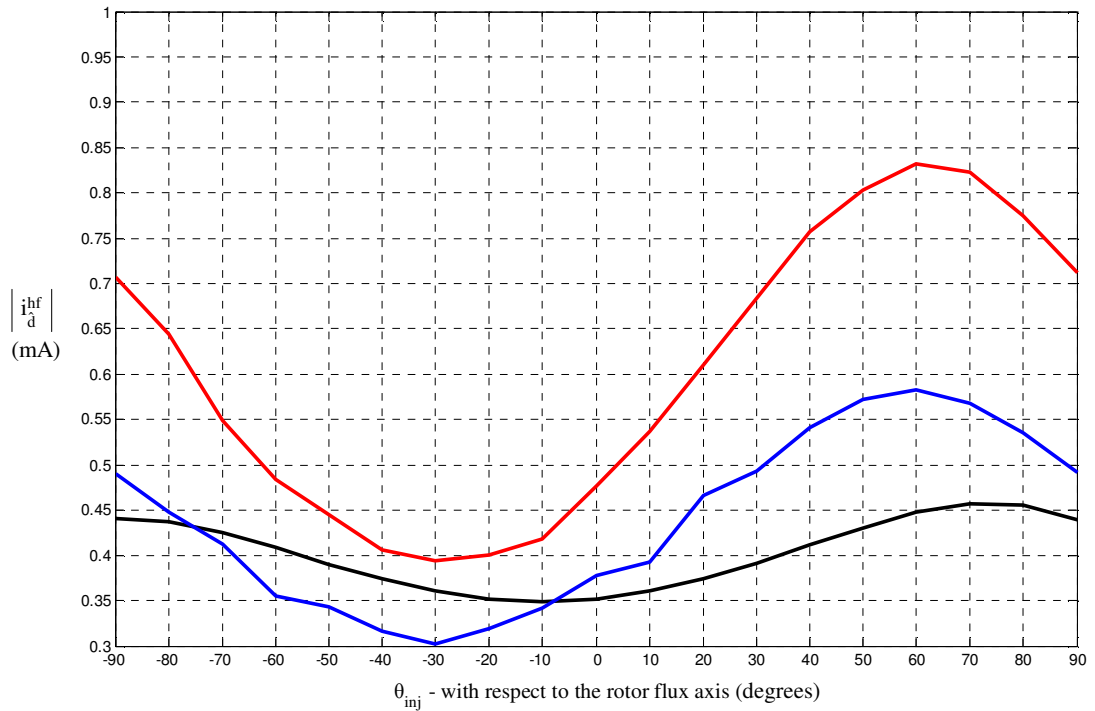
Figure 7.5 Admittance characteristics of the induction motor under no-load (black), 10% load (blue), 25% load (red) (ω_r=25 rpm, V_{inj}=75 V, f_{inj}=500 Hz).

In Figure 7.6 below, the admittance difference signal, which is the output of the estimation error detection algorithm, is recorded for different estimation error values. The induction motor is driven and the speed is controlled based on the encoder feedback and the estimation error is created step by step. The admittance difference signal (Y_{Mdiff}) is observed, which is expected to be proportional to the estimation error. However, the zero point of the admittance difference signal, to which the tracker converges, is deviated by 30°, which would be a result of incorrect field orientation due to the parameter errors, although the field orientation is based on the encoder feedback. Although there is an error of 30°, the tracker is expected to compensate for the admittance difference and converge to the rotor flux angle with an error of 30°.

200
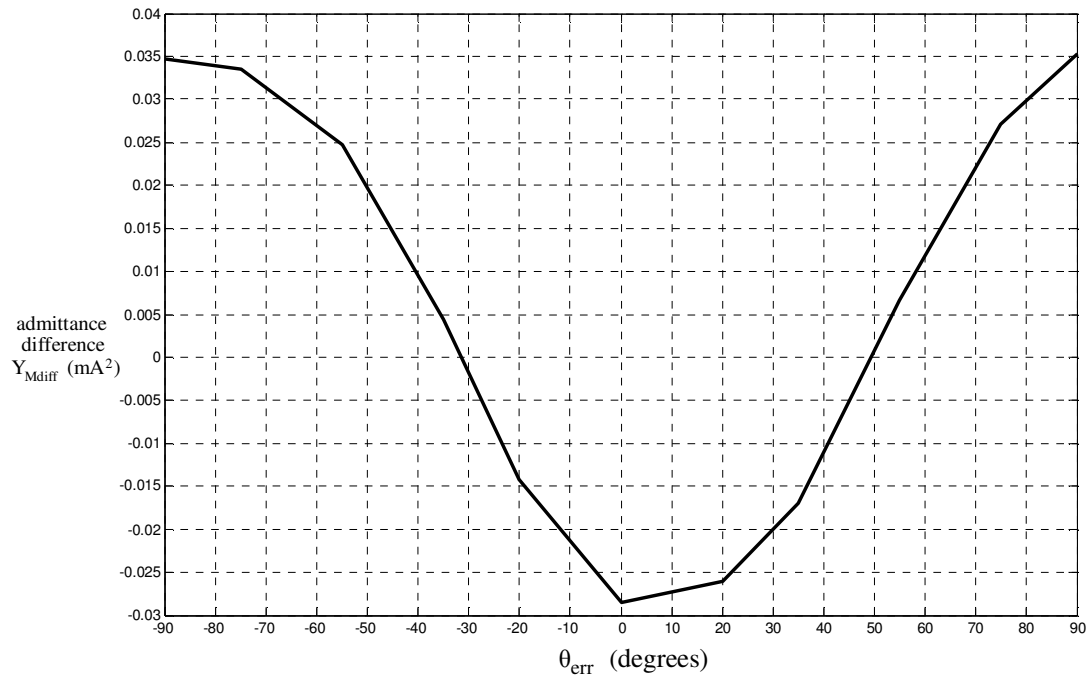
Figure 7.6 Admittance difference characteristics of the induction motor (ω_r=50 rpm, V_{inj}=75 V, f_{inj}=500 Hz).

The convergence of the tracker algorithm to the actual flux axis is investigated; however, the induction motor can not be closed loop vector controlled based on the rotor flux angle estimation of the high frequency signal injection algorithm. This situation can be a result of large deviation of the minimum admittance point with loading or incorrect tuning of the tracker. However, the saliency of the induction motor, which arises artificially due to the saturation effect, is observed and investigated for different loading conditions in this section. And the sensorless vector control and speed control of the induction motor are performed based on the fundamental model based speed adaptive flux observer algorithm, in the following section.

7.3 The Fundamental Model Based Speed Adaptive Flux Observer

7.3.1 Theory of The Speed Adaptive Flux Observer

Flux observers, which use pure integrators, for the induction motor have some stability problems and provide low estimation accuracy performance, even do not produce reliable results, especially at low and zero speed regions. Therefore, adaptive methods are preferred in order to improve the estimation performance of the flux observers, which are based on the fundamental model of the induction motor; and high performance is obtained at medium and high speed regions. In this thesis, speed adaptive flux observer algorithm of Kubota [15], based on the adaptive control theory is implemented for sensorless vector control and sensorless speed control of the induction motor at medium and high speed region. This speed adaptive flux observer method relies on the well-known state observer theory, which is given in Figure 7.7. The speed variable is estimated using a state-error function based on the Lyapunov's stability theorem. The flux observer is implemented in the stationary frame, independent of the synchronous frame transformations. The state space equations of the model and the state observer are given in (7.23) – (7.28).
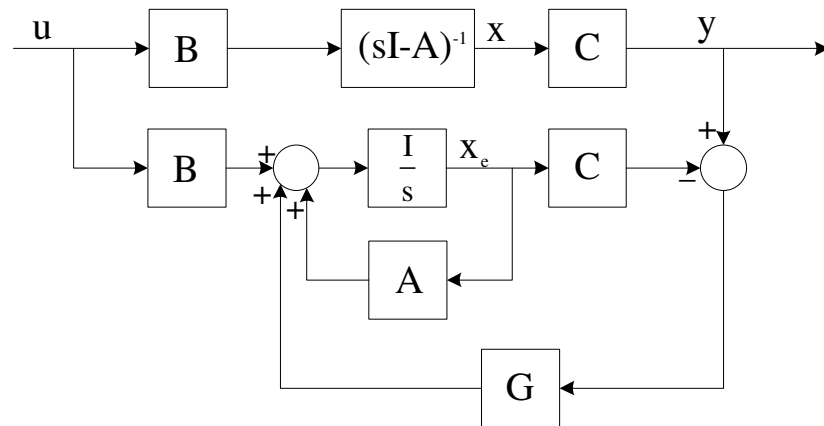
Figure 7.7 State observer block diagram.

$$\frac{d}{dt}x = Ax + Bu \qquad (7.23)$$

$$\frac{d}{dt}x_e = Ax_e + Bu + G(y - Cx_e) \qquad (7.24)$$

$$y = Cx \qquad (7.25)$$

$$e = x - x_e \qquad (7.26)$$

$$\frac{d}{dt}e = \frac{d}{dt}x - \frac{d}{dt}x_e = Ax + Bu - Ax_e - Bu - GC(x - x_e) \qquad (7.27)$$

$$\frac{d}{dt}e = (A - GC)e \qquad (7.28)$$

For the state observer of the induction motor, the states (x) are the stator currents and rotor fluxes; input (u) is the stator terminal voltage. Stator currents are the measurable states and input stator voltages are known within the drive via the reference stator voltages. Fluxes, which are the unknown states, are observed by the flux observer and the unknown motor speed variable, which exists in the state matrix A, is estimated and fed to the observer as an adaptation feedback.

Stationary frame equations of the induction motor are given in (7.29) and (7.30) below

$$v_{qds}^s = pi_{qds}^s L_{\sigma s} + r_s' i_{qds}^s - \frac{L_m}{L_r}\omega_{br}\lambda_{qdr}^s \qquad (7.29)$$

$$p\lambda_{qdr}^s = \frac{L_m}{L_r}r_r i_{qds}^s - \omega_{br}\lambda_{qdr}^s \qquad (7.30)$$

,where

$$\omega_{br} = \frac{r_r}{L_r} - j\omega_r \qquad (7.31)$$

The state space representation of the induction motor, based on the stationary frame equations (7.30) and (7.31) is given in (7.32) – (7.41) in the following.

$$
\frac{d}{dt}\begin{bmatrix} i^s_{ds} \\ i^s_{qs} \\ \lambda^s_{dr} \\ \lambda^s_{qr} \end{bmatrix} = \begin{bmatrix} a_{r11} & 0 & a_{r12} & -a_{i12} \\ 0 & a_{r11} & a_{i12} & a_{r12} \\ a_{r21} & 0 & a_{r22} & -a_{i22} \\ 0 & a_{r21} & a_{i22} & a_{r22} \end{bmatrix} \begin{bmatrix} i^s_{ds} \\ i^s_{qs} \\ \lambda^s_{dr} \\ \lambda^s_{qr} \end{bmatrix} + \begin{bmatrix} b_1 & 0 \\ 0 & b_1 \end{bmatrix} \begin{bmatrix} v^s_{ds} \\ v^s_{qs} \end{bmatrix}
\tag{7.32}
$$

$$
\frac{d}{dt}x = Ax + Bv_s
\tag{7.33}
$$

$$
i_s = Cx
\tag{7.34}
$$

$$
a_{r11} = -\left\{ \frac{r_s}{L_{\sigma s}} + \frac{(1-\sigma)}{\sigma \tau_r} \right\}
\tag{7.35}
$$

$$
a_{r12} = \frac{L_m}{\sigma L_s L_r}\frac{1}{\tau_r}
\tag{7.36}
$$

$$
a_{i12} = \frac{L_m}{\sigma L_s L_r}(-\omega_r)
\tag{7.37}
$$

$$
a_{r21} = \frac{L_m}{\tau_r}
\tag{7.38}
$$

$$
a_{r22} = -\frac{1}{\tau_r}
\tag{7.39}
$$

$$
a_{i22} = \omega_r
\tag{7.40}
$$

$$
b_1 = \frac{1}{L_{\sigma s}}
\tag{7.41}
$$

The flux observer is based on the stationary frame state-space equations of the induction motor in (7.32) – (7.41). The motor speed variable is estimated via an adaptation law and used within the motor model, as described in Figure 7.8.
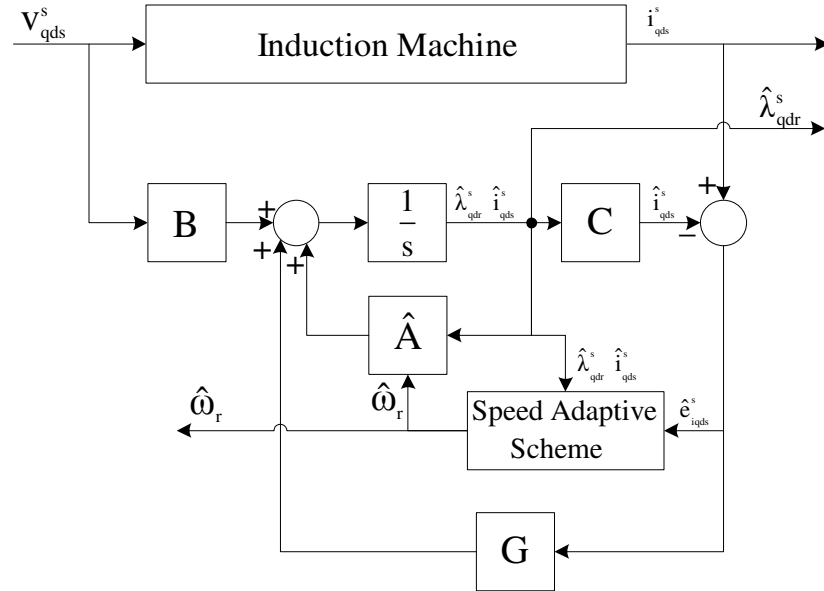
Figure 7.8 Speed adaptive flux observer block diagram.

The speed adaptive scheme estimates the rotor speed and the estimated speed is fed back to the state matrix (A) and also used for the sensorless speed control of the induction motor. The error state equation from the general observer theory is written for the speed adaptive flux observer in (7.42) – (7.47).

$$\frac{d}{dt}\hat{x}=\hat{A}x+Bu+G(i_{qds}^{s}-\hat{i}_{qds}^{s}) \tag{7.42}$$

$$\frac{d}{dt}e=\frac{d}{dt}(x-\hat{x})=(A-GC)(x-\hat{x})+(A-\hat{A})\hat{x}=(A-GC)e-\Delta A\hat{x} \tag{7.43}$$

where,

$$e=x-\hat{x} \tag{7.44}$$

$$\Delta A = \hat{A} - A = \begin{pmatrix} 0 & -\Delta\omega_r j/c \\ 0 & \Delta\omega_r j \end{pmatrix} \qquad (7.45)$$

$$c = \frac{(\sigma L_s L_r)}{L_m} \qquad (7.46)$$

$$\Delta\omega_r = \hat{\omega}_r - \omega_r \qquad (7.47)$$

Error in the state matrix (A) is due to the parameter estimation errors, however mainly due to the speed estimation error. The Lyapunov function representing the state-error of the observer is defined in (7.48).

$$V = e^T e + (\hat{\omega}_r - \omega_r)^2 / \lambda \qquad (7.48)$$

Lyapunov's stability theorem gives a sufficient condition for the uniform asymptotic stability of a nonlinear system by using the Lyapunov function in (7.48). The defined function satisfies the criteria to be continuous, differentiable and positive definite. A sufficient condition for uniform asymptotic stability is that the derivative of Lyapunov function is negative definite. Derivative of the Lyapunov function is defined in (7.49), where K is a constant.

$$\frac{d}{dt} V = e^T \{(A+GC)^T + (A+GC)\} e - 2\Delta\omega_r (e_{ids}\hat{\lambda}_{qr}^s - e_{iqs}\hat{\lambda}_{dr}^s)/c + 2\Delta\omega_r \frac{d}{dt}\hat{\omega}_r / K \qquad (7.49)$$

$$e_{ids} = i_{ds} - \hat{i}_{ds} \qquad (7.50)$$

$$e_{iqs} = i_{qs} - \hat{i}_{qs} \qquad (7.51)$$

In order the observer to be stable, the first term in (7.49) should be negative semi-definite and the second term must be equal to the third term. The first term can be negative semi-definite naturally or by proper selection of observer matrix G. Based

on the condition such that second term must be equal to the third term in (7.49), the relation for the speed estimation can be derived. If the speed estimation equation in (7.52) is employed, which is equalizing the second term to the third term in (7.49), then the Lyapunov's stability will be satisfied and system will operate stably.

$$\frac{d}{dt}\hat{\omega}_r = K(e_{ids}\hat{\lambda}_{qr}^s - e_{iqs}\hat{\lambda}_{dr}^s)/c \qquad (7.52)$$

The motor speed can be estimated by integrating the speed estimation equation (7.52). However, since rotor speed can change very quickly, speed estimation dynamics can be improved by using a proportional term in addition to the integration term, as in (7.53).

$$\hat{\omega}_r = K_p(e_{ids}\hat{\lambda}_{qr}^s - e_{iqs}\hat{\lambda}_{dr}^s) + K_I \int (e_{ids}\hat{\lambda}_{qr}^s - e_{iqs}\hat{\lambda}_{dr}^s)dt \qquad (7.53)$$

As a result, the stationary frame rotor fluxes are estimated with the speed adaptive flux observer and rotor speed is estimated and used as an adaptation mechanism. The estimated speed is used in the sensorless speed control loop and also for calculation of the rotor flux angle within the indirect vector control implementation. The estimated rotor fluxes can also be used directly to calculate the rotor flux angle for the direct field oriented control. In this thesis, indirect field oriented control with the estimated speed is implemented and the estimated speed is also used for the speed feedback of the speed control loop.

The observer gain matrix (G) can be calculated such that the observer poles are proportional to the poles of the induction motor and the stability of the observer is satisfied. The stability of the observer is provided without any observer gain matrix for medium and high speed region, hence the observer gain matrix is realized as zero matrix within the implementation of the speed adaptive flux observer in this thesis. Since the sampling period in the experiments is small enough with 10 kHZ sampling frequency, discretization of the speed adaptive flux observer is limited to be first order, for digital implementation of the speed adaptive flux observer.

The speed adaptive flux observer is improved, especially for the stability of the observer at low speeds and at regenerating mode in [18]. Similar to the adaptive rotor speed estimation, stator resistance adaptation mechanism is developed in parallel to this observer in [15]. Additionally, in order to compensate for the errors resulting from the nonlinearity of the voltage source inverter, adaptation schemes for voltage references are designed. Such improvements are not implemented within this thesis. The sensorless vector control and sensorless speed control algorithms based on the speed adaptive flux observer method is given in Figure 7.9.
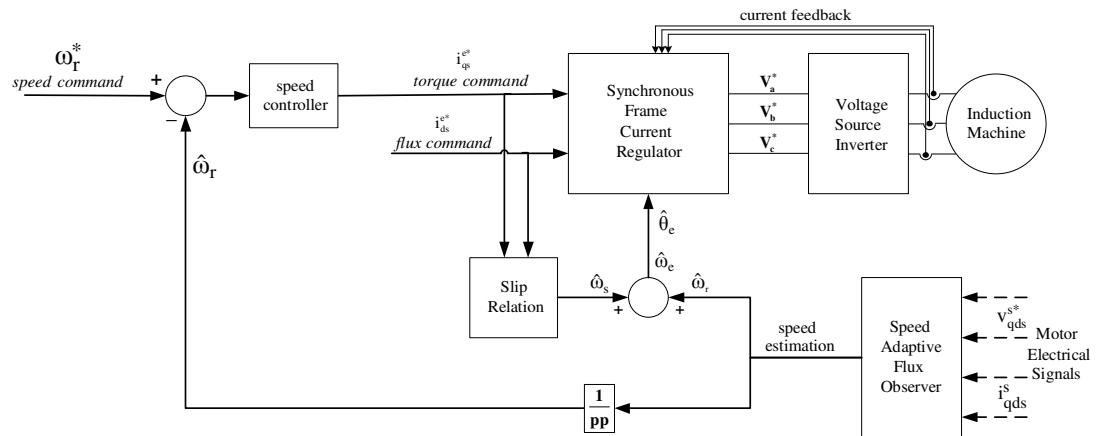
Figure 7.9 Sensorless speed control of the induction motor with the speed adaptive flux observer algorithm.

The speed adaptive flux observer theory is verified by simulations within the SIMPLORER software. However, the simulation results are omitted and only the experimental results of the sensorless control of the induction motor with the speed adaptive flux observer theory is given in the following section.

7.3.2 Experimental Results of The Speed Adaptive Flux Observer

The same closed slot induction motor, whose parameters are given in Table 7.1, and the experimental setup are utilized for the experimental verification of the speed adaptive flux observer theory. For the experiments in Figure 7.10-7.11, the

sensorless vector control and speed control of the induction motor is performed based on the speed adaptive flux observer theory as given in Figure 7.9, with the parameters in Table 7.2. For loading; a coupled servo motor is used in torque mode and up to 50% load torque is applied (due to the limited rating of the load drive), in opposite direction to the induction motor rotation. As seen in the experimental results below, the speed adaptive flux observer performs well and provides accurate speed estimation with dynamic performance.

Table 7.2 Parameters used within the speed adaptive flux observer experiments

Synchronous Frame Current Regulator	K_p	100
	K_I	16400
	LPF on the feedback path	2nd order with 1 kHz cut-off frequency
Adaptive Scheme Gains	K_P of the compensator	0.5
	K_I of the compensator	100
Speed Controller	K_{pr}	1
	K_p	0.072
	K_I	2
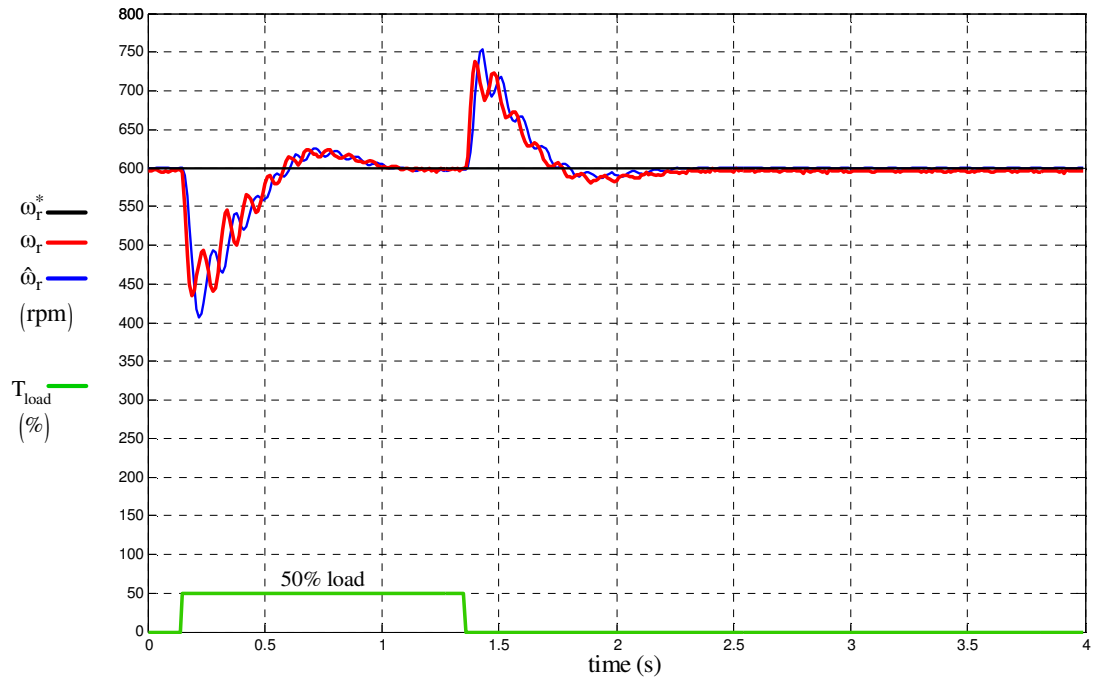
Figure 7.10 The commanded speed (black), actual speed (red), estimated speed (blue) and the load (green) for 50% step load and removal at constant 600 rpm.
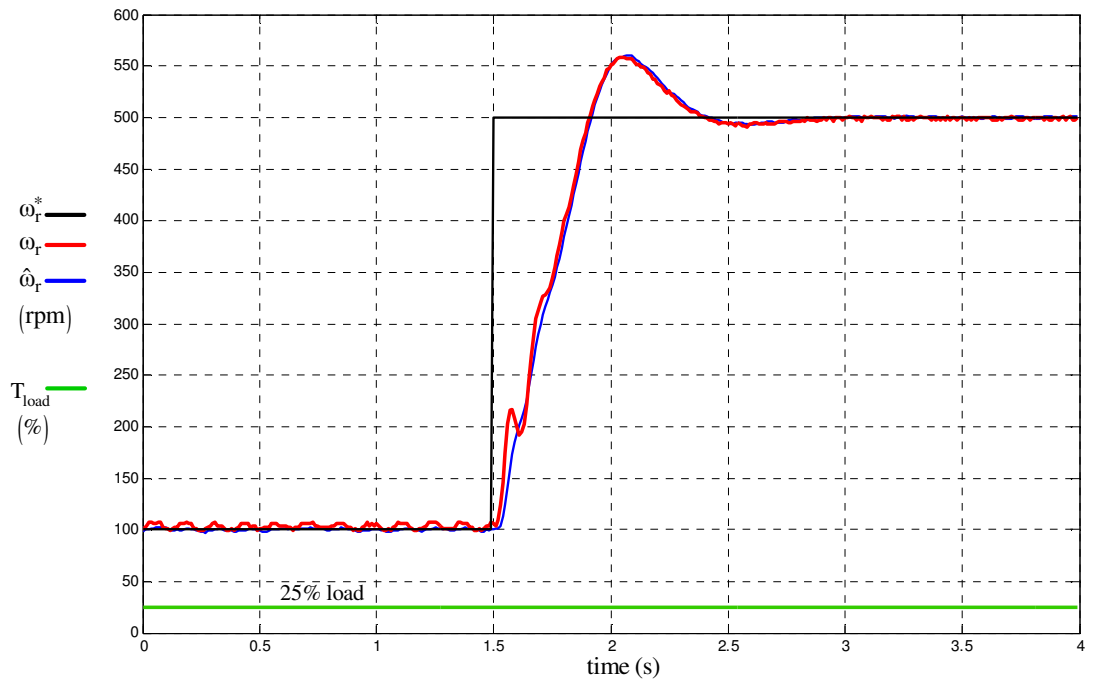
Figure 7.11 The commanded speed (black), actual speed (red), estimated speed (blue) and the load (green) for acceleration from 100 rpm to 500 rpm under constant 25% load.

CHAPTER 8

CONCLUSION

The IPM motor, which has high energy efficiency and high power density characteristics, has been important for the energy-hungry modern world and it is widely used in both industrial and servo applications requiring high efficiency and/or dynamic performance, in recent years. It is forecasted that the IPM motor will be employed more in the future applications. The structure of the IPM motor makes it favorable for the sensorless speed/position control applications, and important research has been made on the sensorless control of the IPM motor in recent years.

The fundamental model based estimation algorithms have been well developed for the IPM motor. The zero and low speed problems of the fundamental model based estimators are eliminated successfully by the use of saliency based estimation algorithms, which rely on the spatial (physical) anisotropy of the IPM motor. The hybrid approach combining the two types of estimation algorithms for the whole speed range sensorless operation have been developed and implemented in the industrial drives.

In this thesis, the above mentioned sensorless control algorithms for the vector/speed/position control of the IPM motor are implemented and experimentally investigated. The saliency based high frequency signal injection algorithm is utilized for the low and zero speed sensorless operation. The fundamental model based flux observer algorithm is utilized for moderate and high speed operation. The hybrid algorithm is implemented for the whole speed range operation. Similar performance

results of the modern sensorless drives are obtained for the whole speed range, including zero speed and for the loaded operating conditions.

The high frequency signal injection algorithm provided successful results for zero and low speed operation since it relies on the saliency of the IPM motor which exists independent of the speed of the motor. The saliency of the IPM motor is extracted and tracked; and the rotor flux angle is estimated with an accuracy of 10°, which is acceptable for the vector control conditions. Dynamics of the high frequency signal injection algorithm is analyzed and it is shown that the bandwidth of the rotor flux angle estimation is greater than 3 Hz. Also high performance speed and position control of the IPM motor is provided with high accuracy. The performance of the rotor flux angle and speed estimations, in the manner of ripple and dynamic response, is improved by the speed command feedforward method, which is developed in this thesis. The speed and position control loops, which are based on the estimations of the high frequency signal injection algorithm, are also verified under step and constant loading cases. The effect of the loading on the saliency of the IPM motor is investigated and it is shown that the minimum impedance point deviates from the rotor flux axis by an angle of 15° due to the saturation issue.

The flux observer algorithm performed successfully for motor speed greater than 100 rpm. The same rotor flux angle estimation accuracy of 10° is also obtained with the flux observer algorithm. The speed of the motor is estimated with high accuracy and low ripple, based on the flux observer algorithm.

Hybrid method combining the two methods, such that the high frequency signal injection algorithm is executed for the zero and low speed region and transition to the flux observer method is provided when the rotor accelerates to moderate and high speed region, and the inverse transition for deceleration, is realized depending on the estimated speed of the motor. The problematic transition conditions are eliminated by the adaptation of the parameters of the current/speed control loops and smooth transition is obtained between the two algorithms.

The saliency based high frequency signal injection algorithm and a speed adaptive flux observer algorithm are also implemented for the induction motor, in this thesis. The saliency of the induction motor, which arises due to the saturation on the flux axis, is extracted experimentally. However, the accuracy of the rotor flux angle estimation is found to be low; hence vector control could not be performed with the saliency based high frequency signal injection algorithm for the induction motor. However, sensorless vector control and speed control of the induction motor is accomplished successfully with the speed adaptive flux observer algorithm, which is utilized for medium and high speed region. The speed of the induction motor is close loop controlled based on the speed estimation of the speed adaptive flux observer algorithm, and verified experimentally under step loading and constant load operation.

All the estimation and control algorithms are verified by computer simulations and laboratory experiments. A DSP based inverter and a motor test bench, employing a high performance PMAC (servo) load machine with sensor feedback, are developed for laboratory experiments. Loading operation conditions are tested with the motor test bench and high sensorless torque/speed/position control performance is obtained from the estimation and control algorithms.

For our industrializing country, Turkey, energy prices are becoming more and more important and requirements are increasing for the motion control applications of the industry. Being the first research in Turkey for the sensorless control of the IPM motor, this thesis research has strategic importance for future applications. The scope of this thesis can be expanded by future work to include the necessary improvements related with its topic. As future work, initial position detection of the IPM motor is necessary for starting from an arbitrary position. Initial position detection of the IPM motor can be provided by the high frequency signal injection algorithm, based on the saturation of the flux [36], [56]. Also as a future work, effect of the loading on the saliency of the IPM motor can be investigated in detail, since the minimum impedance point can deviate from the rotor flux angle due to loading. Magnitude of the deviation can be analyzed and compensation methods, such as lookup tables can

be developed for performance improvement. Another challenging topic is the optimization for the maximum torque per ampere (MTPA) and field weakening for high speed operation which can be provided by optimization of the current references for the torque and flux axes. These optimizations will result in more efficient drives. Moreover, hybrid method can be improved by advanced algorithms utilizing the two estimation methods simultaneously as sensor fusion for improvement of the estimation performance and hence the torque/speed/position control performance.

Additionally, the high frequency injection method should be improved for the induction motor such that vector control is possible at low speed. This requires enhanced compensator design and gain selection for the observer and motion control loops.

REFERENCES

[1]   F. Blaschke. *Das Verfahren der Feldorientierung zur Regelung der Drehfeldmachine.* PhD thesis, TU Braunschweig, 1974.

[2]   K. Hasse. *Zur Dynamik Drehzahlgeregelter Antriebe mit Stromrichterge-speisten Asynchron-Kurzschlusslaufermachinen.* PhD thesis, TH Darmstadt, 1969.

[3]   T. M. Jahns, G. B. Kliman, and T. W. Neumann, " Interior PM Synchronous Motors for Adjustable Speed Drives," *IEEE Transactions on Industry Applications*, Vol. 22, No.4, pp. 738-747, 1986.

[4]   M. A. Rahman, T. A. Little, and G. R. Slemon, "Analytical Models for Interior-Type Permanent Magnet Synchronous Motors", *IEEE Transactions on Magnetics*, vol. MAG-21, No.5, pp. 1741-1743, 1985.

[5]   Jang-Mok Kim, Seung-Ki Sul, "Speed control of interior permanent magnet synchronous motor drive for the flux weakening operation, IEEE *Transactions on Industry Applications*, vol.33, pp. 43-48, January/February 1997.

[6]   T. M. Jahns, "Flux-weakening regime operation of an interior permanent-magnet synchronous motor drive,'' *IEEE Transactions on Industry Applications*, vol. IA-23, pp. 681-689, July/August 1986.

[7] M. A. Rahman, "Recent Advances of IPM Motor Drives in Power Electronics World," In *Power Electronics and Drive Systems Conference Records*, pp. 24-31, 2005

[8] K. Rajashekara and A. Kawamura, "Sensorless Control of AC Motor Drives, Speed and Position Sensorless Operation," IEEE Press, 1996.

[9] J. Holtz, "State of the Art of Controlled AC Drives without Speed Sensor", In *Power Electronics and Drive Systems Conference Records*, pp. 1-6, Singapore, 1995.

[10] R. Joetten and G. Maeder, "Control Methods for Good Dynamic Performance Induction Motor Drives Based on Current- and Voltage as Measured Quantities," *IEEE Transactions on Industry Applications*, Vol-IA-19, No.3, pp. 356-363, 1983.

[11] A. Abbondanti. "Method of flux control in induction motors driven by variable frequency, variable voltage supplies," In *IEEE-IAS Conf. Records.*, pp. 177-184, 1977.

[12] T. Ohtani, N. Takada, and K. Tanaka, "Vector control of induction motor without shaft encoder," In *IEEE-IAS Conf. Records*, pp. 500–507, San Diego, USA, 1989.

[13] H. Tajima and Y. Hori, "Speed sensor-less field orientation control of induction motor," In *IEEE-IAS Conf. Records*, pp. 385–391, Dearborn, USA, 1991.

[14] C. Schauder, "Adaptive speed identification for vector control of induction motor without rotational transducers," In *IEEE-IAS Conf. Records*, pp. 493-499, 1989.

[15] H. Kubota, K. Matsuse, and T. Nakano, "DSP-based speed adaptive flux observer of induction motor," *IEEE Transactions on Industry Applications*, vol. 29, no. 2, pp. 344-348, March/April 1993.

[16] Y.-R. Kim, S.-K. Sul, and M.-H. Park, "Speed sensorless vector control of induction motor using extended Kalman filter," *IEEE Transactions on Industry Applications*, vol. 30, pp. 1125–1233, September/October 1994.

[17] B. Akin, U. Orguner, A. Ersak, and M. Ehsani, "Simple derivative-free nonlinear state observer for sensorless AC drives," *IEEE/ASME Transactions on. Mechatronics,* vol. 11, no. 5, pp. 634–643, October 2006.

[18] H. Kubota, I. Sato, Y. Tamura, K. Matsuse, H. Ohta, and Y. Hori, "Regenerating-mode low-speed operation of sensorless induction motor drive with adaptive observer," *IEEE Transactions on Industry Applications*, vol. 38, no. 4, pp. 1081-1086, July/August 2002.

[19] M. Depenbrock, C. Foerth, and S. Koch, "Speed sensorless control of induction motors at very low stator frequencies," In *European Power Electronics Conference Records*, Lausanne, Switzerland, 1999.

[20] P. L. Jansen and R. D. Lorenz, "Transducerless field orientation concepts employing saturation-induced saliencies in induction machines," In *IEEE-IAS Conf. Records*, pp. 174–181, Orlando, USA, 1995.

[21] P. L. Jansen and R. D. Lorenz, "Transducerless Position and Velocity Estimation in Induction and Salient AC Machines," *IEEE Transactions on Industry Applications*, Vol. 31, No. 2, pp. 240-247, March/April 1995.

[22] J. I. Ha and S. K. Sul, "Sensorless field-orientation control of an induction machine by high-frequency signal injection," *IEEE Transactions on Industry Applications*, vol. 35, no. 1, pp. 45–51, January/February 1999.

[23] K. Ide, J. I. Ha, M. Sawamura, H. Iura, and Y. Yamamoto, "A novel hybrid speed estimator of flux observer for induction motor drives," In *IEEE International. Symposium on Industrial Electronics Records*, vol. 3, pp. 822-827, L Aquila, Italy, July 2002.

[24] E. Robeischl, M. Schroedl, and M. Krammer, "Position-sensorless biaxial position control with industrial PM motor drives based on INFORM-and back EMF model," In *IEEE Industrial Electronics Society Annual Conference Records*, vol. 1, pp. 668-673, Seville, Spain, November 2002.

[25] C. Silvia, G. M. Asher, and M. Sumner, "An HF signal-injection based observer for wide speed range sensorless PM motor drives including zero speed," In *European Power Electronics Conference Records*, vol. 1, pp. 1-9, Toulouse, France, September 2003.

[26] M. Tursini, R. Petrella, and F. Parasiliti, "Sensorless control of an IPM synchronous motor for city-scooter application," In *IEEE-IAS Conf. Records*, vol. 3, pp. 1472-1479, Salt Lake City, USA, October 2003.

[27] A. Pippo, M. Hinkkanen, and J. Luomi, "Sensorless control of PMSM drives using a combination of voltage model and HF signal injection," In *IEEE-IAS Conf. Records*, vol. 2, pp. 964-970, Seattle, USA, October 2004.

[28] K.Ide, J.I.Ha, M.Sawamura "A hybrid speed estimator of flux observer for induction motor drives" *IEEE Transactions on Industry Electronics*, vol. 53, no.1 pp. 130-137, February 2006.

[29] R. C. Becerra, M. Ehsani, and T. M. Jahns, "Four-quadrant brushless ECM drive with integrated current regulation," *IEEE Transactions on Industry Applications*, vol. 28, pp. 833–841, July 1992.

[30] R. Wu. And G. R. Slemon, "A Permanent motor drive without shaft sensor," In *IEEE-IAS Conf. Records*, pp. 553-558, 1990.

[31] Y. Li and N. Ertugrul, "A Novel, Robust DSP-Based Indirect Rotor Position Estimation for Permanent Magnet AC Motors Without Rotor Saliency," *IEEE Transactions on Power Electronics*, Vol. 18, No. 2, pp. 539-546, March 2003.

[32] A. B. Kulkarni and M. Eshani, "A novel position sensor elimination technique for the interior permanent magnet synchronous motor drive," *IEEE Transactions on Industry Applications*, pp144-150, January/February 1992.

[33] M. Corley and R. D. Lorenz, "Rotor position and velocity estimation for a permanent magnet synchronous machine at standstill and high speeds," *IEEE Transactions on Industry Applications*, vol. 34, pp. 784-789, July/August 1998.

[34] J.-I. Ha, K. Ide, T. Sawa, and S. Sul, "Sensorless position control and initial position estimation of an interior permanent magnet motor," In *IEEE-IAS Conf. Records*, pp. 2607-2613, Chicago, USA, September/October 2001.

[35] Y. Jeong, R. D. Lorenz, T. M. Jahns, and S. K. Sul, "Initial rotor position estimation of an interior permanent magnet synchronous machine using carrier-frequency injection methods," In *International Electrical Machine and Drive Conference Records*, pp. 1218-1223, June 2003.

[36] J. I. Ha, K. Ide, T. Sawa, and S. K. Sul, "Sensorless rotor position estimation of an interior permanent magnet motor from initial states," *IEEE Transactions on Industry Applications*, vol. 39, no. 3, pp. 761–767, May/June 2003.

[37] J. H. Jang, S. K. Sul, J. I. Ha, K. Ide, and M. Sawamura, "Sensorless drive of surface mounted permanent magnet motor by high frequency signal injection based on magnetic saliency," *IEEE Transactions on Industry Applications*, vol. 9, no. 4, pp. 1031–1039, July/August 2003.

[38] N. Patel, T. O'Meara, J. Nagashima, R. Lorenz "Encoderless IPM Traction Drive for EV/HEV's", In *IEEE-IAS Conf. Records*, pp. 1703-1707, September/October 2001.

[39] D. W. Novotny, "ECE511 Theory of Synchronous Machines Lecture Notes," University of Wisconsin, Madison, 1997

[40] D. W. Novotny and T. A. Lipo. "Vector Control And Dynamics Of AC Drives," Oxford University Press, 1996.

[41] C. D. Schauder and R. Coddy. "Current control of voltage source inverters for fast four-quadrant drive performance," *IEEE Transactions on Industry Applications*, pp. 163-171, March/April 1982.

[42] A. M. Hava, R. J. Kerkman, T. A. Lipo, "Simple Analytical and Graphical Methods For Carrier Based PWM-VSI Drives," *IEEE Transactions on Power Electronics*, Vol.14, pp. 49-61, January 1999.

[43] C. D. Schauder and R. Caddy, "Current control of voltage-source inverters for fast four-quadrant drive performance," *IEEE Transactions on Industry Applications*, vol. IA-18, pp. 163–171, March/April 1982.

[44] T. R. Rowan and R. L. Kerkman, "A new synchronous current regulator and an analysis of current-regulated PWM inverters," *IEEE Transactions on Industry Applications*, vol. IA-22, pp. 678–690, July/August 1986.

[45] L. J. Garces, "Current control of field oriented induction motor drives," In *IEEE Tutorial: Microprocessor Control of Motor Drives and Power Converters*, pp. 5.1–5.46, New York, USA, 1995.

[46] F. Briz, M. W. Degner, and R. D. Lorenz, "Analysis and design of current regulators using complex vectors," *IEEE Transactions on Industry Applications,* vol. 36, no. 3, pp. 817-825, May/June 2000.

[47] F. Briz, M. W. Degner, R. D. Lorenz, "Dynamic analysis of current regulators for AC motors using complex vectors," In *IEEE-IAS Conf. Records*, vol. 2, pp. 1253–1260, 1998.

[48] G. Ellis, R.D. Lorenz, "Comparison of motion control loops for industrial applications," In *IEEE-IAS Conf. Records*, vol. 4, pp. 2599 – 2605, October 1999.

[49] D. Y. Ohm, "Analysis of PID and PDF compensators for motion control systems," In IEEE-IAS Conf. Records, vol. 3 pp. 1923-1929, October 1994.

[50] W. Leonhard, "*Control of Electrical Drives*," 2nd Edition, Berlin, Springer, 1996.

[51] K. Ogata, "Modern control engineering," 3rd Edition, Prentice-Hall Inc., 1997.

[52] S. Ogasawara and H. Akagi, "Implementation and position control performance of a position-sensorless IPM motor drive system based on magnetic saliency," *IEEE Transactions on Industry Applications*, vol. 34, pp. 806-812, July/August 1998.

[53] J.-I. Ha, S.-K. Sul, K. Ide, I. Murokita, and K. Sawamura, "Physical understanding of high frequency injection method to sensorless drives of an induction machine," In *IEEE-IAS Conf. Records*, vol. 3, pp. 1802-1808, Rome, Italy, October 2000.

[54] M. Schroedl, "Sensorless control of AC machines at low speed and standstill based on the "INFORM" method," In *IEEE-IAS Conf. Records*, vol. 2, pp. 270-277, San Diego, USA, October 1996.

[55] C. Caruana, G.M. Asher, M. Summer, "Performance of HF signal injection techniques for zero-low-frequency vector control of induction Machines under sensorless conditions", *IEEE Transactions on Industrial Electronics,* vol 53, pp. 225-238, February 2006.

[56] J. M. Kim, S. J. Kang, and S. K. Sul, "Vector control of interior permanent magnet synchronous motor without a shaft sensor," In *Applied Power Electronics Conference Records,* vol. 2, pp. 743-748, 1997.

[57] C-H Choi, J.-K. Seok, "Pulsating Signal Injection-Based Axis Switching Sensorless Control of PMSM for Minimal Zero Current Clamping Effects," In *International Electric Machines and Drives Conference Records,* vol. 1, pp. 220-224, May 2007.

[58] J.-H. Jang, S.-K. Sul, J.-I. Ha, K. Ide, and M. Sawamura, "Sensorless drive of SMPM motor by high frequency signal injection," In *Applied Power Electronics Conference Records*, vol. 1, pp. 279-285, 2002.

[59] S. Östlund and M. Brokemper, "Sensorless rotor-position detection from zero to rated speed for an integrated PM synchronous motor drive," *IEEE Transactions on Industry Applications*, vol. 32, pp. 1158-1165, September/October 1996.

[60] Ansoft Simplorer V7.0. A power electronics simulation software, Ansoft Corporation, 2004.

[61] eZdsp^{TM} F2808 USB Technical Reference, Spectrum Digital, November 2004.

[62] "Code Composer Studio Getting Started Guide," Texas Instruments, November 2001.

[63] Matlab 7.4 (R2006b). A numerical computation software, Mathworks Inc., September 2006

[64] Texas Instruments, "TMS320x280x Enhanced Quadrature Encoder Pulse (eQEP) Module Reference Guide," Literature Number: SPRU790A, November 2004-Revised January 2006

[65] Texas Instruments, "TMS320x280x Enhanced Pulse Width Modulator (ePWM) Module Reference Guide," Literature Number: SPRU791D, November 2004-Revised October 2007